Chem Soc Rev

# Emerging Trends in Anion Storage Materials for Capacitive and Hybrid Energy Storage and Beyond



| | |
|---|---|
| Journal: | *Chemical Society Reviews* |
| Manuscript ID | CS-SYN-06-2020-000721.R2 |
| Article Type: | Review Article |
| Date Submitted by the Author: | 22-Mar-2021 |
| Complete List of Authors: | Dou, Qingyun; Sungkyunkwan University College of Natural Science<br>Wu, Nanzhong; Shenzhen Institutes of Advanced Technology Chinese Academy of Sciences<br>Yuan, Haocheng; Sungkyunkwan University College of Natural Science<br>Shin, Kang Ho; Sungkyunkwan University School of Chemical Engineering,<br>Tang, Yongbing; Shenzhen Institutes of Advanced Technology Chinese Academy of Sciences, Functional Thin Films Research Center<br>Mitlin, David; University of Texas at Austin<br>Park, Ho Seok; Sungkyunkwan University College of Natural Science, School of Chemical Engineering |
| | |

ARTICLE

# Emerging Trends in Anion Storage Materials for Capacitive and Hybrid Energy Storage and Beyond

Received 00th January 20xx,
Accepted 00th January 20xx

DOI: 10.1039/x0xx00000x

Qingyun Dou,†[a] Nanzhong Wu,†[cd] Haocheng Yuan,[a] Kang Ho Shin,[a] Yongbing Tang,*[cd] David Mitlin,*[e] Ho Seok Park*[ab]

Electrochemical capacitors charge and discharge more rapidly than batteries over longer cycles, but their practical applications remain limited owing to their significantly lower energy densities. Pseudocapacitors and hybrid capacitors have been developed to extend Ragone plots to higher energy density values, but they are also limited by insufficient breadth of options for electrode materials, which require materials storing alkali metal cations such as $Li^+$ and $Na^+$. Herein, we report a comprehensive and systematic review of emerging anion storage materials for performance- and functionality-oriented applications in electrochemical and battery-capacitor hybrid devices. The operating principles and types of dual-ion and whole-anion storage in electrochemical and hybrid capacitors are addressed along with the classification, thermodynamic and kinetic aspects, and associated interfaces of anion storage materials in various aqueous and non-aqueous electrolytes. Subsequently, the charge storage mechanism, structure-property correlation, and electrochemical features of anion storage materials are comprehensively discussed. The recent progress in emerging anion storage materials is also discussed, focusing on high-performance applications, such as dual-ion- and whole-anion-storing electrochemical capacitors in a symmetric or hybrid manner, and functional applications including micro- and flexible capacitors, desalination, and salinity cells. Finally, we present our perspective on the current impediments and future directions in this field.

## 1. Introduction

Electrochemical energy storage technologies have received significant attention owing to the ever-increasing demand for sustainable renewable energy and emerging applications in electrical vehicles, future electronic systems, and grid power storage.[1-3] Among various electrochemical energy storage devices, electrochemical capacitors store and deliver charges on the surface of electrode materials in a much more rapid manner over an order of magnitude longer life cycles compared to batteries do inside the internal structure.[3-8] However, the practical and emerging applications of electrochemical double-layer capacitors (EDLCs) are limited because of the low energy density associated with their intrinsic physical charge storage mechanism.[8-10] To resolve this issue, high-capacitance pseudocapacitive materials that store energy via a Faradaic reaction on an electrode surface have been developed,[11-18] while hybrid capacitors integrating capacitive electrodes with high-capacity battery-type or pseudocapacitive electrodes in an asymmetric manner have been exploited to further increase the cell voltage.[19-26] Classical pseudocapacitors and hybrid capacitors are limited to the combination of non-Faradaic and Faradaic electrodes that store alkali metal cations such as $Li^+$ and $Na^+$,[21, 23] leading to insufficient breadth of options for electrode materials. Accordingly, very few examples of successfully commercialized hybrid capacitors are asymmetric cells of activated carbon (AC) pairing with lithiated graphite, lithium titanium oxides, and lithium manganese oxides.[19, 23, 24]

Since the pioneering works on anion storage of graphite cathodes in metal-graphite batteries date back to 1971,[27, 28] in the past decade, anion storage materials have been extensively investigated to increase the cell voltage of full cells for the enhanced energy density.[29, 30] Despite previous review articles on battery-type anion storage materials,[29-34] comprehensive and systematic reviews focusing on battery-capacitor hybrid cells and functional capacitors have not yet been reported. Future design of anion storage materials and associated full cells can be benchmarked to overcome the limited energy density and functionality of electrochemical capacitors.[35-38] In contrast to metal-cation-storing hybrid capacitors and dual-ion-storing EDLC-type capacitors, advanced electrochemical and hybrid capacitors based on dual-ion, and whole-anion cells can be devised to improve energy density while preserving the outstanding kinetic and cyclic performances.[36, 38-41] Such a cell configuration can be further extended into functional capacitors such as microcapacitors, flexible or wearable designs, desalination, and salinity cells.[42-50] To maintain the

[a] School of Chemical Engineering, Sungkyunkwan University (SKKU), 2066 Seobu-ro, Jangan-gu, Suwon 440-746, Korea.
[b] Department of Health Sciences and Technology, Samsung Advanced Institute for Health Sciences and Technology (SAIHST), Sungkyunkwan University, 2066, Seoburo, Jangan-gu, Suwon 440-746, Korea.
[c] Functional Thin Films Research Center, Shenzhen Institute of Advanced Technology, Chinese Academy of Sciences, Shenzhen 518055, China.
[d] Shenzhen College of Advanced Technology, University of Chinese Academy of Sciences, Shenzhen 518055, China.
[e] Walker Department of Mechanical Engineering, The University of Texas at Austin, Austin, Texas 78712-1591, United States.

kinetic and cyclic features of electrochemical capacitors, high-capacity (or capacitive) anion storage materials need to be paired with capacitive (or capacity) materials and balanced both energetically and kinetically at various rates and for long cycles at the cell level.[19, 21, 51, 52] Given these criteria, this review focuses on potential anion storage materials that can be applied in electrochemical and hybrid capacitor design, considering a wide scope of materials and technologies from EDLC-type and pseudocapacitive carbon materials,[53-55] to Faradaic graphite,[36, 56, 57] transition metal hydroxides,[38, 52, 58, 59] oxides,[60-65] nitrides,[66-68] sulfides,[69-71] phosphides,[72, 73] selenides,[74, 75] carbonate hydroxides,[76, 77] halides/oxyhalides,[78-81] perovskite oxides and fluorides,[39, 82, 83] bismuth (Bi)-based materials,[84-86] lead (Pb)-based materials,[87-89] small molecule- and polymer-based p-type organics,[31, 90] and metal organic and covalent organic frameworks (MOFs and COFs) and their derivatives,[91-95] as shown in **Fig. 1**. These anion storage materials can store various anion carriers, such as hydroxyl ion ($OH^-$), nitrate ($NO_3^-$), and sulfate ($SO_4^{2-}$), chloridion ($Cl^-$), fluorinion ($F^-$), trifluoromethane sulfonate ($OTf^-$), bis(fluorosulfonyl) imide ($FSI^-$), bis(trifluoromethanesulfonyl) imide ($TFSI^-$), hexafluorophosphate ($PF_6^-$), perchlorate ($ClO_4^-$), tetrafluoroborate ($BF_4^-$), and tetrachloroaluminate ($AlCl_4^-$), in either non-Faradaic or Faradaic manner or both.[8, 29, 30, 33, 38, 84, 96-99] Anion storage systems in aqueous electrolytes have advantages in terms of their high ionic conductivity, low cost, easy practical fabrication process, and environmental friendliness,[33, 38, 58, 65-67, 96, 97] and they are compatible with desalination and salinity cells that use salt water as electrolytes.[48-50, 84, 100-102] Anion storage in non-aqueous electrolytes provides an unique opportunity to enlarge cell voltage by means of different operating potentials in the two electrodes and the kinetic stability of the passivating interface layers, allowing greatly improved energy density.[21, 30, 35, 36, 41, 103] More research attention may be beneficial for the design of electrochemical capacitors considering the abnormal electrochemical features of anion storage materials, which are otherwise difficult to achieve with cation-storing systems of identical electrode materials. For instance, negative graphite electrodes storing $Li^+$ cations are kinetically sluggish, limiting the charging rate, while positive graphite electrodes storing anions are kinetically rapid, reaching an operating potential >4.5 V versus $Li^+/Li$, despite a lack of clear understanding of their mechanism.[56, 104, 105]

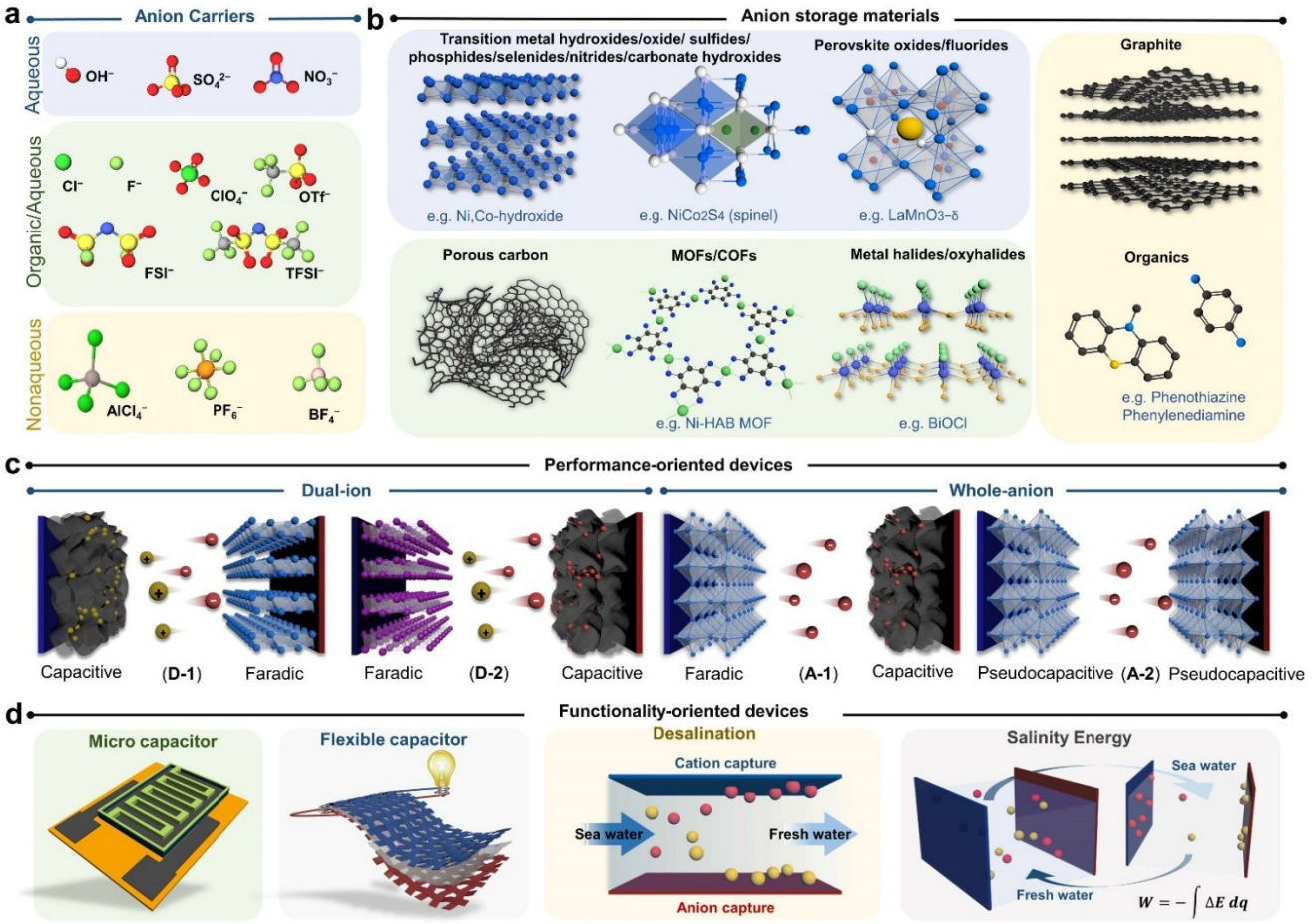


**Fig. 1** Schematic representation of the structures of typical (**a**) anion carriers, (**b**) anion storage materials, (**c**) configurations of performance-oriented dual-ion and whole-anion-storing electrochemical capacitors, and (**d**) functionality-oriented applications including micro- and flexible capacitors, desalination, and salinity cells.

Motivated by this fundamental and technical importance of anion storage materials, we report a comprehensive and timely review on energy storage mechanisms, chemical and physical features, and electrochemical performances of various anion storage materials for performance- and functionality-oriented applications in electrochemical and hybrid capacitors. First, the classification and operating principles of dual-ion and whole-anion-storing hybrid capacitors are discussed, and the correlation between anion storage materials with anion carriers and electrolytes is discussed in **Section 2**. In **Section 3**, the mechanisms and physical and chemical/electrochemical characteristics of various anion storage materials are discussed, including (1) capacitive carbon materials storing various anions via electrostatic adsorption; (2) transition metal hydroxides, oxides, sulfides, phosphides, selenides, nitrides, oxygen-anion intercalated perovskite oxides, metal organic frameworks and their derivatives, and zinc (Zn) metals storing $OH^-$ ions; (3) anion intercalation graphite, p-type organics, metal organic, and covalent organic frameworks storing large-sized polyatomic anions ($PF_6^-$, $ClO_4^-$, $AlCl_4^-$); and (4) Pb-based materials storing $SO_4^{2-}$ ions and metal halides/oxyhalides storing $Cl^-$ and $F^-$ ions. In **Section 4**, the cell configurations and performances of anion-storing electrochemical and hybrid capacitors are introduced, including high-performance dual-ion-storing hybrid capacitors (a combination of a Faradaic anion storage positive electrode with a capacitive negative electrode, or a capacitive positive electrode with a Faradaic cation storage negative electrode) and whole-anion-storing electrochemical capacitors (a combination of a Faradaic anion storage negative electrode with a capacitive positive electrode, or two pseudocapacitive anion storage electrodes). Moreover, we discuss the recent progress in functional capacitive applications, such as micro/flexible capacitors, desalination, and salinity cells. Finally, we discuss the present challenges and potential future directions for anion storage-based electrochemical capacitors and hybrid devices in **Section 5**.

## 2. Classification and mechanism of anion storage materials

To discuss the operating principles of anion-storing electrochemical capacitors and the associated anion storage mechanisms, we classify their cell configurations as dual-ion- and whole-anion-storing electrochemical capacitors (**Fig. 1c**). When two electrodes in an asymmetric full cell operate in different charge storage mechanisms, including one capacitive electrode, this cell is defined as a hybrid electrochemical capacitor. In the case of dual-ion-storing full cells, anion storage materials can be either (**D-1**) Faradaic (pseudocapacitive or battery-type) or (**D-2**) capacitive electrodes, while cation storage counterparts can be (D-1) capacitive or (D-2) Faradaic electrodes in hybrid capacitors. Conventional symmetric EDLCs also store both cations and anions on the surface of oppositely charged carbon electrodes. Whole-anion-storing capacitors can be divided into two types of cell configurations. When one electrode is capacitive and the other is Faradaic, whole-anion-storing capacitors become (**A-1**) hybrid capacitors. Alternatively, (**A-2**) two-electrode anion storage shows Faradaic pseudocapacitance in a symmetric manner. In this review, dual-ion- and whole-anion-storing full cells consisting of two battery-type electrodes are excluded because this review focuses on capacitor-based cells. The fundamentals of these anion storing capacitors are addressed in terms of the thermodynamic and kinetic aspects of electrode and electrolyte materials. The mechanisms and features of anion-storing electrodes are discussed in detail in Sections 2.2 and 3.

### 2.1 Thermodynamic & kinetic aspects of anion storing capacitors and materials

**Operating principles and thermodynamics of anion storing capacitors and materials. Figs. 2a and 2b** show schematic illustrations of the operating principles and thermodynamic aspects of representative dual-ion and whole-anion-storing hybrid capacitors. On charging, electrons are transferred from the positive electrode to the negative electrode via an external circuit, while the ion carries are captured or released by the electrodes to retain charge neutrality. For the (D-1) dual-ion hybrid capacitors (**Fig. 2a**), the anions are transported to the Faradaic positive electrode, where charge transfer occurs at the electrode/electrolyte interface. Cations are electrostatically adsorbed on the capacitive negative electrode to balance the accumulated negative charge. For the (A-1) whole-anion hybrid capacitors (**Fig. 2b**), the anions are released from the negative electrode to the electrolyte, and the active anions are adsorbed on the positive electrode. On discharging, the electrochemical processes are reversed in the dual-ion- and whole-anion-storing capacitors. The electrochemical stability window (ESW) of the electrolyte is defined by its oxidative potential limit ($P_O$) and reductive potential limit ($P_R$) for electrolyte oxidation and reduction, respectively. The redox potentials of the positive and negative electrodes need to be located within the ESW of the electrolyte, unless a stable solid electrolyte interface (SEI) (or a cathode electrolyte interphase (CEI) for the positive electrode) is formed to provide kinetic stability for electrolyte decomposition. The cell voltage, which is the potential gap between the positive and negative electrodes, can be particularly enlarged in a dual-ion hybrid cell.

For Faradaic (pseudocapacitive or battery-type) anion storage materials, the half reaction can be expressed as:

$$([A]^+anion^-)^0 + e^- \leftrightarrow [A]^0 + anion^- \quad (1)$$

where the solid-state $[A]^0$ and $([A]^+anion^-)^0$ have a unit activity. The anion storage process follows the Nernst equation:

$$E = E^o - (RT/nF)\ln(a_{[anion-]}) \quad (2)$$

where $a_{[anion-]}$ is the activity of anion; $E$ and $E^o$ are the real-time potential and standard potential of the redox couple; $R$ is the gas constant; $T$ is the absolute temperature; $n$ is the mole number of transferred electrons ($n$ = 1); and $F$ is the Faraday constant.

According to the Nernst equation (2), an increase in electrolyte concentration leads to an increase in $a_{[anion-]}$, thus negatively shifting the electrode potential of the anion storage materials and vice versa.[114-116] As a side note, the potential of cation storage materials shifts positively with increasing electrolyte concentration. This behavior can be used to distinguish anion storage materials from cation storage materials.

Because liquid electrolytes consist of anion carriers and solvents, their physical and chemical properties affect thermodynamic aspects of anion-storing capacitors. **Fig. 1a** shows various anion carriers, including $OH^-$, $Cl^-$, $F^-$, $ClO_4^-$, $NO_3^-$, $SO_4^{2-}$, $PF_6^-$, $AlCl_4^-$, $FSI^-$, $TFSI^-$, $BF_4^-$, and $OTf^-$, which can be dissolved in aqueous, organic, and ionic liquid (IL) solvents. Accordingly, the ESWs of electrolytes are dependent on the types and concentrations of anion carriers and solvents, as shown in **Figs. 2c and 2d**.

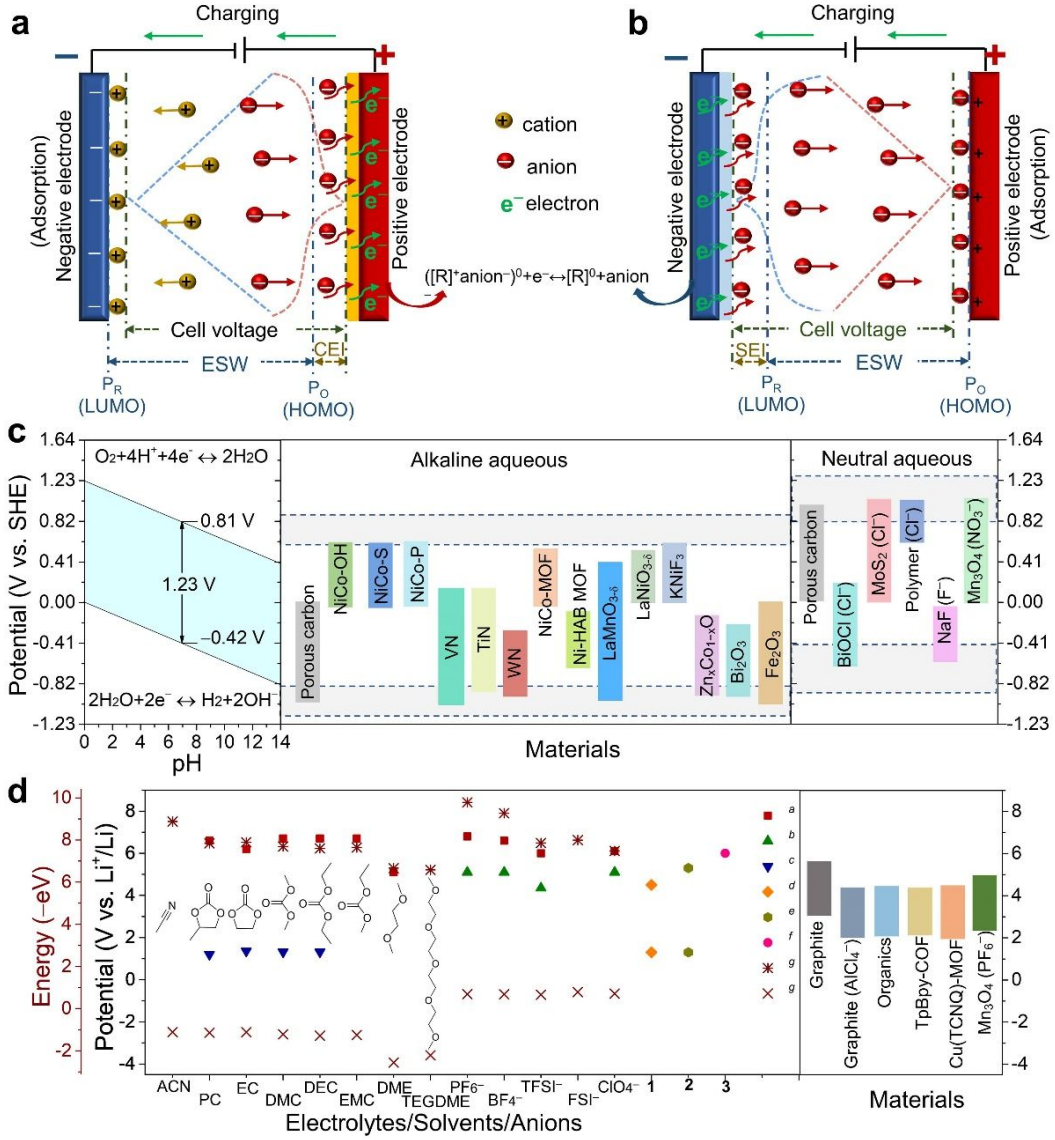


**Fig. 2** (**a**) Schematic showing the working principles of the dual-ion-storing hybrid capacitor combining a Faradaic positive electrode and a capacitive negative electrode, and (**b**) whole-anion-storing hybrid capacitor combining a Faradaic negative electrode and a capacitive positive electrode. (**c**) Schematic showing the thermodynamic ESW of water (1.23 V) dependent on pH values, and potential ranges of selected anion storage materials in alkaline aqueous electrolytes and neutral aqueous electrolytes. (**d**) Schematic showing the potential limits of selected anions, solvents, and electrolytes determined by experimental or computational methods, and the potential ranges of selected anion storage materials in non-aqueous electrolytes. [a] The oxidative potential limits of 0.65 M $NEt_4$-$BF_4$ in different solvents, or 0.65 M $NEt_4^+$-based salts in PC solvent, measured on glassy carbon electrode.[106, 107] [b] The oxidative voltage limits of 1 M $Li^+$-based salts in EC+DMC (1:1) solvent, measured on $LiMn_2O_4$ composite electrode.[108] [c] The reductive voltage limits of 0.1 M $LiClO_4$ in different solvents, measured on Pt electrode.[109] [d] The oxidative and reductive voltage limits of the 1 M $LiPF_6$ EC/DEC electrolyte (1).[109, 110] [e] The oxidative and reductive voltage limits of the LiTFSI+EMIM-TFSI IL electrolyte (2).[111] [f] The oxidative voltage limit of the 7.5 m LiFSI in EC/DMC electrolyte (3).[112] [g] The HOMO and LUMO of the solvents and $K^+$-based salts calculated from the B3LYP/6-31G.[113]

In aqueous electrolytes, the thermodynamic ESW of water is 1.23 V, where the hydrogen and oxygen evolutions respectively occur at −0.42 and 0.81 V versus standard hydrogen electrode (SHE) at a pH of 7.[117] The potentials of hydrogen and oxygen evolutions shift to lower values as the pH values of solutions increases, while the thermodynamic ESW of water remains 1.23 V as shown in **Fig. 2c**. The measured ESWs of aqueous electrolytes can exceed 1.23 V due to the kinetic suppression of water decomposition and decreased water activity.[118-122] $OH^-$ anion carriers are typically used in alkaline aqueous electrolytes with a high pH >14. $SO_4^{2-}$ can be used as anion carriers in sulfuric acid ($H_2SO_4$) aqueous electrolyte. Compared to alkaline and acidic aqueous electrolytes, neutral aqueous electrolytes have advantages in terms of their wider ESW values, more combinations of ion carriers (e.g., $Cl^-$, $F^-$, $NO_3^-$, $SO_4^{2-}$, and $ClO_4^-$ anions coupled with $Li^+$, $Na^+$, and $K^+$ cations), and less corrosion.[123-126]

Despite the benefits of safety and manufacturing simplicity,[118-120, 127] the major disadvantage of aqueous electrolytes is the narrow ESW that limits the energy density of full cells. To resolve this limitation, highly concentrated aqueous electrolytes, also called “water in salt” (WiS) electrolytes, are prepared by dissolving high-solubility salts, such as imide-based salts and zinc chloride ($ZnCl_2$), in extremely small amounts of water.[114, 121, 122, 128-130] These WiS electrolytes (e.g., 21 m (mol $kg^{-1}$) LiTFSI and 35 m NaFSI) exhibit widened ESWs, which is attributed to the absence of free water molecules, leading to reduced water activity.[121, 122, 128, 129] Hybrid electrolytes, where the salts are dissolved in mixed aqueous/organic solvents,[131-133] could widen ESWs further than those of WiS electrolytes owing to the extremely low water content in the major organic solvent.[132, 133] Given the widened electrolyte ESWs and a negative shift in the electrode potential (equation 2), WiS and hybrid electrolytes allow more anion storage materials with high potential to be used as positive electrodes, as compared to dilute aqueous electrolytes.[115, 130, 134-136] This rationale is also applied to anion storage electrodes in highly concentrated organic electrolytes (as discussed below).

In addition to highly concentrated aqueous and hybrid electrolytes, organic and IL electrolytes increase cell voltage due to wide ESWs and kinetic stability by passivating layers (SEI and CEI).[103, 137, 138] As shown in **Fig. 2d**, the oxidative and reductive potential limits also depend on the combination of anions and solvents, as determined by experimental or computational methods. It notes that the experimentally determined potential limits are influenced by measurement conditions and evaluation methods. For instance, oxidative potentials can be higher on less catalytically active surfaces owing to kinetic suppression of electrolyte decomposition.[139] The highest occupied molecular orbital (HOMO) and lowest unoccupied molecular orbital (LUMO) energies are correlated with the electronic properties (e.g., ionization potential and electron affinity) of isolated solvents and salts, which roughly predict their oxidative and reductive potential limits.[113, 140] Among the organic electrolytes, carbonate-based electrolytes show a suitable combination of oxidative and reductive stabilities. Acetonitrile (ACN)-based electrolytes exhibit high oxidative stability, but they are incompatible with low-potential negative electrodes (as discussed below).[141, 142] Ether-based electrolytes exhibit superior reductive stability but poor oxidative stability.[137] In case of anions, $PF_6^-$ and $BF_4^-$ are high-oxidation-tolerant anions. The oxidative and reductive stabilities of the electrolytes can be altered because they are determined by various factors, including solvent, salt, solvation/ion-pairing, and concentration.

It is known that anion intercalation into graphite occurs at high potentials (>4.5 V versus $Li^+/Li$) beyond the oxidative limit of conventional carbonate electrolytes, causing severe electrolyte decomposition. In an analogous manner to WIS aqueous electrolytes, highly concentrated organic electrolytes are beneficial for anion intercalation in graphite owing to their wide ESW and reduced anion-intercalation potential, which enhance the anion intercalation stability.[112, 143, 144] Despite the high dielectric constant ($\varepsilon_r$=89.8) of ethylene carbonate (EC), it is difficult to dissolve a high concentration (>1 M) of $PF_6$-based salts in EC-based solutions, and the tight binding between EC and $PF_6^-$ prevents the intercalation of $PF_6^-$ in graphite electrodes.[145, 146] Accordingly, ethyl methyl carbonate (EMC) is commonly used as a solvent for high-concentration electrolytes for $PF_6^-$ anion intercalation into graphite.[56, 105, 144, 147-150] EMC is capable of achieving high concentrations and resolving strong bindings with anions.[105, 147, 148, 151] For instance, when the electrolyte concentration increases from 1 to 4 M (mol $L^{-1}$) in a Li–graphite cell with $LiPF_6$/EMC electrolytes, the anion intercalation potential decreases from 4.45 to 4.34 V, while the specific capacity increases from 54 to 84 mAh $g^{-1}$.[147] In sharp contrast to $PF_6$-based salts, FSI-based salts can achieve high concentrations in an EC-dimethylene carbonate (DMC) solution.[112, 152] In a 5 M KFSI EC-DMC electrolyte, $FSI^-$ anions were intercalated into graphite within a potential range of 3.2–5.25 V versus $K^+/K$.[152] While in a 5 m KFSI-tetramethylene sulfone (TMS) electrolyte, the capacity fading over 300 cycles was negligible for a K–graphite cell in a potential range of 3.0–5.4 V versus $K^+/K$.[153] Along with the graphite positive electrode, highly concentrated organic electrolytes can be applied for p-type organic materials.[116, 154] When the concentration of $LiClO_4$ in the EC-DMC electrolyte increases, the dissolution of small-molecule p-type organic materials is suppressed, and the potential of the organic positive electrode decreases within the ESW of the electrolyte, thereby improving cycling performance and specific capacity.[116] Despite the benefits of cycling stability and capacity enhancements, concentrated electrolytes have disadvantages in terms of their low conductivity, high viscosity and density, and high cost of salts, which should be considered in their practical application.

ILs are entirely composed of ions in a liquid state at temperatures less than 100 °C.[155] They considered promising candidates for anion-intercalating graphite owing to their wide

electrochemical stability, high oxidative stability, negligible volatility, low flammability, and exclusion of solvent co-intercalation.[35, 57, 156-159] IL-based electrolytes for anion intercalation in graphite are generally in a mixed form, physically integrated with metal salts.[57, 157-159] For instance, the intercalation of $TFSI^-$ into graphite occurs over 5 V versus $Li^+/Li$ using 1 M LiTFSI+N-butyl-N-methylpyrrolidinium ($Pyr_{14}$)-TFSI with an ethylene sulfite (ES) additive.[57] The eutectic solvents, an analogue of ILs, have been investigated for anion storage.[104, 160, 161] A typical example is a mixture of aluminum chloride ($AlCl_3$) with 1-ethyl-3-methylimidazolium chloride (EMIMCl) that provides $AlCl_4^-$ anions.[104, 160] This EMIMCl-$AlCl_3$ electrolyte was applied to an Al–graphite battery operating through electrochemical Al deposition in the anode and intercalation of $AlCl_4^-$ into graphite cathode.[104] $AlCl_4^-$ intercalation into graphite occurs at a relatively mild redox potential of approximately 2 V versus Al anode

**Table 1** Physical features of anion carriers and aqueous electrolyte.

| Anions | $M$ [a] | $R$ [b] | $R_H$ [b] | $V_c$ [c] | $\sigma_0$ [d] | Electrolytes | $\sigma$ [e] |
|---|---|---|---|---|---|---|---|
| $OH^-$ | 17 | 1.76 | 3.0 | | 198 | $Li^+$/1 M | 134.5 |
| | | | | | | $Na^+$/1 M | 160 |
| | | | | | | $K^+$/1 M | 184 |
| | | | | | | $K^+$/6 M | ~600 |
| $F^-$ | 19 | 1.36 | 3.52 | | 55.4 | $Na^+$/1 M | 60 |
| $Cl^-$ | 35.5 | 1.81 | 3.32 | | 76.3 | $Na^+$/1 M | 74.3 |
| $NO_3^-$ | 62 | 2.64 | 3.35 | 56.7 | 71.4 | $Na^+$/1 M | 65.9 |
| $SO_4^{2-}$ | 96 | 2.90 | 3.79 | 77.7 | 80.0 | $Na^+$/1 M | 50.8 |
| $ClO_4^-$ | 99.5 | 2.92 | 3.8 | 77.1 | 67.3 | $Na^+$/1 M | 65 |

[a] $M$ (g $mol^{-1}$) is the molar mass of anion. [b] $R$ (Å) and $R_H$ (Å) are the bare and hydrated anion size, respectively.[162] [c] $V_c$ ($Å^3$) is the cosmo volume of anion.[163] [d] $\sigma_0$ (S $cm^2$ $mol^{-1}$) is the equivalent ionic conductivity of anion.[164] [e] $\sigma$ (mS $cm^{-1}$) is the ionic conductivity of electrolyte.[164]

**Table 2** Physical features of anion carriers in non-aqueous electrolyte.

| Anions | $M$ [a] | $R$ [b] | $V_v$ [c] | BMIM$^+$-based IL | | Li salt/EC+DMC |
|---|---|---|---|---|---|---|
| | | | | $D_{cat}$ [d] | $D_{an}$ [d] | $\sigma$ [e] |
| $PF_6^-$ | 145 | 3.5 | 69 | 1.5 | 1.8 | 10.7 |
| $BF_4^-$ | 87 | 2.6 | 49 | 1.4 | 2.8 | 4.9 |
| $TFSI^-$ | 280 | 8.0×3.9 | 147 | 1.1 | 1.3 | 9.0 |
| $OTf^-$ | 149 | - | 80 | 0.8 | 1.8 | - |
| $ClO_4^-$ | 99.5 | 2.92 | 54 | - | - | 8.4 |
| $AlCl_4^-$ | 169 | 5.28 | 96 | - | - | - |

[a] $M$ (g $mol^{-1}$) is the molar mass of anion. [b] $R$ (Å) is the estimated sizes of anion (HyperChem. 7.52). [c] $V_v$ ($Å^3$) is the Van der Waals volumes of anion.[165] [d] $D_{cat}$ and $D_{an}$ ($10^{-7}$ $cm^2$ $s^{-1}$) are the diffusion coefficients of cations and anions, respectively, in BMIM$^+$-based ILs.[166, 167] [e] $\sigma$ (mS $cm^{-1}$) is the ionic conductivity of Li salts/EC+DMC (1:1) electrolytes (1 M).[138]

**Table 3** Physical features of organic solvents.

| Solvents | $M$ [a] | $\rho$ [b] | $\varepsilon_r$ [c] | $\eta$ [d] | $T_m$ [e] | $T_b$ [e] |
|---|---|---|---|---|---|---|
| Acetonitrile (ACN) | 41 | 0.78 | 36.0 | 0.34 | −49 | 82 |
| Propylene carbonate (PC) | 102 | 1.20 | 64.9 | 2.5 | −49 | 242 |
| Ethylene carbonate (EC) | 88 | 1.32 [f] | 89.8 [f] | 1.9 [f] | 36.4 | 248 |
| Dimethylene carbonate (DMC) | 90 | 1.06 | 3.1 | 0.59 | 4.6 | 91 |
| Diethylene carbonate (DEC) | 118 | 0.97 | 2.8 | 0.75 | −74 | 126 |
| Ethyl-methyl carbonate (EMC) | 104 | 1.01 | 2.9 | 0.65 | −53 | 110 |
| 1,2-Dimethoxyethane (DME) | 90 | 0.86 | 7.2 | 0.46 | −58 | 84 |
| Tetraethylene glycol dimethyl ether (TEGDME) | 222 | 1.01 | 7.5 | 3.4 | −30 | 275 |
| Tetramethylene sulfone (TMS) | 120 | 1.26 [g] | 43.3 [g] | 10.28 [g] | 28 | 287 |

[a] $M$ (g $mol^{-1}$) is molar mass. [b] $\rho$ (g $cm^{-3}$) is the density. [c] $\varepsilon_r$ is the relative dielectric constant. [d] $\eta$ (cp) is the viscosity. [e] $T_m$ and $T_b$ (°C) are the melting point and boiling point, respectively. [f] At 40 °C. [g] At 20 °C. Physical properties are cited from ref.[138] and [113].

**Kinetic aspects of anion storing capacitors and materials.** In addition to the thermodynamic aspects of anion storage materials, such as theoretical capacity, electrode potential, and ESW, kinetic parameters such as charge transfer, electronic and ionic conductivities, and ion access to the active sites need to be considered because they significantly affect the kinetic (rate and power) performance, stability (*vide infra*), and efficiency of anion-storing capacitors.

The physical features of the selected anions and solvents in aqueous and non-aqueous electrolytes are summarized in **Tables 1, 2, and 3**. Similar to the ESWs of electrolyte solutions, their kinetic properties also depend on the combination of ion carriers and solvents. In aqueous electrolytes, $OH^-$ carriers have a much higher ionic conductivity than other carriers (**Table 1**). The ionic conductivity of $OH^-$ carriers is dependent on the types of counter cations and the solution concentrations; this is evident by the fact that the highest ionic conductivity performance of approximately 600 mS $cm^{-1}$ was achieved in a 6 M KOH electrolyte among various alkaline aqueous electrolytes.[164]

In EDLCs, organic electrolytes usually consist of ternary ammonium salts (e.g., tetraethylammonium ($NEt_4$)-$BF_4$, $Pyr_{14}$-$BF_4$) and imidazolium-based salts (e.g., EMIM-$BF_4$) dissolved in ACN or propylene carbonate (PC) solvents.[168, 169] ACN-based electrolytes exhibit higher ionic conductivity than PC-based electrolytes due to the lower viscosity and higher solvating power despite lower dielectric constant (**Table 3**).[142, 170] However, ACN is more flammable and toxic than PC.[168] For solutes, $BF_4^-$-based salts (e.g., $NEt_4$-$BF_4$, and EMIM-$BF_4$) are preferred owing to their wide ESW and high ionic conductivity.[127, 171]

In faradaic anion storage systems, carbonate-based electrolytes are widely used owing to the formulation of cyclic carbonate (with a high dielectric constant) and linear carbonate (with low viscosity) and the formation of a stable SEI. The physical properties of these carbonate electrolytes, including metal salts such as $LiPF_6$, $NaPF_6$, $KPF_6$, $LiClO_4$, $NaClO_4$, and $LiBF_4$, are dependent on the type of anions (**Table 2**). Although $BF_4^-$ itself has high mobility, $BF_4^-$-based metal salts (e.g., $LiBF_4$) have low solubility and high viscosity in carbonate solutions, thereby demonstrating low ionic conductivity. $ClO_4^-$-based salts exhibit satisfactory solubility and relatively high ionic conductivity. However, the strong oxidation of $ClO_4^-$ arising from the high valence state of Cl (VII) may result in safety issues.[138] $PF_6^-$-based salts are preferred because of their balanced properties such as ionic conductivity, viscosity, stability against oxidation, and stable SEI formation.[138] The $PF_6^-$-based carbonate electrolytes generally require a mixture of EC and linear carbonates (e.g., DMC and diethylene carbonate (DEC)) owing to the melting point depression of EC ($T_m$=36.4 °C) with a high dielectric constant and less viscous linear carbonate (**Table 3**).[94, 172-175] At an appropriate ratio of the two carbonate solvents, the resultant mixture has advantages in terms of high conductivity, low viscosity, and wide ESW.

Along with the thermodynamic ESWs of organic electrolytes, the electrode/electrolyte interface should be considered because the formation of SEI affects the kinetic stability and transportation properties. Because organic electrolytes are thermodynamically unstable at low-potential negative electrodes (e.g., Li, Na, and K metals and Li-intercalation graphite), SEIs are formed to operate beyond the thermodynamic limit of the electrolytes, as shown in **Fig. 2**. Likewise, stable CEIs are sometimes required for high-potential positive electrodes. Among various organic electrolytes, most carbonate-based electrolytes can be used for low-potential negative electrodes by forming stable SEIs, which, coupled with their high oxidative stability, can be expected to achieve high energy. In contrast, ACN-based electrolytes are not extensively applied because of the poor reductive stability of ACN and the failure of stable SEI formation on the negative electrodes.[141, 142] Thus, the anion storage materials as positive electrodes are coupled with high-potential negative electrodes (e.g., Li-storage $Li_4Ti_5O_{12}$, Mg-storage organics, and EDLC-type electrodes) in ACN-based electrolytes.[154, 176] Ether-based electrolytes are suitable for low-potential negative electrodes because the associated SEI layers offer high ionic conductivity and stability.[177-179] However, ether-based electrolytes are incompatible with high-voltage anion storage materials because of their intrinsic oxidative instability.[116, 137, 151] For example, using LiTFSI/tetraethylene glycol dimethyl ether (TEGDME) electrolyte, the organic positive electrode for $TFSI^-$ storage yields a moderate average potential of 3.4 V versus $Li^+$/Li.[154]

### 2.2 Mechanisms of anion storage materials

**Fig. 3** illustrates the energy storage mechanisms, electrochemical reaction formula, operating potential, and charging/discharging profiles of anion storage materials for dual-ion and whole-anion-storing electrochemical capacitors. EDLC-type materials such as porous carbons can electrostatically adsorb all of the anions in both aqueous and non-aqueous electrolytes when the electrode is positively charged (**Fig. 3a**).[8] These materials are characterized by surface-confined electrochemistry, demonstrating linear galvanostatic charge/discharge (GCD) curves and rectangular cyclic voltammetry (CV) shapes.

The $OH^-$ ions in aqueous electrolytes can be stored in various anion storage materials, such as porous carbon materials, transition metal compounds, and MOFs, with different mechanisms. For Faradaic $OH^-$ storage in alkaline aqueous electrolytes, the $OH^-$ ions can react with Lewis acidic groups of functionalized carbon materials and organic ligands of MOFs, demonstrating pseudocapacitive behavior within relatively negative potential ranges.[55, 93]

In contrast, nickel (Ni)-, cobalt (Co)-, and manganese (Mn)-based hydroxides,[38, 58] oxides,[60, 62, 65, 180] nitrides,[68] sulfides,[70, 71] phosphides,[72, 73] selenides,[74] and carbonate hydroxides,[76, 77] MOFs (with active sites of metal centers),[181, 182] Zn metals,[183-186] and Bi-based and iron (Fe)-based materials[63, 64, 85, 86] can store charge under $OH^-$ ions via a conversion reaction in alkaline aqueous electrolytes. Among these, Ni and Co-based hydroxides and oxides demonstrate a battery-like behavior in a positive potential range of 0–0.7 V versus SHE (**Fig. 3b**). Their charge storage mechanism is based on the conversion reaction

between hydroxide ($M^{II}(OH)_2$), oxy-hydroxide ($M^{III}OOH$), and even oxide ($M^{IV}O_2$) via the breaking and formation of O–H bonds in the presence of $OH^-$ ions from alkaline aqueous electrolytes.[59, 65, 187] The other Ni, Co-based materials show a change in the valence states of metal centers during the charging/discharging process in an analogous manner to the battery-like behavior of Ni, Co-based hydroxides/oxides. Although the observed behaviors of Zn metals, Bi- and Fe-based materials also show battery-like characteristics, they operate in negative potential ranges of approximately −1.2 to 0 V versus SHE. In particular, early transition metal nitrides, such as vanadium nitrides (VN), titanium nitride (TiN), and tungsten nitride (WN), exhibit a pseudocapacitive behavior in alkaline aqueous electrolytes, demonstrating a sloped GCD profile within negative potential ranges.[42, 45, 66, 67, 188] For example, the surface nitride of VN is easily oxidized to form vanadium oxide in aqueous electrolytes, where the surface redox reactions occur on a few atomic layers of surface vanadium oxide interacting with $OH^-$ ions (**Fig. 3c**).[42, 66, 67] The valence state of V varies from II to IV depending on the selected potential window.[42, 67]

The oxygen vacancies of perovskite oxides ($ABO_3$) act as storage sites and migration path for the oxygen anion ($O^{2-}$).[39, 189] The anion storage of substoichiometric perovskite oxides such as $LaMnO_{3-\delta}$, $La_{0.2}Sr_{0.8}MnO_{3-\delta}$, and $SrCo_{0.9}Ni_{0.1}O_{3-\delta}$ is based on the oxygen anion intercalation mechanism in alkaline aqueous electrolytes.[39, 82, 83] Upon charging, $O^{2-}$ ions transferred from the adsorbed $OH^-$ ions are intercalated into the oxygen vacancy and diffused to the lattice, along with the oxidation of transition metals (B sites) (**Fig. 3d**). In particular, the type of B sites available determines the electrode potentials of perovskite oxides. For instance, the potential of $La_{1-x}Sr_xBO_{3-\delta}$ perovskite oxides changes from negative to positive in the order B = Fe, Mn, Co.[83] Other polyatomic anions such as $PF_6^-$, $ClO_4^-$, $FSI^-$, $TFSI^-$, and $AlCl_4^-$ can be stored in non-aqueous electrolytes when storing materials possess sufficient ion accommodation space. Graphite can store polyatomic anions via the anion intercalation into graphite lattice,[29,30] where electrons are transferred removing delocalized π electrons of graphene layers.[190, 191] The intercalated anions are periodically arranged along the stacking direction of the graphene layers.[29] Anion intercalation of graphite features several transition stages, indicating multiple potential plateaus in the GCD curves (**Fig. 3f**). The potential ranges of anion intercalation graphite are 4.5–5.3 V versus $Li^+/Li$ for $PF_6^-$, $FSI^-$, and $TFSI^-$,[56, 57, 112] and 1.5–2.5 V versus Al anode for $AlCl_4^-$.[104, 160]

p-Type organic materials can also accommodate various types of polyatomic anions such as $PF_6^-$, $ClO_4^-$, and $AlCl_4^-$ and halide ions of $Cl^-$ in both non-aqueous and aqueous electrolytes.[173, 192-194] The charge transfer of small and polymeric p-type materials results in the extraction of electrons from their original neutral state to a positively charged state via oxidation, which is balanced by anion uptake (**Fig. 3g**). Compared to anion intercalation graphite, the p-type organics operate within a lower positive voltage range of 3–4 V versus $Li^+/Li$.

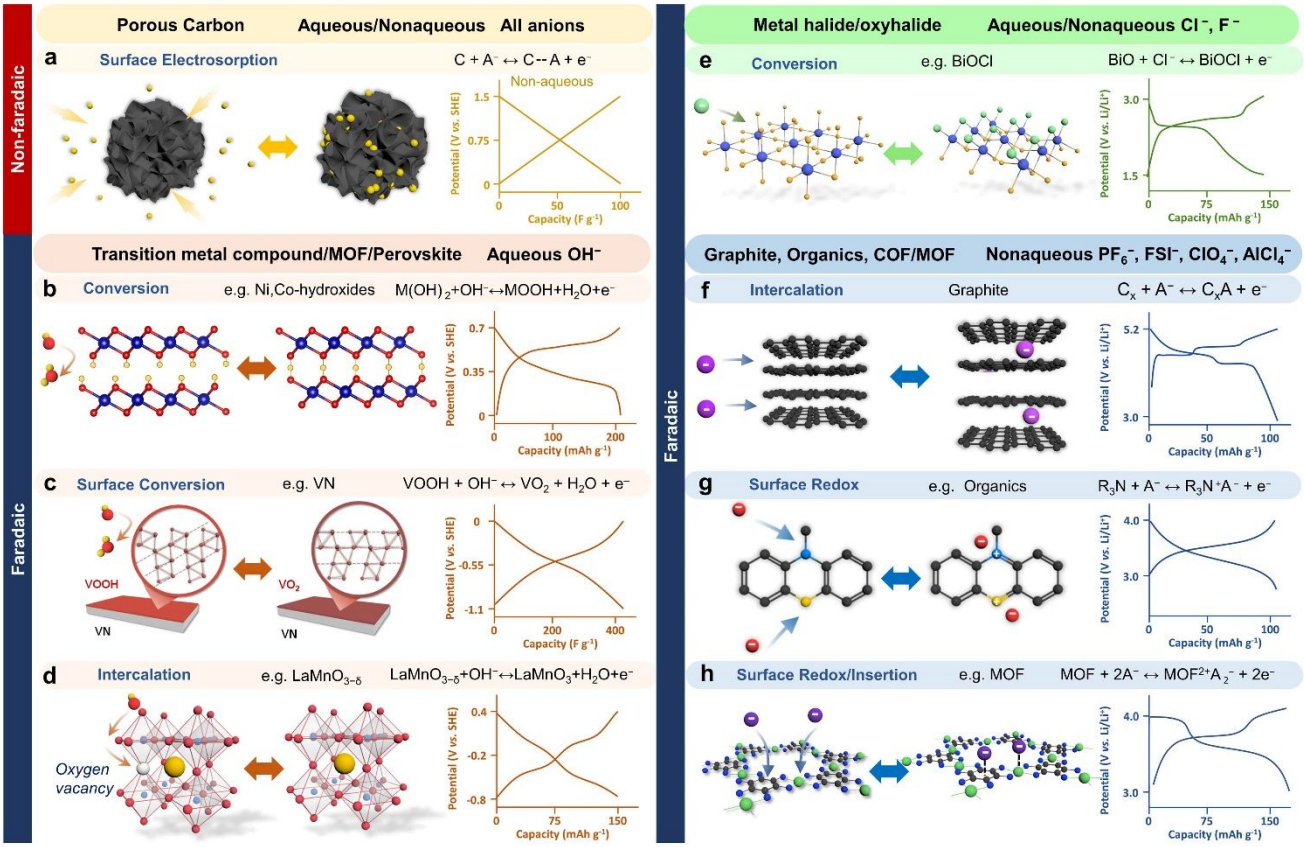


**Fig. 3** Schematic showing the storage mechanisms of typical anion storage materials and their characteristic GCD profiles.

Similar to p-type organic materials, the organic molecules on COFs and MOFs can act as hosts for polyatomic anion intercalation such as $PF_6^-$, $ClO_4^-$, and $AlCl_4^-$.[94, 195, 196] COFs and MOFs are advantageous because of the regularly interconnected porous channels facilitating anion transport. In addition to organic ligands, the metal centers of MOFs can react with anions, resulting in two plateaus on the GCD curves and high reversible capacity (**Fig. 3h**).[196]

Metal halides/oxyhalides as electrodes can store halide ions such as $Cl^-$ and $F^-$ ions in non-aqueous electrolytes via conversion reactions.[79-81, 197] The BiOCl electrode shows evident plateaus of battery-like behavior in the GCD curves (**Fig. 3e**).[197] In contrast to use in non-aqueous electrolytes, various halide ion storage materials in different mechanisms were exploited in aqueous electrolytes.[84, 198] In addition, both Pb and $PbO_2$ can be converted to $PbSO_4$ coupled with $SO_4^{2-}$ anions in $H_2SO_4$ aqueous electrolyte.[87-89]

## 3. Types and features of anion storage materials

In this section, we present a comprehensive overview of the charge storage mechanisms and physical, chemical, and electrochemical features of various anion storage materials, including (1) EDLC-type anion storage materials such as porous carbons; (2) Faradaic materials based on $OH^-$ ions such as functionalized carbons, Ni, Co-based hydroxides, oxides, nitrides, sulfides, phosphides, selenides, carbonate hydroxides, VN, TiN, MOFs, perovskite oxides/fluorides, Zn metals, Fe- and Bi-based materials; (3) Faradaic materials storing polyatomic anions (e.g., $PF_6^-$, $ClO_4^-$, $FSI^-$, $AlCl_4^-$) such as graphite, organics, COFs, and MOFs; and (4) Faradaic materials storing halide ions ($Cl^-$ and $F^-$) such as metal halides/oxyhalides and Pb-based materials storing $SO_4^{2-}$ anions.

### 3.1 EDLC-type anion storage materials.

Carbon-based materials are recognized as the principle EDLC-type materials owing to their large specific surface area, high electrical conductivity, as well as thermal, mechanical, and electrochemical stabilities.[6-8] Although carbon-based EDLC materials have been summarized in recent reviews,[8, 199-201] this review focuses on anion storage. Carbon electrodes electrostatically interact with and rapidly store anions via a non-Faradaic ion adsorption/desorption process at the electrode/electrolyte interface. Upon charging, contrary to the conventional understanding that the storage of anions is simply driven through adsorption on the positive electrode, anion desorption may also be involved on the negative electrode.[8, 202] Specifically, at a null potential, the pores of the carbon materials spontaneously fill with the same amounts of anions and cations from electrolytes owing to the ionophilicity of the carbon surface.[202-205] When two electrodes are positively and negatively polarized under an applied potential, the charge density is balanced because excess oppositely charged ions is adsorbed onto the electrodes. Given that anions and cations pre-exist in the carbon pores, the anions would undergo different adsorption/desorption behaviors of the two electrodes to ensure the neutrality of the electrode/electrolyte interface. On the positive electrode, anions can be solely adsorbed to compensate the positive charge of electrode through the counter-ion adsorption process, so-called permselectivity mechanism. Moreover, the positive charge of electrode can be also compensated by the adsorption of anions together with desorption of cations, which is known as ion swapping or permselectivity failure mechanism. In contrast, on the negative electrode, anion desorption accompanied by simultaneous cation adsorption sometimes occurs via an ion-swapping mechanism.

Various computational and experimental methods have been developed to investigate the charging mechanisms of EDLC-type materials.[203-218] Computational simulations can provide a theoretical understanding of charge storage behavior.[205, 206] Using molecular dynamics (MD) simulations, the arrangements of 1-butyl-3-methylimidazolium ($BMIM^+$) and $PF_6^-$ ions inside carbon pores electrified at varying potentials were investigated (**Fig. 4a**).[205] The carbon pores were filled with the same number (82) of $BMIM^+$ and $PF_6^-$ ions at a null potential. Upon charging, both electrodes experience ion swapping, and the electrolyte volume inside the carbon pores remains almost unchanged. The number of $PF_6^-$ anions in the positive electrode (115) increased, whereas it decreased in the negative electrode (55). Electrochemical quartz crystal microbalance (EQCM) technique can be used to monitor tiny mass changes of electrodes arising from the adsorption/desorption of electrolyte ions through an EDLC mechanism.[207-210] The ion adsorption and desorption behavior are dependent on the polarization degree of the carbon electrode in various electrolytes. Under the highly positive polarization of the electrode, the charging process was dominated by anion adsorption. Such a permselectivity mechanism failed on the low-polarized electrodes because both anions and cations were involved in charge storage (**Fig. 4b1**).[208] Moreover, different charging behaviors were observed for different halide anions, showing that smaller anions play more significant roles in charging (**Fig. 4b2**). Nuclear magnetic resonance (NMR) spectroscopy can be used to quantitatively distinguish between in-pore anions and cations.[204, 211, 212] Further, *ex-situ* $^{13}C$ and $^{11}B$ NMR measurements of the respective concentrations of $EtN_4^+$ and $BF_4^-$ ions in the carbon pores indicated that the $BF_4^-$ anions participate in charge storage via ion swapping on both positive and negative electrodes.[211] To avoid cell dismantling issues, *in situ* $^{31}P$ and $^{19}F$ NMR experiments were employed to capture tetraethylphosphonium ($PEt_4^+$) and $BF_4^-$ ions inside the carbon pores, respectively (**Figs. 4c1 and 4c2**).[204] A balanced population of in-pore cations and anions was observed at a null potential. During the charging process, anions and cations were exchanged along with the simultaneous change of charge populations on the positive electrode (permselectivity failure), whereas anions made no contribution and cations dominated on the negative electrode (permselectivity) (**Fig. 4c3**). In addition to the global ion population change observed in carbon pores, the local ion rearrangement as a function of the carbon pore size can be characterized by small-angle scattering techniques.[203, 213-216] A combination of *in situ* small-angle X-ray scattering (SAXS) with Monte Carlo simulations was performed to quantify ion confinement.[213] Strong confinement of ions can be conceptualized as ions accumulating on smaller pores (**Fig. 4d1**). Consequently, the charge storage of the carbon electrodes was accomplished by ion swapping in a CsCl aqueous electrolyte (**Fig. 4d2**). At the applied positive potential, the anion concentration drastically increased within the strongly confining pores more than within the weakly confining pores.

The movement of anions to strongly confining sites minimized electrostatic repulsion, thereby reducing energy cost. Overall, EDLC-type materials act as anion storage materials when positively charged, and the excess accumulated anions are equilibrated by the positive electrodes. The exact causal process of various EDLC charging mechanisms with permselectivity or permselectivity failure remains unclear, and the effects of charging mechanisms on the electrochemical performances such as specific capacitance and rate capability require further investigation. Moreover, various charging mechanisms have been demonstrated to have significant effects on capacitive desalination where permselectivity leads to the failure of ion removal (see Section 4.2.2).

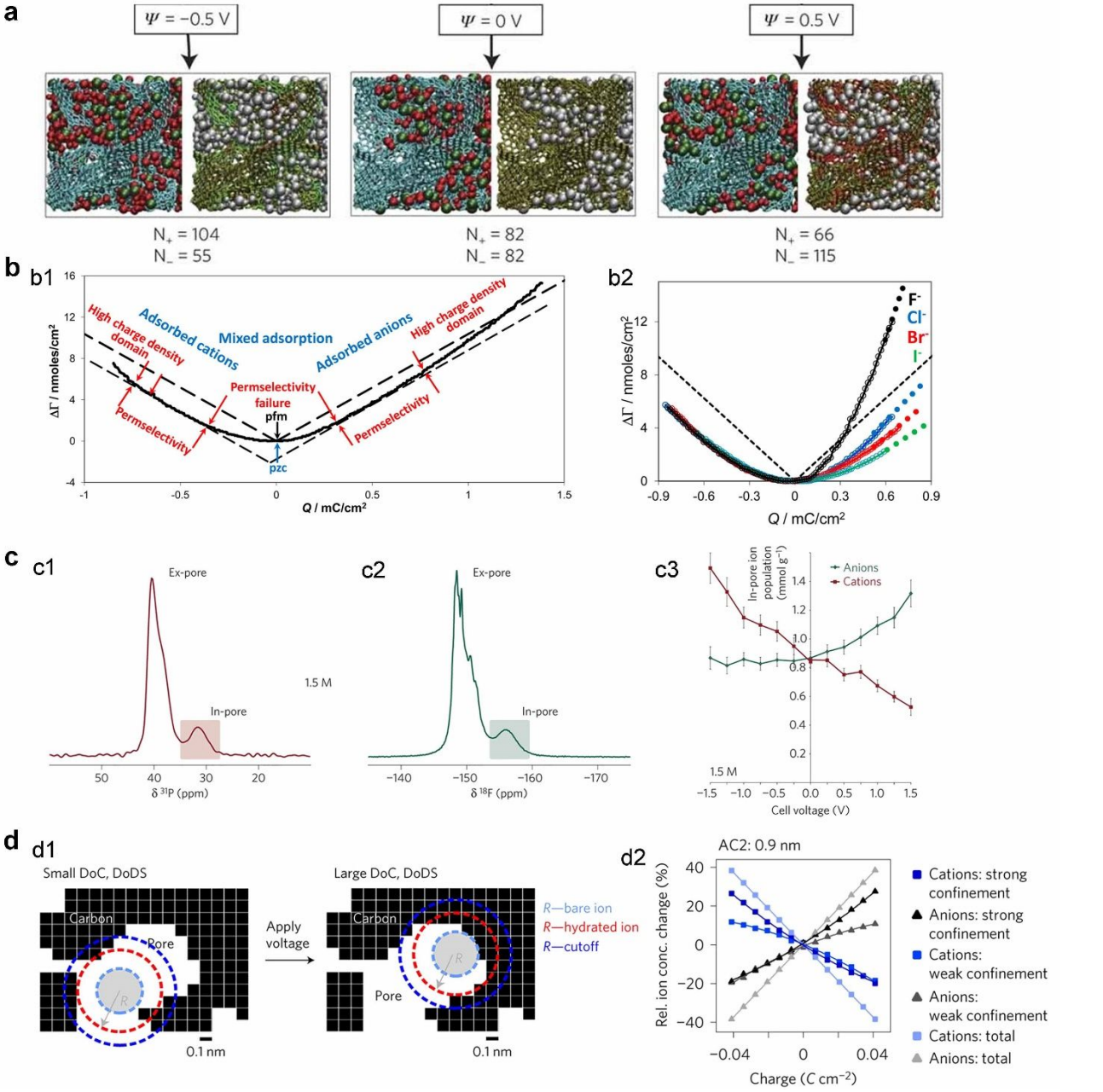


**Fig. 4** Mechanism study of EDLC-type anion storage materials. (**a**) MD simulations. The structure of simulation electrode consists of a BMIM-$PF_6$ IL electrolyte for various voltages. Reproduced with permission from ref. [205], Copyright 2012 Springer Nature. (**b**) EQCM technique. (b1) Analysis of ion population change as a function of charge density for carbon electrode in KCl electrolyte, (b2) ion population change as a function of charge density for carbon electrode in KF, KCl, KBr and KI electrolytes. Reproduced with permission from ref. [208], Copyright 2013 American Chemical Society. (**c**) NMR technique. (c1) NMR spectra showing in- and ex-pore cation, and (c2) anion environments, (c3) in-pore ion populations at different charging states of carbon electrode. Reproduced with permission from ref. [204], Copyright 2015 Springer Nature. (**d**) SAXS technique and Monte Carlo simulations. (d1) Sketch visualizing the concept of degree of confinement (DoC) (large DoC indicates strong confinement), (d2) Cation and anion concentration changes as a function of the state of charge for the two classes of confinement. Reproduced with permission from ref. [213], Copyright 2017 Springer Nature.

Despite the improved energy density of hybrid capacitors, their energy density is mainly limited by the lower capacitance of EDLC-type electrodes compared to Faradaic electrodes.[21, 22] When EDLC-type materials are used for anion storage in hybrid capacitors or whole-anion-based devices, the electrochemically available surface area is key to accommodate more anions to attain the maximum capacitance.[6-8, 219] The pore structure of carbon materials is also a critical factor in abnormal capacitance.[220] Sub-nanopores with sizes close to ion size achieve the highest areal capacitance.[220, 221] Diffusion and sieving effects should also be considered. The larger pores provide fast ion transfer channels and reduce ion diffusion distance.[221-223] To satisfy both capacitances and kinetics, hierarchical porous structures with multiscale pores are preferred to achieve high capacitance and rate performance.[222, 223] Nonetheless, the large surface area of carbon materials is in contrast to the low packing density (<0.5 g $cm^{-3}$), where volumetric capacitance is typically below 100 F $cm^{-3}$, and high mass loading (100–200 μm thickness for commercial electrodes) required for high energy applications is difficult.[224, 225] The volumetric capacitance significantly drops at the device level when including other cell components such as current collectors, separators, and electrolytes.[224] This calls for careful design of the carbon material structures to ensure high capacitance without affecting the packing density of thick electrode.[53, 225, 226] Although EDLC-type materials have been developed considerably, the capacitance of anion storage remains unsatisfactory. In a hybrid capacitor, the specific capacitance of an EDLC-type electrode is typically lower than a Faradaic electrode, and thus, a large mass ratio of EDLC-type to Faradaic electrode is needed to balance the charge of the two.[19, 21] Even two identical electrodes in dual-ion EDLCs are conventionally balanced owing to their different specific capacitances and different operating potential windows. The total capacity of a full cell is always limited by the low-capacity electrode, making it necessary to discover alternative anion-storage materials with high capacity and rate capabilities.

### 3.2 Faradaic materials based on $OH^-$ ions in aqueous electrolytes.

**3.2.1 Functionalized carbons.** In sharp contrast to anion-storing EDLC-type materials, functionalized carbon materials can achieve enhanced capacitance owing to the Faradaic charge storage of redox active functional groups.[227] Various heteroatoms, such as oxygen (O), nitrogen (N), boron (B), sulfur (S), and phosphorous (P), can be incorporated into the carbon lattice to modify the electronic and chemical properties (**Fig. 5a**). The redox capacitance of heteroatom-containing groups reacting with $OH^-$ ions is revealed through the specific redox reaction pathways in alkaline aqueous electrolytes.[227] As a side note, the enhanced capacitance of functionalized carbon materials could be also attributed to the contributions of cationic pseudocapacitance and changes in the electronic and chemical structures of carbon materials.[51, 227-230] For instance, the wettability by heteroatom-doping can be improved for easier ion access. The doping of electron-rich atoms contributes electrons to conjugated π-systems of carbon, promoting electronic conduction. Further, the structural distortion and topological defects arising from heteroatoms can improve EDLC capacitance. Therefore, we can observe that enhanced capacitance in alkaline aqueous electrolytes is clearly multifactorial, and no single specific factor seems to be responsible. Moreover, enhanced capacitance of the heteroatom-functionalized carbons was also observed in neutral aqueous and non-aqueous electrolytes.[227, 228, 51, 55, 231]

Among the functional groups, O-containing groups act as acidic sites such as carboxyl, phenol, hydroxyl, and lactone, as well as basic sites such as carbonyl ketone, quinone, and aldehyde. The redox reactions of acidic sites with $OH^-$ ions play a dominant role in achieving high anionic pseudocapacitance (**Fig. 5b**).[232-234] N-containing groups, including amines, pyrrolic/pyridone-N (N-5), pyridine-N (N-6), quaternary-N (N-Q), and oxidized pyridine-N (N-X), prefer to react with $H^+$ ions owing to the electron-rich and basic property of N atom.[235, 236] Nonetheless, they may contribute to revealing the redox capacitance with $OH^-$ ions (**Fig. 5c**).[237-239] In addition, carbon materials with B-,[54, 240] S-,[241-243] and P-containing groups[244, 245] have been developed to increase capacitance in alkaline aqueous electrolytes. However, the exact origin of the redox reactions with $OH^-$ ions remains elusive. Heteroatom-incorporated structures can also improve EDLC capacitance by increasing the adsorption of ions. Moreover, various multiple heteroatom-doped carbon materials were reported to achieve high capacitance in alkaline aqueous electrolytes. For example, N/O/S-enriched carbon foam showed a capacitance of 455 F $g^{-1}$ in KOH electrolyte,[246] while B/N co-doped carbon nanosheet displayed a capacitance of 233 F $g^{-1}$ in KOH electrolyte,[247] and N/P/O co-doped porous carbon spheres were found to have a volumetric capacitance of 760 F $cm^{-3}$ in KOH electrolyte.[55]

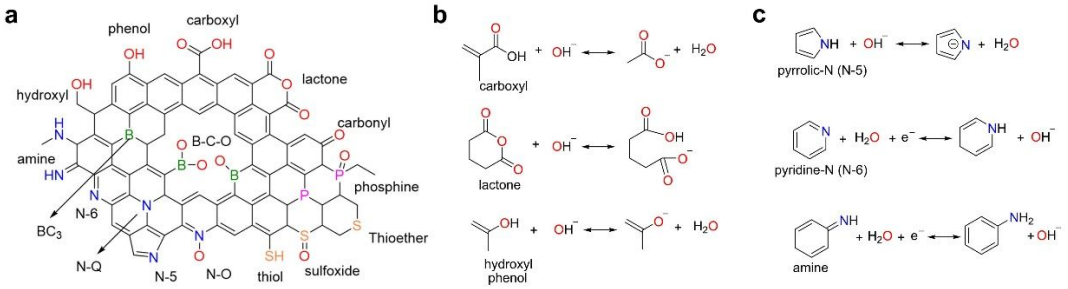


**Fig. 5** (**a**) Configurations of heteroatom-containing groups in graphene matrix. (**b**) Possible redox reactions of O-containing groups and (**c**) N-containing groups with $OH^-$ ions.

**3.2.2 Transition metal hydroxides/oxides.** Transition metal hydroxides/oxides have been developed as high-capacitance electrodes for aqueous hybrid capacitors (**Table 4**), because of their abundant redox active sites of metal centers and hydrophilicity.[33, 34] Among Ni- and Co-based hydroxides, the two-dimensional (2D) layered double hydroxides (LDHs) consist of positively charged alternating layers of metal centers coordinated with hydroxyl groups, with anions and water intercalated between layers.[248-250] The formula is $[M_{1-x}M'_x(OH)_2]^{x+}$ $A^{n-}_{x/n}\cdot mH_2O$, where M and M′ are the metal cations with bivalence and trivalence, respectively, and $A^{n-}$ is the interlayer anions balancing the positive charge of metal hydroxide layers arising from the presence of trivalence cations. The electrochemical response of Ni- and Co-based hydroxides in alkaline aqueous electrolytes is characterized by a battery-type behavior, indicating reversible conversion reactions as shown in the following equations.

$$Ni(OH)_2 + OH^- \leftrightarrow NiOOH + H_2O + e^- \quad (3)$$

$$Co(OH)_2 + OH^- \leftrightarrow CoOOH + H_2O + e^- \quad (4)$$

$$CoOOH + OH^- \leftrightarrow CoO_2 + H_2O + e^- \quad (5)$$

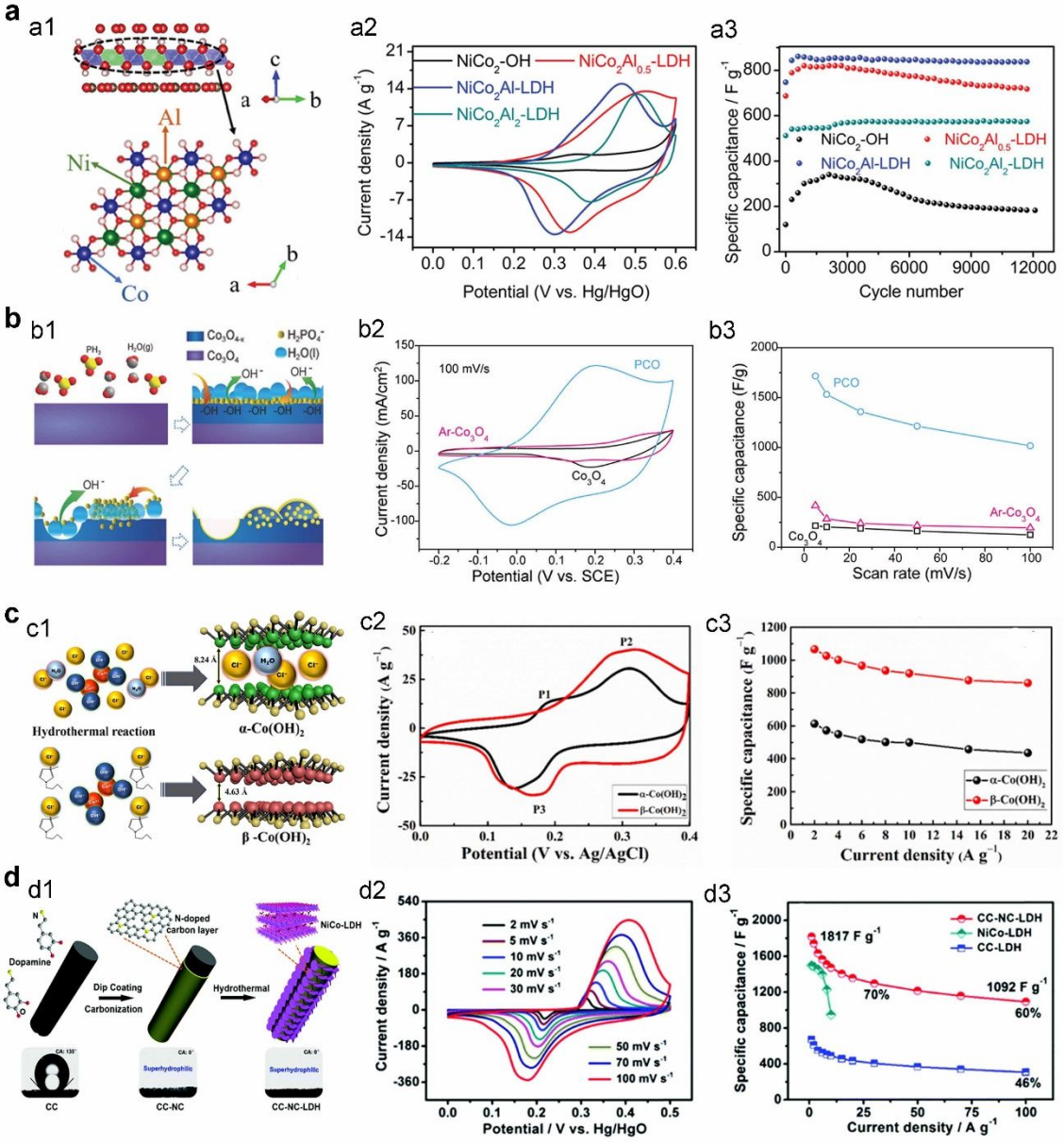


**Fig. 6** Influential factors of electrochemical performance of transition metal oxides/hydroxides. (**a**) Incorporation of multiple metals. (a1) Schematic illustration of Al substitution, (a2) CV curves at 5 mV $s^{-1}$, and (a3) cycling performance at 5 A $g^{-1}$ for a series of $NiCo_2Al_x$ hydroxides. Reproduced with permission from ref. [261], Copyright 2019 Wiley-VCH. (**b**) Defective engineering. (b1) Schematic illustration of the morphology evolution mechanism of phosphate ion functionalized $Co_3O_4$ (P-$Co_3O_4$), (b2) CV curves, and (b3) rate performance of various $Co_3O_4$-based electrodes. Reproduced with permission from ref. [61], Copyright 2017 Wiley-VCH. (**c**) Tuning of anions and interlayer spacing. (c1) Schematic illustration of the synthesis of α- and β-$Co(OH)_2$, (c2) CV curves, and (c3) rate performance of α- and β-$Co(OH)_2$. Reproduced with permission from ref. [274], Copyright 2019 Elsevier. (**d**) Combination with conductive substrate. (d1) Schematic illustration of the preparation procedure of CC-NC-LDH composite with N-doped carbon layer as the structural coupling bridge, (d2) CV curves, and (d3) rate performance of various Ni,Co-based LDHs. Reproduced with permission from ref. [277], Copyright 2017 Royal Society of Chemistry.

The reaction of $Ni(OH)_2$ takes one step through the breaking of the O–H bond and the transition of $Ni^{2+}$ to $Ni^{3+}$, forming NiOOH species with the participation of $OH^-$ ions. This reaction occurs at 0.5 V versus SHE.[187, 251, 252] The reaction of $Co(OH)_2$ can be divided into two steps. The first step, similar to that of $Ni(OH)_2$, is to produce CoOOH species, and the potential of the $Co^{2+}/Co^{3+}$ redox couple is 0.2 V versus SHE. At the second redox step, CoOOH species lose H, which can react with $OH^-$ ions, thereby forming $CoO_2$ species. At this step, the potential of $Co^{3+}/Co^{4+}$ redox couple is 0.7 V versus SHE, higher than 0.2 V at the first step, but it is sometimes unstable and incomplete in the oxidation process of $Co(OH)_2$.[75, 253]

Transition metal oxides such as NiO, $Co_3O_4$, and $NiCo_2O_4$ have been used as the positive electrodes for hybrid capacitors.[254-258] These metal oxides can be converted from the oxidation of the corresponding hydroxides at 300–500 °C, showing higher electrical conductivity.[257-259] Metal oxides with spinel structure, with the formula $MM'_2O_4$, store charge through the formation of metal oxyhydroxides (MOOH) in alkaline aqueous electrolytes, as shown in the following equation for $NiCo_2O_4$.

$$NiCo_2O_4 + OH^- + H_2O \leftrightarrow NiOOH + 2CoOOH + e^- \quad (6)$$

The as-formed NiOOH and CoOOH species undergo reversible Faradaic reactions, as shown in equations (3–5).

Transition metal hydroxides/oxides are limited by their low electrical conductivity and inferior structural stability, resulting in low rate and cycling capabilities.[33, 34] Incorporating multiple metal cations into the host of metal hydroxides/oxides has been proposed to enhance the electrochemical performance.[72, 77, 260-264] For example, the effect of Al stoichiometry on the electrochemical performance of ternary ($NiCo_2Al_x$) hydroxides was investigated (**Fig. 6a1**).[261] The introduction of Al into Ni, Co-based hydroxide leads to a transition from β-phase to α-phase, along with the expansion of interlayer spacing. In addition, the partial dissolution of Al during the cycling process can generate more defects and active sites. Consequently, $NiCo_2Al_x$ hydroxide shows a higher specific capacity of 158 mAh $g^{-1}$ at 0.5 A $g^{-1}$ and superior cycling stability of 97.3% over 12000 cycles, compared to 68 mAh $g^{-1}$ at 0.5 A $g^{-1}$ and 53.5% capacity retention of $NiCo_2$ hydroxide (**Figs. 6a2 and 6a3**). However, excess Al content in $NiCo_2Al_2$ is unable to increase specific capacity (103 mAh $g^{-1}$ at 0.5 A $g^{-1}$). The effects of Co- and Mn-substitution on the electrochemical performance of Ni-based hydroxides were explored.[260] Both Mn- and Co-substitution enhanced the capacity and stability, where Mn substitution was found to be more effective for increasing capacity, while Co substitution contributes mainly to improve structural stability. The composition of transition metals also affected the electrochemical performance. For instance, the size and composition of Ni, Co, and Mn-based ternary hydroxides were controlled by adjusting the ratio of Ni to Co and Mn sources.[265] Subsequently, the Ni-rich ternary hydroxide achieved the highest capacity of 165 mAh $g^{-1}$ (or 1188 F $g^{-1}$) at 1 A $g^{-1}$.

Defect engineering strategies modify the electronic structure to provide redox active sites for metal hydroxides and oxides. Incorporation methods for defects include chemical reduction,[61, 266, 267] plasma etching,[268-270] and electrochemical treatment.[52, 60, 271] For instance, the surface of $Co_3O_4$ was modified by the functionalization of phosphate ions under annealing of $NaH_2PO_2{\cdot}H_2O$ in an Ar atmosphere.[61] The reduced $Co_3O_{4-x}$ at the near surface of $Co_3O_4$ was converted to phosphate ion-functionalized $Co_3O_4$ (P-$Co_3O_4$) through ion exchange between $H_2PO_4^-$ and $OH^-$, resulting in a porous structure (**Fig. 6b1**). The functionalization of phosphate ions promotes electron transport and increases the number of active sites, improving capacity. Broad redox peaks of the P-$Co_3O_4$ electrode were observed in the CV curves, and the capacity of P-$Co_3O_4$ was 286 mAh $g^{-1}$ (or 1716 F $g^{-1}$) at 5 mV $s^{-1}$, which is higher than 215 F $g^{-1}$ of pristine $Co_3O_4$ electrode (**Figs. 6b2 and 6b3**). The ferricyanide ($Fe(CN)_6^{4-}$)-grafted P-$Co_3O_4$ exhibited a reduced self-discharge rate and high capacity of 1960 mC $cm^{-2}$ at 3 mA $cm^{-2}$.[272] Oxygen vacancies could also be introduced to the $Co_3O_4$ compound via electrochemical lithiation, where Co–O bonds were weakened and neighboring Co atoms were activated.[60] The resulting Li-$Co_3O_4$ electrode achieved a high capacity of 260 mAh $g^{-1}$ at 1 A $g^{-1}$, nearly four times greater than that of the pristine $Co_3O_4$ electrode in KOH electrolyte.

Transition metal hydroxides/oxides possess an alternating layered structure with charge-balancing anions between layers. The interlayer distance and type of anions significantly affect the electrochemical performance of electrode materials.[273-276] For example, $Co(OH)_2$ was synthesized with different crystalline phases depending on the presence of BMIM-$BF_4$ IL.[274] The interlayer distances of α-$Co(OH)_2$ and β-$Co(OH)_2$ were 8.24 and 4.63 Å, respectively (**Fig. 6c1**). The presence of $Cl^-$ ions in α-$Co(OH)_2$ hinders the diffusion of $OH^-$ ions into the interlayers of α-$Co(OH)_2$. Therefore, β-$Co(OH)_2$ showed a higher specific capacity and rate capability (118 mAh $g^{-1}$ at 2 A $g^{-1}$, with 80% retention at 20 A $g^{-1}$) than α-$Co(OH)_2$ (68 mAh $g^{-1}$, 70% retention) (**Figs. 6c2 and 6c3**). To improve the rate capability of Ni, Co-based LDHs, the original anions (usually $CO_3^{2-}$, $NO^{3-}$) were exchanged using long-chain anions with multiple carboxylic ends to promote the diffusion of $OH^-$ ions.[273] Accordingly, NiCo-LDH intercalated with moderate-sized 1,4-benzenedicarboxylic achieved the smallest $R_{ESR}$ and the best rate performance, attaining a high rate capacity of 45.5 mAh $g^{-1}$ (410 F $g^{-1}$) at 150 A $g^{-1}$.

The integration of metal hydroxides/oxides with conductive substrates is a chemical strategy to address the limitations of low electrical conductivity and inferior structural stability.[62, 277-280] When nanostructured metal hydroxides/oxides are directly grown on conductive substrates, the surface structures and chemistries of substrates are important for achieving robust growth and finely modulated electroactive structures. A superhydrophilic N-doped carbon (NC) layer was employed as the coupling bridge between the carbon cloth (CC) substrate

and NiCo-LDH, thus controlling the compatibility of the two species for realizing the uniform and robust growth of NiCo-LDH (**Fig. 6d1**).[277] The as-obtained CC-NC-LDH electrode showed a pair of redox peaks in CV curves, delivering the specific capacity of 252 mAh $g^{-1}$ at 1 A $g^{-1}$, greater than 93 mAh $g^{-1}$ of CC-LDH electrode without the NC layer in KOH electrolyte (**Figs. 6d2 and 6d3**). Park et al. synthesized $NiCo_2O_4$ nanoneedles deposited on rGO-coated Ni foam for improved capacitance and cyclability.[62] The interlayer rGO strongly adhered between $NiCo_2O_4$ and Ni-foam, regulating the $NiCo_2O_4$ dimensions toward a small size and providing superior electrochemical stability. The layer-by-layer assembly of composites has also been applied to combine electroactive metal hydroxides/oxides with conductive substrates.[281, 282] For instance, the $NiCo_2O_4$/rGO composite was synthesized through the self-assembly of positively charged LDH and negatively charged GO, followed by annealing treatment.[281] The resultant composite electrodes exhibited higher capacities (193 and 116 mAh $g^{-1}$ at 0.5 and 30 A $g^{-1}$, respectively) compared to the $NiCo_2O_4$ composite owing to improved electronic conductivity and abundant active sites. Other conductive substrates such as MXene and conductive polymers have also been used to synthesize composite metal hydroxides/oxides. A representative example demonstrated the direct growth of NiCoAl-LDH onto $V_4C_3T_x$ MXene sheets and $Ni(OH)_2$ nanosheets grown on the surface of polypyrrole (PPy) nanospheres to enable greatly improved capacitive performance.[252, 283]

The non-stoichiometric transition metal oxides with vacancy defects can demonstrate a pseudocapacitive behavior in KOH electrolyte.[40] The presence of oxygen-vacancy-rich nanofacets is associated with rapid oxygen-anion intercalation into bulk $Zn_xCo_{1-x}O$. The Faradaic charge storage of $Zn_xCo_{1-x}O$ is associated with the valence state changes of Co ions via oxygen-anion intercalation, as shown in the following equation.

$$Zn_xCo_{1-x}O_{1-\delta} + (2\delta + 2y)OH^- \leftrightarrow Zn_xCo_{1-x}O_{1+y} + (2\delta + 2y)e^- + (\delta + y)H_2O \quad (7)$$

Moreover, uniform Zn doping allows $Zn_xCo_{1-x}O$ to achieve higher electrical conductivity compared to that of pristine CoO. Accordingly, the $Zn_xCo_{1-x}O$ electrode delivered the high capacitance of 1065 and 450 F $g^{-1}$ at 5 and 1000 mV $s^{-1}$, respectively, within a potential window of −1.0 to −0.2 V versus Ag/AgCl.

**3.2.3 Transition metal sulfides, selenides, nitrides, phosphides, and carbonate hydroxides.** Transition metal sulfides,[70, 284-288] selenides,[74, 289-293] nitrides,[68, 294-296] and phosphides,[73, 297-300] generally possess better electronic conductivity compared to the corresponding hydroxides/oxides and are applied for anion storage materials (**Table 4**). For example, the charge storage of $NiCo_2X_4$ (X = S, Se, N, P) in alkaline aqueous electrolytes has been considered through a series of redox reactions as follows.

$$NiCo_2X_4 + 4OH^- \leftrightarrow NiXOH + 2CoXOH + XOH^- + 3e^- \quad (8)$$

$$NiXOH + OH^- \leftrightarrow NiXO + H_2O + e^- \quad (9)$$

$$CoXOH + OH^- \leftrightarrow CoXO + H_2O + e^- \quad (10)$$

Because $NiCo_2X_4$ is thermodynamically less stable than the corresponding metal oxides/hydroxides, it can be transformed into metal oxides/hydroxides as the precursors of metal hydroxides/oxides when cycled in alkaline aqueous electrolytes.[74, 301-303] Consequently, the capacity of $NiCo_2X_4$ electrodes increases during the first several hundred cycles.[74, 75, 302] An irreversible phase transition of $NiCo_2S_4$ is observed during the charge storage process.[302] In particular, the desulfuration reaction is involved between $NiCo_2S_4$ and $OH^-$ ions, offering the formation of Ni, Co-based hydroxides as follows:

$$NiCo_2S_4 + OH^- \rightarrow Ni(OH)_2 + Co(OH)_2 + SO_4^{2-} + H_2O + e^- \quad (11)$$

Similarly, $NiCoSe_2$ itself is not redox active, but the electrooxidation-generated NiCo-hydroxides are responsible for the redox charge storage reactions.[74]

Although metal sulfides, selenides, nitrides, and phosphides are potentially transferred into metal hydroxides/oxides in alkaline aqueous electrolytes, these compounds need to be studied. Their electrochemical performance, which is higher than that of the corresponding metal oxides/hydroxides, can be understood from the following perspective.[301] Phase transformation can introduce defects and numerous active sites in transition metal compounds. Moreover, metal chalcogenides, nitrides, and phosphides generally achieve higher electronic conductivities than metal oxides/hydroxides, as the untransformed phases in the bulk internal structure act as conductive scaffolds to promote electron transfer.

In this regard, chemical methods to convert metal oxides/hydroxides into corresponding metal sulfides, selenides, nitrides, and phosphides have been exploited to achieve enhanced electrochemical performance.[68, 72, 73, 290, 294-298] Electrodeposited $NiCo_2O_4$ on graphene paper (GP) was annealed under a $NH_3$ atmosphere to afford Ni, Co-based nitride (Ni-Co-N/GP) (**Fig. 7a1**).[294] In comparison to the $NiCo_2O_4$/GP electrode, the Ni-Co-N/GP electrode showed higher capacities of 133 mAh $g^{-1}$ at 4 $Ag^{-1}$ and 115 mAh $g^{-1}$ at 20 $Ag^{-1}$ (**Figs. 7a2 and a3**). Substitutions of Co-based oxides by cation (Zn, Ni) and anion (P) were accomplished to synthesize ZnNiCo-phosphide (ZnNiCo-P), which provides more charge carriers for the facile redox reaction and lowers adsorption energy of $OH^-$ ions for enhancing capacity.[72] The Se doping for a stable $Co^{3+}$-rich state in Co-based compound was demonstrated.[75] The $Co^{3+}/Co^{4+}$ redox pair operates at a higher voltage plateau than the $Co^{2+}/Co^{3+}$ redox pair (**Fig. 7b1**). However, the $Co^{3+}/Co^{4+}$ redox pair is unstable owing to the rapid transition of $Co^{3+}$ to $Co^{2+}$ (**Fig. 7b2**). $CoSe_{2-x}$ underwent a phase transformation to $Co_xO_ySe_z$ during several CV cycles; thus, the content of Se drastically decreased from 58.47% to 0.38% after pre-activation (**Fig. 7b3**). The $Co_xO_ySe_z$ with residual trace of Se doping inhibited the transition of $Co^{3+}$ to $Co^{2+}$, thereby stabilizing the $Co^{3+}/Co^{4+}$ redox pair. Consequently, the $CoSe_{2-x}$ electrode operated at a high voltage along with an increased capacity (**Fig. 7b4**).

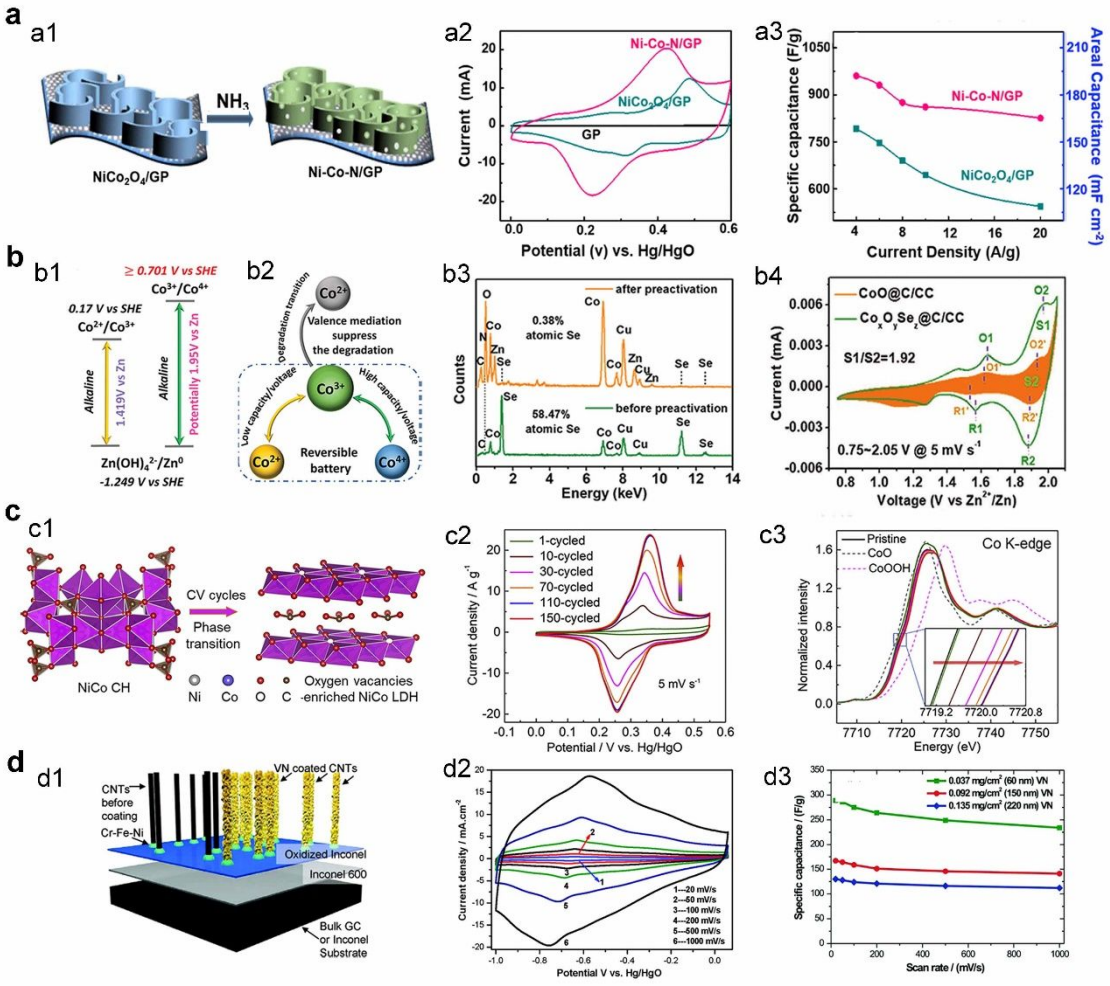


**Fig. 7** Electrochemical performance and structural features of the transition metal nitrides, selenides, and carbonate hydroxides. (**a**) Ni, Co-based nitrides. (a1) Schematic illustration of the synthesis of Ni-Co-N/GP, (a2) comparison of CV curves, and (a3) rate performance of Ni-Co-N/GP and $NiCo_2$/GP electrodes. Reproduced with permission from ref. [294], Copyright 2019 Elsevier. (**b**) Co-based selenides. (b1) Illustration of the high voltage of $Co^{3+}/Co^{4+}$ redox pair, (b2) illustration of the stabilization of $Co^{3+}/Co^{4+}$ redox pair, (b3) Energy dispersive spectroscopy (EDS) spectra of cycled and pristine $CoSe_{2-x}$, and (b4) CV curves of $CoSe_{2-x}$ electrode. Reproduced with permission from ref. [75], Copyright 2020 Wiley-VCH. (**c**) Ni, Co-based carbonate hydroxides (CHs). (c1) Schematic illustration of the phase transformation of metal CH to LDH, (c2) CV curves for the NiCo CH–$Ni(OH)_2$ electrode during 1 to 150 cycles, and (c3) Co K-edge recorded by operando XANES spectra during CV cycles. Reproduced with permission from ref. [76], Copyright 2020 Elsevier. (**d**) VN/CNTs arrays (d1) Schematic illustration of the VN/CNTs arrays, (d2) CV curves in KOH electrolyte, and (d3) rate performance of the VN/CNTs arrays. Reproduced with permission from ref. [66], Copyright 2011 American Chemical Society.

Transition-metal carbonate hydroxides (CHs) have also been used as high-capacitance electrodes for hybrid capacitors.[76, 77, 304] Qiu and Liu et al. systematically investigated electronic and structural transformations of Ni,Co-based CH into corresponding LDH (**Fig. 7c1**).[76] The NiCo CH-$Ni(OH)_2$ electrode was prepared by growing NiCo CH on $Ni(OH)_2$-covered carbon fiber paper. After 150 cycles, the integrated CV area of the NiCo CH-$Ni(OH)_2$ electrode increased by a factor of 12 (**Fig. 7c2**). Simultaneously, the CH phase was transformed into the LDH phase, as confirmed by synchrotron X-ray diffraction (XRD) and high-resolution transmission electron microscopy (TEM). As verified by the gradual shift of the Co K-edge position to high energy via operando X-ray absorption near-edge structure (XANES) spectra, the valence state of Co increased, while no obvious change was observed for the valence state of Ni (**Fig. 7c3**). The cycled CH-$Ni(OH)_2$ electrode with abundant oxygen vacancies exhibited specific capacities of 151 and 114 mAh $g^{-1}$ at 1 and 100 $Ag^{-1}$, respectively, along with a capacity retention of 86% after 10000 cycles. Phase transformation may deteriorate the electrochemical performance. The phase transformation of nickel bicarbonate ($Ni(HCO_3)_2$) into disordered β-$Ni(OH)_2$ during long charge-discharge cycles is associated with the destruction of the $Ni(HCO_3)_2$ structure and hindered ion diffusion, leading to poor cycling stability of the $Ni(HCO_3)_2$ electrodes.[305] This issue was resolved by synthesizing a $Ni(HCO_3)_2$/rGO composite that showed improved cycling stability owing to the stabilization of the $Ni(HCO_3)_2$ structure.

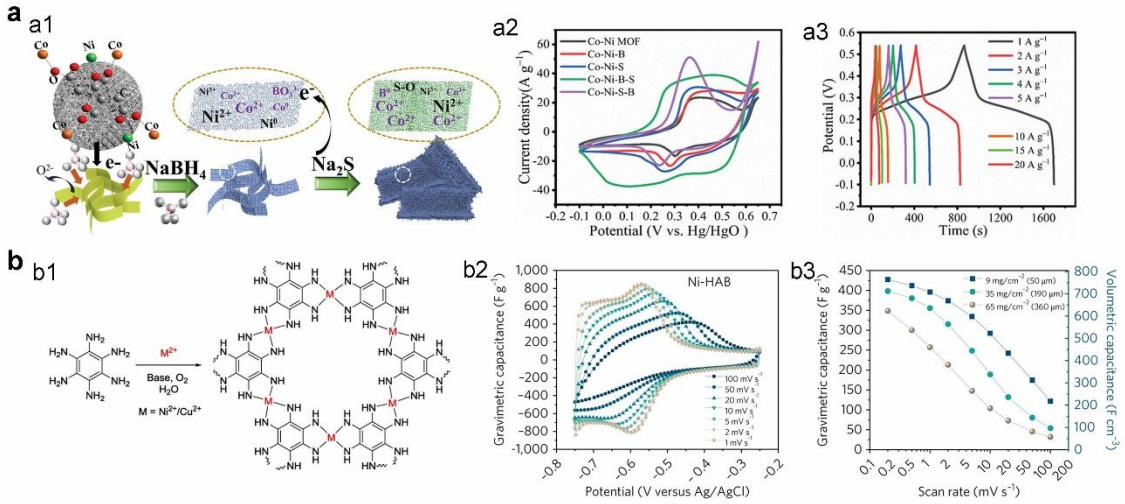


**Fig.8** Electrochemical performance MOFs and their derived materials. (**a**) Co-Ni-B-S derived from Co-Ni MOFs. (a1) Schematic illustration of the activation approach of Co-Ni MOFs, (a2) CV curves and (a3) GCD curves of the Co-Ni-B-S electrode. Reproduced with permission from ref. [320], Copyright 2019 Wiley-VCH. (**b**) Ni-HAB MOF. (b1) Chemical structure of Ni-HAB MOFs, (b2) CV curves and (b3) rate performance of the Ni-HAB MOFs electrode. Reproduced with permission from ref. [93], Copyright 2018 Springer Nature.

As the special case of transition metal nitrides, early transition metal nitrides such as VN, TiN, and WN are considered as pseudocapacitive negative electrodes in alkaline aqueous conditions.[42, 45, 66, 67, 188, 306] Nano-sized VN with a surface area of 38.8 $m^2$ $g^{-1}$ was synthesized and tested in KOH electrolyte, displaying a series of broad redox pecks within a potential window of −1.2 to 0 V versus Hg/HgO.[67] The charging mechanism of VN electrodes was attributed to the combination of redox reactions of surface $VN_xO_y$ with $OH^-$ ions and electrical double layer formation as follows.

$$VN_xO_y + OH^- \leftrightarrow mVN_xO_y\text{–}OH + (1\text{–}m)VN_xO_y\|OH^- \quad (12)$$

Similarly, VN prepared by the sputtering method showed a surface redox reaction of amorphous vanadium oxides with $OH^-$ ions in alkaline aqueous electrolytes, while the bulk VN nanocrystals served as a conducting platform.[42] The average valence state of V changed from 3.56 to 3.66, as determined by *in situ* X-ray absorption spectroscopy as shown below.

$$V^{4+}O_2 + H_2O + e^- \leftrightarrow V^{3+}OOH + OH^- \quad (13)$$

In contrast, the charge storage mechanism associated with valence state change of the near-surface VN, which is not related to vanadium oxides, was observed in alkaline aqueous electrolytes.[307]

In addition to VN, the surfaces of TiN and WN are easily oxidized owing to the oxyphilicity of early transition metal nitrides.[45, 188] The low electrochemical stability of early transition metal nitrides was attributed to their irreversible conversion to amorphous oxides in alkaline aqueous electrolytes during cycling.[45, 46, 308, 309] Moreover, the rate capability is not sufficiently high.[67, 310] Thin-film-based electrodes have proven beneficial for achieving high capacitance at high rates and for special applications in micro- and flexible capacitors.[188, 311, 312] For example, a WN thin film with a thickness of 7.93 μm, fabricated using the magnetron sputtering deposition technique, achieved a capacitive behavior in a KOH electrolyte, with a high capacitance per unit area of 550 mF $cm^{-2}$.[188] The details of micro- and flexible capacitors based on early transition metal nitrides are discussed in Section 4.2.1. In contrast, thick electrodes with high mass loadings are required for the high energy applications, but the specific capacitance may be lowered.[67, 310] For example, a VN electrode at a low mass loading of 0.25 mg $cm^{-2}$ delivered a specific capacitance up to 1300 F $g^{-1}$ at 2 mV $s^{-1}$, while the capacitance decreased to 110 F $g^{-1}$ at 0.99 mg $cm^{-2}$ and 100 mV $s^{-1}$.[67] An analogous approach to the composite of metal hydroxides/oxides with conductive substrate can be applied to resolve issues of low stability and rate performance of metal nitrides.[46, 309, 313-318] For instance, 3D arrays consisting of nanocrystalline VN coated on carbon nanotubes (CNTs) (**Fig. 7d1**), exhibited all the capacitive CV shapes from 20 to 1000 mV $s^{-1}$, with the high capacitance of 289 F $g^{-1}$ at 20 mV $s^{-1}$ in KOH electrolyte (**Figs. 7d2 and 7d3**),[66] while ultrathin carbon-coated TiN and VN electrodes showed a secure cycling stability over 15000 cycles,[308] and VN nanodots intercalated carbon nanosheets achieved a high capacitance of 334.8 F $g^{-1}$ even at 100 A $g^{-1}$ along with a high VN content of 91.3%, a high packing density of 2.1 g $cm^{-3}$, a high mass loading of 3.5 mg $cm^{-2}$.[46]

**3.2.4 Metal organic frameworks and their derived materials.** MOFs, which are crystalline porous materials constructed from metal centers and organic ligands, are characterized by large specific surface areas, tunable porous structures, and controllable compositions. MOFs can be used as sacrificial templates to construct well-defined porous structures of transition metal hydroxides/oxides, while the organic ligands are removed via hydrolysis and annealing (**Table 4**).[181, 319-324] For instance, MOFs with nearly 28% $\mu_3$-OH from $M_3(\mu_3\text{-OH})$ clusters coordinated with $OH^-$ ions were used to synthesize Ni, Co-based

LDHs via alkaline hydrolysis.[181] NiCo-LDH with a Ni/Co molar ratio of 7:3 delivered a maximum capacity of 229 mAh $g^{-1}$ (1652 F $g^{-1}$) at 1 A $g^{-1}$. NiCoZn-LDH could be derived from Zn-MOF in the presence of $Ni^{2+}$ and $Co^{2+}$ ions in deionized water at 120 °C.[319] To enhance the capacity, $Co_9S_8$ quantum dots were embedded *in situ* within LDH layers through the selective vulcanization of Co metal. The as-prepared NiCoZn-LDH/$Co_9S_8$ electrode with a hierarchical structure and abundant active sites achieved a high capacity of 350 mAh $g^{-1}$ at 1 A $g^{-1}$. Xia and Park et al. prepared NiCo-based boride/sulfide (Co-Ni-B-S) via boronization and subsequent sulfurization of MOFs (**Fig. 8a1**).[320] The presence of B and S species leads to relatively low valence states in metals and a high electronic conductivity in Co-Ni-B-S. The specific capacities of Co-Ni-B-S electrode were 231 and 216 mAh $g^{-1}$ at 1 and 10 A $g^{-1}$, respectively, which are larger than those of the initial Co-Ni MOF electrode (**Figs. 8a2 and 8a3**). The CoNi-MOF was synthesized using the inverted method, where $Co(OH)_2$ was electrodeposited on carbon fiber paper, and then, $Ni^{2+}$ ions and p-benzenedicarboxylic were added.[182] The vertically oriented CoNi-MOF achieved a high capacity of 130 mAh $g^{-1}$ (1044 F $g^{-1}$) at 2 A $g^{-1}$. The charge storage mechanisms of these MOFs are based on the Faradaic reactions of transition metals with $OH^-$ ions, thereby demonstrating similar electrochemical responses to transition metal hydroxides/oxides.[182, 325-327]

Since the first application of MOFs to capacitive materials,[92] various MOFs have been investigated.[93, 328, 329] Redox-active MOFs storing $OH^-$ ions via a pseudocapacitive mechanism were prepared by coordinating small-sized hexaaminobenzene (HAB) ligands with $Ni^{2+}$ or $Cu^{2+}$ centers (**Fig. 8b1**).[93] The as-obtained Ni-HAB and Cu-HAB MOFs contain honeycomb-like pores smaller than 1 nm, along with a high packing density of 1.77 to 1.80 g $cm^{-3}$. Such dense frameworks are beneficial for increasing the density of redox-active sites to enable high capacitance density. In addition, the Ni-HAB and Cu-HAB MOFs exhibit a fully conjugated structure owing to the strong orbital hybridization of HAB ligands with Ni and Cu metal centers. Their electrical conductivities are 70±15 S $m^{-1}$ and 11±3 S $m^{-1}$, respectively, which are sufficient for the design of electrodes without conducting additives. The strong metal-ligand orbital interaction also provides high chemical stability of Ni-HAB and Cu-HAB MOFs in both acidic and alkaline aqueous electrolytes. Consequently, in KOH aqueous electrolyte, the Ni-HAB MOF achieved a high volumetric capacitance of 760 F $cm^{-3}$ at 0.2 mV $s^{-1}$, showing broad redox peaks in a potential window of −0.75 to −0.25 V versus Ag/AgCl (**Figs. 8b2 and b3**). The pseudocapacitive feature of Ni-HAB MOFs is attributed to HAB ligands in a similar manner to the redox behavior of the HAB-based organic molecules, as confirmed by the absence of an obvious change in the valence state of Ni 2p during the charging and discharging processes.

**3.2.5 Perovskite oxides and fluorides.** Perovskite-type oxides, consisting of $ABO_3$ and derivatives such as double perovskite oxides of $AA'BB'O_6$ and Ruddlesden–Popper oxides of $AA'BO_4$, are regarded as promising anion storage materials (**Table 4**). The A sites are lanthanide or alkaline earth metals such as lanthanum (La), protactinium (Pr), strontium (Sr), barium (Ba), and calcium (Ca), which act to stabilize the crystal structure. The B sites are transition metals such as Ni, Co, Mn, and Fe, which contribute to redox reactions by changing their valence states.

$LaMnO_3$ perovskite is the first example of an oxygen anion ($O^{2-}$) intercalation pseudocapacitive material as demonstrated in 2014.[39] The specific capacitance of substoichiometric $LaMnO_{3-\delta}$ electrode was found to be higher than that of superstoichiometric $LaMnO_{3+\delta}$ electrode in KOH electrolyte, indicating the importance of oxygen vacancies. For varying concentrations of KOH electrolytes, the redox peak potentials shift negatively with increasing pH, indicating that the $OH^-$ ions rather than $K^+$ or $H^+$ cations are responsible for the redox peaks (**Fig. 9a1**). During the charging process, $OH^-$ ions are initially dissociated into $O^{2-}$ and $H^+$ ions, and $H^+$ ions react with bulk $OH^-$ ions to form $H_2O$ molecules. Then, the $O^{2-}$ ions diffuse along grain boundaries and are intercalated into the oxygen vacancy, while the Mn center is oxidized from $Mn^{2+}$ to $Mn^{3+}$ (**Fig. 9a2**). Finally, $LaMnO_3$ can further accommodate superstoichiometric $O^{2-}$ ions entering the lattice as interstitial species, leading to the formation of $LaMnO_{3+\delta}$ and oxidation of $Mn^{3+}$ to $Mn^{4+}$ as shown in the following equations.

$$La[Mn^{2+}{}_{2\delta};Mn^{3+}{}_{(1-2\delta)}]O_{3-\delta} + 2\delta OH^- \leftrightarrow LaMn^{3+}O_3 + 2\delta e^- + \delta H_2O \quad (14)$$

$$LaMn^{3+}O_3 + 2\delta OH^- \leftrightarrow La[Mn^{4+}{}_{2\delta};Mn^{3+}{}_{(1-2\delta)}]O_{3+\delta} + 2\delta e^- + \delta H_2O \quad (15)$$

These reactions are associated with two pairs of redox peaks in the CV curves (**Fig. 9a1**).

The oxygen anion intercalation mechanism is universal with other perovskite oxides containing oxygen vacancies, such as $LaNiO_{3-\delta}$,[330, 331] $LaCoO_{3-\delta}$,[332] and $CaMnO_{3-\delta}$.[333] As the oxygen vacancies in perovskite oxides play a role in accommodating $O^{2-}$ ions and facilitating $O^{2-}$ intercalation during charging, several strategies to increase the number of oxygen vacancies have been developed to enhance the specific capacity and rate performance.[330, 332] In addition to the direct synthesis methods,[330, 334] the content of oxygen vacancies in perovskites can be increased by methods such as annealing the perovskites at high temperatures under a reduced atmosphere,[39, 333] and carrying out the plasma etching technique.[332] For instance, the oxygen elements in the $LaCoO_3$ crystal lattice can be removed by hydrogen ($H_2$) plasma etching, which generated oxygen vacancies and reduced $Co^{3+}$ to $Co^{2+}$ (**Fig. 9b1**).[332] The $Co^{2+}/Co^{3+}$ atomic ratio on the surface of $LaCoO_3$ increased from 0.97 to 1.54 after 5 min of $H_2$ plasma etching. The as-etched $LaCoO_{3-\delta}$ electrode exhibited a capacitance of 706.9 F $g^{-1}$ (147.3 mAh $g^{-1}$) at 1 A $g^{-1}$, which was twice higher than 339.8 F $g^{-1}$ of original $LaCoO_3$ (**Figs. 9b2 and 9b3**). In addition, a series of nonstoichiometric $LaMn_{1\pm x}O_3$ perovskites showed that the presence of oxygen vacancies and Mn defects synergistically contributed to the improved electrochemical performance of

$LaMn_{1\pm x}O_3$ electrodes.[335] In particular, the $LaMn_{1.1}O_3$ sample with the highest $Mn^{4+}/Mn^{3+}$ ratio showed the highest specific capacity of 202.1 mAh $g^{-1}$ at 1 A $g^{-1}$.

The electronic and physical properties of perovskite oxides can be improved substituting A and B sites by other metal elements with different valence states.[82, 83, 336, 337] In this case, the electron per formula unit can be changed, then compensated generating oxygen vacancy and/or altering the valence of B sites. Therefore, various substituted perovskite oxides have been developed to achieve enhanced electrochemical performance by means of the modified electronic and chemical structures.[82, 336, 337] The electrochemical performances of $La_{0.85}Sr_{0.15}MnO_3$ and $LaMnO_3$ perovskites synthesized by the same sol-gel method were compared in KOH electrolyte (**Fig. 9c1**).[337] The capacitance was higher for $La_{0.85}Sr_{0.15}MnO_3$ than $LaMnO_3$ electrode (**Figs. 9c2 and 9c3**). For a series of $La_xSr_{1-x}Co_{0.1}Mn_{0.9}O_{3-\delta}$ ($0.3 \le x \le 1$) perovskites synthesized by electrospinning method,[336] the capacitances initially increased and then, decreased with respect to the Sr content. A maximum capacitance of 485 F $g^{-1}$ at 1 A $g^{-1}$ was achieved for $La_{0.7}Sr_{0.3}Co_{0.1}Mn_{0.9}O_{3-\delta}$ (x = 0.7) perovskite. The $SrCo_{0.9}Nb_{0.1}O_{3-\delta}$ perovskite achieved a high oxygen vacancy amount of 19.4% due to the presence of Nb treated in $H_2$/Ar atmosphere.[82] This $SrCo_{0.9}Nb_{0.1}O_{3-\delta}$ electrode displayed pseudocapacitive behavior in KOH electrolyte, delivering a volumetric capacitance of 2034.6 F $cm^{-3}$ (773.6 F $g^{-1}$ and 107.4 mAh $g^{-1}$) at 0.5 A $g^{-1}$.

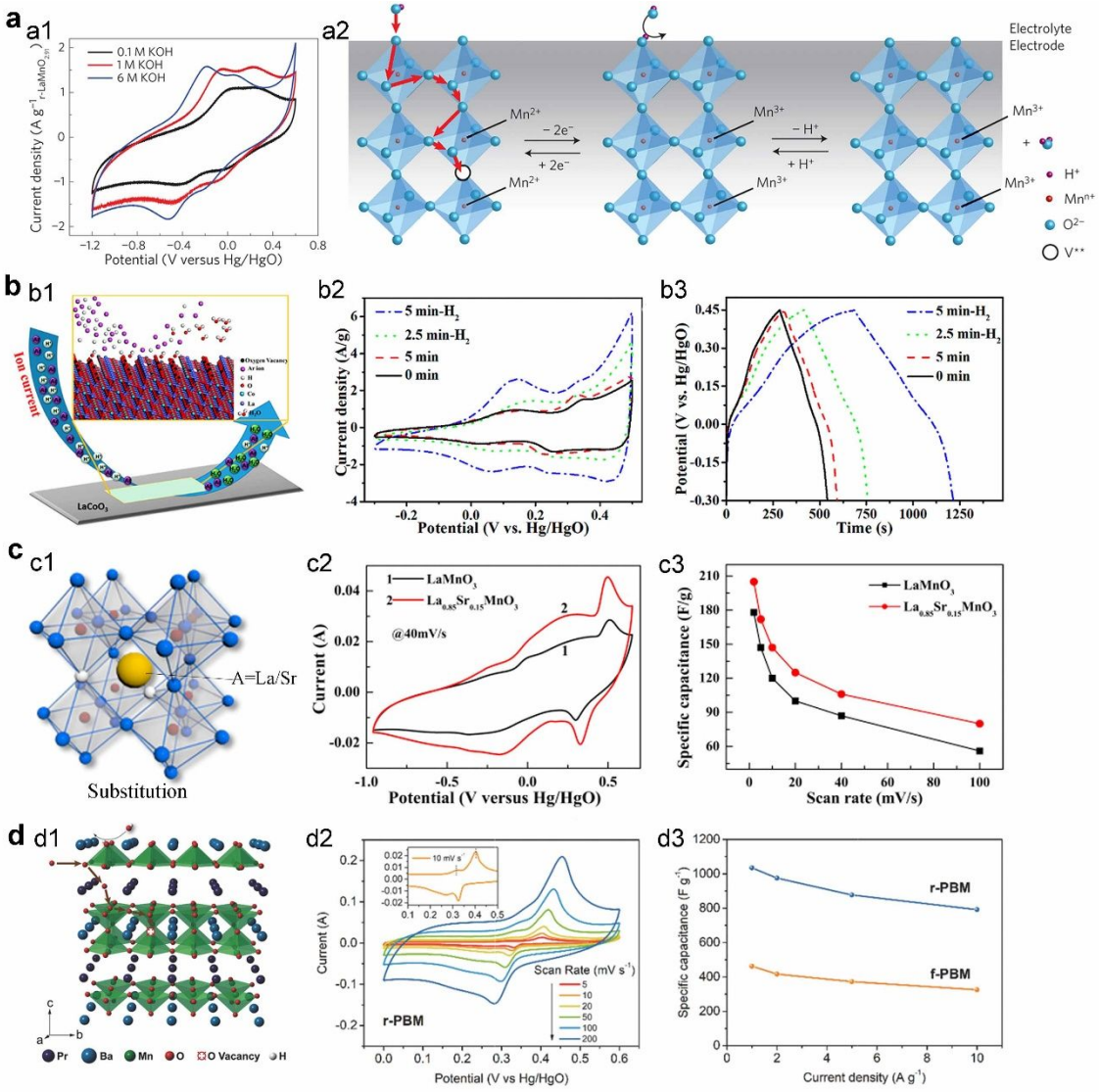


**Fig. 9** Mechanism and electrochemical performance of perovskite oxides. (**a**) Mechanism study of $LaMnO_{3-\delta}$ perovskite oxide. (a1) CV curves of $LaMnO_{3-\delta}$ electrode in different concentrations of KOH electrolytes, (a2) schematic illustration of the oxygen intercalation mechanism of $LaMnO_{3-\delta}$. Reproduced with permission from ref. [39], Copyright 2014 Springer Nature. (**b**) Effects of oxygen vacancy on electrochemical performance. (b1) Schematic illustration of the plasma etching process for increased oxygen vacancy, (b2) comparison of CV curves, and (b3) specific capacitance of $LaCoO_{3-\delta}$ electrodes treated with $H_2$ plasma at different time. Reproduced with permission from ref. [332], Copyright 2020 American Chemical Society. (**c**) Effects of atomic substitution on electrochemical performance. (c1) Cubic structure of perovskite showing the substitution of A sites, (c2) comparison of CV curves and (c3) specific capacitance of $La_{0.85}Sr_{0.15}MnO_3$ and $LaMnO_3$ electrodes. Reproduced with permission from ref. [337], Copyright 2016 Elsevier. (**d**) Effects of derivative structure on electrochemical performance. (d1) Schematic illustration of oxygen intercalation into $PrBaMn_2O_{6-\delta}$ during charging, (d2) CV curves of $PrBaMn_2O_{6-\delta}$ electrode,

and (d3) comparison of specific capacitance of $PrBaMn_2O_{6-\delta}$ and $PrBaMn_2O_6$ electrodes. Reproduced with permission from ref. [338], Copyright 2018 Wiley-VCH.

Derivatives of perovskite oxides such as double perovskite oxides and Ruddlesden–Popper oxides have been investigated as anion intercalation materials.[83, 333, 338-341] The reduction of $PrBaMn_2O_{6-\delta}$ double perovskite oxide resulted in the phase transition from a mixed hexagonal and cubic phase to a pure cubic phase.[338] As predicted by density-functional theory (DFT) calculations, oxygen vacancies are easier to be formed in the cubic phase than in the hexagonal phase. Accordingly, the cubic-phase $PrBaMn_2O_{6-\delta}$ achieved a high concentration of oxygen vacancies, demonstrating an anion storage mechanism similar to the $LaMnO_{3-\delta}$. Upon charging, the $O^{2-}$ ions enter the oxygen vacancies through the intercalation into the crystal lattice, and extra $O^{2-}$ ions occupy the surface of the crystal (**Fig. 9d1**). The $PrBaMn_2O_{6-\delta}$ electrode exhibited two pairs of redox peaks in KOH electrolyte, assigned to the redox couples of $Mn^{2+}/Mn^{3+}$ and $Mn^{3+}/Mn^{4+}$, as shown in CV curves (**Fig. 9d2**). The capacitance of $PrBaMn_2O_{6-\delta}$ was 1034.8 F $g^{-1}$ (or 143.7 mAh $g^{-1}$) and 2535.3 F $cm^{-3}$ at 1 A $g^{-1}$, twice greater than 462.3 F $g^{-1}$ of original $PrBaMn_2O_6$ (**Fig. 9d3**). In addition, electrochemical performances of $Ca_2MnO_{4-\delta}$ Ruddlesden–Popper oxide (r-CMO RP) and $CaMnO_{3-\delta}$ perovskite (r-CMO) were investigated and both showed the increased capacitances in KOH electrolyte by means of more oxygen vacancies incorporated via annealing in a reducing atmosphere.[333] Moreover, the capacitance of $Ca_2MnO_{4-\delta}$ electrode was higher than $CaMnO_{3-\delta}$ electrode at a low scan rates, but at high rates, this trend was reversed. The $Ca_2MnO_{4-\delta}$ electrode store $O^{2-}$ ions via oxygen vacancies in the perovskite and via interstitial sites in the rock salt, which is attributed to a high capacitance at low scan rates. However, the diffusion of $O^{2-}$ ions through the rock salt is slow, in which lowers the capacitance of $Ca_2MnO_{4-\delta}$ electrode at high scan rates.

The redox potentials of perovskite oxides are dependent on the nature of B sites, whose valences changes during charging and discharging processes.[83, 342, 343] In a comparison of the CV curves of $La_{1-x}Sr_xBO_{3-\delta}$ (B = Fe, Mn, Co) perovskite oxides in KOH electrolytes,[83] the $La_{1-x}Sr_xFeO_{3-\delta}$ showed a pair of evident redox peaks at the most negative potential ($E_{1/2}$ is −0.8 V versus Hg/HgO) originating from the $Fe^{2+}/Fe^{3+}$ redox couple. In contrast, the redox potentials of $La_{1-x}Sr_xMnO_{3-\delta}$ indicating the $Mn^{2+}/Mn^{3+}$ and $Mn^{3+}/Mn^{4+}$ redox couples were observed at the middle regions between −0.3 and −0.1 V versus Hg/HgO. The $La_{1-x}Sr_xCoO_{3-\delta}$ displayed more positive redox potentials between 0.1 and 0.3 V versus Hg/HgO, which are associated with the $Co^{2+}/Co^{3+}$ redox couple. Various $LaNi_{1-x}Fe_xO_{3-\delta}$ perovskites were characterized in KOH electrolyte.[342] When the content of Fe in $LaNi_{1-x}Fe_xO_{3-\delta}$ increased, the redox potentials of $Ni^{2+}/Ni^{3+}$ redox couple shifted positively ($E_{1/2}$ from 0.45 to 0.55 V versus Hg/HgO), while the peak potentials of $Fe^{3+}/Fe^{4+}$ redox couple shifted negatively ($E_{1/2}$ from −0.20 to −0.50 V versus Hg/HgO).

Perovskite fluorides ($ABF_3$) have been used as positive electrode materials in alkaline aqueous electrolytes.[344-349] In different manners from perovskite oxides, A sites of perovskite fluorides are alkaline metals such as Na and K, and B sites are transition metals with a valence of II (perovskite oxides with III of B sites). The perovskite fluorides, such as $NaNiF_3$,[346] $KNiF_3$,[348] $KNi_{1-x}Co_xF_3$[345], and $KNi_{1-x-y}Co_xMn_yF_3$[347], react with $OH^-$ ions, which is not promoted by oxygen vacancy like perovskite oxides. These perovskite fluorides delivered the specific capacities of approximately 150 to 230 mAh $g^{-1}$ in a mixed aqueous electrolyte (3 M KOH + 0.5 M LiOH).

**3.2.6 Others.**

**Iron-based oxides.** Fe-based oxides are important in aqueous energy storage because of their eco-friendliness, worldwide abundance, and low cost.[350, 351] In alkaline aqueous electrolytes, Fe oxides are generally used as negative electrodes because of their relatively low redox potentials. The charge storage of Fe oxides are attributed to several redox couples (Fe ↔ $Fe(OH)_2$ ↔ $FeOOH/Fe_2O_3$ ↔ $Fe_3O_4$) reacting with $OH^-$ ions.[352]

Despite their high theoretical capacity, Fe oxides are limited by the low utilization of storage sites and poor cyclic stability. In order to circumvent these issues, the morphology, crystal structure, and exposed facets of Fe oxides have been rationally designed.[350, 353] Moreover, the composites of nano-sized Fe oxides and conductive substrates have been exploited to increase the electronic conductivity and to suppress volume expansion.[63, 354-357] Along with graphene and CNTs, AC was used as a conductive substrate to prepare $FeO_x$-based composites, where the crystalline $FeO_x$ particles were distributed in nanopores of AC.[63] The porous AC can promote electron transport, control the size of $FeO_x$ (<5 nm), and prevent $FeO_x$ agglomeration. The discharge capacity of the $FeO_x$/AC electrode reached 600 mAh $g^{-1}$, with 85% capacity retention after 200 cycles. After synthesis of $Fe_2O_3$ nanorods on CNTs, conductive PPy was coated to further enhance energy storage performance.[354] The volumetric capacities of the $Fe_2O_3$@PPy/CNT electrode in KOH electrolyte were 620 and 330 mAh $cm^{-3}$ at 1 to 10 A $cm^{-3}$, respectively.

The electrochemical performance of Fe oxides has been improved via sulfuration and nitridation.[64, 295, 358-360] In this approach, sulfur-doped $Fe_2O_3$ (S-$Fe_2O_3$) nanowires were deposited onto CNT fibers (**Fig. 10a1**).[64] Theoretical calculations demonstrated that sulfuration of $Fe_2O_3$ decreases the band gap, thus enhancing electronic conductivity. The S-$Fe_2O_3$/CNT electrode displayed battery-type behavior in a potential window of −1.3 to 0 V versus Ag/AgCl, delivering an areal capacity of 0.81 mAh $cm^{-2}$ at 4 mA $cm^{-2}$, higher than 0.12 mAh $cm^{-2}$ of the $Fe_2O_3$ electrode (**Figs. 10a2 and 10a3**). NiFe nitride on N-doped graphene (NiFeN/NG) was synthesized through the pyrolysis of a mixture of GO, metal sources, and cyanamide.[295] The NiFeN/NG electrode achieved specific capacities of 262 and

206 mAh $g^{-1}$ at 1 and 50 A $g^{-1}$, respectively, in KOH electrolyte within a potential window of −1.0 to 0 V versus Ag/AgCl.

In contrast to battery-type Fe oxides, a low-crystalline and amorphous FeOOH exhibited a pseudocapacitive behavior.[361] The $Fe_2O_3$ on the carbon fiber cloth was irreversibly transformed into FeOOH in a KOH electrolyte. The FeOOH electrode showed a quasi-rectangular CV shape within −1.2 to 0 V versus $Hg/Hg_2Cl_2$ because of the reversible reaction between FeOOH and $Fe(OH)_2$. The specific capacitances were 1066 F $g^{-1}$ (355 mAh $g^{-1}$) at 1 $g^{-1}$ and 796 F $g^{-1}$ (265 mAh $g^{-1}$) at 30 $g^{-1}$, respectively, with a cycling stability of 91% over 10000 cycles.

**Bismuth and bismuth oxides.** Bi and $Bi_2O_3$ are promising negative electrodes materials for use in alkaline aqueous electrolytes.[85, 86, 362-365] The electrochemical reactions of Bi and $Bi_2O_3$ with $OH^-$ ions can be described as follows.

$$Bi_2O_3 + H_2O + 2e^- \leftrightarrow Bi_2O_2 + 2OH^- \quad (16)$$

$$Bi_2O_2 + 2H_2O + 4e^- \leftrightarrow 2Bi + 4OH^- \quad (17)$$

The conversion between $Bi_2O_3$ and Bi can transfer six electrons, resulting in a high theoretical specific capacity. Similar to Fe oxides, Bi and $Bi_2O_3$ suffer from low rates and cycling capabilities. To enhance the electrochemical performance, a hollow hexagonal prism $Bi_2O_3$ was synthesized via a template-induced method,[86] where precursor BiFe-based turnbull blue analogues were transformed into $Bi_2O_3$ in a KOH solution (**Fig. 10b1**). The specific capacity of the $Bi_2O_3$ electrode was 327 mAh $g^{-1}$ at 1 A $g^{-1}$, which is 94.8% of the theoretical capacity. At 20 A $g^{-1}$, the capacity was retained at 220 mAh $g^{-1}$ (**Figs. 10b2 and 10b3**). The $Bi_2O_3$ electrode also exhibited 80% capacity retention after 3000 cycles. Moreover, highly crystalline α-$Bi_2O_3$ was applied as a positive electrode for an alkaline Zn battery, and it exhibited a flat discharge-charge plateau, with specific capacities of 323 and 155 mAh $g^{-1}$ at 0.1 and 20 A $g^{-1}$, respectively.[362]

**Zinc metal.** Zn metals as two-electron redox ($Zn^{0/2+}$) anodes have advantages in terms of their low cost and high theoretical capacity (820 mAh $g^{-1}$) in aqueous electrolytes. [183, 184, 366, 367] In comparison to the Zn plating/stripping potential in neutral aqueous electrolytes (−0.76 V versus SHE), one in alkaline aqueous electrolytes is more negative (−1.26 V versus SHE).[183, 184] Upon discharging, the redox processes on Zn anode in alkaline aqueous electrolytes involve the electrooxidation of Zn metal to $Zn^{2+}$ ions, which combine with $OH^-$ ions to form soluble $Zn(OH)_4^{2-}$ ions as follows.

$$Zn + 4OH^- \leftrightarrow Zn(OH)_4^{2-} + 2e^- \quad (18)$$

The $Zn(OH)_4^{2-}$ ions can form insulating solid ZnO, which passivates Zn surface, thereby lowering the mass of active materials. In particular, the Zn metal anodes face the critical issues of dendrite formation and hydrogen evaluation. In order to resolve these issues, various strategies have been developed, including the monolithic nanoporous Zn anode,[185, 186, 368, 369] modification of electrode surface,[370, 371] and additive incorporation to Zn anode and electrolyte.[372, 373] For example, using a 3D monolithic sponge Zn anode for a Ni-Zn cell, a Zn depth of discharge (DOD) of 40% was achieved over 100 cycles, along with a higher specific energy comparable to that of Li-ion.[186] Moreover, ion-sieving $TiO_2$ layer was coated ZnO nanorods to suppress both passivation and hydrogen evolution. The resultant ZnO@$TiO_2$ anode exhibited a high capacity of 616 mAh $g^{-1}$ at 100% DOD in lean electrolyte.[371]

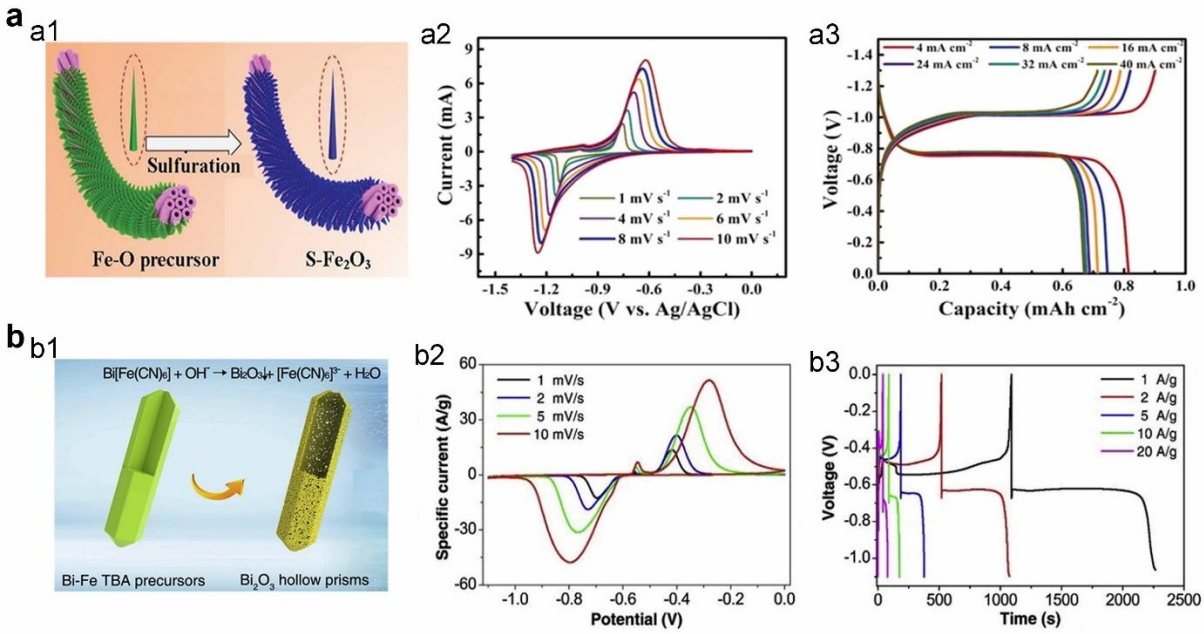


**Fig. 10** Fe- and Bi-based materials in alkaline aqueous electrolytes (**a**) Sulfur-doped $Fe_2O_3$ (S-$Fe_2O_3$). (a1) Schematic illustration of the synthesis of S-$Fe_2O_3$, (a2) CV curves and (a3) GCD curves of S-$Fe_2O_3$ electrode. Reproduced with permission from ref. [64], Copyright 2020 Wiley-VCH. (**b**) $Bi_2O_3$. (b1) Schematic illustration of the synthesis of $Bi_2O_3$ from BiFe-based TBA, (b2) CV curves and (b3) GCD curves of $Bi_2O_3$ electrode. Reproduced with permission from ref. [86], Copyright 2020 Elsevier.

**Table 4** Summary of transition metal hydroxides/oxides, sulfides, selenides, phosphides, nitrides, perovskite oxides, MOFs, and others in alkaline aqueous electrolytes.

| Electrode [ref] | Electrolyte | Potential window | Capacity | |
|---|---|---|---|---|
| NiCoMn-OH/rGO [260] | 2 M KOH | −0.1–0.45V vs. Ag/AgCl | 169 mAh $g^{-1}$ @ 5 A $g^{-1}$ | 119 mAh $g^{-1}$ @ 20 A $g^{-1}$ |
| NiMn-LDH [266] | 2 M KOH | 0.1–0.55 V vs. Hg/HgO | 328 mAh $g^{-1}$ @ 1 A $g^{-1}$ | 209 mAh $g^{-1}$ @ 30 A $g^{-1}$ |
| EA-CoOOH [52] | 6 M KOH | 0–0.55 V vs. Hg/HgO | 127 mAh $g^{-1}$ @ 1 A $g^{-1}$ | 99 mAh $g^{-1}$ @ 200 A $g^{-1}$ |
| Li-$Co_3O_4$ [60] | 6 M KOH | 0–0.5 V vs. Hg/HgO | 260 mAh $g^{-1}$ @ 1 A $g^{-1}$ | 224.4 mAh $g^{-1}$ @ 20 A $g^{-1}$ |
| P-$Co_3O_4$ [61] | 6 M KOH | −0.2–0.4 V vs. Hg/$Hg_2Cl_2$ | 286 mAh $g^{-1}$ @ 5 mV $s^{-1}$ | 169 mAh $g^{-1}$ @ 100 mV $s^{-1}$ |
| NiCo-LDH-CBD [273] | 6 M KOH | 0–0.4 V vs. Ag/AgCl | 235 mAh $g^{-1}$ @ 1 A $g^{-1}$ | 45.5 mAh $g^{-1}$ @ 150 A $g^{-1}$ |
| CC-NC-LDH [277] | 6 M KOH | 0–0.5 V vs. Hg/HgO | 252 mAh $g^{-1}$ @ 1 A $g^{-1}$ | 152 mAh $g^{-1}$ @ 100 A $g^{-1}$ |
| $NiCo_2O_4$@rGO [62] | 2 M KOH | 0–0.45 V vs. Ag/AgCl | 178 mAh $g^{-1}$ @ 8 A $g^{-1}$ | 117 mAh $g^{-1}$ @ 64 A $g^{-1}$ |
| $NiCo_2O_4$@rGO [281] | 6 M KOH | 0–0.5 V vs. Hg/HgO | 193 mAh $g^{-1}$ @ 0.5 A $g^{-1}$ | 116 mAh $g^{-1}$ @ 30 A $g^{-1}$ |
| NiCoAl-OH/$V_4C_3T_x$ [283] | 1 M KOH | −0.1–0.45 V vs. Ag/AgCl | 174 mAh $g^{-1}$ @ 1 A $g^{-1}$ | 83 mAh $g^{-1}$ @ 20 A $g^{-1}$ |
| $NiCo_2S_4$ [69] | 6 M KOH | 0–0.4 V vs. Hg/$Hg_2Cl_2$ | 262 mAh $g^{-1}$ @ 2.5 A $g^{-1}$ | 179 mAh $g^{-1}$ @ 40 A $g^{-1}$ |
| Ni-Co-S/graphene [70] | 6 M KOH | 0–0.5 V vs. Hg/HgO | 207 mAh $g^{-1}$ @ 1 A $g^{-1}$ | 199 mAh $g^{-1}$ @ 50 A $g^{-1}$ |
| $NiCoSe_2$ [74] | 6 M KOH | −0.2–0.4 V vs. Hg/$Hg_2Cl_2$ | 125 mAh $g^{-1}$ @ 1 A $g^{-1}$ | 110 mAh $g^{-1}$ @ 10 A $g^{-1}$ |
| $Ni_3Se_2$ [289] | 3 M KOH | 0–0.55 V vs. Hg/HgO | 122 mAh $g^{-1}$ @ 3 A $g^{-1}$ | 65 mAh $g^{-1}$ @ 20 A $g^{-1}$ |
| Ni-Co-N/GP [294] | 3 M KOH | 0–0.5 V vs. Hg/HgO | 133 mAh $g^{-1}$ @ 4 A $g^{-1}$ | 115 mAh $g^{-1}$ @ 20 A $g^{-1}$ |
| ZnNiCo-P [72] | 6 M KOH | 0–0.5 V vs. Hg/HgO | 266 mAh $g^{-1}$ @ 1 A $g^{-1}$ | 218 mAh $g^{-1}$ @ 20 A $g^{-1}$ |
| NiCo-CH-$Ni(OH)_2$ [76] | 6 M KOH | 0–0.5 V vs. Hg/HgO | 151 mAh $g^{-1}$ @ 1 A $g^{-1}$ | 114 mAh $g^{-1}$ @ 100 A $g^{-1}$ |
| C@ZnNiCo-CHs [77] | 2 M KOH | 0–0.5 V vs. Hg/HgO | 267 mAh $g^{-1}$ @ 1 A $g^{-1}$ | 194 mAh $g^{-1}$ @ 50 A $g^{-1}$ |
| VN [67] | 1 M KOH | −1.2–0 V vs. Hg/HgO | 1340 F $g^{-1}$ @ 2 mV $s^{-1}$ | 554 F $g^{-1}$ @ 100 mV $s^{-1}$ |
| VN/C [313] | 6 M KOH | −1.2–0 V vs. Ag/AgCl | 800 F $g^{-1}$ @ 4 A $g^{-1}$ | 584 F $g^{-1}$ @ 80 A $g^{-1}$ |
| VN/C [315] | 6 M KOH | −1.2–0 V vs. Hg/$Hg_2Cl_2$ | 392 F $g^{-1}$ @ 0.5 A $g^{-1}$ | 267 F $g^{-1}$ @ 5 A $g^{-1}$ |
| VN/NG [309] | 6 M KOH | −1.2–0 V vs. Ag/AgCl | 445 F $g^{-1}$ @ 1 A $g^{-1}$ | 278 F $g^{-1}$ @ 50 A $g^{-1}$ |
| VN/CNTs [66] | 1 M KOH | −1.0–0.06 V vs. Hg/HgO | 289 F $g^{-1}$ @ 20 mV $s^{-1}$ | 276 F $g^{-1}$ @ 100 mV $s^{-1}$ |
| VNNDs/CNS [46] | 1 M KOH | −1.0–−0.1 V vs. Hg/HgO | 573 F $g^{-1}$ @ 0.1 A $g^{-1}$ | 335 F $g^{-1}$ @ 100 A $g^{-1}$ |
| VNQDs/PC [374] | 6 M KOH | −1.15–0 V vs. Hg/$Hg_2Cl_2$ | 281 F $g^{-1}$ @ 0.5 A $g^{-1}$ | 190 F $g^{-1}$ @ 5 A $g^{-1}$ |
| TiN@C [308] | 1 M KOH | −1.0–0 V vs. Ag/AgCl | 159 F $g^{-1}$ @ 0.25 A $g^{-1}$ | 124.5 F $g^{-1}$ @ 5 A $g^{-1}$ |
| TiN [45] | 1 M KOH | −1.0–0 V vs. Ag/AgCl | 123 F $g^{-1}$ @ 10 mV $s^{-1}$ | 78.7 F $g^{-1}$ @ 400 mV $s^{-1}$ |
| WN (177 nm-thick) [188] | 1 M KOH | −1.0–−0.4 V vs. Hg/HgO | 1150 F $cm^{-3}$ @ 2 mV $s^{-1}$ | - |
| MOF-NiCo-LDH [181] | 6 M KOH | 0–0.5 V vs. Hg/HgO | 229 mAh $g^{-1}$ @ 1 A $g^{-1}$ | 180 mAh $g^{-1}$ @ 25 A $g^{-1}$ |
| NiCoZn-LDH/$Co_9S_8$ [319] | 3 M KOH | 0–0.5 V vs. Hg/HgO | 350 mAh $g^{-1}$ @ 1 A $g^{-1}$ | 217 mAh $g^{-1}$ @ 20 A $g^{-1}$ |
| Co-Ni-B-S [320] | 6 M KOH | −0.1–0.55V vs. Hg/HgO | 231 mAh $g^{-1}$ @ 1 A $g^{-1}$ | 216 mAh $g^{-1}$ @ 10 A $g^{-1}$ |
| CoNi-MOF [182] | 1 M KOH | 0–0.45 V vs. Hg/$Hg_2Cl_2$ | 130 mAh $g^{-1}$ @ 2 A $g^{-1}$ | 71 mAh $g^{-1}$ @ 32 A $g^{-1}$ |
| Ni-HAB MOF [93] | 1 M KOH | −0.75–−0.25 V vs. Ag/AgCl | 400 F $g^{-1}$ @ 0.2 mV $s^{-1}$ | - |
| $Zn_xCo_{1-x}O$ [40] | 6 M KOH | −1.0–−0.2 V vs. Ag/AgCl | 1065 F $g^{-1}$ @ 5 mV $s^{-1}$ | 450 F $g^{-1}$ @ 1000 mV $s^{-1}$ |
| $LaCoO_{3-\delta}$ [332 ] | 6 M KOH | −0.3–0.45 V vs. Hg/HgO | 147 mAh $g^{-1}$ @ 1 A $g^{-1}$ | - |
| $LaMn_{1.1}O_3$ [335] | 1 M KOH | −1.0–0.56 V vs. Hg/HgO | 202 mAh $g^{-1}$ @ 1 A $g^{-1}$ | 36.1 mAh $g^{-1}$ @ 30 A $g^{-1}$ |
| $LaNiO_3$ [331] | 6 M KOH | 0–0.45 V vs. Hg/$Hg_2Cl_2$ | 139 mAh $g^{-1}$ @ 1 A $g^{-1}$ | 122 mAh $g^{-1}$ @ 16 A $g^{-1}$ |
| $SrCo_{0.9}Mo_{0.1}O_{3-\delta}$[375] | 6 M KOH | 0–0.5 V vs. Ag/AgCl | 169 mAh $g^{-1}$ @ 1 A $g^{-1}$ | 87.5 mAh $g^{-1}$ @ 10 A $g^{-1}$ |
| $SrCo_{0.9}Nb_{0.1}O_{3-\delta}$ [82] | 6 M KOH | 0–0.5 V vs. Hg/HgO | 107 mAh $g^{-1}$ @ 0.5 A $g^{-1}$ | 103 mAh $g^{-1}$ @ 10 A $g^{-1}$ |
| $PrBaMn_2O_{6-\delta}$[338] | 6 M KOH | 0–0.5 V vs. Hg/HgO | 144 mAh $g^{-1}$ @ 1 A $g^{-1}$ | 110 mAh $g^{-1}$ @ 10 A $g^{-1}$ |
| $PrBaCo_2O_{5+\delta}$ [339] | 6 M KOH | −0.1–0.55 V vs. Hg/HgO | 119 mAh $g^{-1}$ @ 1 mV $s^{-1}$ | - |
| $Sr_2CoMo_{1-x}Ni_xO_{6-\delta}$ [340] | 6 M KOH | −0.1–0.5 V vs. Hg/HgO | 129 mAh $g^{-1}$ @ 1 A $g^{-1}$ | 108 mAh $g^{-1}$ @ 10 A $g^{-1}$ |
| $Sr_2CoMoO_{6-\delta}$ [341] | 6 M KOH | 0–0.4 V vs. Ag/AgCl | 82.6 mAh $g^{-1}$ @ 1 A $g^{-1}$ | 46.3 mAh $g^{-1}$ @ 10 A $g^{-1}$ |
| $La_2NiO_{4+\delta}$@Ag [376] | 1 M KOH | 0.2–0.6 V vs. Hg/HgO | 130 mAh $g^{-1}$ @ 1 mV $s^{-1}$ | 65.1 mAh $g^{-1}$ @ 50 mV $s^{-1}$ |
| $KNi_{0.8}Co_{0.2}F_3$ [345] | 3 M KOH/0.5 M LiOH | 0.1–0.55 V vs. Hg/HgO | 187 mAh $g^{-1}$ @ 1 A $g^{-1}$ | 172 mAh $g^{-1}$ @ 16 A $g^{-1}$ |

| | | | | |
|---|---|---|---|---|
| $KNi_{1-x-y}Co_xMn_yF_3$ [347] | 3 M KOH/0.5 M LiOH | 0–0.5 V vs. Hg/HgO | 196 mAh $g^{-1}$ @ 1 A $g^{-1}$ | 149 mAh $g^{-1}$ @ 16 A $g^{-1}$ |
| $KNiF_3$@CNTs [348] | 3 M KOH/0.5 M LiOH | 0–0.5 V vs. Hg/HgO | 229 mAh $g^{-1}$ @ 1 A $g^{-1}$ | 191 mAh $g^{-1}$ @ 16 A $g^{-1}$ |
| $Fe_2O_3$/PPy/CNT [354] | 3 M KOH | −1.2–0 V vs. Ag/AgCl | 620 mAh $cm^{-3}$ @ 1 A $cm^{-3}$ | 330 mAh $cm^{-3}$ @ 10 A $cm^{-3}$ |
| $Fe_3O_4$@rGO [356] | 4 M KOH | −1.1–0 V vs. Hg/HgO | 135 mAh $g^{-1}$ @ 3 A $g^{-1}$ | 131 mAh $g^{-1}$ @ 30 A $g^{-1}$ |
| FeOOH [361] | 2 M KOH | −1.2–0 V vs. $Hg/Hg_2Cl_2$ | 355 mAh $g^{-1}$ @ 1 A $g^{-1}$ | 265 mAh $g^{-1}$ @ at 30 A $g^{-1}$ |
| $FeS_2$/GNS [358] | 2 M KOH | −1.1–0 V vs. Hg/HgO | 220 mAh $g^{-1}$ @ 3 A $g^{-1}$ | 220 mAh $g^{-1}$ @ 30 A $g^{-1}$ |
| NiFeN/NG [295] | 3 M KOH | −1.0–0 V vs. Ag/AgCl | 262 mAh $g^{-1}$ @ 1 A $g^{-1}$ | 180 mAh $g^{-1}$ @ at 50 A $g^{-1}$ |
| porous Bi/C [85] | 6 M KOH | −1.4–0 V vs. $Hg/Hg_2Cl_2$ | 166 mAh $g^{-1}$ @ 6 mA $cm^{-2}$ | 91 mAh $g^{-1}$ @ 120 mA $cm^{-2}$ |
| $Bi_2O_3$ [86] | 6 M KOH | −1.1–0 V vs. Ag/AgCl | 327 mAh $g^{-1}$ @ 1 A $g^{-1}$ | 220 mAh $g^{-1}$ @ at 20 A $g^{-1}$ |
| Bi nanosheets [365] | 1 M KOH | −1.2–0.2 V vs. $Hg/Hg_2Cl_2$ | 366 mAh $g^{-1}$ @ 0.2 A $g^{-1}$ | 175 mAh $g^{-1}$ @ at 20 A $g^{-1}$ |
| $Bi_2S_3$/NC [377] | 6 M KOH | −0.95–−0.4 V vs. Ag/AgCl | 71.2 mAh $g^{-1}$ @ 1 A $g^{-1}$ | 45.7 mAh $g^{-1}$ @ 8 A $g^{-1}$ |

**3.3 Faradaic materials storing other polyatomic anions.**

**3.3.1 Graphite and other carbons.** Graphite, which has a hexagonal honeycomb structure of stacked graphene layers of $sp^2$ hybridization along the *c* axis, is semimetallic, demonstrating no band gap and a negligible density of states at the Fermi level.[378, 379] Because the unique electronic band structure allows graphite to be redox-amphoteric, both anion and cation carriers can be intercalated into graphite galleries while the π electrons are taken and given in. Pre-lithiated graphite has been used as a high-capacity negative electrode paired with AC positive electrode for applications in lithium-ion capacitors.[19, 21, 380] In contrast to Li cation storage mechanism of LICs, anion storing graphite offers an opportunity to configure distinct hybrid capacitors as positive electrodes (**Table 5**).

**Anion intercalation mechanism and kinetics of graphite.** In intercalation of anions into graphite, *ab initio* calculations such as Bader analysis suggest that charges are mainly compensated by electron transfers of graphite rather than the anion.[190, 381] The Raman G band of graphite corresponds to the $E_{2g}$ phonon of the in-plane carbon atom displacement in the graphene layer. In quantum theory, the position of the G-band peak is not affected by electron extraction. However, a blueshift is observed during the anion intercalation process because the strong electron-phonon coupling breaks the adiabatic rearrangement of the Fermi surface.[382] Through X-ray Raman spectroscopy (XRS) and DFT calculations, the evolution of the electronic structure of graphite during anion intercalation was thoroughly investigated.[191] As shown in **Fig. 11a1**, compared to the pristine graphite containing only π* and σ* features (labelled as 2 and 4, respectively), the extra pre-π* and π*-shift features (labelled as 1 and 3, respectively) appear in the anion-intercalated graphite. The pre-π* feature implies that the delocalized π electrons of graphite are removed to compensate for the charge of the intercalated anions (**Fig. 11a1**, top). The removal of π electrons empties the pre-occupied states and decreases the Fermi energy level (**Fig. 11a2**). Consequently, the appearance of pre-π* features is a direct evidence of the generation of new unoccupied states above the Fermi level. The decreased Fermi level greatly increases the density of states, indicating that the graphite is transformed from semimetallic to metallic with an enhanced electronic conductivity upon anion intercalation. The π*-shift feature upon anion intercalation is attributed to the effective nuclear charge increase of the C atom of oxidized graphite, which increases the energy required for the core electron transition. Along with the change in the electronic structure and properties upon anion intercalation, the staging process needs to be discussed to gain a fundamental understanding of the anion intercalation mechanism. In an analogous manner to $Li^+$ intercalation,[379] the anions are periodically arranged along the stacking direction of graphene layers at each stage. Thus, the special structure of anion-intercalated graphite is described by the stage order *n* (expressed as stage-*n*), which is defined as the number of graphene layers between two neighboring anion layers.[383, 384] For example, stage-2 graphite shows that $PF_6^-$ anions are separated by two graphene layers (**Fig. 11b**). While increasing the degree of anion intercalation, the graphite structure undergoes a transition to a lower stage order.[160, 383, 384]

Because the blueshift of the Raman G band is proportional to the hole concentration with graphite oxidation, the stage transition can be analyzed qualitatively by Raman spectra. In stage-4 and 3, there are two kinds of carbon layers, that is the boundary and inner layers, which are the nearest and second neighbor layers of anion intercalant, respectively. Since the boundary layer has a higher degree of oxidation than the inner layer, the signal $E_{2g}$(b) of boundary layer has a larger blueshift than the $E_{2g}$(i) of inner layer and thus, the G band splits into a doublet. The stage-2 and 1 are indistinguishable by Raman G band and shows singlet G band due to the absence of inner layer. The G band of stage-6 or 5 is expected to split into a triplet because of the existence of third neighbor graphene layer,[385] however, the experimental observations cannot distinguish well at such high order stage.[161]

The geometric features of anion-intercalated graphite can be calibrated by XRD. The periodic repeated distance ($d_c$) along stacking direction of crystal planes of graphene layers satisfies the Bragg's law when diffraction occurs:

$$2d_c \sin\theta_{00l} = l\lambda \quad (19)$$

where $\lambda$ is the X-ray wavelength, $\theta_{00l}$ is the glancing angle for *l* order reflection. Upon the intercalation of anions, the diffraction peaks caused by discrete $d_c$ can appear[152, 160, 383, 384] (**Fig. 11c**). For a graphite at specific stage, the XRD peaks come from different reflection orders with the same $d_c$. For the splitting peaks of pristine graphite (002) peak, the *l* difference is

generally 1. Substituting the diffraction angle into the Bragg equation, $d_c$ can be solved.[386, 387] As shown in **Fig. 11b**, for the stage-*n* graphite, $d_c$ also satisfies the following expression.

$$d_c = d_i + (n-1)d_0 \quad (20)$$

where $d_0$ is the non-intercalant gallery height (3.35 Å) and $d_i$ is the intercalant gallery height which reflects structural expansion. Compared to the alkali-ion intercalation (13% for $LiC_6$, 60% for $KC_8$),[388, 389] anion intercalation causes a much larger volume expansion of graphite (130-140% for $PF_6^-$, $BF_4^-$, $TFSI^-$; 180% for $AlCl_4^-$).[160, 384, 390] Despite such a huge volume change, the graphite as an anion-intercalation material exhibits high rate capability and long stability over tens of thousands of cycles.[56] This allows graphite to be a suitable positive electrode material for battery-capacitor hybrid devices.

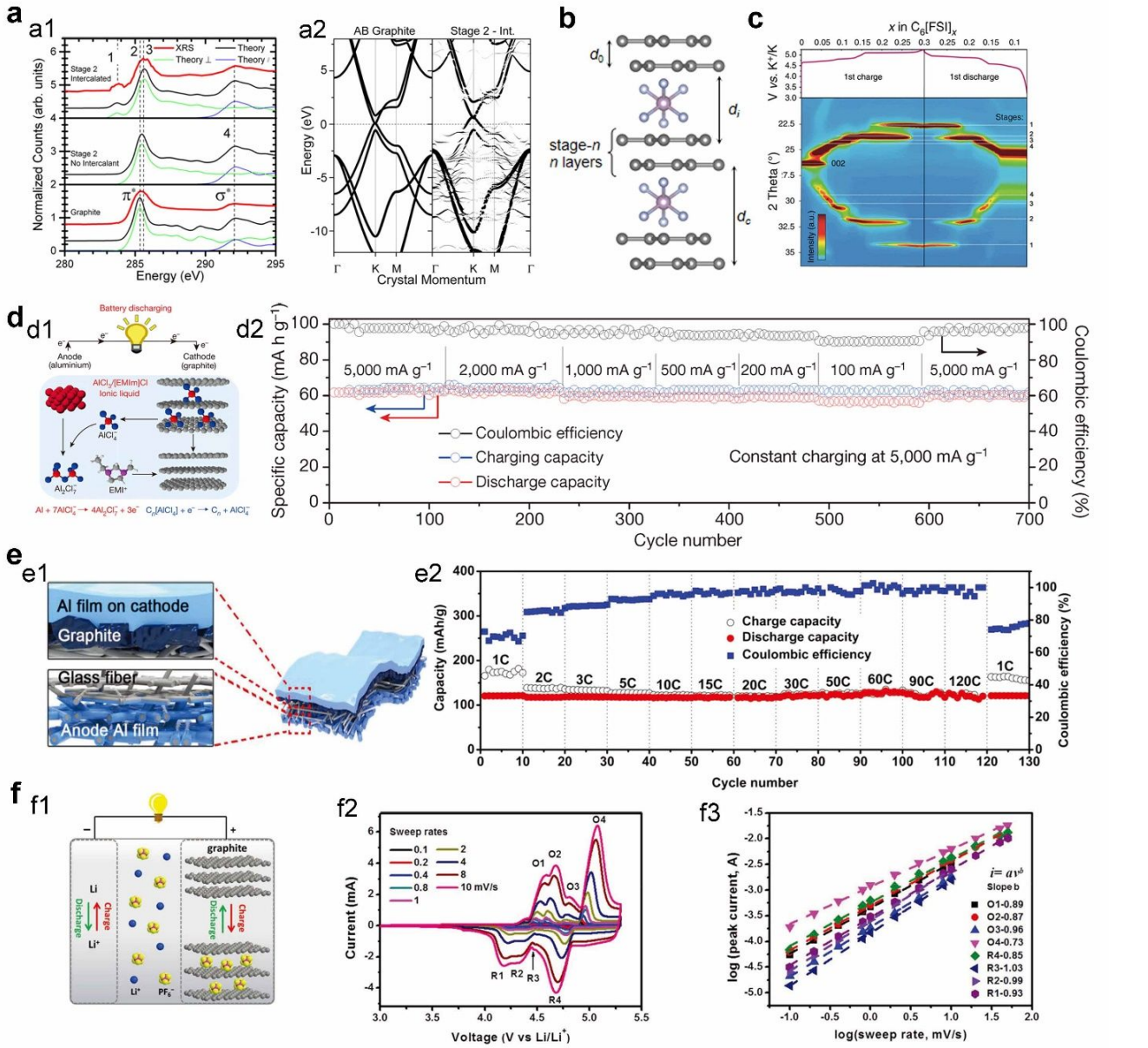


**Fig. 11** Fundamental mechanism and fast kinetics of anion intercalation into graphite**.** (**a**) The evolution of the electronic structure of anion intercalated graphite. (a1) Experimental and theoretical XRS spectra for $PF_6^-$-intercalated graphite (top), imaginary graphite without intercalant (middle) and pristine graphite (down). (a2) Band structure of pristine graphite (left) and $PF_6^-$-intercalated graphite (right). Reproduced with permission from ref. [191], Copyright 2020 American Chemical Society. (**b**) The geometric features of a stage-2 $PF_6^-$-intercalated graphite, where *n* is stage order, $d_c$ is the periodic repeat distance, $d_0$ and $d_i$ are the non-/intercalant gallery height, respectively. (**c**) *In situ* XRD patterns of graphite during $FSI^-$ intercalation/deintercalation. The white horizontal dashed lines show the diffraction peak positions ascribed to the stage-4 to stage-1 of anion-intercalated graphite. Reproduced with permission from ref. [152], Copyright 2018 Springer Nature. (**d**) A cell configured by graphite cathode, Al deposition anode and EMIMCl-$AlCl_3$ IL electrolyte. (d1) Schematic illustration of the intercalation of $AlCl_4^-$ into graphite cathode, (d2) ultrafast rate performance at discharge current from 100 to 5000 mA $g^{-1}$. Reproduced with permission from ref. [104], Copyright 2015 Springer Nature. (**e**) A cell configured by graphite cathode, alloying-type Al anode and $LiPF_6$ carbonate electrolyte. (e1) Schematic illustration of the integrated configuration design of the cell, (e2) ultrafast rate performance at current rate from 1 to 120 C. Reproduced with permission from ref. [105], Copyright 2017 Wiley-VCH. (**f**) A Li-graphite half cell using $LiPF_6$ carbonate electrolyte. (f1) Schematic illustration of the half cell with $PF_6^-$ intercalation, (f2) CV curves at various sweep rates and (f3) corresponding calculated *b*-values. Reproduced with permission from ref. [56], Copyright 2018 Wiley-VCH.

For the construction of hybrid cells, two electrodes having different energy storage mechanisms and operating potentials should be energetically and kinetically balanced in terms of a mass loading and electrode area. Accordingly, high-capacity electrode needs to have sufficient rate and cycling capabilities to pair with capacitive electrode. Surprisingly, graphite as an anion storing intercalation battery-type material achieves the outstanding electrochemical stability for high voltage and long cyclability, and the extraordinary fast charge storage kinetics. Dai et al. reported ultrafast anion intercalation behavior of 3D graphitic-foam cathode paring with Al metal anode and EMIMCl-$AlCl_3$ electrolyte (**Fig. 11d1**).[104] At an ultrahigh current density of 5000 mA $g^{-1}$ (75 C), the graphitic-foam cathode preserved the stable charge-discharge curves and high capacity of 60 mAh $g^{-1}$ (**Fig. 11d2**). It means that graphitic cathode is fully and quickly charged within less than one minute and high power output is available by fast discharge. Furthermore, the electrode achieved an excellent stability over 7500 cycles without the significant capacity decline at 4000 mA $g^{-1}$. Using the natural graphite particles as cathode, alloy-type Al as anode and an organic $LiPF_6$ carbonate electrolyte, the ultrafast anion intercalation behavior was observed and attributed to the kinetic properties of graphite.[105] In this integrated cell, the Al anode is deposited on one side of a glass fiber separator to form an interpenetrating network structure, while the natural graphite is loaded on the other side of glass fiber with an Al sputtering layer as current collector (**Fig. 11e1**). Such an integrated design significantly improves the kinetics of Li-Al alloying reaction on anode, ensuring that the anion intercalation reaction at cathode is not limited by the kinetics of anode. As shown in **Fig. 11e2**, the anion de-/intercalation reaction was completed at an ultrahigh rate of 120 C (or 12000 mA $g^{-1}$) within 30 seconds. Furthermore, a high capacity of 116.1 mAh $g^{-1}$ and a middle discharge voltage of 3.8 V were maintained even at 120 C. In order to deeply investigate the anion intercalation kinetics of graphite, commercial graphite with limited surface area (5 $m^2$ $g^{-1}$) as cathode and Li metal as anode were tested in a $LiPF_6$ carbonate electrolyte (**Fig. 11f1**).[56] The high-rate performance of graphite was confirmed demonstrating the high capacities of 99.4 mAh $g^{-1}$ at 2 C and 78 mAh $g^{-1}$ even at 100 C. Moreover, the anion intercalation of graphite cathode is dominated by a fast surface-controlled electrochemistry (**Figs. 11f2 and 11f3**). In addition, the charge transfer resistance of graphite cathode continuously decreases and the mass transfer is activated and facilitated during cycling. A long-term stability is confirmed by 81% of capacity retention over 10000 cycles.

The ultrafast anion intercalation kinetics of graphite is abnormal considering the larger size of anions and larger volume expansion compared to cation intercalation. Generally speaking, the kinetic properties of an electrode material are closely related to the electronic conductivity and energy barriers of ion diffusion. As discussed above, anion intercalated graphite becomes metallic, thus improving the electronic conductivity. After resolving the controversies about the geometry and intercalant gallery height ($d_i$),[104, 391, 392] the nudged elastic band method was used to calculate the diffusion energy barrier (12–29 meV) of $AlCl_4^-$ in the graphite.[390] Similar result of 21–28 meV was also obtained by Sun el al.[393] Such a diffusion barrier is much smaller than 420 meV of $Li^+$ diffusion in graphite anode,[394] which may be associated with the ultrafast anion intercalation. Moreover, the $PF_6^-$ exhibited the ultrafast kinetics although it has a larger diffusion barrier in graphite, about 140–160 meV.[190] The fast anion intercalation phenomenon is found in bulk natural graphite[56, 105, 395], different electrolyte system and anion (even large $TFSI^-$),[395] which suggest that the ultrafast kinetics is the intrinsic property of graphite. However, the diffusion energy barrier alone cannot fully elucidate this abnormal kinetics of anion intercalation and thus, further research on the origin of ultrafast anion intercalation needs to be carried out as future work.

**Influential factors on the anion intercalation of graphite.** Parameters of anion intercalation that may affect the electrochemical performance of graphite were investigated. A higher degree of graphitization tends to result in a higher anion intercalation capacity and lower voltage hysteresis.[396, 397] Although a smaller size of graphite particles is beneficial to achieve a high capacity, stability issues along with reduced electrical conductivity can be expected.[398] The abundant edge sites or surface defects of graphite can induce irreversible side reactions, lowering the Coulombic efficiency.[399, 400]

Controlling geometry and crystalline structure of few-layer graphene exfoliated from graphite can increase the redox activity and cycling stability upon anion intercalation (**Fig. 12a1**). For instance, a reduction of the vertical size along the layer stacking direction promotes kinetic performance, while an enlarged lateral graphene size improves structural stability.[401] Consequently, the large lateral-sized graphene (L-graphene) exhibited better rate performance (**Fig. 12a2**) and cycling stability (**Fig. 12a3**) than small graphite/graphene samples. The defect-free conjugated structure of graphene layers improves the reversibility and kinetic performance, suppressing side reactions and improving electronic conductivity. After high-temperature reduction at 3000 °C, defect-free few-layer graphene showed an $AlCl_4^-$ storing capacity of 100 mAh $g^{-1}$ at 5 A $g^{-1}$, along with a retention of 97% over 25000 cycles.[402] The Co-treated defect-free few-layer graphene also displayed a high $PF_6^-$ storing capacity of 150 mAh $g^{-1}$ along with an evident voltage plateau in the range of 2.0–5.0 V.[403] Besides, the different electrode preparation strategies, such as dense stacking[404] and monolithic vertically aligning,[405] have been developed to improve the anion storage performance while preserving the intrinsic properties of few-layer graphene.

Integrating the Faradaic intercalation with non-Faradaic adsorption mechanism can improve the capacity of carbon-based anion storage materials with the compromised operating voltage (**Fig. 12b1**). One design strategy is to construct functional structure for anion adsorption on graphite. Through thermal shock treatment, the flexuous graphite (FG) with the disordered and defective structure was synthesized.[406] In an Al–FG cell using EMIMCl-$AlCl_3$ electrolyte, the FG cathode reveals an integrated intercalation–adsorption mechanism for $AlCl_4^-$ storage within a voltage of 0.5 to 2.45 V. The specific capacities of 149 and 93 mAh $g^{-1}$ at 1.5 and 7.5 A $g^{-1}$, respectively, and a

 

long cycling stability over 8000 cycles at 3 A $g^{-1}$ were obtained (**Figs. 12b2 and12b3**). Moreover, a porous graphitic carbon prepared through one-step activation and catalytic graphitization method delivered the $TFSI^-$ storage capacity of 204.2 mAh $g^{-1}$, significantly greater than that of mechanically mixed graphite and AC.[407] Another way is to introduce graphite domains into the adsorption carbon structure. For instance, the nanosheet-bricked porous graphitic carbon showed a $AlCl_4^-$ storage capacity of 104 mAh $g^{-1}$ at 10 A $g^{-1}$ with a cyclic stability for 3000 cycles.[408] The 3D porous microcrystalline carbon exhibited specific capacities of 191.4 and 77.8 mAh $g^{-1}$ at 0.1 and 10.0 A $g^{-1}$, respectively, owing to the intercalation and adsorption of $PF_6^-$ anion.[409]

A stable CEI as well as an electrolyte with a wide ESW is necessary for high-voltage anion intercalation graphite. The CEI alleviates the electrolyte decomposition and solvent co-intercalation kinetically and energetically.[149, 150, 410] An anodic SEI on graphite electrode surface was pre-formed by operating few cycles of graphite electrode at low potential of 0.3–2.0 V versus $Li^+/Li$.[149] Such SEI-modified graphite was used as the cathode of a dual-ion battery configuring a Li anode and a 1 M $LiPF_6$ carbonate electrolyte. During the subsequent anion de-/intercalation process (3.0–5.0 V versus $Li^+/Li$), the SEI layer on the graphite cathode reconstructs as an artificial CEI, which inhibits the electrolyte decomposition and brings higher capacity and better cycling stability compared to the unmodified one. Moreover, a $Li_4Ti_5O_{12}$ (LTO) layer coated on the mesocarbon microbeads (MCMB) forms an oxidation-resistant CEI layer through the ring opening polymerization of sulfolane owing to the electrocatalysis by the Lewis acidic sites (**Fig. 12c1**).[150] Accordingly, the solvent co-intercalation and electrolyte decomposition are inhibited (**Fig. 12c2**), leading to improved graphite stability. The LTO-CEI modified MCMB exhibited a capacity of 96.7 mAh $g^{-1}$ with 85.1% retention after 2000 cycles even at the high cut-off potential of 5.4 V versus $Li^+/Li$ (**Fig. 12c3**).

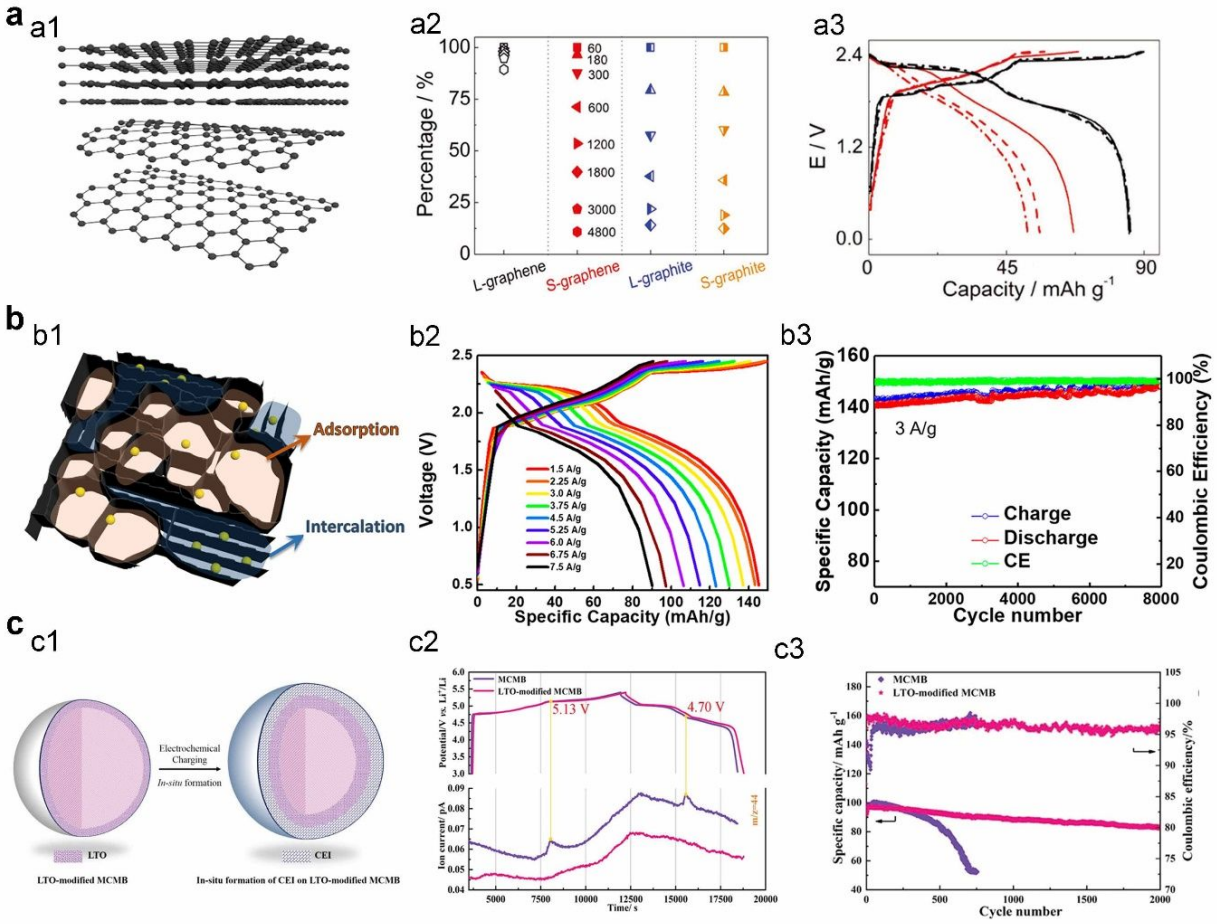


**Fig. 12** Influential factors on the anion intercalation of graphite. (**a**) Preparation of few-layer graphene. (a1) Schematic illustration, (a2) Rate capability of L-graphene, S-graphene, L-graphite and S-graphite, and (a3) GCD curves of L-graphene (black) and S-graphene (red) in the 1st, 500th, and 1000th cycle. Reproduced with permission from ref. [401], Copyright 2017 Wiley-VCH. (**b**) Integration of intercalation and adsorption mechanism. (b1) Schematic illustration, (b2) GCD curves of Al//FG cell at different current densities, (b3) cycling stability of Al//FG cell at 3 A $g^{-1}$. Reproduced with permission from ref. [406] Copyright 2020 American Chemical Society. (**c**) Modification of stable CEI. (c1) *In situ* modification of CEI on $Li_4Ti_5O_{12}$-coated MCMB, (c2) $CO_2$ differential electrochemical mass spectrometry signal of un-/modified MCMB during the first cycle, (c3) cycling stability of LTO-CEI modified and pristine MCMB with potential range of 3.0-5.4 V versus $Li^+/Li$. Reproduced with permission from ref. [150], Copyright 2019 Wiley-VCH.

**3.3.2 Organic electrodes.** In sharp contrast to inorganic materials, organic materials have advantages in terms of abundant sources and modification chemistries, low cost, and easy recycling.[411-417] In particular, flexible designability toward diverse chemical structures provides a variety of electrochemical and physical properties for anion storage. The p-type organic materials are reversibly oxidized from a neutral state to a positively charged state upon anion insertion.[31, 412] **Fig. 13** summarizes typical p-type organic materials and their corresponding redox reactions for anion storage, including the reversible extraction of aromatic π electrons and unbound electrons of thioether and amine. In contrast to previous review articles about organic electrodes,[31, 32, 411-417] this section focuses on anion storage mechanism and structural features of p-type organic electrodes (**Table 5**). The p-type organic materials can be classified as small molecules and polymers.

**Small molecules.** The p-type organic materials of monomeric molecules are characterized by diverse and tunable structures through molecular engineering based on organic chemistry, resulting in improved anion storage performance. Polyaromatic hydrocarbons (PAHs), consisting of a few-fused $sp^2$-hybridized $C_6$ rings with peripheral H atoms, have a much shorter conjugated structure than infinitely conjugated graphite. PAHs, such as pyrene and coronene, store anions along with an obvious plateau and mild anion insertion potential that can avoid electrolyte decomposition.[418] The coronene retains its molecular structure and forms carbocations upon anion intercalation (**1** in **Fig. 13**).[90] Although polymeric and amorphous organic molecules generally achieve a better performance,[412, 415] crystalline coronene demonstrated an impressive stability up to 5000 cycles and low polarization.[90, 419] The stability of crystalline coronene is attributed to the self-assembly and long-range ordering via van der Waals forces rather than covalently chained rigid frameworks. Moreover, structural flexibility that can adjust morphology and long-range order allows anions to be intercalated.

In addition to PAHs, organic structures based on amine redox centers can electrochemically accommodate anions. To enhance the electronic conductivity and electrochemical stability, a conjugated aromatic rubicene core was coupled with two amino-groups to afford the 5,12-diaminorubicene (DARb, **2** in **Fig. 13**).[420] The conjugated apolar rubicene framework provides the planar π-orbital for intermolecular electronic delocalization, stabilizing the positive charges and unpaired electrons upon anion insertion and inhibiting the dissolution of DARb molecules in the polar solvents. This DARb electrode stores $PF_6^-$ anions through two-electron transfer via the formation of a radical cation followed by electron delocalization on the aromatic structure, delivering a specific capacity of 115 mAh $g^{-1}$ in $LiPF_6$-based EC-DMC electrolyte with an average potential of 3.4 V versus $Li^+/Li$.

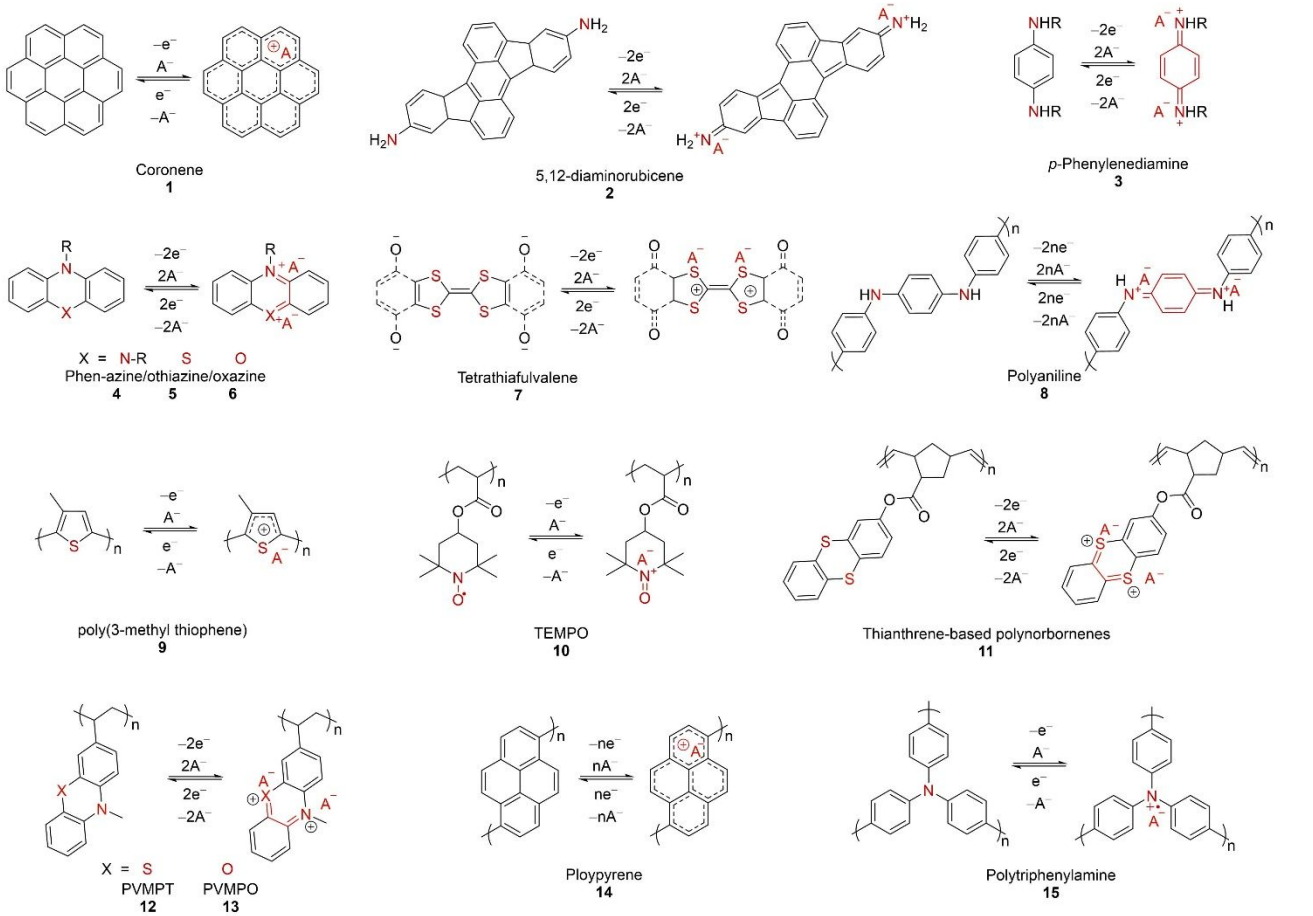


**Fig. 13** p-Type organics and their electrochemical redox reactions for anion storage.

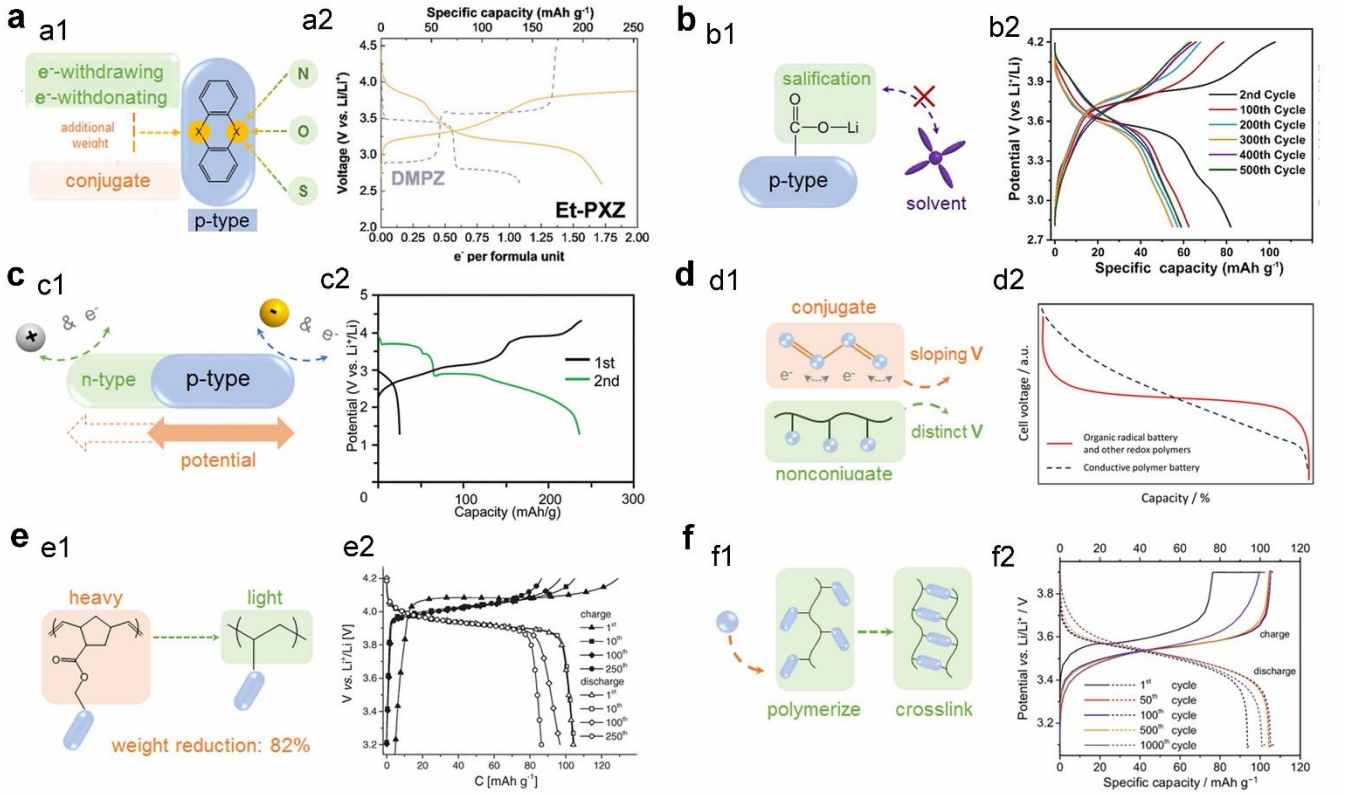


**Fig. 14** Influential factors of the performance of p-type organics and their derivatives. (**a**) Structure adjustment of introducing functional groups and substituting by heteroatom. (a1) Schematic illustration. (a2) GCD curves of Et-PXZ as an example. Reproduced with permission from ref. [116], Copyright 2020 Wiley-VCH. (**b**) Salification. (b1) Schematic illustration. (b2) GCD curves of LiPHB as an example. Reproduced with permission from ref. [192], Copyright 2020 Wiley-VCH. (**c**) Activate low potential range. (c1) Schematic illustration. (c2) GCD curves of fused tetrathiafulvalene as an example. Reproduced with permission from ref. [422], Copyright 2019 Royal Society of Chemistry. (**d**) Non-/conjugated structure. (d1) Schematic illustration. (d2) Typical GCD curves Non-/conjugated p-type organics. Reproduced with permission from ref. [413], Copyright 2016 American Chemical Society. (**e**) Lightweight backbone. (e1) Schematic illustration. (e2) GCD curves of poly(2-vinylthianthrene) as an example. Reproduced with permission from ref. [439], Copyright 2017 Wiley-VCH. (**f**) Cross-link. (f1) Schematic illustration. (f2) GCD curves of PVMPT as an example. Reproduced with permission from ref. [441], Copyright 2018 Wiley-VCH.

Modification of the amine units with functional groups affects the electrochemical properties. Taking *p*-phenylenediamine (**3** in **Fig. 13**) as an example, it can be oxidized sequentially to dication at 3.58 and 4.07 V versus $Li^+/Li$ upon two $ClO_4^-$ anion storage.[421] After phenyl-substitution of two primary amines, the redox potentials increased to 3.75 and 4.15 V versus $Li^+/Li$ probably due to π-delocalization by mesomeric effect. By contrast, the electron donating tetramethyl-substitution decreased the redox potentials to 3.41 and 3.95 V due to the inductive effect. In contrast to introducing functional groups, heteroatom incorporation is an effective means of tuning the electrochemical properties of p-type organics without increasing molecular weight (**Fig. 14a1**). The 5,10-dimethyl phenazine (DMPZ **4** in **Fig. 13**) is featured with two-electron oxidation by quaternary nitrogen formation, delivering high theoretical capacity but low operating potentials of 3.1 and 3.7 V versus $Li^+/Li$.[154] In order to mitigate the trade-off between capacity and voltage, either one of the two N atoms of DMPZ is replaced by weaker electron-donating S (**5**, phenothiazine, in **Fig. 13**) and O (**6**, phenoxazine, in **Fig. 13**) heteroatoms.[116] This replacement enhances the redox potential and capacity. For example, the 10-ethyl-10H-phenoxazine (Et-PXZ) in $LiClO_4$-glyme-based organic electrolyte showed redox potentials of 3.17 and 3.82 V versus $Li^+/Li$ and a specific capacity of 218 mAh $g^{-1}$, higher than 2.78/3.44 V and 137.7 mAh $g^{-1}$ of the DMPZ, respectively (**Fig. 14a2**).

The dissolution of small organic molecules into electrolytes results in their poor cycling stability. Tethering highly polar ionic groups to small molecules, so-called salification into organic salts, leads to suppressed dissolution, thereby improving cycling stability (**Fig. 14b1**).[412] For example, the electrochemically stable phenothiazine-based lithium 4-(10H-phenothiazin-10-yl) benzoate salt (LiPHB) achieved an initial capacity of 82 mAh $g^{-1}$ with an average potential plateau of 3.7 V versus $Li^+/Li$ and a capacity retention of 72% over 500 cycles for $ClO_4^-$ storage (**Fig. 14b2**).[192]

It notes that p-type organic molecules display higher redox potentials than n-type ones. However, p-type organic materials are always redox inactive in the relatively low potential regions, resulting in limited capacity. Grafting n-type groups capable of storing cations onto p-type organics, which is known as bipolar, is an effective strategy to improve the total capacity within wide potential ranges (**Fig. 14c1**).[422, 423] For instance, the p-type tetrathiafulvalene (**7** in **Fig. 13**) was fused with n-type benzoquinone group.[422] The fused molecule possesses two redox active sites of thioether and carbonyl reacting with the

$PF_6^-$ and $Li^+$ at high and low potential regions, respectively, delivering a high capacity of 236 mAh $g^{-1}$ at an average potential of 2.8 V verses $Li^+$/Li (**Fig. 14c2**).

**Polymers.** Despite their diverse and controllable structures, most p-type small organic molecules are limited by their higher solubility and lower stability compared to their polymeric counterparts with identical redox active sites.[31, 412] The synthesis of p-type polymers from monomers is a chemical strategy to resolve these problems. The p-type polymers can be classified into conjugated (**8**, **9** in **Fig. 13**) and non-conjugated (**10**, **11**, **12**, **13**, **14**, **15** in **Fig. 13**) polymers, which is discussed below in terms of their structural features and properties. The conjugated polymers, where the long-range backbone possesses overlapped π-orbitals for charge delocalization upon anion insertion, have advantages in terms of high electrical conductivity. The redox-active sites are usually embedded in the polymer backbone (**Fig. 14d1**). The poly(aniline) (PANI, **8** in **Fig. 13**) is regarded as a representative conjugated polymer for anion storage.[424-427] The $PF_6^-$ storage of PANI electrode in $KPF_6$ polymer-gel electrolyte was demonstrated with a discharge capacity of 138 mAh $g^{-1}$ at a sloping voltage profile of 2.0–4.0 V versus $K^+$/K.[424] Moreover, PANI possesses both oxidation and reduction states as a result of the presence of C–N bonds along with long-range conjugated backbone of the polymer.[425] Upon the insertion of cations, PANI could be converted from p-type to bipolar polymer storing both cations and anions. A bipolar PANI mechanism was demonstrated in an aqueous $Zn(OTf)_2$-based electrolyte, and the resulting PANI delivered a specific capacity of 200 mAh $g^{-1}$ and 92% capacity retention after 3000 cycles at 5 A $g^{-1}$.[425]

The poly(3-methyl thiophene) (PMT, **9** in **Fig. 13**) as a anion storing conjugated polymer was studied in non-aqueous electrolytes such as $NEt_4$-$BF_4$/PC, EMIM-TFSI/ACN, and $Pyr_{14}$-TFSI.[37, 428-432] The PMT for $BF_4^-$ and $TFSI^-$ storage delivers a pseudocapacitive behavior within a positive potential range of 0–1 V versus $Ag^+$/Ag. In order to decrease contact resistance and improve electrolyte diffusion, PMT was electrodeposited on the vertically aligned CNTs (VACNT) grown on Al foil, which delivered a capacitance of 170 F $g^{-1}$ and a long cyclic stability over 19000 cycles.[37]

Although conjugated polymers are featured with high electrical conductivity, they have disadvantages such as insufficient active-site utilization and sloping redox potential.[411, 413, 415] In contrast, non-conjugated polymers consisting of non-conjugated backbone can bear abundant redox-active pendant groups for high capacity and distinct potential plateau (**Figs. 14d1 and 14d2**). For instance, 2,2,6,6-tetramethylpiperidinyl-*N*-oxyl (TEMPO, **10** in **Fig. 13**) as a pendant redox-active group can be grafted to non-conjugated backbones such as methacrylate, vinylether, norbornene and glycidyl ether to synthesize TEMPO radical polymers.[433-436] The unpaired electron of neutral TEMPO group can be oxidized to oxoammonium cation upon anion storage. The electron transport of TEMPO is realized by its outer-sphere self-exchange.[437, 438] Moreover, the singly occupied molecular orbital (SOMO) promotes charge transfer for fast redox kinetics. The poly(TEMPO methacrylate) showed a specific capacity of 62 mAh $g^{-1}$ at 10 A $g^{-1}$ in a $(NH_4)_2SO_4$ aqueous solution[98] and the poly(TEMPO vinylether) exhibited the insertion of $SO_4^{2-}$ at higher potential (1.77 V vs $Zn^{2+}$/Zn) and better stability of 77% capacity retention over 1000 cycles than those with $OTf^-$ and $ClO_4^-$ in Zn salt-based aqueous electrolytes.[477]

To further improve the capacity and voltage of non-conjugated polymers, non-radical groups of uncharged state are explored for anion storage of p-type polymers.[413] Redox-active pendant group of thianthrene can be tethered onto polynorbornene backbone (**11** in **Fig. 13**) to increase the redox potential.[172] This thianthrene-based polynorbornene stores $PF_6^-$ at a high potential up to 4.1 V versus $Li^+$/Li. However, the low capacity of 66 mAh $g^{-1}$ was revealed due to the high molecular weight of polynorbornene backbone. Accordingly, low molecular weight backbone can improve the specific capacity of p-type polymers (**Fig. 14e1**). Replacing polynorbornene backbone by polyvinyl backbone, poly(2-vinylthianthrene) was synthesized to deliver a high capacity of 105 mAh $g^{-1}$ at a potential plateau of 3.95 V versus $Li^+$/Li in a $LiClO_4$-based carbonate electrolyte (**Fig. 14e2**).[439]

Subsequently, phenothiazine as redox-active pendant group was incorporated to prepare poly(3-vinyl-*N*-methylphenothiazine) (PVMPT) (**12** in **Fig. 13**).[173] The PVMPT in $LiPF_6$-based carbonate electrolyte exhibited a specific capacity of 56 mAh $g^{-1}$ at 10 C rate along with a cycling stability of 93.5% over 10000 cycles. Upon anion insertion, the strong π-π interaction between the neighbor oxidized pendant groups stabilizes radical cation of phenothiazine and facilitates supramolecular charge transport. Moreover, PVMPT offers a special solubility.[440] During charging upon anion insertion, the oxidized PVMPT is dissolved in the electrolyte. Since the dissolved PVMPT containing radical cations is chemically inert to the $LiPF_6$ salt and Li metal electrode, it can be re-deposited during subsequent discharging along with the outstanding stability. Nonetheless, the strong π-π interaction of pendant groups causes the incomplete utilization of active PVMPT, where its discharged state is arranged alternately by neutral and cationic states rather than complete reduction configuration, resulting in a low capacity of 56 mAh $g^{-1}$.[173] To reach the high capacity, cross-linking chemistry was applied to prohibit the rearrangement of phenothiazine group (**Fig. 14 f1**).[441] The cross-linked PVMPT showed a 1C capacity up to 107 mAh $g^{-1}$ at a voltage plateau of 3.35 V versus $Li^+$/Li and a capacity of 102 mAh $g^{-1}$ retained after 1000 cycles (**Fig. 14 f2**). Even at a high rate of 10 C, cross-linked PVMPT maintained a high capacity of 85 mAh $g^{-1}$ for 1000 cycles. Substituting the S of phenothiazine by O to regulate the π-π interaction, cross-linked phenoxazine-based polymer (PVMPO, **13** in **Fig. 13**) was synthesized, achieving a 100 C capacity of 96 mAh $g^{-1}$ and 74% of capacity retention after 10000 cycles.[442]

There are some non-conjugated polymers without the redox-active pendant groups. For example, pyrenes, a type of PAHs, can be polymerized to be non-conjugated polypyrene (**14** in **Fig. 13**) avoiding dissolution and gaseous by-products.[193, 194, 443, 444] The theoretical capacity of polypyrenes based on one-electron transfer per monomer is 133 mAh $g^{-1}$, comparable to that (e.g., 121 mAh $g^{-1}$ for $C_{20}PF_6$) of graphite cathode. In an analogous

manner to the design of small molecules, the electrochemical performances of polypyrenes can be improved by the chemical modification of introducing functional groups. For example, Kovalenko et al. grafted electron-withdrawing $NO_2$ group to pyrene units, synthesizing the poly(nitropyrene-co-pyrene) for $AlCl_4^-$ insertion.[193] The resulting poly(nitropyrene-co-pyrene) electrode achieved a specific capacity of 100 mAh $g^{-1}$ at an average voltage of 1.7 V versus Al anode, higher than 70 mAh $g^{-1}$ of non-modified polypyrene. However, the conjugation length of PAH-based polymers remains very short due to the orthogonality between monomers, which leads not to achieve high electronic conductivity comparable to the conjugated polymers.[443, 445]

Moreover, non-conjugated poly(triphenylamine) (PTPAn, **15** in **Fig. 13**) in carbonate electrolyte for $PF_6^-$ storage delivered a capacity of 71 mAh $g^{-1}$ at 100 mA $g^{-1}$ with a voltage plateau at approximately 3.5 V versus $K^+/K$.[175] Additionally, PTPAn exhibited the high kinetics performance and stability in $Mg(ClO_4)_2$/ACN solution, as demonstrated by the specific capacity of 73 mAh $g^{-1}$ at 1 A $g^{-1}$ and 88% of capacity retention after 5000 cycles.[176] Upon $ClO_4^-$ insertion, the formation of quinoid-type dimers and radical cations is inferred from the double redox couples of the CV curves. In LiTFSI/ethyl acetate electrolyte, low temperature performance of PTPAn was confirmed demonstrating a specific capacity of 99 mAh $g^{-1}$ at −40°C, comparable to the value at room temperature, and a capacity of 69 mAh $g^{-1}$ even at −70°C.[446]

### 3.3.3 Porous frameworks

**Covalent organic frameworks (COFs).** Because p-type polymers are always nonporous solids, ion diffusion into and utilization efficiency of active sites are lowered due to larger sizes of anions.[91, 413] COFs, a class of porous polymeric materials, have advantages over p-type polymers in terms of their tunable porosity, controllable ion channels, and large surface areas. COFs are also used as anion storing materials (**Table 5**).

The 2D TpBpy-COF was synthesized through a condensation reaction of 2,4,6-triformylphloroglucinol and 5,5'-diamino-2,2'-bipyridine for $AlCl_4^-$ storage (**Fig. 15 a1**).[195] The robust framework resisted the corrosion of the Lewis acidic electrolyte and accommodated a large size of anions. The C-N and C=N groups are active sites, while the carbonyl groups are redox-inert. The hierarchically porous, hexagonal layered structure of TpBpy-COF is beneficial for a large specific surface area of 1794 $m^2$ $g^{-1}$, electrolyte infiltration, and anion diffusion. Additionally, electron delocalization of the π-conjugated skeleton facilitates electron transportation. Accordingly, TpBpy-COF delivered a high discharge capacity of 126 mAh $g^{-1}$ at 2 A $g^{-1}$, showing a gradual increase in capacity up to 150 mAh $g^{-1}$ for 13000 long-term cycles (**Figs. 15a2 and 15a3**).

The covalent triazine-based framework (CTF) was synthesized by dynamic trimerization of *para*-dicyanobenzene for anion storage.[95, 174, 447] In particular, the amorphous CTF (ACTF) with a short-range-ordered 2D honeycomb structure achieves better performance than crystalline alternatives.[95, 174] The aromatic triazine rings of $C_3N_3$ are the redox-active sites that can be transformed into oxidation, neutral, and reduction states and enable continuous bipolar reactions for both anion ($PF_6^-$ or $ClO_4^-$) and cation storage. Consequently, the ACTF electrode exhibited a high operating potential, high rate capability (60 mAh $g^{-1}$ at 20 A $g^{-1}$),[174] and long cycling life (over 7000)[95]. To inhibit dissolution and improve the conductivity of CTF, a covalent bonding composite (G-PPF) was synthesized using polyacrylonitrile-modified graphene as nucleation anchors for the trimerization of *ortho*-, *meta*-, or *para*-dicyanobenzene.[448] G-PPTs showed a high rate capacity of 135 mAh $g^{-1}$ at 15 A $g^{-1}$.

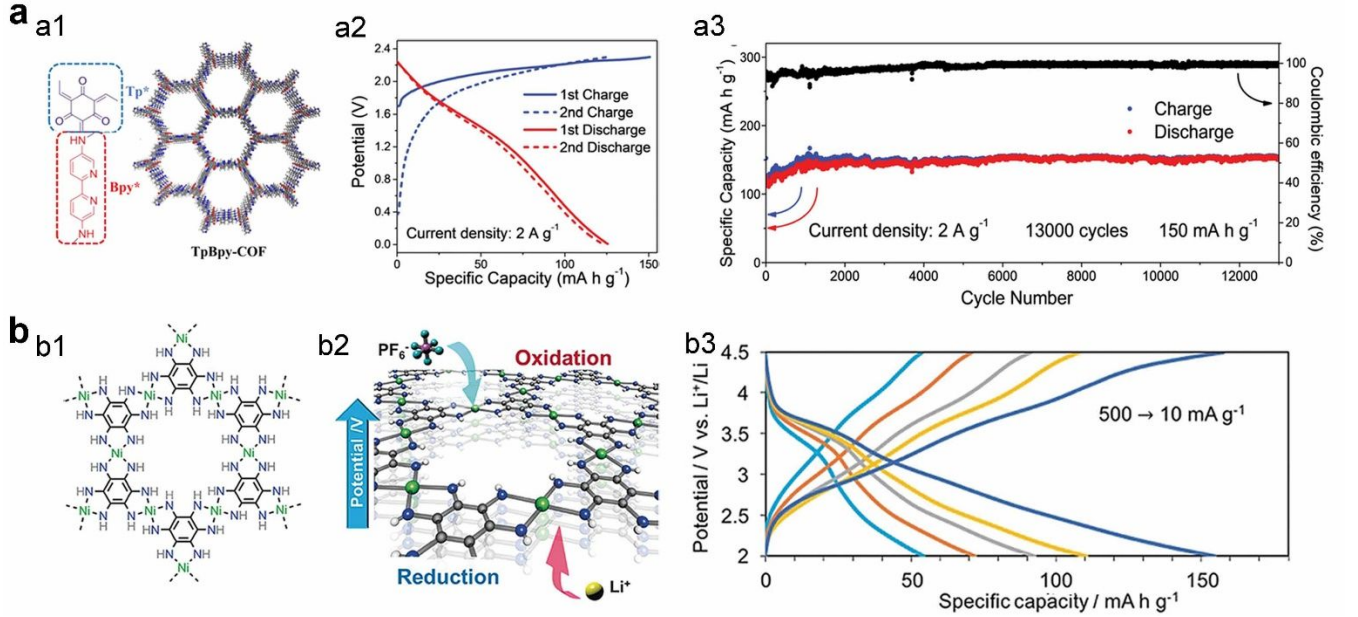


**Fig. 15** COFs and MOFs for anion storage. (**a**) Redox TpBpy-COF. (a1) Chemical structure, (a2) GCD curves, and (a3) cycling stability. Reproduced with permission from ref. [195], Copyright 2020 Wiley-VCH. (**b**) Redox NiDI MOF. (b1) Chemical structure, (b2) schematic illustration of the redox reaction, and (b3) GCD curves. Reproduced with permission from ref. [451], Copyright 2018 Wiley-VCH.

**Metal-organic frameworks (MOFs).** Organic molecules as ligands can coordinate with metals to form metal-organic compounds. Among them, MOFs can store large-sized polyatomic anions as well as $OH^-$ in alkaline aqueous electrolytes owing to their designable chemical and porous structures. A pioneering work is the reversible anion insertion of $Fe_2$(dobpdc) (dobpdc = 4,4′-dioxidobiphenyl-3,3′-dicarboxylate) MOFs.[94] The $Fe_2$(dobpdc) with a large channel of 21 Å can accommodate a variety of polyatomic anions in organic electrolytes such as $BF_4^-$, $PF_6^-$, and $TFSI^-$. A short Fe-Fe distance of 3.04 Å is expected to achieve bulk electronic conductivity. During anion insertion, charge compensation is accomplished by both metal and ligand oxidation; however, only metal oxidation is fully reversible. In a $NaPF_6$-based organic electrolyte, the $Fe_2$(dobpdc) obtained a capacity of 90 mAh $g^{-1}$ within a potential range of 2.0–3.65 V versus $Na^+$/Na.

In a similar manner to p-type organics, the redox reaction of ligands for anion insertion of MOFs can occur at high potentials, which may deteriorate the reversibility and stability.[94] Bipolar redox MOFs combining both anion and cation de-/insertion have been proposed to resolve this problem. For instance, $Mn_7$(2,7-AQDC)$_6$(2,6-AQDC)(DMA)$_6$ (Mn-MOF) with multi-redox centers was designed to achieve a bipolar feature.[449] During charging, the $Li^+$ ions are first deserted on ligand oxidation at a low potential (2.4 V versus $Li^+$/Li), and then $PF_6^-$ ions are inserted into Mn-MOF by the oxidation of $Mn^{2+}$ to $Mn^{3+}$ at a high potential (4.1 V versus $Li^+$/Li). Such a bipolar process allows Mn-MOF to deliver a high capacity of 200 mAh $g^{-1}$.

Low electronic conductivity of MOFs is a technical limitation lowering the stability and kinetic performances.[450] In this regard, metallically conductive MOFs, bis(diimino)nickel 2D frameworks (NiDI), were developed (**Fig. 15b1**).[451] The metallic conductivity of NiDI is attributed to the large density of states around the Fermi level from both Ni atoms and ligands. Moreover, the NiDI in $LiPF_6$-based organic electrolyte exhibited a bipolar multi-redox feature, showing a capacity of 155 mAh $g^{-1}$ at 10 mA $g^{-1}$ within a potential range of 2–4.5 V versus $Li^+$/Li (**Figs. 15b2 and 15b3**). The ion storage of NiDI is based on the topotactic insertion into the in-plane pore structure rather than conversion reactions,[451, 452] where the latter can induce the dissolution of active materials in the electrolyte.[196]

Another challenge of MOFs is dissolution in polar solvents.[196, 453] Cu-7,7,8,8-tetracyanoquinodimethane (CuTCNQ) was designed for multiple electron reactions, where the reversible transformations of $Cu^{2+}$/$Cu^+$ (4.1–3.7 V) and $TCNQ^0$/$TCNQ^{-1}$ (3.7–3.0 V) are associated with $ClO_4^-$ de-/insertion and that of $TCNQ^{-1}$/$TCNQ^{-2}$ (3.0–2.0 V) with $Na^+$ de-/insertion.[196] The total high capacity of 255 mAh $g^{-1}$ was obtained. Nonetheless, $TCNQ^{x-}$ intermediates are dissolved in carbonate electrolyte (1 M $NaClO_4$ in EC/PC) within the potential ranges of activating ligand. In order to resolve this, the CuTCNQ was encapsulated by a thin carbon film acting as an interlayer to suppress the dissolution of materials. The CuTCNQ/carbon film achieved a cycling stability of 50 cycles with a negligible capacity fading. Besides, the $Cu^{2+}$/$Cu^+$ redox couple in CuTCNQ is active even at higher redox potential than that of $Cu^{3+}$/$Cu^{2+}$ redox couple in layered metal oxide,[454] suggesting that the redox potential of Cu metal could be effectively regulated via an induction effect of ligands.

Non-framework metal organic compounds have been developed for anion storage. The dissolution of ferrocene was mitigated by carbon encapsulation, using highly-concentrated 30 m $ZnCl_2$ aqueous electrolyte.[114] The carbon encapsulated ferrocene delivered a specific capacity of 106 mAh $g^{-1}$ through $ZnCl_4^{2-}$ insertion of $Fe^{3+}$/$Fe^{2+}$ redox couple. Interestingly, this ferrocene could be used as a negative electrode material due to its low potential of anion insertion (0.05 V versus Ag/AgCl). Metal organic compounds solely with the redox activity of ligand have been also developed.[455, 456] For example, Cu tetraaminephthalocyanine (CuTAPc) showed a specific capacity of 109 mAh $g^{-1}$ at a high current density of 20 A $g^{-1}$ owing to the redox activity of π-electron configuration of CuTAPc monomer (2 π-electron oxidation per CuTAPc monomer for anion insertion).[456]

### 3.3.4 Others

**Metal/Metal oxides storing polyatomic anions.** The Pb and $PbO_2$ have been used as the negative and positive electrodes of the typical lead-acid batteries, respectively.[87, 89] Their electrochemical reactions coupled with $SO_4^{2-}$ anions in $H_2SO_4$ electrolyte can be described as follows.

$$Pb + SO_4^{2-} \leftrightarrow PbSO_4 + 2e^- \quad (21)$$

$$PbO_2 + SO_4^{2-} + 4H^+ + 2e^- \leftrightarrow PbSO_4 + 2H_2O \quad (22)$$

The lead-acid batteries using the Pb and $PbO_2$ electrodes have advantages in terms of their stable voltage profile, low cost and safety, but suffer from low energy density and limited cycle life.[89, 457] The main failure is attributed to the crumbling and sulfation of electrode materials, grid corrosion, and hydrogen evolution.[89, 457-461] The crumbling is caused by the volume change of electrodes during conversion reactions. On the other hand, the sulfation is associated with the accumulation of large-sized non-conducting $PbSO_4$ on the positive and negative electrodes upon discharging, which cannot take part in the reversible reactions upon charging. The sulfation issue becomes more serious on the Pb negative electrode due to its slower reaction kinetics than the $PbO_2$ positive electrode. Several methods have been developed to improve the electrochemical performance of Pb and $PbO_2$ electrodes, of which the most effective one is to synthesize the composite with carbonaceous materials.[89, 457-460] The carbonaceous materials serve as multiple functions that can control the size of $PbSO_4$, alleviate volume expansion, reduce hydrogen revolution, and enhance electrical conductivity.

In addition to Pb and $PbO_2$, other examples on large-sized polyatomic anion storage of metal/metal oxides were less reported. The reversible $NO_3^-$ insertion inside $Mn_3O_4$ was accomplished in an $NH_4NO_3$ aqueous electrolyte.[97] The inserted $NO_3^-$ ions are proposed to reside on the defects or amorphous regions of $Mn_3O_4$, leading to the de-crystallization of $Mn_3O_4$ structure. The $Mn_3O_4$ electrode achieved a capacity up to 183 mAh $g^{-1}$ at 0.1 A $g^{-1}$ and a capacity retention up to 50 mAh $g^{-1}$ at 1 A $g^{-1}$ over 3500 cycles.

Anion storing pseudocapacitance of $Mn_3O_4$ was revealed in a $LiPF_6$-based organic electrolyte.[462] When the potential window

 

of $Mn_3O_4$ electrode against a Li metal was measured in a range of 1.5 to 4.8 V, the charge storage is coupled with both $Li^+$ intercalation and $PF_6^-$ adsorption as verified by two pairs of redox peaks in CV curves (**Figs. 16a1 and 16a2**). Kinetic analysis based on power-law relationship indicates that the pair of redox peaks below 2.75 V versus $Li^+/Li$ (labelled A and C) is converged to combined surface- and diffusion-controlled processes, whereas those at higher potentials (labelled B and D) are dominated by a surface-controlled behavior. The charge transfer between $PF_6^-$ and $Mn_3O_4$ occurs via the Mn–F bond, and fluoride ion is the redox center. The exploited $PF_6^-$-based pseudocapacitance boost the total capacity of $Mn_3O_4$ up to 250 mAh $g^{-1}$ at 60 mA $g^{-1}$ (**Fig. 16a3**).

In addition, co-(de)intercalation of $Na^+$ and $ClO_4^-$ into layered $Na_{0.5}Ni_{0.25}Mn_{0.75}O_2$ was demonstrated in $NaClO_4$/PC electrolyte.[463] Upon charging, $Na^+$ ions are first released during charging, which is accompanied with the oxidation of transition metals. Then, $ClO_4^-$ ions are intercalated into the interlayer at high potential plateau, which further leads to the anionic oxidation ($O^{2-}$ to $O^-$) to provide extra capacity. The capacity of $Na_{0.5}Ni_{0.25}Mn_{0.75}O_2$ electrode in an organic $NaClO_4$/PC electrolyte was 180 mAh $g^{-1}$ at 0.02 A $g^{-1}$, higher than the theoretical capacity of 134 mAh $g^{-1}$ assuming solely $Na^+$ storage.

**Metals halides/oxyhalides storing $F^-$ and $Cl^-$ ions.** Although halide anions are not included in polyatomic anions, this subsection focuses on the $F^-$ and $Cl^-$ storage of metal halides/oxyhalides for halide ion batteries based on the shuttling of halide ions. In halide ion batteries, metal halides, such as $BiCl_3$, $BiF_3$, $VCl_3$, $CuF_2$, and $LaF_3$, and metals, such as Li, Mg, La, and Ce, have been used as positive and negative electrodes, respectively.[79, 464-466] Because most of these materials react easily or dissolve in water, they are generally studied in solid-state and non-aqueous electrolytes. Nonetheless, one limitation of metals and metal halides is related to their dissolution in non-aqueous electrolytes and large volume changes during ion storage, both of which deteriorate the cycling performance. Metal oxychlorides, FeOCl, BiOCl, and VOCl can be used as positive electrodes for chloride ion batteries.[81, 197] Metal oxychlorides generally exhibit higher stability than metal chlorides because the metals are strongly bound to the Lewis basic oxygen ions. Among various oxychlorides, FeOCl storing $Cl^-$ ions delivers the discharge capacity of 158 mAh $g^{-1}$.[197] When incorporated into graphene, the capacity of FeOCl/graphene composite increased to 184 mAh $g^{-1}$.[467] However, the low electrical conductivity and contact loss with the conductive substrate caused by volume change resulted in a deterioration of cycling stability in FeOCl. To circumvent this issue, a nanoconfined structure design of FeOCl/porous carbon nanocomposite (FeOCl/CMK) was proposed.[80] Moreover, organic molecules and electrolyte components were intercalated into the FeOCl layers before cycling, facilitating the conversion reaction from FeOCl to FeO upon $Cl^-$ insertion (**Fig. 16b1**). The FeOCl/CMK electrode showed the maximum capacity of 202 mAh $g^{-1}$ within a potential window of 1.6 to 3.5 V, preserving 80.2% of initial capacity after 30 cycles (**Figs. 16b2 and 16b3**). Additionally, a chloride ion battery was configured using VOCl as a positive electrode material. The VOCl electrode delivered an initial capacity of 189 mAh $g^{-1}$ at 0.5 C and a relatively long cycling stability with 113 mAh $g^{-1}$ retained at 2 C over 100 cycles.[81]

There are metals and metal oxyhalides storing $F^-$ and $Cl^-$ ions in aqueous electrolytes. The first aqueous chloride ion battery was configured using the BiOCl as negative electrode, Ag as positive electrode, and NaCl aqueous electrolyte.[198] The $Cl^-$ ions are released from BiOCl electrode and intercalated into Ag electrode during charging, and vice versa. The capacity of the battery was 92.1 mAh $g^{-1}$ at 0.5 A $g^{-1}$. Subsequently, stibium oxyhalide ($Sb_4O_5Cl_2$) was used as negative electrode for a chloride ion battery.[468] $BiF_2$ was developed to release and capture $F^-$ ions in NaF aqueous electrolyte for a negative electrode of dual-ion battery with a positive electrode of sodium manganese oxides.[96] $Zn_{0.2}Mn_3O_4$ demonstrated a reversible $Cl^-$ storage , showing a capacity of 200 mAh $g^{-1}$ at an average voltage of 1.6 V versus $Zn^{2+}/Zn$.[469] Moreover, Bi was explored to store $Cl^-$ via the formation of BiOCl in NaCl aqueous electrolyte for applications into desalination cells.[84] The details of materials regarding $F^-$ and $Cl^-$ storage in desalination and salinity cells will be discussed in Section 4.2.2.

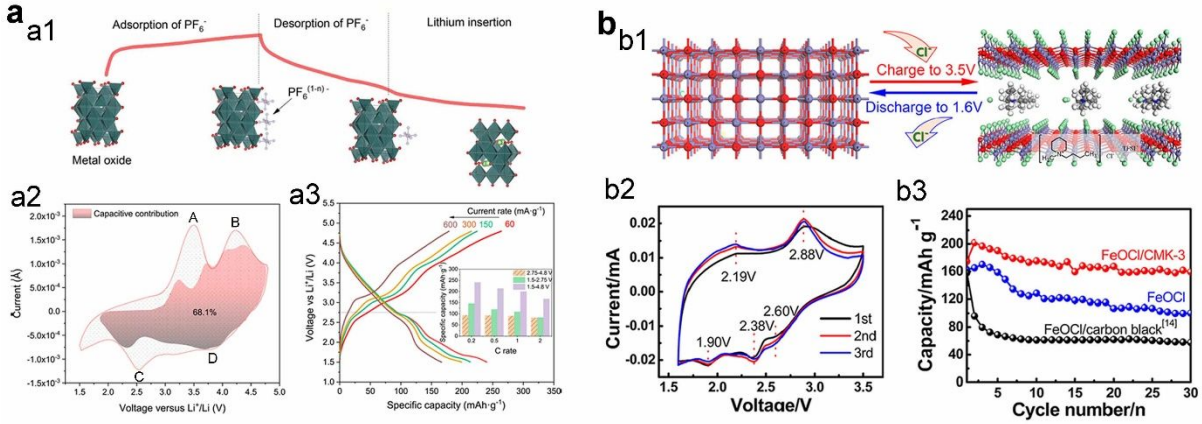


**Fig. 16** (**a**) $Mn_3O_4$ storing both $Li^+$ and $PF_6^-$ ions. (a1) Schematic illustration the reaction mechanism of $Mn_3O_4$ involving the $PF_6^-$ adsorption and $Li^+$ intercalation, (a2) CV curve of $Mn_3O_4$ electrode at 2 mV $s^{-1}$ showing the capacitive contribution, and (c3) rate performance of $Mn_3O_4$ electrode. Reproduced with permission from ref. [462], Copyright 2020 Elsevier. (**b**) FeOCl storing $Cl^-$ ions. (b1) Schematic illustration of the conversion from FeOCl to FeO upon $Cl^-$ ions transfer, (b2) CV curves, and (b3) cycling stability of FeOCl electrode. Reproduced with permission from ref. [80], Copyright 2017 American Chemical Society.

**Table 5** Summary of the graphite, organics, COFs and MOFs for anion storage

| Negative//Positive Electrodes [Ref] | Electrolyte | Voltage range | Capacity | | Cycling Stability |
|---|---|---|---|---|---|
| Li//Graphite [56] | 2 M $LiPF_6$/EMC | 3.0–5.3 V | 99.4 mAh $g^{-1}$ @ 200 mA $g^{-1}$ | 78 mAh $g^{-1}$ @ 10000 mA $g^{-1}$ | 81%, 10000 cycles @1000 mA $g^{-1}$ (3–5 V) |
| Li//SEI-modified graphite [149] | 1 M $LiPF_6$/EMC | 3.0–5.0 V | ~85 mAh $g^{-1}$ @ 200 mA $g^{-1}$ | - | 96%, 500 cycles @ 200 mA $g^{-1}$ |
| Li//LTO-modified MCMB [150] | 1 M $LiPF_6$/EMC-Sulfolane | 3.0–5.4 V | 96.7 mAh $g^{-1}$ @ 100 mA $g^{-1}$ | ~95 mAh $g^{-1}$ @ 1000 mA $g^{-1}$ | 85.1%, 2000 cycles @500 mA $g^{-1}$ |
| Al//Graphite [56] | 2 M $LiPF_6$/EMC+3 wt% VC | 3.0–5.0 V | ~99 mAh $g^{-1}$ @ 100 mA $g^{-1}$ | ~78 mAh $g^{-1}$ @ 2000 mA $g^{-1}$ | ~100%, 500 cycles @1000 mA $g^{-1}$ |
| Al//Graphite [148] | 4 M $LiPF_6$/EMC+2 wt% VC | 3.0–4.95 V | 110 mAh $g^{-1}$ @ 100 mA $g^{-1}$ | 88.8 mAh $g^{-1}$ @ 1000 mA $g^{-1}$ | 92.4%, 1000 cycles @ 200 mA $g^{-1}$ |
| Al//Graphite [112] | 7.5 m LiFSI/EC-DMC | 3.0–5.0 V | 94 mAh $g^{-1}$ @ 200 mA $g^{-1}$ | 68.1 mAh $g^{-1}$ @ 500 mA $g^{-1}$ | 96.8%, 500 cycles @ 200 mA $g^{-1}$ |
| Al//Graphite [470] | $LiPF_6$ gel polymer electrolyte | 3.0–4.95 V | 103 mAh $g^{-1}$ @ 200 mA $g^{-1}$ | 82 mAh $g^{-1}$ @ 1000 mA $g^{-1}$ | 92%, 2000 cycles @ 500 mA $g^{-1}$ |
| Al//Natural graphite [105] | 4 M $LiPF_6$/EMC+4% VC | 2.0–4.95 V | 120.6 mAh $g^{-1}$ @100 mA $g^{-1}$ | 116.1 mAh $g^{-1}$ @ 12000 mA $g^{-1}$ | 61%, 1500 cycles @ 6000 mA $g^{-1}$ |
| Al//Natural graphite [471] | 3.8 M $LiPF_6$+0.2 M $LiBF_4$/EMC+2 wt% VC | 3.0–4.8 V | 97.8 mAh $g^{-1}$ @ 200 mA $g^{-1}$ | 90.5 mAh $g^{-1}$ @ 1500 mA $g^{-1}$ | ~100%, 500 cycles @ 500 mA $g^{-1}$ |
| Al//MCMB [157] | 2 M LiTFSI/$Pyr_{14}$TFSI+10 wt% FEC | 3.0–4.8 V | 100 mAh $g^{-1}$ @ 50 mA $g^{-1}$ | 85 mAh $g^{-1}$ @ 500 mA $g^{-1}$ | 98%, 300 cycles @ 50 mA $g^{-1}$ |
| Al// Electrochemically exfoliated Graphene [403] | 2M $LiPF_6$/EMC | 2.0–5.0 V | ~153 mAh $g^{-1}$ @ 100 mA $g^{-1}$ | ~153 mAh $g^{-1}$ @ 3000 mA $g^{-1}$ | ~87%, 500 cycles @ 200 mA $g^{-1}$ |
| Graphite//Graphite [472] | 2 M $LiPF_6$/MP+10 % FEC | 2.5–5.1 V | ~82 mAh $g^{-1}$ @ 80 mA $g^{-1}$ (23°C)<br>~73 mAh $g^{-1}$ @ 8 mA $g^{-1}$ (−60°C) | ~75 mAh $g^{-1}$ @ 800 mA $g^{-1}$ (23°C)<br>~50 mAh $g^{-1}$ @ 800 mA $g^{-1}$ (−60°C) | ~91%, 30 cycles @ 80 mA $g^{-1}$ (23°C) |
| Graphite//Graphite [57] | 1 M LiTFSI/$Pyr_{14}$TFSI+2 wt% ES | 3.0–5.2 V | 121 mAh $g^{-1}$ @ 10 mA $g^{-1}$ | 113 mAh $g^{-1}$ @ 50 mA $g^{-1}$ | ~94%, 500 cycles @ 500 mA $g^{-1}$ (3–5.1 V) |
| Pre-lithiated graphite//Graphite [144] | 2 M $LiPF_6$/EMC-Sulfolane | 3.0–5.3 V | 96.7 mAh $g^{-1}$ @ 100 mA $g^{-1}$ | 91.0 mAh $g^{-1}$ @ 2000 mA $g^{-1}$ | 94.7%, 1000 cycles @ 500 mA $g^{-1}$ |
| Pre-lithiated MCMB//Graphite [473] | 3 M $LiPF_6$/EMC-TMP | 3.0–5.2 V | ~124 mAh $g^{-1}$ @ 50 mA $g^{-1}$ | ~99mAh $g^{-1}$ @ 400 mA $g^{-1}$ | ~52%, 100 cycles @ 50 mA $g^{-1}$ |
| Na//Graphite [474] | $NaPF_6$ quasi-solid-state electrolyte | 3.0–5.0 V | 115.1 mAh $g^{-1}$ @ 10 mA $g^{-1}$ | 84.3 mAh $g^{-1}$ @ 500 mA $g^{-1}$ | 86.7%, 1000 cycles @ 100 mA $g^{-1}$ |
| Sn//Graphite [475] | $NaPF_6$ quasi-solid-state electrolyte | 3.0–5.0 V | 96.8 mAh $g^{-1}$ @ 500 mA $g^{-1}$ | 91.6 mAh $g^{-1}$ @ 1200 mA $g^{-1}$ | 97.5%, 600 cycles @ 500 mA $g^{-1}$ |
| Sn//Microcrystalline carbon [409] | 1 M $NaPF_6$/EC-EMC-DMC | 1.0–4.5 V | 191.4 mAh $g^{-1}$ @ 100 mA $g^{-1}$ | 77.8 mAh $g^{-1}$ @ 10000 mA $g^{-1}$ | 70%, 2000 cycles @ 1000 mA $g^{-1}$ |
| K//Graphite [152] | 5 M KFSI/EC-DMC | 3.2–5.25 V | 98 mAh $g^{-1}$ @ 50 mA $g^{-1}$ | 47 mAh $g^{-1}$ @ 500 mA $g^{-1}$ | ~92%, 300 cycles @ 100 mA $g^{-1}$ |
| Graphite//Graphite [159] | 0.3 M KTFSI/$Pyr_{14}$TFSI+2 wt% ES | 3.4–5.0 V (cathode, vs. $K/K^+$) | 47 mAh $g^{-1}$ @ 50 mA $g^{-1}$ | 42 mAh $g^{-1}$ @ 250 mA $g^{-1}$ | 95%, 1500 cycles @ 250 mA $g^{-1}$ |
| Graphite//Graphite [153] | 5.2 m KFSI/TMS | 3.0–5.4 V | 83.4 mAh $g^{-1}$ @ 100 mA $g^{-1}$ | 34.8 mAh $g^{-1}$ @ 400 mA $g^{-1}$ | ~100%, 300 cycles @100 mA $g^{-1}$ |
| Zn//Graphite [395] | 1.2 M $Zn(TFSI)_2$/ACN | 1.2–2.65 V | 52 mAh $g^{-1}$ @ 208 mA $g^{-1}$ | 40.8 mAh $g^{-1}$ @ 10400 mA $g^{-1}$ | 98%, 1000 cycles @ 5200 mA $g^{-1}$ |
| Zn//Graphite [476] | 0.5 M $Zn(TFSI)_2$+2 M $LiPF_6$/EMC | 0.7–2.7 V | 105 mAh $g^{-1}$ @ 100 mA $g^{-1}$ | 97 mAh $g^{-1}$ @ 2000 mA $g^{-1}$ | 97.5%, 2000 cycles @ 1000 mA $g^{-1}$ |
| Al//Graphite [56] | EMIMCl-$AlCl_3$ | 0.5–2.45 V | 92.0 mAh $g^{-1}$ @ 100 mA $g^{-1}$ | 79.4 mAh $g^{-1}$ @ 2000 mA $g^{-1}$ | ~100%, 150 cycles @1000 mA $g^{-1}$ |
| Al//Graphite [160] | EMIMCl-$AlCl_3$ | 1.0–2.4V (4°C)<br>1.0–2.55V (−20°C) | 80 mAh $g^{-1}$ @ 300 mA $g^{-1}$ (4°C)<br>80 mAh $g^{-1}$ @ 100 mA $g^{-1}$ (−20°C) | 75 mAh $g^{-1}$ @ 500 mA $g^{-1}$ (4°C)<br>65 mAh $g^{-1}$ @ 700 mA $g^{-1}$ (−20°C) | ~91%, 20000 cycles @ 500 mA $g^{-1}$ (4°C) |

| | | | | | |
|---|---|---|---|---|---|
| | | | | | ~100%, 1200 cycles @ 100 mA $g^{-1}$ (−20°C) |
| Al//Natural graphite [399] | EMIMCl-$AlCl_3$ | 0.5–2.45 V | 110 mAh $g^{-1}$ @ 66 mA $g^{-1}$ | ~45 mAh $g^{-1}$ @ 792 mA $g^{-1}$ | ~100%, 6000 cycles @ 660 mA $g^{-1}$ |
| Al//Natural graphite [400] | EMIMCl-$AlCl_3$ | 0.5–2.45 V | 115 mAh $g^{-1}$ @ 60 mA $g^{-1}$ | 23 mAh $g^{-1}$ @ 3840 mA $g^{-1}$ | 90%, 140 cycles @ 60 mA$g^{-1}$ |
| Al//Graphitic foam [104] | EMIMCl-$AlCl_3$ | 0.5–2.45 V | ~72 mAh $g^{-1}$ @ 1000 mA $g^{-1}$ | ~57 mAh $g^{-1}$ @ 6000 mA $g^{-1}$ | ~100%, 7500 cycles @ 4000 mA $g^{-1}$ |
| Al//3D graphitic foam [405] | EMIMCl-$AlCl_3$ | 0.4–2.45 V | 60 mAh $g^{-1}$ @ 2000 mA $g^{-1}$ | 60 mAh $g^{-1}$ @ 12000 mA $g^{-1}$ | ~100%, 4000 cycles @ 12000 mA $g^{-1}$ |
| Al//Flexuous graphite [406] | EMIMCl-$AlCl_3$ | 0.5–2.45 V | 149 mAh $g^{-1}$ @ 1500 mA $g^{-1}$ | 93 mAh $g^{-1}$ @ 7500 mA $g^{-1}$ | ~100%, 8000 cycles @ 3000 mA $g^{-1}$ |
| Al//Nanosheet-bricked graphite [408] | EMIMCl-$AlCl_3$ | 0.1–2.46 V | ~103 mAh $g^{-1}$ @ 150 mA $g^{-1}$ | ~103 mAh $g^{-1}$ @ 2000 mA $g^{-1}$ | ~100%, 3000 cycles @10000 mA $g^{-1}$ (0.1–2.5 V) |
| Al//Large-sized few-layer graphene [401] | PMIMCl-$AlCl_3$ | 0.1–2.45V | 85 mAh $g^{-1}$ @ 60 mA $g^{-1}$ | ~77 mAh $g^{-1}$ @ 6000 mA $g^{-1}$ | ~100%, 10000 cycles @ 4800 mA $g^{-1}$ |
| Al//Few-layer graphene nanosheets [404] | EMIMCl-$AlCl_3$ | 0–2.51 V | 173 mAh $g^{-1}$ @ 1000 mA $g^{-1}$ | 101 mAh $g^{-1}$ @ 10000 mA $g^{-1}$ | 96%, 10000 cycles @10000 mA $g^{-1}$ |
| Al//Electrochemically exfoliated graphene [403] | EMIMCl-$AlCl_3$ | 0.1–2.45 V | ~132 mAh $g^{-1}$ @ 200 mA $g^{-1}$ | ~119 mAh $g^{-1}$ @ 2000 mA $g^{-1}$ | ~100%, 3500 cycles @ 1000 mA $g^{-1}$ |
| Li//Coronene [90] | 1 M $LiPF_6$/EC-DEC | 2.5–4.2 V | 40 mAh $g^{-1}$ @ 20 mA $g^{-1}$ | 21 mAh $g^{-1}$ @ 500 mA $g^{-1}$ | 92%, 960 cycles @ 20 mA $g^{-1}$ |
| Li//Lithium 4-(10*H*-phenothiazin-10-yl) benzoate [192] | 1.0 M $LiClO_4$/PC | 2.8–4.2 V | 86 mAh $g^{-1}$ @ 16.5 mA $g^{-1}$ | 26 mAh $g^{-1}$ @ 82.5 mA $g^{-1}$ | 72%, 500 cycles @ 16.5 mA $g^{-1}$ |
| Li//10-ethyl-10*H*-phenoxazine [116] | 5.0 M $LiClO_4$/EC-DMC | 2.6–4.5 V | 218 mAh $g^{-1}$ @ 50 mA $g^{-1}$ | - | 86%, 100 cycles @ 50 mA $g^{-1}$ |
| Li//5,12-diaminorubicene [420] | 1 M $LiPF_6$/EC-DMC | 2.0–4.0 V | 115 mAh $g^{-1}$ @ 15 mA $g^{-1}$ | - | 65%, 10 cycles @ 15 mA $g^{-1}$ |
| Li//Q-TTF-Q [422] (bipolar) | 2.5 M LiTFSI/PC | 1.3–4.3 V | 236 mAh $g^{-1}$ @ 20 mA $g^{-1}$ | 33 mAh $g^{-1}$ @ 480 mA $g^{-1}$ | 25%, 10 cycles @ 20 mA $g^{-1}$ |
| Na//Coronene [419] | 1 M $NaPF_6$/EC-DEC | 2.5–4.0 V | 43 mAh $g^{-1}$ @ 10 mA $g^{-1}$ | 15 mAh $g^{-1}$ @ 200 mA $g^{-1}$ | 85%, 1000 cycles @ 100 mA $g^{-1}$ |
| Na//Oligopyrene [443] | 1 M $NaClO_4$/PC | 2.0–4.5 V | 120 mAh $g^{-1}$ @ 20 mA $g^{-1}$ | 10 mAh $g^{-1}$ @ 500 mA $g^{-1}$ | ~68%, 50 cycles @ 20 mA $g^{-1}$ |
| Li//Polypyrene sulfide [444] | 1.0 M $LiClO_4$/PC | 2.0–4.3 V | 148 mAh $g^{-1}$ @ 30 mA $g^{-1}$ | 90 mAh $g^{-1}$ @ 1000 mA $g^{-1}$ | ~94%, 1000 cycles @ 1000 mA $g^{-1}$ |
| Zn//Polypyrene [194] | 30 M $ZnCl_2$ aqueous | 0.6–1.8 V | 180 mAh $g^{-1}$ @ 50 mA $g^{-1}$ | 105 mAh $g^{-1}$ @ 3000 mA $g^{-1}$ | 96.4%, 38000 cycles @ 3000 mA $g^{-1}$ |
| Al//Polypyrene [193] | EMIMCl-$AlCl_3$ | 1.05–2.2 V | 70 mAh $g^{-1}$ @ 200 mA $g^{-1}$ | - | ~81%, 300 cycles @ 200 mA $g^{-1}$ |
| Al//Poly(nitropyrene-co-pyrene) [193] | EMIMCl-$AlCl_3$ | 1.05–2.2 V | 100 mAh $g^{-1}$ @ 200 mA $g^{-1}$ | 48 mAh $g^{-1}$ @ 2000 mA $g^{-1}$ | ~80%, 1000 cycles @ 200 mA $g^{-1}$ |
| K//Polyaniline [424] | $KPF_6$ gel polymer electrolyte | 2.0–4.0 V | 138 mAh $g^{-1}$ @ 10 mA $g^{-1}$ | 95 mAh $g^{-1}$ @ 200 mA $g^{-1}$ | 98%, 100 cycles @ 50 mA $g^{-1}$ |
| Zn//Polyaniline [425] (bipolar) | 1 M $Zn(OTf)_2$ aqueous | 0.5–1.5 V | 200 mAh $g^{-1}$ @ 0.05 A $g^{-1}$ | 95 mAh $g^{-1}$ @ 5 A $g^{-1}$ | 92%, 3000 cycles @ 5 A $g^{-1}$ |
| Zn//Poly(TEMPO vinyl ether) [477] | 1 M $Zn(OTf)_2$ aqueous | 1.3–1.95 V | ~84 mAh $g^{-1}$ @ 0.2 A $g^{-1}$ | 52 mAh $g^{-1}$ @ 10 A $g^{-1}$ | 77%, 1000 cycles @ 1 A $g^{-1}$ |
| SCE//Poly(TEMPO methacrylate) [98] | 1 M $(NH_4)_2SO_4$ aqueous | 0.1–1.0 V | 80 mAh $g^{-1}$ @ 0.5 A $g^{-1}$ | 62 mAh $g^{-1}$ @ 10 A $g^{-1}$ | - |
| Li//Thianthrene-substituted polynorbornenes [172] | 1 M $LiPF_6$/EC-DMC | 3.3–4.4 V | 66 mAh $g^{-1}$ @ 73 mA $g^{-1}$ | ~39 mAh $g^{-1}$ @ 365 mA $g^{-1}$ | 31%, 100 cycles @ 73 mA $g^{-}$ |
| Li//Poly(vinylthianthrene) [439] | 1 M $LiClO_4$/EC-DMC | 3.2–4.2 V | 105 mAh $g^{-1}$ @ 110 mA $g^{-1}$ | 94 mAh $g^{-1}$ @ 550 mA $g^{-1}$ | 90%, 250 cycles @ 550 mA $g^{-1}$ |
| Li//Poly(vinylphenothiazine) [173] | 1 M $LiPF_6$/EC-DMC | 3.0–4.0 V | 56 mAh $g^{-1}$ @ 0.112 A $g^{-1}$ | 26 mAh $g^{-1}$ @ 11.2 A $g^{-1}$ | 93.5%, 10000 cycles @ 1.12 A $g^{-1}$ |
| Li//Poly(vinylphenothiazine) [441] | 1 M $LiPF_6$/EC-DMC | 3.1–3.9 V | 107 mAh $g^{-1}$ @ 0.112 A $g^{-1}$ | 85 mAh $g^{-1}$ @ 1.12 A $g^{-1}$ | ~100%, 1000 cycles @ 1.12 A $g^{-1}$ |

| | | | | | |
|---|---|---|---|---|---|
| Li//Poly(vinylphenoxazine) [442] | 1 M $LiPF_6$/EC-DMC | 3.0–4.0 V | 118 mAh $g^{-1}$ @ 0.06 A $g^{-1}$ | 96 mAh $g^{-1}$ @ 12 A $g^{-1}$ | 74%, 10000 cycles @ 12 A $g^{-1}$ |
| PNTCDA//PTPAn [446] | 2 M LiTFSI/ethyl acetate | 0.05–2.1 V | 91 mAh $g^{-1}$ @0.1 A $g^{-1}$ (25°C)<br>69 mAh $g^{-1}$ @ 0.05 A $g^{-1}$ (−70°C) | 70 mAh $g^{-1}$ @ 10 A $g^{-1}$ (25°C)<br>18 mAh $g^{-1}$ @ 0.5 A $g^{-1}$ (−70°C) | 83%, 500 cycles @ 0.5 A $g^{-1}$ (25°C) |
| Graphite//PTPAn [175] | 0.8 M $KPF_6$/EC-DEC | 1.0–4.0 V | 60 mAh $g^{-1}$ @ 50 mA $g^{-1}$ | 28 mAh $g^{-1}$ @ 300 mA $g^{-1}$ | 75.5%, 500 cycles @ 100 m A $g^{-1}$ |
| PDI-EDA//PTPAn [176] | 1 M $Mg(ClO_4)_2$/ACN | 0.01–1.6 V | 113 mAh $g^{-1}$ @ 0.05 A $g^{-1}$ | 91 mAh $g^{-1}$ @ 1 A $g^{-1}$ | 88%, 5000 cycles @ 1 A $g^{-1}$ |
| Al//TpBpy-COF [195] | EMIMCl-$AlCl_3$ | 0.01–2.3 V | 307 mAh $g^{-1}$ @ 0.1 A $g^{-1}$ | 113 mAh $g^{-1}$ @ 5 A $g^{-1}$ | ~100%, 13000 cycles @ 2 A $g^{-1}$ |
| Li//Amorphous CTF [174] (bipolar) | 1 M $LiPF_6$/EC-DEC | 1.5–4.5 V | 160 mAh $g^{-1}$ @ 0.05 A $g^{-1}$ | 60 mAh $g^{-1}$ @ 20 A $g^{-1}$ | 84%, 1000 cycles @ 5 A $g^{-1}$ |
| Na//Amorphous CTF [95] (bipolar) | 1 M $NaClO_4$/PC | 1.3–4.1 V | 200 mAh $g^{-1}$ @ 0.01 A $g^{-1}$ | ~43 mAh $g^{-1}$ @ 5 A $g^{-1}$ | 80%, 7000 cycles @ 1 A $g^{-1}$ |
| Li//CuTAPc [456] | 1 M $LiPF_6$/EC-DMC-EMC | 1.5–4.5 V | 236 mAh $g^{-1}$ @ 50 mA $g^{-1}$ | 109 mAh $g^{-1}$ @ 20 A $g^{-1}$ | 50%, 4000 cycles @ 4 A $g^{-1}$ |
| Na//$Fe_2$(dobpdc) [94] | 0.6 M $NaPF_6$/EC-DMC | 2.0–3.65 V | ~108 mAh $g^{-1}$ @ 7 mA $g^{-1}$ | ~77 mAh $g^{-1}$ @ 280 mA $g^{-1}$ | ~92%, 50 cycles @ 140 mA $g^{-1}$ |
| Li//$Mn_7$(2,7-AQDC)$_6$(2,6-AQDC)$(DMA)_6$ [449] (bipolar) | 1 M $LiPF_6$/EC-DEC | 1.3–4.5 V | 205 mAh $g^{-1}$ @ 1 mA | 105 mAh $g^{-1}$ @ 5 mA | 93%, 50 cycles @ 1 mA |
| Li//Bis(diimino)nickel framework [451] (bipolar) | 1 M $LiPF_6$/EC-DEC | 2.0–4.5 V | 155 mAh $g^{-1}$ @ 10 mA $g^{-1}$ | ~54 mAh $g^{-1}$ @ 500 mA $g^{-1}$ | ~65%, 300 cycles @ 250 mA $g^{-1}$ |
| Na//CuTCNQ [196] (bipolar) | 1 M $NaClO_4$/EC-PC | 2.0–4.1 V | 255 mAh $g^{-1}$ @ 20 mA $g^{-1}$ | 214 mAh $g^{-1}$ @ 50 mA $g^{-1}$ | 93%, 50 cycles @ 50 mA $g^{-1}$ |

## 4. Applications of anion storage materials in electrochemical capacitors

This section focuses on performance- and functionality-oriented applications of anion storage materials for electrochemical capacitors and battery-capacitor hybrid devices. Performance-oriented devices are classified into two types according to their operating mechanism (**Fig. 1c**). First, the dual-ion cells are configured by an anion storage electrode and a cation storage electrode, where both anions and cations are involved in the charge storage process. Second, anion storage materials are used as both positive and negative electrodes, where anions are shuttled between two electrodes during charge/discharge in a "rocking chair" manner. Functionality-oriented cells include micro- and flexible capacitors, desalination cells, and salinity cells, which further expands the applications of electrochemical capacitors based on anion storage materials.

### 4.1 High-energy electrochemical capacitors based on anion storage materials

**4.1.1 Dual-ion-storing hybrid capacitors.** Dual-ion hybrid capacitors are of great interest because they provide many options to discover high-capacity electrode materials that are otherwise realized with current cation-storing materials. In addition, the cell voltages of dual-ion electrochemical capacitors can be increased when both positive and negative electrodes operate in different potential ranges, thereby further increasing the energy density of the full cells. Dual-ion hybrid capacitors can be divided into two types. (D-1) Hybrid capacitors are comprised of Faradaic anion storage materials as the positive electrodes and capacitive cation-storing materials as the negative electrodes, whereas another type of (D-2) hybrid capacitors are configured using capacitive anion-storing materials as the positive electrodes and Faradaic cation storing materials as the negative electrodes.

**Faradaic anion storing positive electrode and capacitive cation storing negative electrode (D-1).** The Faradaic $OH^-$ storing transition metal compounds, such as Ni, Co-based hydroxides/oxides,[52, 60-62, 260, 266, 273, 277, 281, 283] sulfides,[70, 285, 287, 288] selenides,[289, 291] phosphides,[72, 73, 297] nitrides,[68, 294] carbonate hydroxides,[76, 77] MOFs and their derivatives,[182, 320, 324] perovskite oxides,[82, 331, 332, 375, 478] and perovskite fluorides[344-348] in alkaline aqueous electrolytes can be used as positive electrode with relatively positive potential windows for hybrid capacitors. Despite the high power and cyclic performance of EDLCs in aqueous systems, the capacitances of EDLC-type materials are limited, which lower their energy densities. The energy density of typical EDLCs can be improved by pairing with Faradaic $OH^-$ storing materials, while preserving kinetic performance and stability. The cell configurations and corresponding electrochemical performances are summarized in **Table 6**. As discussed in Section 2, KOH solution is generally chosen as an alkaline aqueous electrolyte owing to its high ionic conductivity.

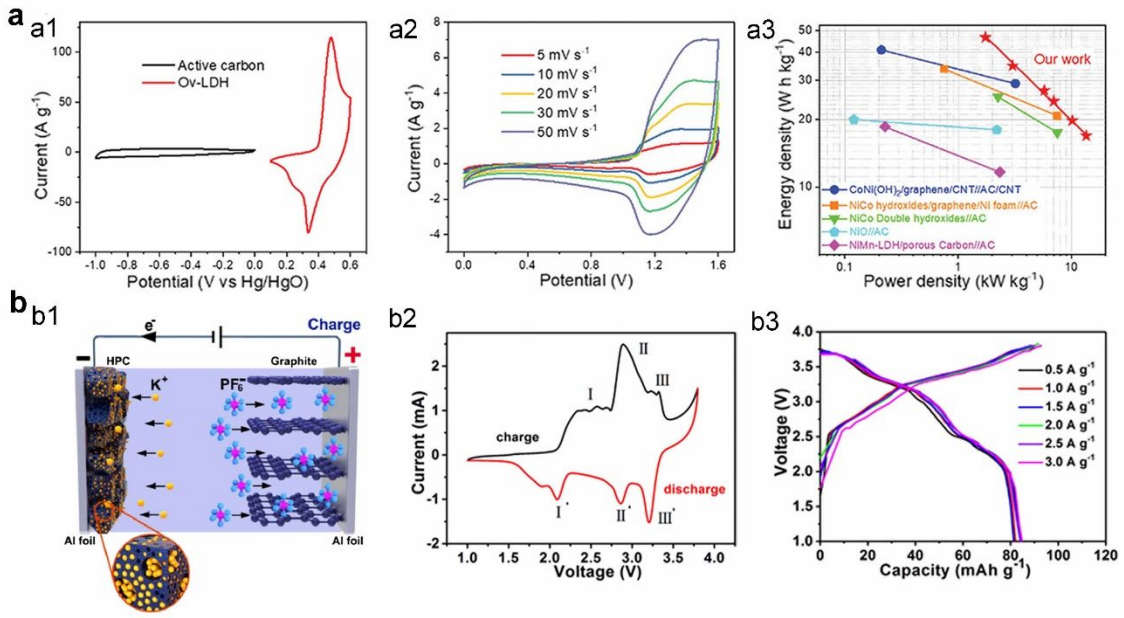


**Fig. 17** Dual-ion hybrid capacitors with Faradaic anion storing positive electrode (D-1). (**a**) A hybrid electrochemical capacitor configured by NiMn-LDH and AC electrodes in KOH electrolyte. (a1) CV curves of NiMn-LDH and AC electrodes, (a2) CV curves, and (a3) Ragone plots of NiMn-LDH//AC device. Reproduced with permission from ref. [266], Copyright 2020 Wiley-VCH. (**b**) A hybrid electrochemical capacitor configured by graphite and porous carbon electrodes in $KPF_6$-based carbonate electrolyte. (b1) Schematic illustration of the configuration and mechanism, (b2) CV curve at a voltage range of 1–3.8 V, and (b3) GCD curves at current densities of 0.5–3.0 A $g^{-1}$. Reproduced with permission from ref. [485], Copyright 2018 American Chemical Society.

In particular, two electrodes with different energy storage mechanisms should be properly matched on a basis of energetic and kinetic balances, which optimize the cell performances of dual-ion hybrid capacitors. For the charge balance of two electrodes, the larger mass loading is needed for capacitive negative electrodes due to their lower capacity than Faradaic positive electrodes. For example, a hybrid capacitor, which was assembled with NiMn-LDH positive electrode and AC negative electrode, is charge-balanced as a high mass ratio (4.35) of AC/NiMn-LDH,[266] considering the high capacity of NiMn-LDH electrode (328 and 232 mAh $g^{-1}$ at 1 and 10 A $g^{-1}$, respectively) and the low capacitance of AC electrode (161 and 123 F $g^{-1}$ at 1 and 10 A $g^{-1}$, respectively) (**Fig. 17a1**). Consequently, the 1.6 V hybrid capacitor showed relatively low energy densities of 46.7 and 16.9 Wh $kg^{-1}$ at 1.7 and 13.5 kW $kg^{-1}$, respectively (**Figs. 17a2 and 17a3**). Given by the parallel configuration of two electrodes, the energy density of full cells is limited by the low capacitance and high mass loading of capacitive electrodes. Accordingly, a N-incorporated porous carbon with high capacitance (468 F $g^{-1}$ at 1 A $g^{-1}$) was assembled into a hybrid electrochemical capacitor pairing with a $Ni(OH)_2$/CNTs material.[51] The mass ratio of negative/positive electrodes decreased to 1.6 along with the cell voltage of 1.8 V. Considering that high energy density of 90.1 Wh $kg^{-1}$ could be achieved for this hybrid capacitor, the capacity gaps of high-capacity two electrodes need to be as small as possible in different working potentials within the kinetically stable region. To circumvent capacity imbalance issue of positive and negative electrodes, redox couples were added in electrolyte to compensate the low capacitance of capacitive electrode by means of the contribution of additional Faradaic capacity.[479] This approach allowed the NiCo-LDH and AC electrodes to achieve the same mass loading for the configuration of hybrid capacitor, dramatically increasing energy density by 4 times greater than that of the unbalanced cell. On the other hand, the power performance and cycling stability of these hybrid electrochemical capacitors are mostly determined by the Faradaic positive electrodes, because of their slower kinetics of electron transfer and ion transport and less stable structure than the capacitive negative electrodes. Moreover, even though the charge is balanced by mass adjustment at low (or high) current density, it will be unbalanced at high (or low) current density due to the different rate capacities of two electrodes. To resolve this problem, electrically converse-voltage-activated CoOOH (EA-CoOOH) with rational configuration of defects and disorders was fabricated to promote the kinetics and stability.[52] The EA-CoOOH electrode exhibits a surface redox reaction-dominated behavior, showing a high rate capability of 78% retention from 1 A $g^{-1}$ (832 F $g^{-1}$) to even 200 A $g^{-1}$ (649 F $g^{-1}$). The assembled hybrid capacitor achieved a high power density of 35.8 kW $kg^{-1}$ at 23.5 Wh $kg^{-1}$, and long cycling stability of 86% capacitance retention after 20000 cycles.

The Faradaic $PbO_2$ can be converted to $PbSO_4$ along with $SO_4^{2-}$ anions in $H_2SO_4$ electrolyte, which has been used as the positive electrode of lead–carbon hybrid capacitors coupled with capacitive carbon negative electrode.[88, 480-483] In order to achieve high-performance lead–carbon hybrid capacitors, two electrodes were optimized using thin-layer $PbO_2$ positive electrodes and heteroatom-doped carbon negative electrodes. These hybrid capacitors delivered a cell voltage of over 2 V and cycling life of tens of thousands of cycles.[482, 483]

Despite the advantages of high ionic conductivity, safety, low cost and mild manufacturing process in aqueous electrolytes, the energy density of aqueous dual-ion hybrid capacitors is still insufficient due to the low cell voltage and the number of cells connected in series increases when high output voltage is required for the practical

applications. Dual-ion hybrid capacitors in non-aqueous electrolytes are regarded as the potential candidate to resolve these issues. Graphite or modified graphite as positive electrode have been assembled into hybrid capacitors in the non-aqueous electrolytes (**Table 7**).[35, 36, 146, 156, 484-487] In such a dual-ion hybrid cell, the anions such as $PF_6^-$ and $BF_4^-$ are intercalated into graphite, while the cations, such as $EMIM^+$, $Na^+$, and $K^+$ are stored in the capacitive negative electrodes. Early studies of anion-storing graphite for hybrid capacitors focused on non-aqueous electrolytes including organic cations.[35, 146, 156, 486, 487] For example, a hybrid capacitor was configured by a graphite positive electrode and a rGO negative electrode in 1 M EMIM-$PF_6$/PC electrolyte.[35] This hybrid full cell achieved a cell voltage of 4 V, delivering an energy density of 70 Wh $kg^{-1}$ at 1333 W $kg^{-1}$. However, the cycling stability was not sufficient as evaluated to be 74% capacity retention after 50 cycles. The electrochemical performances of hybrid capacitors can be improved when alkali metal cations are used.[36, 484,485] For instance, the hybrid capacitor was designed using an expanded graphite as positive electrode material and a hierarchical porous carbon as negative electrode in 1 M $KPF_6$-based carbonate electrolyte (**Fig. 17 b1**). This full cell is featured with the stage intercalation of graphite positive electrode in three discrete oxidation or reduction regions (**Fig. 17b2**).[485] Taking advantage of fast reaction kinetics of two electrodes, the full cell exhibited outstanding rate performance of 82 mA h $g^{-1}$ (based on mass of graphite) when the current density increased from 0.5 to 3 A $g^{-1}$ (**Fig. 17b3**). The energy density (based on the mass of total electrodes) of full cell was 117 Wh $kg^{-1}$ at 1300 W $kg^{-1}$, along with a capacity retention of 74.2% for 2000 cycles at 1 A $g^{-1}$. Further investigation should be carried out on the origin of the improved cycling stability of using alkali metal cations compared to using organic cations.

In addition, thiophene-,[41, 428-432, 488, 489] triphenylamine-,[489] fluorene-,[490] and TEMPO[491]-based organic polymers storing anions such as $BF_4^-$ and $TFSI^-$ have been explored as the positive electrodes of non-aqueous hybrid capacitors coupling with capacitive negative electrodes storing cations such as $EMIM^+$, $NEt_4^+$, and $Pyr_{14}^+$ (**Table 7**). A common hybrid configuration is the combination of a PMT positive electrode and an AC negative electrode.[37, 428-430] Among them, an energy density of 52 Wh $kg^{-1}$ was achieved for a 2.5 V hybrid capacitor utilizing PMT/vertically aligned CNTs nanocomposite as the positive electrode and AC as the negative electrode in EMIM-TFSI/ACN electrolyte.[37] Using an IL electrolyte such as $Pyr_{14}$-TFSI increased the cell voltage up to 3.6 V and operating temperature to 60 °C.[432] Moreover, a porous polymer was produced by the electropolymerization of π-conjugated 3,8-di([2,2'-bithiophen]-5-yl)-6-oxophenanthridine-5(6H)-carboxylate (PNBTH-Boc) monomer and subsequent annealing process removing labile side chains.[41] The hybrid capacitor based on PNBTH polymer and CNTs electrodes in $Pyr_{14}$-TFSI/PC electrolyte displayed a capacity retention of 85% over 10000 cycles.

The advances in dual-ion hybrid capacitors lag behind dual-ion batteries using anion storage graphite and p-type organics. These non-aqueous dual-ion hybrid capacitors encounter technical challenges such as the low initial Coulombic efficiency, unsatisfactory energy density and limited cycles of <10000, which restricts the practical applications on a full cell level. As shown in **Table 7**, the capacitive carbon materials were usually used as cation storing negative electrodes with the limited capacitances. The advanced pseudocapacitive negative electrodes that can match with anion storage graphites and p-type organics need to be further investigated for high performance dual-ion hybrid capacitors.[492] In addition, other Faradaic anion storage materials should be explored to greatly improve the cell performances of hybrid capacitors. For instance, porous frameworks such as MOFs and COFs can be the promising candidate owing to their structural diversity and tunability for hybrid capacitors.

**Capacitive anion storing positive electrode and Faradaic cation storing negative electrode (D-2).** Typical hybrid capacitors, which combine capacitive positive electrodes with Faradaic negative electrodes storing monovalent cations such as $Li^+$, $Na^+$, and $K^+$, have been intensively investigated. Because there have been numerous prior related reviews in this field,[19, 21] these hybrid capacitors are beyond the scope of this review. Therefore, this section focuses on emerging dual-ion hybrid capacitors based on multivalent metal cations (e.g., $Zn^{2+}$, $Ca^{2+}$, $Mg^{2+}$ and $Al^{3+}$) and anion carriers (e.g., $SO_4^{2-}$, $OTf^-$, $PF_6^-$, $TFSI^-$ and $AlCl_4^-$). Multivalent metal anodes and ion carriers have advantages over their monovalent counterparts in terms of multielectron-redox properties providing high capacity feasibility. Considering the main focus of anion storage materials, progress of research on metal anodes is excluded in this review.

Among multivalent metal anodes, the compatible Zn plating/stripping potential of −0.76 V versus SHE is within the ESWs of neutral aqueous electrolytes. Accordingly, Zn-based hybrid capacitors can be configured using Zn metals (or Zn hosting materials) and capacitive anion storing materials as negative and positive electrodes, respectively, in neutral aqueous electrolytes. Various strategies such as hierarchical porous architecture,[493-496] and heteroatom doping[497, 498] have been explored to enhance the capacitance of carbon-based positive electrodes storing anions such as $SO_4^{2-}$ and $OTf^-$. The capacitance of positive electrodes could be also enhanced using pseudocapacitive materials such as graphite-PANI composites storing $SO_4^{2-}$ anions.[426, 499] Moreover, the low temperature operation of an aqueous Zn-ion hybrid capacitor at −20 °C was demonstrated using a hybrid electrolyte containing water, ethylene glycol (EG), and $ZnSO_4$ salt.[500] The hybrid cells consist of the Zn metal deposition negative electrode and AC positive electrode (**Figs. 18a1 and 18a2**). Theoretical calculations elucidate that the high ionic conductivity of 6.9 mS $cm^{-1}$ even at −40 °C is attributable to the unique solvation interaction of $Zn^{2+}$ with EG that effectively enhances the EG–$H_2O$ hydrogen bonding and weakens the $Zn^{2+}$–$H_2O$ solvation interaction. Consequently, the competitive rate performance from 0.1 A $g^{-1}$ (60 mAh $g^{-1}$) to 5 A $g^{-1}$ (20 mAh $g^{-1}$) (**Fig. 18a3**), and long cycling

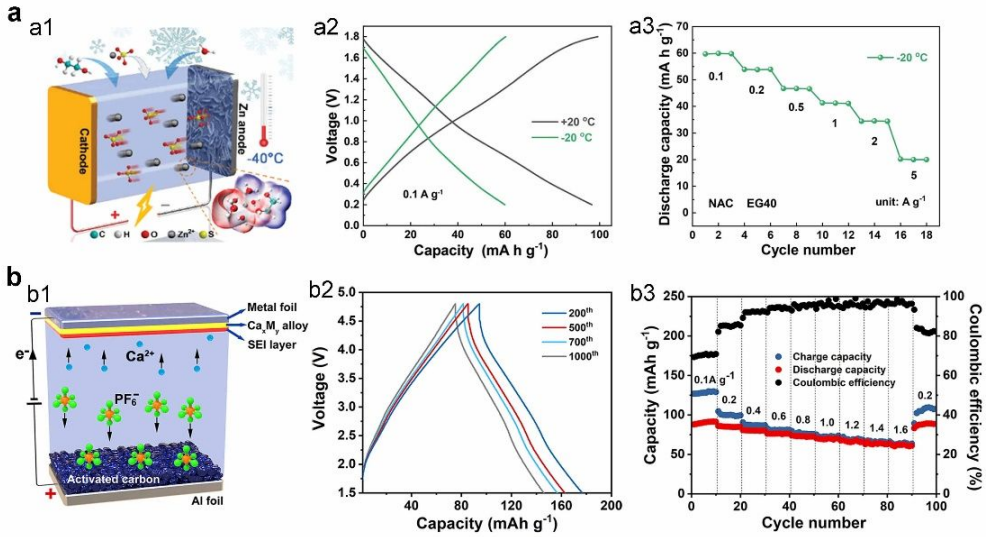


**Fig. 18** Dual-ion hybrid capacitors with EDLC-type anion storing positive electrode (D-2). (**a**) Zn-based hybrid capacitor with water/ethylene glycol electrolyte solvent. (a1) Schematic illustration of device structure, (a2) GCD curves at ±20 °C at 0.1 A $g^{-1}$, and (a3) rate performance at −20 °C. Reproduced with permission from ref. [500], Copyright 2020 Royal Society of Chemistry. (**b**) Ca-based hybrid capacitor. (b1) Schematic illustration of device structure, (b2) GCD curves of 200–1000 cycles at 0.1 A $g^{-1}$, and (b3) rate performance. Reproduced with permission from ref. [502], Copyright 2019 Wiley-VCH.

stability over 5000 cycles could be obtained at −20 °C. A drawback of aqueous Zn-ion hybrid capacitor is that the voltage of full cells is restricted to below 1.8 V. Recently, non-carbonous phosphorene as a capacitive positive electrode was fabricated into Zn-based hybrid capacitors with Zn plate as the negative electrode.[501] The cell voltages can be increased to 2.2 and 2.5 V by using WiS electrolyte (1 m $Zn(OTf)_2$ + 21 m LiTFSI) and organic electrolyte (0.2 m $ZnCl_2$ into $NEt_4$-$BF_4$/PC solvent), along with the capacitance of 146 and 46 F $g^{-1}$ at 6.4 A $g^{-1}$, respectively.

Other multivalent metal-based hybrid capacitors are based on non-aqueous electrolytes that enlarge the cell voltage for high energy density. Recently, the Ca-based hybrid capacitor was designed by Tang et al. using the alloying-type Sn negative electrode and AC positive electrode in a $Ca(PF_6)_2$-based carbonate electrolyte (**Fig. 18b1**).[502] The Faradaic negative electrode possesses a stable and low potential for $Ca^{2+}$ storage, and the positive electrode store $PF_6^-$ carriers up to the upper limit of electrolyte. Thus, Ca-based hybrid capacitor delivered a high capacity of 92 mAh $g^{-1}$ and a large cell voltage of 1.5–4.8 V at 0.1 A $g^{-1}$. In different manners to the sluggish kinetics and low cyclic stability of existing Ca-based cells, this hybrid capacitor achieved 84% of capacity retention over 1000 cycles and high-rate capacitance of 62 mAh $g^{-1}$ at 1.6 A $g^{-1}$ (**Figs. 18b2 and 18b3**). Nonetheless, the appropriate combination of electrode materials and electrolytes remains a critical challenge in the Ca-based energy storage devices.[503, 504]

The Mg-based hybrid capacitors were assembled using Mg metal negative electrodes and AC positive electrodes.[505, 506] When the Grignard-based Mg electrolyte (a solution of Mg organo-haloaluminate complex ions and tetrahydrofuran solvent) was used, the additive LiCl salt was needed because the large-sized Mg-based ionic complexes easily saturate the AC pores.[505] The electrolyte such as $Mg(TFSI)_2$ and $MgCl_2$ salts dissolved in diethylene glycol dimethyl ether solvent was further developed. Upon charging of the hybrid capacitor cell, both cation desorption and anion adsorption are involved on the AC positive electrode at a potential from 0.7 to 2.7 V versus $Mg^{2+}$/Mg, while the Mg plating on the negative electrode occurs at nearly 0 V versus $Mg^{2+}$/Mg.[506]

For the case of Al-based hybrid capacitors, the cells were configured using Al foil as the negative electrode and either multi-walled carbon nanotubes or N-doped graphene as the positive electrode in EMIMCl-$AlCl_3$ IL electrolyte.[507, 508] In particular, these two positive electrodes store $AlCl_4^-$ anions via two storage mechanisms, that is, the main EDLC and the minor intercalation pseudocapacitance. Thousands of cycles are achieved with the capacity retention of >80%.

There are inherent challenges of dual-ion hybrid capacitors. Since both anions and cations from electrolyte participate in electrode reactions, the electrolyte concentration changes dynamically during the operation of hybrid cells. Thus, sufficient concentration and large amount of electrolyte are needed to achieve high performance. However, the diffusion coefficient and ionic conductivity of electrolyte is often lowered and the weight and cost of the whole devices can increase.[137, 509, 510] The other issue is the thick electrolyte layer arising from the large amount of electrolyte, which greatly increase the ohmic and concentration polarization, thus lowering the energy efficiency of full cells.[511] In order to resolve these issues, the ionic conductivity of the electrolyte at high concentrations should be improved and the amount of electrolyte needs to be optimized comprehensively for maximum energy density and efficiency and service life of full cells. Given by $\sigma_{eff} = \sigma \times \varepsilon/\tau$, the effective conductivity of electrolyte layer ($\sigma_{eff}$) can be improved by

increasing porosity ($\varepsilon$) and decreasing tortuosity ($\tau$) of separator.[512] One hand, the non-Faradaic electrodes of the dual-ion hybrid capacitors are often polarized far from the zero charge point during operation, which induces a large leakage current and significant self-discharge.[513, 514] On the other hand, the Faradaic anion storage electrodes usually operate at high potentials, where the nucleophilic attack of anion to solvent molecules seriously degrades the stability of the electrolyte, causing a low Coulombic efficiency and self-discharge.[515-517] Therefore, the solvation structure and electrode interface chemistry of dual-ion devices should be rationally designed.[518, 519]

**4.1.2 Whole-anion-storing electrochemical and hybrid capacitors.** Given that whole-anion capacitors in only alkaline aqueous electrolytes have been reported to date, they are not as advanced as dual-ion hybrid capacitors. Whole-anion capacitors can be classified into two types. (A-1) hybrid capacitors configured by Faradaic anion storage negative electrodes (e.g., VN, $FeO_x$, $Bi_2O_3$) and capacitive positive electrodes, and (A-2) symmetric capacitors based on identical pseudocapacitive anion storage electrodes (e.g., $Zn_xCo_{1-x}O$, perovskite oxides, and VNs). The cell configurations and electrochemical performances of whole-anion capacitors are summarized in **Table 8**.

**Hybrid capacitors (A-1).** There are several examples of hybrid capacitors combining Bi-based materials as negative electrodes with capacitive positive electrodes.[377, 520-522] The composite of $Bi_2S_3$ and nitrogen-doped carbon ($Bi_2S_3$/NC) operates at a potential window of −0.1–0.45 V versus Ag/AgCl in KOH electrolyte, showing a capacity of 68 mAh $g^{-1}$ (466 F $g^{-1}$) at 1 A $g^{-1}$.[377] A hybrid capacitor fabricated by the $Bi_2S_3$/NC negative electrode and NC positive electrode reached a cell voltage of 1.35 V (**Figs. 19a1 and 19a2**), delivering an energy density of 22.2 Wh $kg^{-1}$ at 16.4 W $kg^{-1}$ (**Fig. 19a3**). In addition, hybrid capacitors coupled VN and $La_{0.85}Sr_{0.15}MnO_3$ electrodes with AC electrodes have been also developed.[318, 523] Overall, these hybrid capacitors have been less reported than dual-ion counterparts and their electrochemical performances are unsatisfactory yet because of the mismatch of two electrodes. The high-capacitance anion storage pseudocapacitive materials in organic and IL electrolytes need to be developed to further improve the electrochemical performances of whole-anion-storing capacitors.

**Symmetric capacitors (A-2).** A whole-anion symmetric capacitor has been assembled by using two identical $Zn_xCo_{1-x}O$ electrodes (**Fig. 19 b1**).[40] The $Zn_xCo_{1-x}O$ electrode with oxygen vacancy demonstrates an oxygen anion intercalation mechanism in KOH electrolyte. The symmetric cells operated at a voltage of 1.5 V, demonstrating energy density of 67.3 Wh $kg^{-1}$ at 1.67 kW $kg^{-1}$ and high power density of 68.6 kW $kg^{-1}$ at 27.6 Wh $kg^{-1}$ (**Figs. 19 b2 and 19b3**).

Oxygen anion intercalation perovskite oxides have also been used for whole-anion symmetric capacitors.[39, 341, 523, 524] For instance, a symmetric capacitor was assembled by two $LaMnO_{3-\delta}$ electrodes in KOH electrolyte,[39] showing a 2 V cell voltage along with an energy density of 61.2 Wh $kg^{-1}$ at 220.4 W $kg^{-1}$. Moreover, $Sr_2CoMoO_{6-\delta}$-based symmetric capacitor exhibited a cell voltage of 1.4 V and a specific capacitance of 246 F $g^{-1}$ at 1.25 A $g^{-1}$, delivering an energy density of 64 W h $kg^{-1}$ at 855 W $kg^{-1}$.[341] The whole-anion capacitors based on early transition metal nitrides have been reported.[374, 526, 527] For example, the VN quantum dots/porous carbon (VNQDs/C) sample was fabricated into a symmetric capacitor, which showed an energy density of 10.2 Wh $kg^{-1}$ at 1196 W $kg^{-1}$.[374] The relatively low energy density is due to the low capacitance of VNQDs/C electrodes (53.75 F $g^{-1}$ at 0.5 A $g^{-1}$). Despite the limited energy density, early transition metal nitrides are promising candidates for micro- and flexible capacitors in a form of thin film, as shown in Section 4.2.1.

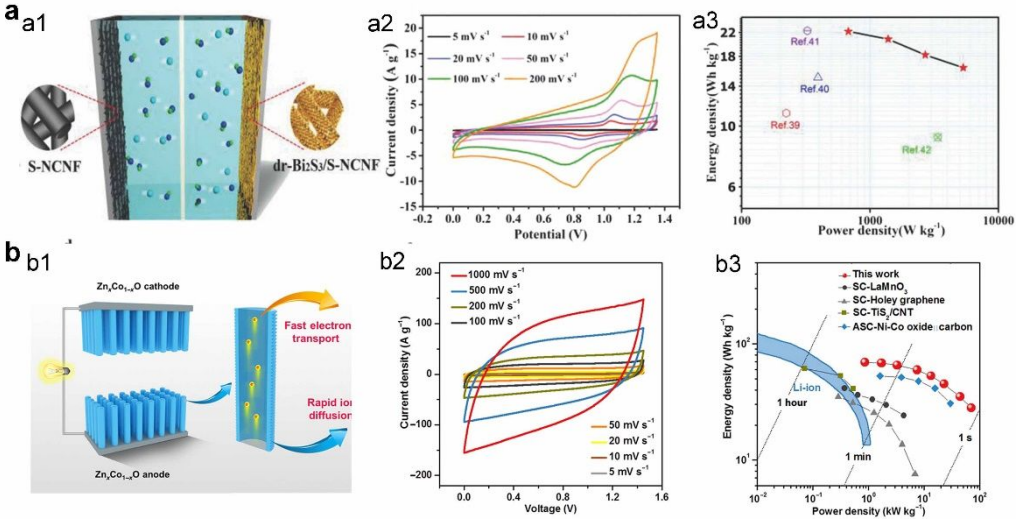


**Fig. 19** Whole-anion-storing electrochemical and hybrid capacitors. (**a**) A hybrid capacitor (A-1) configured by $Bi_2S_3$/NC and NC electrodes. (a1) Schematic illustration of device structure, (a2) CV curves, and (a3) Ragone plots. Reproduced with permission. [377] Copyright 2018 Wiley-VCH. (**b**) A symmetric capacitor (A-2) configured by two identical $Zn_xCo_{1-x}O$ electrodes. (b1) Schematic illustration of device structure, (b2) CV curves, and (b3) Ragone plots. Reproduced with permission from ref. [40], Copyright 2018 American Association for the Advancement of Science.

**Table 6** Summary of aqueous dual-ion hybrid capacitors with Faradaic anion storing positive electrode (D-1).

| Negative/Positive Electrodes [Ref] | Voltage Electrolyte | Maximum Energy | Maximum Power | Cycling Stability |
|---|---|---|---|---|
| AC//NiMn-LDH [266] | 1.6 V 2 M KOH | 46.7 Wh $kg^{-1}$ @ 1700 W $kg^{-1}$ | 16.9 Wh $kg^{-1}$ @ 13.5 kW $kg^{-1}$ | 96.2%, 2000 cycles @ 8 A $g^{-1}$ |
| rGO//NiCoMn-OH/rGO [260] | 1.6 V 2 M KOH | 74.7 Wh $kg^{-1}$ @ 1680 W $kg^{-1}$ | 49.9 Wh $kg^{-1}$ @ 18.5 kW $kg^{-1}$ | 91%, 10000 cycles @ 20 A $g^{-1}$ |
| N-AC//Li-$Co_3O_4$ [60] | 1.5 V 6 M KOH | 76.7 Wh $kg^{-1}$ @ 286 W $kg^{-1}$ | 46.9 Wh $kg^{-1}$ @ 18.7 kW $kg^{-1}$ | 85.5%, 10000 cycles @ 5 A $g^{-1}$ |
| AC//EA-CoOOH [52] | 1.6 V 6 M KOH | 65.4 Wh $kg^{-1}$ @ 560 W $kg^{-1}$ | 23.5 Wh $kg^{-1}$ @ 35.8 kW $kg^{-1}$ | 86%, 20000 cycles @ 10 A $g^{-1}$ |
| CNS-SCN//NiCoZn-LDH/$Co_9S_8$ [319] | 1.75 V 3 M KOH | 56.4 Wh $kg^{-1}$ @ 875 W $kg^{-1}$ | 42 Wh $kg^{-1}$ @ 8.2 kW $kg^{-1}$ | 95.3%, 8000 cycles @ 3 A $g^{-1}$ |
| AC//NiCo-LDH-CBD [273] | 1.6 V 6 M KOH | 57.5 Wh $kg^{-1}$ @ 900 W $kg^{-1}$ | 11.2 Wh $kg^{-1}$ @ 30.7 kW $kg^{-1}$ | 80.9%, 5000 cycles @ 50 A $g^{-1}$ |
| Graphene//P-$Co_3O_4$ [61] | 1.5 V 6 M KOH | 72.6 Wh $kg^{-1}$ @ 1500 W $kg^{-1}$ | 50 Wh $kg^{-1}$ @ 24 kW $kg^{-1}$ | 95%, 2000 cycles @ 5 mV $s^{-1}$ |
| AC//CC-NC-LDH [277] | 1.6 V 6 M KOH | 69.7 Wh $kg^{-1}$ @ 800 W $kg^{-1}$ | 41.5 Wh $kg^{-1}$ @ 21.6 kW $kg^{-1}$ | 87%, 20000 cycles @ 10 A $g^{-1}$ |
| AC//NiCoAl-OH/$V_4C_3T_x$ [283] | 1.6 V 1 M KOH | 71.7 Wh $kg^{-1}$ @ 830 W $kg^{-1}$ | 45 Wh $kg^{-1}$ @ 20 kW $kg^{-1}$ | 98%, 10000 cycles @ 20 A $g^{-1}$ |
| AC//$NiCo_2O_4$/rGO [281] | 1.5 V 6 M KOH | 57 Wh $kg^{-1}$ @ 375 W $kg^{-1}$ | 31 Wh $kg^{-1}$ @ 15 kW $kg^{-1}$ | 83.2%, 10000 cycles @ 5 A $g^{-1}$ |
| P-C//NiCoS/G [70] | 1.6 V 6 M KOH | 43.2 Wh $kg^{-1}$ @ 800 W $kg^{-1}$ | 28.4 Wh $kg^{-1}$ @ 22.1 kW $kg^{-1}$ | 85%, 10000 cycles @ 10 A $g^{-1}$ |
| AC//NiCoSe-4 [291] | 1.6 V 3 M KOH | 61.24 Wh $kg^{-1}$ @ 800 W $kg^{-1}$ | 38.1 Wh $kg^{-1}$ @ 16 kW $kg^{-1}$ | 91%, 12000 cycles@ 10 A $g^{-1}$ |
| AC//$Ni_3Se_2$ [289] | 1.6 V 3 M KOH | 38.4 Wh $kg^{-1}$ @ 794 W $kg^{-1}$ | 15.6 Wh $kg^{-1}$ @ 8 kW $kg^{-1}$ | 71.4%, 10000 cycles @ 2 A $g^{-1}$ |
| rGO//ZnNiCo-P [72] | 1.6 V 6 M KOH | 60.1 Wh $kg^{-1}$ @ 960 W $kg^{-1}$ | 30.4 Wh $kg^{-1}$ @ 19.54 kW $kg^{-1}$ | 89%, 8000 cycles @ 10 A $g^{-1}$ |
| AC//CoP/NiCoP [73] | 1.6 V 1 M KOH | 51.6 Wh $kg^{-1}$ @ 800 W $kg^{-1}$ | 28.4 Wh $kg^{-1}$ @ 12 kW $kg^{-1}$ | 95%, 3200 cycles @ 10 A $g^{-1}$ |
| AC//Co-Ni-B-S [320] | 1.7 V 6 M KOH | 45 Wh $kg^{-1}$ @ 857 W $kg^{-1}$ | 36.8 Wh $kg^{-1}$ @ 13.6 kW $kg^{-1}$ | 87.7%, 5000 cycles @ 12 A $g^{-1}$ |
| PC//NiCo-N [68] | 1.5 V 1 M KOH | 29.08 Wh $kg^{-1}$ @ 980 W $kg^{-1}$ | 20.4 Wh $kg^{-1}$ @ 9.85 kW $kg^{-1}$ | 82.4%, 5000 cycles@ 2 mA $cm^{-2}$ |
| rGO//C@ZnNiCo-CHs [77] | 1.6 V 2 M KOH | 70.9 Wh $kg^{-1}$ @ 966 W $kg^{-1}$ | 47.4 Wh $kg^{-1}$ @ 17.25 kW $kg^{-1}$ | 91%, 20000 cycles @ 20 A $g^{-1}$ |
| AC//NiCo-CH-$Ni(OH)_2$ [76] | 1.6 V 6 M KOH | 85.6 Wh $kg^{-1}$ @ 800 W $kg^{-1}$ | 52.5 Wh $kg^{-1}$ @ 22.5 kW $kg^{-1}$ | - |
| N-C//Ni-MDH [324] | 1.7 V 2 M KOH | 81 Wh $kg^{-1}$ @ 1900 W $kg^{-1}$ | 42 Wh $kg^{-1}$ @ 11.5 kW $kg^{-1}$ | 91.3%, 10000 cycles @ 13.5 A $g^{-1}$ |
| AC//CoNi-MOF [182] | 1.5 V 1 M KOH | 28.5 Wh $kg^{-1}$ @ 1500 W $kg^{-1}$ | 13.3 Wh $kg^{-1}$ @ 24 kW $kg^{-1}$ | 94%, 5000 cycles |
| GO//$LaCoO_{3-\delta}$ [332] | 1.6 V 6 M KOH | 47.64 Wh $kg^{-1}$ @ 804 W $kg^{-1}$ | 35.02 Wh $kg^{-1}$ @ 37.1 kW $kg^{-1}$ | 100%, 4000 cycles @ 5 A $g^{-1}$ |
| Graphene//$LaNiO_3$ [331] | 1.8 V 6 M KOH | 65.84 Wh $kg^{-1}$ @ 1800 W $kg^{-1}$ | 38.1 Wh $kg^{-1}$ @ 10.8 kW $kg^{-1}$ | 92.4%, 10000 cycles @ 150 mV $s^{-1}$ |
| rGO//$SrCo_{0.9}Mo_{0.1}O_{3-\delta}$ KOH [375] | 1.5 V 6 M KOH | 74.8 Wh $kg^{-1}$ @ 734.5 W $kg^{-1}$ | 33 Wh $kg^{-1}$ @ 6.6 kW $kg^{-1}$ | 97.6%, 10000 cycles @ 10 A $g^{-1}$ |
| AC//$SrCo_{0.9}Nb_{0.1}O_{3-\delta}$ [82] | 1.5 V 6 M KOH | 37.6 Wh $kg^{-1}$ @ 434 W $kg^{-1}$ | 32.9 Wh $kg^{-11}$ @ 9.86 kW $kg^{-1}$ | 98.3%, 5000 cycles @ 5 A $g^{-1}$ |
| CC//$La_{0.7}Sr_{0.3}CoO_{3-\delta}$/Ag [478] | 1.8 V 1 M KOH | 21.9 Wh $L^{-1}$ @ 90.1 W $L^{-1}$ | 10.6 Wh $L^{-1}$ @ 1.43 kW $L^{-1}$ | 81.2%, 3000 cycles @ 50 mA $cm^{-2}$ |
| AC//$La_2NiO_{4+\delta}$@Ag [376] | 1.6 V 1 M KOH | 44.7 Wh $kg^{-1}$ @ 800 W $kg^{-1}$ | 35.6 Wh $kg^{-1}$ @ 16 kW $kg^{-1}$ | 91%, 5000 cycles @ 5 A $g^{-1}$ |
| AC//$KNi_{0.8}Co_{0.2}F_3$ [345] | 1.5 V 3 M KOH/0.5 M LiOH | 42.7 Wh $kg^{-1}$ @ 242 W $kg^{-1}$ | 13.8 Wh $kg^{-1}$ @ 18.8 kW $kg^{-1}$ | 98%, 10000 cycles @ 4 A $g^{-1}$ |
| AC//$NaNiF_3$ [346] | 1.65 V 3 M KOH/0.5 M LiOH | 51.78 Wh $kg^{-1}$ @ 1650 W $kg^{-1}$ | 40.33 Wh $kg^{-1}$ @ 13.2 W $kg^{-1}$ | 90%, 10000 cycles @ 5 A $g^{-1}$ |
| AC//$KNi_{1-x-y}Co_xMn_yF$ [347] | 1.5 V 3 M KOH/0.5 M LiOH | 50.2 Wh $kg^{-1}$ @ 379 W $kg^{-1}$ | 20.2 Wh $kg^{-1}$ @ 20.0 W $kg^{-1}$ | 74.6%, 5000 cycles @ 1 A $g^{-1}$ |
| AC//$KNiF_3$@CNTs [348] | 1.5 V 3 M KOH/0.5 M LiOH | 63.7 Wh $kg^{-1}$ @ 374 W $kg^{-1}$ | 25.7 Wh $kg^{-1}$ @ 21.8 W $kg^{-1}$ | 95.9%, 5000 cycles @ 2 A $g^{-1}$ |

**Table 7** Summary of non-aqueous dual-ion hybrid capacitors with Faradaic anion storing positive electrode (D-1).

| Negative/Positive Electrodes [Ref] | Voltage Electrolyte | Maximum Energy | Maximum Power | Cycling Stability |
|---|---|---|---|---|
| AC//graphite [156] | 0–3.6 V EMIM-$PF_6$ IL | 65 Wh $kg^{-1}$ @ 378 W $kg^{-1}$ | 35 Wh $kg^{-1}$ @ 1512 W $kg^{-1}$ | 83%, 50 cycles @ 0.42 A $g^{-1}$ |
| rGO//graphite [35] | 0–4.0 V 1 M EMIM-$PF_6$/PC | 70 Wh $kg^{-1}$ @ 1333 W $kg^{-1}$ | - | 74%, 50 cycles @ 1.33 A $g^{-1}$ |
| Porous carbon//graphite [36] | 0–3.8 V 1 M $NaPF_6$/EC-DMC-EMC | 86 Wh $kg^{-1}$ @ 261 W $kg^{-1}$ | 60 Wh $kg^{-1}$ @ 1500 W $kg^{-1}$ | 87%, 1000 cycles @ 1 A $g^{-1}$ |
| Carbon//B-graphite [484] | 0–4 V 1 M $NaPF_6$/EC-DMC | 108 Wh $kg^{-1}$ @ 495 W $kg^{-1}$ | 20 Wh $kg^{-1}$ @ 6100 W $kg^{-1}$ | 97%, 5000 cycles @ 1 A $g^{-1}$ |
| Porous carbon//graphite [485] | 1.0–3.8 V 1 M $KPF_6$/EC-DMC-EMC | 117 Wh $kg^{-1}$ @ 1300 W $kg^{-1}$ | - | 74.2%, 2000 cycles @ 1 A $g^{-1}$ |
| AC//PMT [428] | 1–3 V 1 M $NEt_4$-$BF_4$/PC | 31 Wh $kg^{-1}$ | 510 W $kg^{-1}$ | 70%, 1000 cycles @ 20 mA $cm^{-2}$ |
| AC//PMT [429] | 1.0–3.0 V 1 M $NEt_4$-$BF_4$/PC | 31 Wh $kg^{-1}$ @ 512 W $kg^{-1}$ | 17 Wh $kg^{-1}$ @ 1820 W $kg^{-1}$ | >60%, 10000 cycles @ 20 mA $cm^{-2}$ |
| AC//PMT/CNT [430] | 0–2.5 V 1 M $NEt_4$-$BF_4$/PC | 33.4 Wh $kg^{-1}$ | - | 85%, 1000 cycles @ 1.25 A $cm^{-2}$ |
| AC// PMT/VACNT [37] | 0–2.5 V 1 M EMIM-TFSI/ACN | 52 Wh $kg^{-1}$ | 10000 W $kg^{-1}$ | 78%, 20000 cycles @ 3 A $cm^{-2}$ |
| AC//PMT [432] | 1.5–3.6 V $Pyr_{14}$-TFSI IL | 14 Wh $kg^{-1}$ | 1900 W $kg^{-1}$ | 50%, 16000 cycles @ 10 mA $cm^{-2}$ (60 °C) |
| AC//polyfluorene [490] | 1.0–3.2 V 1 M $NEt_4$-$BF_4$/PC | 47 Wh $kg^{-1}$ | - | 62%, 10000 cycles @ 20 A $g^{-1}$ |
| CNTs//Poly-PNBTH [41] | 0–2.8 V $Pyr_{14}$-TFSI/PC (1:1) | 23.5 μW $cm^{-2}$ @ 1.4 mW $cm^{-2}$ | 17.9 μW $cm^{-2}$ @ 14 mW $cm^{-2}$ | 85%, 10000 cycles @ 10 mA $cm^{-2}$ |

**Table 8** Summary of whole-anion-storing electrochemical and hybrid capacitors (A-1 and A-2)

| Negative/Positive Electrodes [Ref] | Voltage Electrolyte | Maximum Energy | Maximum Power | Cycling Stability |
|---|---|---|---|---|
| $Bi_2S_3$/NC//NC [377] | 1.5 V 6 M KOH | 22.2 Wh $kg^{-1}$ @ 677.3 W $kg^{-1}$ | 16.4 Wh $kg^{-1}$ @ 5.317 kW $kg^{-1}$ | 80.3%, 2000 cycles @ 200 mV $s^{-1}$ |
| BiOCl//AC [520] | 1.0 V 6 M KOH | 17.2 Wh $kg^{-1}$ @ 250.9 W $kg^{-1}$ | 6.2 Wh $kg^{-1}$ @ 4.97 kW $kg^{-1}$ | 82%, 3000 cycles @ 1 A $g^{-1}$ |
| $Fe_3O_4$/C//CNT [352] | 1.7 V PVA-KOH gel | 1.56 mWh $cm^{-3}$ @ 0.028 W $cm^{-3}$ | 0.64 mWh $cm^{-3}$ @ 0.48 W $cm^{-3}$ | 67.7%, 1000 cycles @ 5.5 mA $cm^{-2}$ |
| $Zn_xCo_{1-x}O$ [40] | 1.5 V 6 M KOH | 67.3 Wh $kg^{-1}$ @ 1670 W $kg^{-1}$ | 27.6 Wh $kg^{-1}$ @ 68.6 kW $kg^{-1}$ | - |
| $LaMnO_{3-\delta}$ [39] | 2.0 V 1M KOH | 61.2 Wh $kg^{-1}$ @ 220.4 W $kg^{-1}$ | 23.4 Wh $kg^{-1}$ @ 4.21 kW $kg^{-1}$ | - |
| $Sr_2CoMoO_{6-\delta}$ [341] | 1.4 V 6 M KOH | 64 Wh $kg^{-1}$ @ 855 W $kg^{-1}$ | 26.7 Wh $kg^{-1}$ @ 6.4 kW $kg^{-1}$ | 150%, 10000 cycles @ 10 A $g^{-1}$ |
| rGO/$BiVO_4$ [525] | 1.6 V 6 M KOH | 33.7 Wh $kg^{-1}$ @ 1140 W $kg^{-1}$ | 15.33 Wh $kg^{-1}$ @ 8 kW $kg^{-1}$ | 80.3%, 2000 cycles @ 4 A $g^{-1}$ |
| VNQDs/P [374] | 1.2 V 6 M KOH | 10.2 Wh $kg^{-1}$ @ 1196 W $kg^{-1}$ | 9.25 Wh $kg^{-1}$ @ 3.0 kW $kg^{-1}$ | 79.2%, 4000 cycles @ 2 A $g^{-1}$ |
| VNND/CNS [46] | 1.0 V PVA/KOH gel | 30.9 Wh $L^{-1}$@ 240.1 W $L^{-1}$ | 16.1 Wh $L^{-1}$ @ 64.5 kW $L^{-1}$ | 91%, 10000 cycles @ 10 A $g^{-1}$ |

### 4.2 Functional electrochemical capacitors based on anion storage materials

**4.2.1 Micro- and flexible capacitors.** Micro- and flexible capacitors as energy storage devices have received significant attention because of the ever-increasing demand for miniaturized, wearable, portable, implantable, and integrated electronics.[528-530] In this section, the recent progress in the electrode materials of micro- and flexible capacitors based on anion storage materials is discussed. We also address them in terms of dual-ion hybrid capacitors and whole-anion storage capacitors.

**Microcapacitors.** Microcapacitors have advantages in terms of short diffusion length and patterned electrodes, which can resolve the slow diffusion kinetics of anion carriers and their large footprint in a limited space. There are a few reports regarding dual-ion hybrid microcapacitors. A dual-ion microcapacitor (D-1) was fabricated by using a Faradaic $OH^-$ storage $NiCo_2S_4$ positive electrode and a capacitive carbon nanofiber (CNF) negative electrode in KOH electrolyte (**Fig. 20a1**).[43] Through the mass balance of two electrodes, the full cells achieved a cell voltage of 1.6 V and a specific capacity of 240 μAh $cm^{-2}$ at 5 mA $cm^{-2}$ (**Fig. 20a2**), yielding an energy density of 200 μWh $cm^{-2}$ at 4.4 mW $cm^{-2}$. The functional application was demonstrated by two series connected microcapacitors that lighten a green light-emitting diode (LED) for a minute.

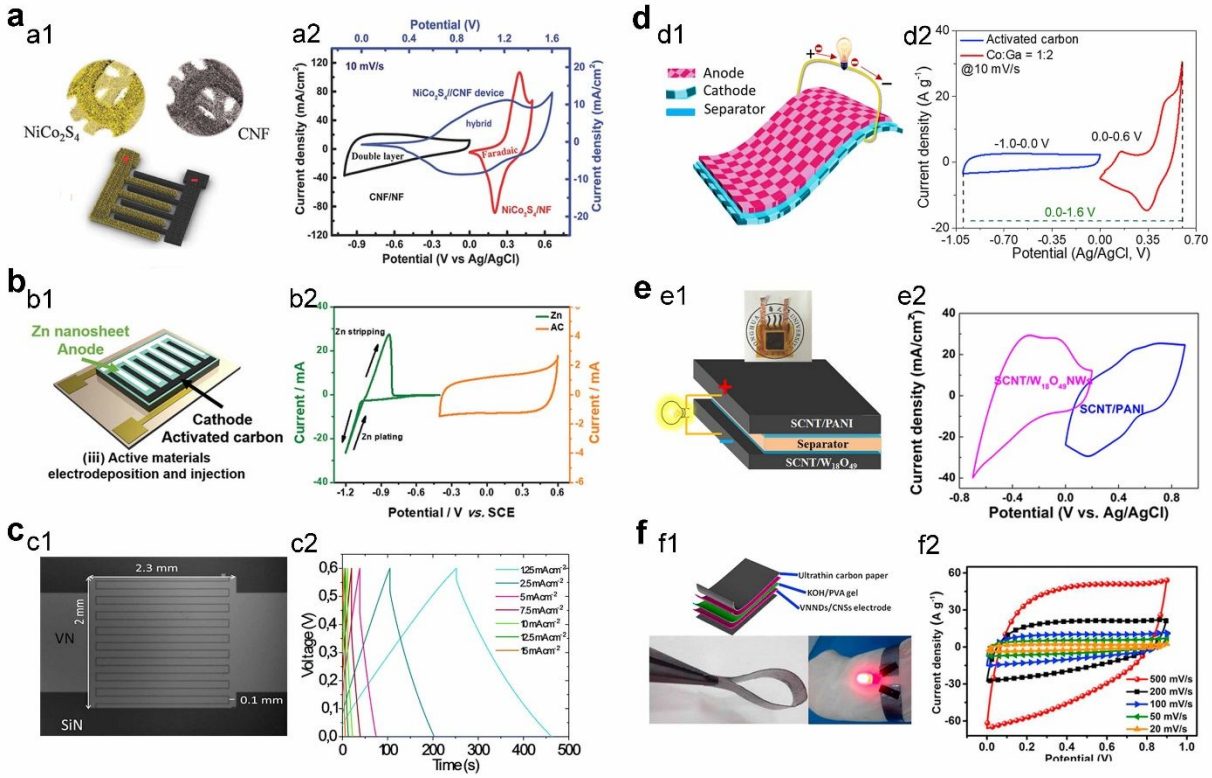


**Fig. 20.** Micro- and flexible capacitors using anion storage materials. (**a**) Dual-ion hybrid micro capacitor (D-1) with $NiCo_2S_4$ and CNF electrodes in KOH electrolyte. (a1) Schematic illustration of the micro capacitor, (a2) CV curves of the $NiCo_2S_4$, CNF electrodes, and device. Reproduced with permission. [43] Copyright 2017 Wiley-VCH. (**b**) Dual-ion hybrid micro capacitor (D-2) with AC and Zn electrodes in $ZnSO_4$ aqueous electrolyte. (b1) Schematic illustration of the micro capacitor, (b2) CV curves of the AC and Zn electrodes. Reproduced with permission. [531] Copyright 2020 Wiley-VCH. (**c**) Whole-anion symmetric micro capacitor (A-2) with identical VN electrodes in KOH electrolyte. (c1) SEM top view of the micro capacitor, (c2) GVD curves of micro capacitor device. Reproduced with permission from ref. [42], Copyright 2020 Royal Society of Chemistry. (**d**) Dual-ion hybrid flexible capacitor (D-1) with $CoGaO_4$ and AC electrodes in KOH electrolyte. (d1) Schematically illustration of the flexible capacitor, (d2) CV curves of $CoGaO_4$ and AC electrodes. Reproduced with permission. [44] Copyright 2020 Elsevier. (**e**) Dual-ion hybrid flexible capacitor (D-2) with SCNT/$W_{18}O_{49}$ and SCNT/PANI electrodes in $AlCl_3$ aqueous electrolyte. (e1) Schematically illustration of flexible capacitor device, (e2) CV curves of SCNT/$W_{18}O_{49}$ and SCNT/PANI electrodes. Reproduced with permission. [544] Copyright 2020 Wiley-VCH. (**f**) Whole-anion symmetric flexible capacitor (A-2) with VNND/CNS electrodes. (f1) Schematic and photographs of the flexible capacitor, (f2) CV curves of the flexible capacitor. Reproduced with permission from ref. [46], Copyright 2018 Elsevier.

Employing electrodeposited Zn nanosheets as negative electrode and AC as positive electrode in $ZnSO_4$ aqueous electrolyte, a Zn hybrid microcapacitor (D-2) was fabricated (**Fig. 20b1**).[531] The charge storage mechanism of this hybrid capacitor is based on the stripping/plating process of $Zn/Zn^{2+}$ on the Zn electrode and $SO_4^{2-}$ adsorption/desorption on the AC electrode (**Fig. 20b2**). Consequently, the full cells extended a voltage up to 1.5 V, delivering an energy density of 115.4 μWh $cm^{-2}$ at 0.16 mW $cm^{-2}$. Higher voltage and capacitance can be achieved by connecting individual units in series and parallel, respectively. For practical applications, a character composed of 33 red LEDs was lightened by two serially connected microcapacitors.

Using magnetron sputtering deposition technique, pseudocapacitive $OH^-$ storage VNs electrodes were prepared for whole-anion interdigitated microcapacitors (A-2).[42, 532] The VN thin films act as a current collector free pseudocapacitive electrode owing to their high electronic conductivity. The microcapacitor based on 16 μm-thick VN electrodes in KOH electrolyte reached a cell voltage of 0.6 V, resulting in a high areal capacitance of 1.2 F $cm^{-2}$ at 5 mV $s^{-1}$ (**Figs. 20c1 and 20c2**).[42] The maximum energy and power densities were 25 μWh $cm^{-2}$ and 4 mW $cm^{-2}$, respectively.

**Flexible capacitors.** Various planar- and fiber-shaped dual-ion hybrid flexible capacitors (D-1) have been fabricated integrating $OH^-$ storage positive electrodes, such as transition metal hydroxides/oxides,[44, 533-535] sulfides,[536] and phosphides,[300, 537] with capacitive negative electrodes. The $CoGaO_4$ electrode, with Co and Ga contributing to capacity and stability, respectively, was assembled into a planar-shaped flexible capacitor with an AC negative electrode (**Figs. 20d1 and 20d2**).[44] The full cells yielded a cell voltage of 1.6 V and a capacity of 382 C $g^{-1}$ at 1.5 A $g^{-1}$. The flexibility was demonstrated by being bent and twisted harshly without deteriorating physical and electrochemical performance. The cycling test at various bending states (from normal to bent state at 180°) showed >90% capacity retention after 200 cycles. The CoNi-LDH was integrated on PPy-coated cotton pads (CoNi-LDH@PCPs) to facilitate charge transfer and redox reaction processes, thereby improving the rate performance of hybrid flexible capacitor.[533] The hybrid flexible capacitor exhibited mechanical integrity at various deformations. For

example, a 95% capacity was achieved after repeated folding over 200 cycles. The reversible $Cl^-$ and $NO_3^-$ storage capability of ferrocyanide immobilized polysilsesquioxane ($Fe(CN)_6$-PSQ) electrodes has been reported.[538, 539] The reversible Faradaic charge storage process is based on the oxidation of Fe from II to III, neutralized by the anions through the formation of ion-pair complex. The $Fe(CN)_6$-PSQ positive electrode coupled with a capacitive graphite negative electrode was configured into a flexible hybrid capacitor in neutral LiCl aqueous electrolyte.[538]

Several Zn hybrid flexible capacitors (D-2) have been developed using capacitive anion storing electrode materials.[498, 540-543] For instance, a high-capacitance layered B/N co-doped porous carbon was assembled into a Zn hybrid flexible capacitor with a Zn foil as the negative electrode.[498] The hybrid cell achieved a voltage window ranging from 0.2 to 1.8 V, delivering specific capacities (based on the positive electrode material) of 116.8 and 55.5 mAh $g^{-1}$ at 0.5 and 20 A $g^{-1}$, respectively. It can withstand different bending states with an almost equal capacity, and power a smart watch for 24 h. A fiber-shaped Zn hybrid capacitor was constructed using the hierarchically nanostructured Zn negative electrode and AC positive electrode, achieving the energy densities from 25 to 12 μWh $cm^{-2}$ at power densities from 50 to 3000 μW $cm^{-2}$ along with the stable cycling performance over 10000 cycles.[542] The Zn hybrid capacitors can light up a red LED even when they were knotted under water immersion, demonstrating high mechanical flexibility and waterproof capability. In addition, Al hybrid flexible capacitors (D-2) were designed.[508, 544] The composite film electrode, consisting of $W_{18}O_{49}$ nanowires and single-walled carbon nanotubes (SCNT/$W_{18}O_{49}$), was used for $Al^{3+}$-storage materials. Al hybrid flexible capacitor was configured integrating SCNT/$W_{18}O_{49}$ composite electrode with SCNT/PANI positive electrode in an $AlCl_3$ aqueous electrolyte (**Fig. 20e1**).[544] The full cell with the cell voltage of 1.8 V exhibited an areal capacitance of 0.792 F $cm^{-2}$ at 6 mA $cm^{-2}$ (**Fig. 20e2**). It can maintain 90% capacity after 500 bending cycles, and be utilized as the power source for an electrochromic device.

In addition, a flexible whole-anion hybrid capacitor (A-1) has been reported.[352] The binder-free $OH^-$ storing $Fe_3O_4$/C negative electrode showed a capacity up to 7776 C $cm^{-3}$ (247.5 mAh $g^{-1}$) in KOH electrolyte. Matching with a capacitive CNT film as positive electrode, 1.7 V flexible capacitor was fabricated, which delivered an energy density of 1.56 mWh $cm^{-3}$ at 0.028 W $cm^{-3}$. The flexible cell can withstand substantial bending tests and mechanical pressures up to 32.9 kPa without essentially deteriorating capacity.

VN and TiN could be applied for whole-anion symmetric flexible capacitors (A-2).[45, 46] The cycling stability of TiN-based flexible capacitor can be improved replacing the 1 M KOH electrolyte by the poly(vinyl alcohol) (PVA)/KOH gel electrolyte.[45] The corresponding cell achieved a voltage of 1.0 V and a volumetric capacitance of 0.33 F $cm^{-3}$ at 2.5 mA $cm^{-3}$. The VN nanodots intercalated carbon nanosheets (VNND/CNS) was designed to improve the electrochemical stability.[46] The flexible capacitor consisting of two VNND/CNS electrodes and PVA/KOH gel electrolyte achieved a high volumetric energy density of 30.9 Wh $L^{-1}$ and cycling stability of 91% capacitance retention over 10000 cycles (**Figs. 20f1 and 10f2**). Its functional operation was realized demonstrating a 2.7 V voltage of three cells connected in series to power a red LED.

#### 4.2.2 Desalination and salinity gradient energy storage.

**Desalination.** Among desalination technologies that can remove ions from saline water, capacitive deionization (CDI) is a promising reversible electrochemical desalination technology to afford fresh water. This ion removal is based on the principle of electrochemical charge storage, where the ionic species from saline water are captured to compensate for the electric charge of the electrodes under an applied potential. Then, the ionic species can be released from the electrodes when a null or reversal potential is exerted on the electrodes.[100, 101, 545, 546] In general, desalination cells are in a dual-ion configuration because anion removal can be accompanied by cation removal to ensure charge balance during deionization. Conventional CDI utilizes two capacitive carbon electrodes in a symmetric configuration. Nonetheless, the ion removal capacity of the carbon electrode is limited owing to the intrinsically low capacitance of capacitive materials. As discussed in Section 3.1, the low-polarized capacitive electrodes usually operate via a non-permselectivity (or ion swapping) mechanism, that is the adsorption of counter-ions accompany with desorption of co-ions. The non-permselectivity mechanism does not change the total number of ions; thus, the resultant ion removal efficiency is low. Although co-ion desorption can be prevented by utilizing ion exchange membranes, their high cost limits their practical applications. To circumvent these limitations, an effective strategy is to develop highly ion-selective Faradaic electrode materials for desalination cells.[547] Thus far, most Faradaic electrode materials have been used for high-capacity negative electrodes for the removal of cations. Therefore, it is important to develop high-capacity anion storage materials for applications in dual-ion desalination cells. This section introduces the applications of anion storage materials in dual-ion desalination cells.

The removal of $Cl^-$ and $Na^+$ ions is the main purpose of seawater desalination. Battery-type materials such as Ag, Bi, and BiOCl are commonly used as high-capacity anion storage materials to remove $Cl^-$ ions from seawater.[47, 84, 548-550] For instance, a flow dual-ion deionization cell consists of BiOCl negative electrode for $Cl^-$ removal, while pseudocapacitive $Na_{0.44}MnO_2$ positive electrode for $Na^+$ removal.[47] Along with a pair of ion exchange membranes, the deionization cell delivered a desalination capacity up to 68.5 mg $g^{-1}$ at 100 mA $g^{-1}$ at feed rate of 760 mg $L^{-1}$. Faradaic organic materials have been applied for anion removal of desalination cell.[48, 551] In a membrane-free desalination cell, poly (TEMPO methacrylate) radical polymer as the positive electrode was coupled with AC as the negative electrode with a mass ratio of 1: 2 (**Fig. 21a1**).[48] The poly (TEMPO methacrylate) electrode store $Cl^-$ ions, demonstrating a typical one-electron redox reaction via the oxidation of neutral nitroxide radical (**Fig. 21a2**). The $Cl^-$ storage capacity was 51 mAh $g^{-1}$ at 0.1 A $g^{-1}$ in 1 M NaCl solution. The

desalination cell delivered desalination capacities of 6.0, 15.8, and 20.9 mg $g^{-1}$ at 0.8, 1.0 and 1.2 V, respectively, in 250 ppm of NaCl solution (**Fig. 21a3**). Several transition metal oxides/hydroxides have been also used as anion removal materials of desalination cells.[552-555] Layered metal oxide (LMO) derived from LDH precursor could selectively capture anions owing to the unique interlayer structure. For instance, a NiCoAl-LMO/rGO composite was used to remove $F^-$ ions, while AC treated by nitric acid (H-AC) was applied for $Na^+$ removal.[552] The desalination capacity of H-AC//NiCoAl-LMO/rGO cell was 24.5 mg $g^{-1}$ at 1.4 V in 500 mg $L^{-1}$ NaF solution. The $Cl^-$ storing $Fe(CN)_6$-PSQ was applied for a desalination cell.[556] Combining with a cation storing nickel hexacyanoferrate, the $Fe(CN)_6$-PSQ could remove 164 mg $L^{-1}$ of $Cl^-$ from real sea water at $7.6\times10^{-8}$ mol $cm^{-2}$ of electrode surface coverage.

2D pseudocapacitive electrode materials such as molybdenum disulfide ($MoS_2$) and MXene have been investigated to remove both cations and anions from saline water.[49, 557-559] The $MoS_2$/CNT composite exhibited similar capacitance values of 200 F $g^{-1}$ and 210 F $g^{-1}$ during both positive and negative polarizations in 1 M NaCl electrolyte.[49]. Subsequently, a desalination cell could be fabricated by two $MoS_2$/CNT electrodes in a symmetric manner. At 0.8 V, the cell delivered desalination capacities of 10 and 25 mg $g^{-1}$ in 5 and 500 mM NaCl solutions, respectively. $Mo_{1.33}$C-MXene was also applied for both $Na^+$ and $Cl^-$ removals.[558] The desalination capacity of $Mo_{1.33}$C-MXene-based symmetric cell was 15 mg $g^{-1}$ in 600 mM NaCl solution at 0.8 V, along with 95% of charge efficiency.

The hybrids of anion capturing capacitive materials and cation capturing Faradaic materials such as polyimide, COF, $Ti_3C_2T_x$-MXene, $MoS_2$, $Na_2Ti_3O_7$, $Na_{0.44}MnO_2$, and $Na_3V_2(PO_4)_3$ have been developed. [560-568] Among them, a deionization cell was assembled using $Na_3V_2(PO_4)_3$@C (NVP@C) negative electrode for $Na^+$ capture and AC positive electrode covered by an anion exchange membrane for $Cl^-$ capture.[564] The cell showed a desalination capacity of 137.2 mg $g^{-1}$ and removal rate of 0.076 mg $g^{-1}$ $s^{-1}$ at 1.0 V in 0.1 M NaCl solution. To achieve a rapid ion removal, a high-rate Faradaic composite electrode of Prussian blue decorated PANI (PB/PANI) was developed.[560] The PB/PANI electrode in $Na_2SO_4$ electrolyte revealed two pairs of redox peaks and rapid $Na^+$-storage capability (**Fig. 21b2**). The hybrid desalination cell is constructed by PB/PANI negative electrode and AC positive electrode, along with ion exchange membranes in front of them (**Fig. 21b1**). In 500 mg $L^{-1}$ of NaCl solution, the cell delivered a desalination capacity of 133.3 mg $g^{-1}$ at 100 mA $g^{-1}$, corresponding to a removal rate of 0.03 mg $g^{-1}$ $s^{-1}$. Moreover, a capacity of 25 mg $g^{-1}$ was retained at a high removal rate of 1.67 mg $g^{-1}$ $s^{-1}$ (**Fig. 21b3**). The cell also achieved the negligible capacity fading over 250 cycles at 500 mA $g^{-1}$.

**Salinity gradient energy generation.** Salinity gradient (SG) energy, which is also known as osmotic power or blue energy, is entropically generated when two solutions with different concentrations, such as freshwater and seawater, are mixed.[569-571] The large-scale SG energy generated when river water flows into the sea is regarded as an important renewable source that can be harvested. As the reverse process of desalination, capacitive mixing (CapMix) and battery mixing (BattMix) technologies have been investigated for the recovery of SG energy. CapMix employs two porous capacitive electrodes,[570] while BattMix utilizes battery-type electrodes instead of capacitive electrodes.[571] In both CapMix and BattMix, electricity is produced cyclically by alternating the salt concentrations to convert SG energy into usable power. As shown in the energy recovery mechanism of CapMix in **Fig. 21c1**,[570] four steps are generally involved in each cycle. The cell is first charged with an external electric potential in saline water (phase A). Then, the circuit is opened, and the saline water is replaced with fresh water, resulting in an increase in the cell voltage due to the reduced salt concentration (phase B). When the circuit is closed, mixing takes place to discharge the cell (phase C). The voltage increases, because of which the energy produced in discharge is higher than the energy required for charging, thereby generating net energy. Finally, the cycle is completed by replacing fresh water with saline water in an open circuit (phase D). **Fig. 21c2** shows the corresponding changes in voltage and current during the cycling process of CapMix. The amount of energy harvested from a single cycle is equal to the designated area of the cell voltage versus charge curve (**Fig. 21c3**).

An asymmetric CapMix with different electrodes was developed to improve the energy-recovery performance. The positively charged quaternized poly(4-vinylpyridine) coated AC and negatively charged nitric acid oxidized AC were assembled into an asymmetric CapMix.[572] When NaCl solutions are switched in 20 mM and 500 mM, the CapMix delivered a voltage rise of 150 mV and an average power density of 65.0 mW $m^{-2}$ without external power supplies and membranes. A hybrid CapMix cell was configured replacing either one of two capacitive electrodes by a Faradaic electrode.[50, 573] In a hybrid CapMix, a pseudocapacitive sodium manganese oxide (NMO) and an AC covered with anion exchange membrane were used for $Na^+$ and $Cl^-$ storage, respectively.[50] Switching in 600 mM and 10 mM NaCl solutions, the hybrid CapMix extracted an energy density up to 130 J $m^{-2}$, along with an average power density of 97 mW $m^{-2}$. Even being evaluated in real river water and seawater containing multiple ions, the hybrid system achieves an energy density of 30 J $m^{-2}$. BattMix consisting of two Faradaic electrodes was also reported.[571, 574] The BattMix based on Ag/AgCl and NMO electrodes was tested in 600 mM and 32 mM NaCl solutions, recovering the net energy of 0.11 kWh $m^{-3}$ at the first cycle [574] In addition, BiOCl and organic polypyrrole for $Cl^-$-storage were applied for BattMix by coupling with $Na^+$-storage battery-type materials.[575, 576]

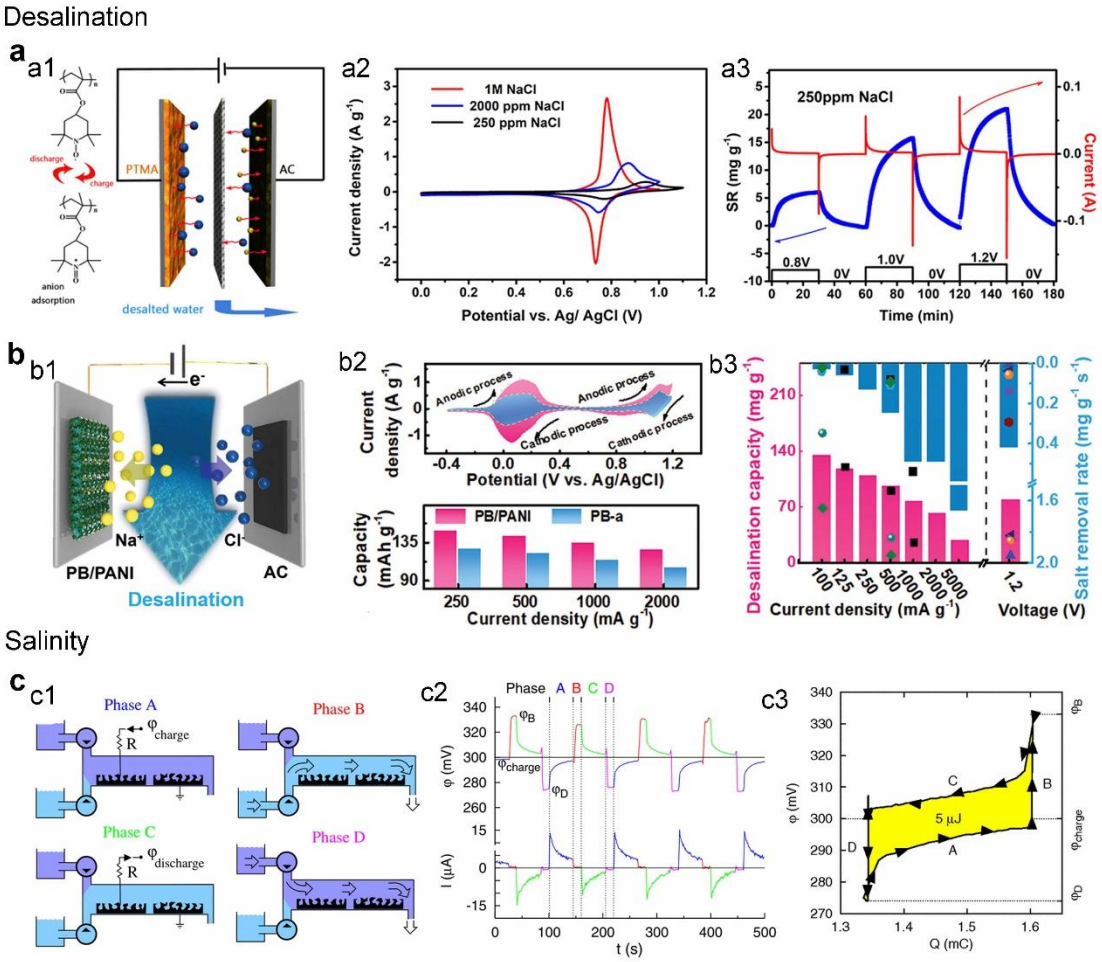


**Fig. 21** Desalination and salinity cells (**a**) Desalination cell configured by PTMA and AC electrodes in NaCl solution. (a1) Schematic illustration of PTMA//AC cell, (a2) CV curves of PTMA electrode in different-concentrated NaCl solutions, (a3) desalination performances of PTMA//AC cell at a different voltage in 250 ppm NaCl solution. Reproduced with permission from ref. [48], Copyright 2020 Elsevier. (**b**) Desalination cell configured by AC and PB/PAIN electrodes in NaCl solution. (b1) Schematic illustration of AC//PB/PAIN cell, (b2) CV curve and specific capacity of PB/PAIN electrode $Na_2SO_4$ electrolyte, (b3) desalination performances of AC//PB/PAIN cell at different current densities/voltage in 500 mg $L^{-1}$ NaCl solution. Reproduced with permission from ref. [560], Copyright 2020 Wiley-VCH. (**c**) Cycle for extracting salinity gradient energy. (c1) Schematic illustration of the four-step CapMix cycle, (c2) cell voltage and current during the CapMix cycle, (c3) cell voltage versus charge curve representing energy cycle of CapMix. Reproduced with permission from ref. [570], Copyright 2009 American Physical Society.

## 5. Conclusion and perspective

In this review, we focused on the thermodynamic and kinetic aspects, energy storage mechanisms, and associated anion carriers and anion storage material interfaces for the four types of electrochemical and hybrid capacitors. Anion storage materials include EDLC-type carbon materials storing various anion carriers, Faradaic anion storage materials storing $OH^-$ ions (functionalized carbons, transition metal hydroxides, oxides, sulfides, phosphides, selenides, nitrides, oxygen-anion intercalated perovskite oxides, metal organic frameworks, and their derivatives), Faradaic anion storage materials storing large-sized polyatomic anions (graphite, p-type organic materials, metal organic, and covalent organic frameworks), and Faradaic anion storage materials storing halide ions (metal halides/oxyhalides). Moreover, the deterministic factors for electrochemical performance and functionalities to facilitate the rational design of anion storage materials in specific applications were discussed.

Despite recent significant advances in anion storage materials, their applications in electrochemical capacitors and battery-capacitor hybrid cells lag behind the battery fields. More importantly, there remain fundamental and technical challenges in the application of anion storage materials for electrochemical and hybrid capacitors. (1) Most anion storage materials have been investigated for the storage of $OH^-$ in alkaline aqueous electrolytes for electrochemical and hybrid capacitors. Despite the high capacity and rate capability of $OH^-$ storage materials (e.g., Ni,Co-hydroxides/oxides, MOFs, and their derivatives), the low cell voltage due to the narrow ESW of alkaline aqueous electrolytes limits the energy density of full

cells. To increase the cell voltage, emerging anion storage materials should be explored in organic and IL electrolytes. (2) Although significant advances in graphite and p-type organics storing $PF_6^-$, $ClO_4^-$, $FSI^-$, and $AlCl_4^-$ have been achieved in organic and IL electrolytes, their specific capacities (nearly 100 mAh $g^{-1}$), Coulombic efficiency, and cycling stability need to be improved. Thus, the available storage sites, electronic/ionic transport pathways, and structural stability of anion storage materials should be rationally designed. Considering the complexity and trade-off of the required properties and the intrinsic limitation of each anion storage material, individual anion storage materials cannot meet all of the requirements. In addition to the engineering of existing materials and the development of new anion storage materials, we propose the design of hybrid materials with multiple components and hierarchical structures. (3) Electrolyte formulations with a wide ESW that match given anion storage materials should be developed for long cyclic stability and high cell voltage. Moreover, the associated CEI with a positive anion storage electrode needs to be investigated to achieve kinetic stability and high interfacial ionic conductivity. Although highly concentrated electrolytes can be used to obtain a wide ESW, the power performance is degraded owing to sluggish ion diffusion in electrolytes, and the potential of anion storage materials governed by the Nernst equation is lowered. To resolve this bottleneck, new combinations of salts, solvents, and additives should be investigated, and the formulation and concentration of electrolytes should be optimized.

In addition to the materials aspect, (4) a fundamental understanding of anion storage has yet to be elusive. Examples include the correlation of oxygen vacancy with electrochemical performance of metal oxides/hydroxides, the origin of the abnormal rate capability of anion intercalation graphite, and the exact role and detailed chemistry of CEI upon anion storage, which are completely different from the cases of storing alkali metal cations. A thorough investigation of anion storage mechanisms, structure/property correlations, reaction kinetics, and electrode degradation would be helpful for offering guidance to overcome current bottlenecks and to develop new storage materials. In addition to commonly used *ex situ* and *in situ* methods, more advanced operando analytical techniques on real-life cell levels, combined with computational analyses, are recommended to achieve a fundamental understanding.

(5) Electrode fabrication and cell engineering are as significant as the development of emerging anion storage materials and their fundamental understanding for practical applications. First, a high mass loading needs to be considered for high-energy electrode applications. The electrochemical performance of anion storage materials is generally reported on a laboratory scale using electrodes with a few milligrams of active materials, which should be increased up to the mass loadings of commercial electrodes, higher than 10 mg $cm^{-2}$. At high mass loadings, the increased electrode thickness (particularly thicker for low-density materials such as porous carbon (<0.5 g $cm^{-3}$) and p-type organics (1–2 g $cm^{-3}$)) lead to long distances for charge transfer and mass transport, thus affecting the capacity and rate performance. To overcome the trade-offs between mass loading and electrochemical performance, the electrode formulation (with optimum binder) and fabrication processes need to be further explored. Second, more requirements should be satisfied when anion storage materials are used for functional applications, such as large-scale patterning and integration techniques for microcapacitors, superior mechanical stability for flexible capacitors, and rapid mass transport for flow-type desalination and salinity cells. Third, a large amount of electrolyte is needed in dual-ion cells when an undesirable irreversible reaction occurs and the transference number is small. For dual-ion hybrid capacitors, electrolytes provide both anion and cation carriers, which act as active species. However, the amount of electrolyte should be minimized to achieve a high energy density at the cell level without deteriorating electrochemical performance. In addition, the weights of other cell components, such as the separator and current collectors, also need to be minimized. Fourth, the balancing of the two electrodes is a crucial part of cell operation for hybrid capacitors configured with capacitive and battery-type electrodes. To date, most capacitive anion storage materials have been developed from EDLC-type porous carbons rather than Faradaic electrodes. However, the considerable gap between EDLC-type and battery-type electrodes makes it difficult to balance both the capacity and rate of the two electrodes at a given current density and cycle. For instance, when the capacity is balanced using several times the mass of EDLC-type electrode compared to the battery-type electrode at low scan rates, it will be highly unbalanced at high rates because of the varied rate capacities. To circumvent this issue, novel methods must be used to construct asymmetric hybrid cells by pairing new pseudocapacitive or high-rate battery-type materials with similar capacity and rate performance.

Overall, the development of anion storage materials is more challenging because of the larger size and less stability of anion carriers compared to metal cations. Nonetheless, anion storage technology is complementary to existing cation storage technology for the realization of dual-ion cells more importantly for electrochemical capacitors because emerging electrode materials can be designed for high-energy dual-ion and whole-anion battery-capacitor hybrid devices, as well as for functional applications such as electrical vehicles, large-scale storage, miniaturized, wearable and integrated electronics, desalination, and salinity cells. Therefore, this review offers rational guidelines for the design of emerging anion storage materials that overcome the technical limitations of existing electrochemical and hybrid capacitors, which will help us expand their fields of application to new concepts of functionality-oriented energy storage devices.

## Conflicts of interest

There are no conflicts to declare.

## Acknowledgements

Q. Dou, H. Yuan, K. H. Shin, and H. S. Park acknowledge financial support from a National Research Foundation of Korea (NRF) grant funded by the Korea government (MSIT) (NRF-2020R1A3B2079803), Republic of Korea. N. Wu and Y. Tang gratefully acknowledge the financial support from National Natural Science Foundation of China (51822210). D. Mitlin was supported by the National Science Foundation, Civil, Mechanical and Manufacturing Innovation (CMMI), Award Number 1911905.

## References

1. B. Dunn, H. Kamath and J.-M. Tarascon, *Science*, 2011, **334**, 928-935.
2. M. Winter, B. Barnett and K. Xu, *Chem. Rev.*, 2018, **118**, 11433-11456.
3. P. Simon, Y. Gogotsi and B. Dunn, *Science*, 2014, **343**, 1210-1211.
4. B. E. Conway, *J. Electrochem. Soc.*, 1991, **138**, 1539-1548.
5. J. R. Miller and P. Simon, *Science*, 2008, **321**, 651-652.
6. B. E. Conway, *Electrochemical Supercapacitors: Scientific Fundamentals and Technological Applications*, Springer, New York, 1999.
7. P. Simon and Y. Gogotsi, *Nat. Mater.*, 2008, **7**, 845-854.
8. H. Shao, Y.-C. Wu, Z. Lin, P.-L. Taberna and P. Simon, *Chem. Soc. Rev.*, 2020, **49**, 3005-3039.
9. N.-S. Choi, Z. Chen, S. A. Freunberger, X. Ji, Y.-K. Sun, K. Amine, G. Yushin, L. F. Nazar, J. Cho and P. G. Bruce, *Angew. Chem., Int. Ed.*, 2012, **51**, 9994-10024.
10. P. Simon and Y. Gogotsi, *Nat. Mater.*, 2020, **19**, 1151-1163.
11. V. Augustyn, P. Simon and B. Dunn, *Energy Environ. Sci.*, 2014, **7**, 1597-1614.
12. T. Brousse, D. Bélanger and J. W. Long, *J. Electrochem. Soc.*, 2015, **162**, A5185-A5189.
13. C. Choi, D. S. Ashby, D. M. Butts, R. H. DeBlock, Q. Wei, J. Lau and B. Dunn, *Nat. Rev. Mater.*, 2020, **5**, 5-19.
14. V. Augustyn, J. Come, M. A. Lowe, J. W. Kim, P.-L. Taberna, S. H. Tolbert, H. D. Abruña, P. Simon and B. Dunn, *Nat. Mater.*, 2013, **12**, 518-522.
15. T. Brezesinski, J. Wang, S. H. Tolbert and B. Dunn, *Nat. Mater.*, 2010, **9**, 146-151.
16. X. Yu, S. Yun, J. S. Yeon, P. Bhattacharya, L. Wang, S. W. Lee, X. Hu and H. S. Park, *Adv. Energy Mater.*, 2018, **8**, 1702930.
17. Q. Mahmood, S. K. Park, K. D. Kwon, S.-J. Chang, J.-Y. Hong, G. Shen, Y. M. Jung, T. J. Park, S. W. Khang, W. S. Kim, J. Kong and H. S. Park, *Adv. Energy Mater.*, 2016, **6**, 1501115.
18. P. Nakhanivej, X. Yu, S. K. Park, S. Kim, J.-Y. Hong, H. J. Kim, W. Lee, J. Y. Hwang, J. E. Yang, C. Wolverton, J. Kong, M. Chhowalla and H. S. Park, *Nat. Mater.*, 2019, **18**, 156-162.
19. Y. Shao, M. F. El-Kady, J. Sun, Y. Li, Q. Zhang, M. Zhu, H. Wang, B. Dunn and R. B. Kaner, *Chem. Rev.*, 2018, **118**, 9233-9280.
20. W. G. Pell and B. E. Conway, *J. Power Sources*, 2004, **136**, 334-345.
21. J. Ding, W. Hu, E. Paek and D. Mitlin, *Chem. Rev.*, 2018, **118**, 6457-6498.
22. D. P. Dubal, O. Ayyad, V. Ruiz and P. Gómez-Romero, *Chem. Soc. Rev.*, 2015, **44**, 1777-1790.
23. H. Wang, C. Zhu, D. Chao, Q. Yan and H. J. Fan, *Adv. Mater.*, 2017, **29**, 1702093.
24. B. Li, J. Zheng, H. Zhang, L. Jin, D. Yang, H. Lv, C. Shen, A. Shellikeri, Y. Zheng, R. Gong, J. P. Zheng and C. Zhang, *Adv. Mater.*, 2018, **30**, 1705670.
25. J. Ding, H. Wang, Z. Li, K. Cui, D. Karpuzov, X. Tan, A. Kohandehghan and D. Mitlin, *Energy Environ. Sci.*, 2015, **8**, 941-955.
26. H. Wang, D. Mitlin, J. Ding, Z. Li and K. Cui, *J. Mater. Chem. A*, 2016, **4**, 5149-5158.
27. J. S. Dunning, W. H. Tiedemann, L. Hsueh and D. N. Bennion, *J. Electrochem. Soc.*, 1971, **118**, 1886-1890.
28. J. Besenhard and H. P. Fritz, *Zeitschrift für Naturforschung B*, 1971, **26**, 1225-1229.
29. X. Zhou, Q. Liu, C. Jiang, B. Ji, X. Ji, Y. Tang and H.-M. Cheng, *Angew. Chem., Int. Ed.*, 2020, **59**, 3802-3832.
30. T. Placke, A. Heckmann, R. Schmuch, P. Meister, K. Beltrop and M. Winter, *Joule*, 2018, **2**, 2528-2550.
31. Y. Lu and J. Chen, *Nat. Rev. Chem.*, 2020, **4**, 127-142.
32. S. Lee, G. Kwon, K. Ku, K. Yoon, S.-K. Jung, H.-D. Lim and K. Kang, *Adv. Mater.*, 2018, **30**, 1704682.
33. T. Nguyen and M. d. F. Montemor, *Adv. Sci.*, 2019, **6**, 1801797.
34. M. Huang, M. Li, C. Niu, Q. Li and L. Mai, *Adv. Funct. Mater.*, 2019, **29**, 1807847.
35. X. Shi, W. Zhang, J. Wang, W. Zheng, K. Huang, H. Zhang, S. Feng and H. Chen, *Adv. Energy Mater.*, 2016, **6**, 1601378.
36. J. Lang, J. Li, F. Zhang, X. Ding, J. A. Zapien and Y. Tang, *Batteries Supercaps*, 2019, **2**, 440-447.
37. T. Vignal, P. Banet, M. Pinault, R. Lafourcade, J. Descarpentries, L. Darchy, H. Hauf, C. Reynaud, M. Mayne-L'Hermite and P.-H. Aubert, *Electrochim. Acta*, 2020, **350**, 136377.
38. H. Wang, H. S. Casalongue, Y. Liang and H. Dai, *J. Am. Chem. Soc.*, 2010, **132**, 7472-7477.
39. J. T. Mefford, W. G. Hardin, S. Dai, K. P. Johnston and K. J. Stevenson, *Nat. Mater.*, 2014, **13**, 726-732.
40. T. Ling, P. Da, X. Zheng, B. Ge, Z. Hu, M. Wu, X.-W. Du, W.-B. Hu, M. Jaroniec and S.-Z. Qiao, *Sci. Adv.*, 2018, **4**, eaau6261.
41. X. Chen, W.-Y. Tung, K. Yang, Y.-M. Chen, K. Liu, C.-F. Cheng and Y. Zhu, *ACS Appl. Polym. Mater.*, 2019, **1**, 1634-1640.
42. K. Robert, D. Stiévenard, D. Deresmes, C. Douard, A. Iadecola, D. Troadec, P. Simon, N. Nuns, M. Marinova, M. Huvé, P. Roussel, T. Brousse and C. Lethien, *Energy Environ. Sci.*, 2020, **13**, 949-957.
43. Q. Jiang, N. Kurra, C. Xia and H. N. Alshareef, *Adv. Energy Mater.*, 2017, **7**, 1601257.
44. M. S. Javed, S. S. A. Shah, T. Najam, S. H. Siyal, S. Hussain, M. Saleem, Z. Zhao and W. Mai, *Nano Energy*, 2020, **77**, 105276.
45. X. Lu, G. Wang, T. Zhai, M. Yu, S. Xie, Y. Ling, C. Liang, Y. Tong and Y. Li, *Nano Lett.*, 2012, **12**, 5376-5381.
46. Q. Li, Y. Chen, J. Zhang, W. Tian, L. Wang, Z. Ren, X. Ren, X. Li, B. Gao, X. Peng, P. K. Chu and K. Huo, *Nano Energy*, 2018, **51**, 128-136.
47. F. Chen, Y. Huang, L. Guo, L. Sun, Y. Wang and H. Y. Yang, *Energy Environ. Sci.*, 2017, **10**, 2081-2089.
48. Y. Li, Z. Ding, J. Li, K. Wang, T. Lu and L. Pan, *Desalination*, 2020, **481**, 114379.
49. P. Srimuk, J. Lee, S. Fleischmann, S. Choudhury, N. Jäckel, M. Zeiger, C. Kim, M. Aslan and V. Presser, *J. Mater. Chem. A*, 2017, **5**, 15640-15649.

50. J. Lee, H. Yoon, J. Lee, T. Kim and J. Yoon, *ChemSusChem*, 2017, **10**, 1600-1606.
51. J.-S. Wei, C. Ding, P. Zhang, H. Ding, X.-Q. Niu, Y.-Y. Ma, C. Li, Y.-G. Wang and H.-M. Xiong, *Adv. Mater.*, 2019, **31**, 1806197.
52. W. Guo, C. Yu, S. Li, X. Song, H. Huang, X. Han, Z. Wang, Z. Liu, J. Yu, X. Tan and J. Qiu, *Adv. Mater.*, 2019, **31**, 1901241.
53. Z. Li, S. Gadipelli, H. Li, C. A. Howard, D. J. L. Brett, P. R. Shearing, Z. Guo, I. P. Parkin and F. Li, *Nat. Energy*, 2020, **5**, 160-168.
54. J. Han, L. L. Zhang, S. Lee, J. Oh, K.-S. Lee, J. R. Potts, J. Ji, X. Zhao, R. S. Ruoff and S. Park, *ACS Nano*, 2013, **7**, 19-26.
55. H. Jin, X. Feng, J. Li, M. Li, Y. Xia, Y. Yuan, C. Yang, B. Dai, Z. Lin, J. Wang, J. Lu and S. Wang, *Angew. Chem., Int. Ed.*, 2019, **58**, 2397-2401.
56. G. Wang, M. Yu, J. Wang, D. Li, D. Tan, M. Löffler, X. Zhuang, K. Müllen and X. Feng, *Adv. Mater.*, 2018, **30**, 1800533.
57. S. Rothermel, P. Meister, G. Schmuelling, O. Fromm, H.-W. Meyer, S. Nowak, M. Winter and T. Placke, *Energy Environ. Sci.*, 2014, **7**, 3412-3423.
58. L. Cao, F. Xu, Y.-Y. Liang and H.-L. Li, *Adv. Mater.*, 2004, **16**, 1853-1857.
59. H. Gao, S. Xin and J. B. Goodenough, *Chem*, 2017, **3**, 26-28.
60. Y. Zhang, Y. Hu, Z. Wang, T. Lin, X. Zhu, B. Luo, H. Hu, W. Xing, Z. Yan and L. Wang, *Adv. Funct. Mater.*, 2020, **30**, 2004172.
61. T. Zhai, L. Wan, S. Sun, Q. Chen, J. Sun, Q. Xia and H. Xia, *Adv. Mater.*, 2017, **29**, 1604167.
62. K. H. Oh, G. S. Gund and H. S. Park, *J. Mater. Chem. A*, 2018, **6**, 22106-22114.
63. D. Lei, D.-C. Lee, E. Zhao, A. Magasinski, H.-R. Jung, G. Berdichevsky, D. Steingart and G. Yushin, *Nano Energy*, 2018, **48**, 170-179.
64. J. Yang, Q. Zhang, Z. Wang, Z. Wang, L. Kang, M. Qi, M. Chen, W. Liu, W. Gong, W. Lu, P. P. Shum and L. Wei, *Adv. Energy Mater.*, 2020, **10**, 2001064.
65. H. Wang, L. Zhang, X. Tan, C. M. B. Holt, B. Zahiri, B. C. Olsen and D. Mitlin, *J. Phys. Chem. C*, 2011, **115**, 17599-17605.
66. L. Zhang, C. M. B. Holt, E. J. Luber, B. C. Olsen, H. Wang, M. Danaie, X. Cui, X. Tan, V. W. Lui, W. P. Kalisvaart and D. Mitlin, *J. Phys. Chem. C*, 2011, **115**, 24381-24393.
67. D. Choi, G. E. Blomgren and P. N. Kumta, *Adv. Mater.*, 2006, **18**, 1178-1182.
68. X. Liu, W. Zang, C. Guan, L. Zhang, Y. Qian, A. M. Elshahawy, D. Zhao, S. J. Pennycook and J. Wang, *ACS Energy Lett.*, 2018, **3**, 2462-2469.
69. F. Lu, M. Zhou, W. Li, Q. Weng, C. Li, Y. Xue, X. Jiang, X. Zeng, Y. Bando and D. Golberg, *Nano Energy*, 2016, **26**, 313-323.
70. J. Yang, C. Yu, X. Fan, S. Liang, S. Li, H. Huang, Z. Ling, C. Hao and J. Qiu, *Energy Environ. Sci.*, 2016, **9**, 1299-1307.
71. B. Y. Guan, L. Yu, X. Wang, S. Song and X. W. Lou, *Adv. Mater.*, 2017, **29**, 1605051.
72. J. Li, Z. Liu, Q. Zhang, Y. Cheng, B. Zhao, S. Dai, H.-H. Wu, K. Zhang, D. Ding, Y. Wu, M. Liu and M.-S. Wang, *Nano Energy*, 2019, **57**, 22-33.
73. Y. Lin, K. Sun, S. Liu, X. Chen, Y. Cheng, W.-C. Cheong, Z. Chen, L. Zheng, J. Zhang, X. Li, Y. Pan and C. Chen, *Adv. Energy Mater.*, 2019, **9**, 1901213.
74. L. Hou, Y. Shi, C. Wu, Y. Zhang, Y. Ma, X. Sun, J. Sun, X. Zhang and C. Yuan, *Adv. Funct. Mater.*, 2018, **28**, 1705921.
75. Y. Tang, X. Li, H. Lv, D. Xie, W. Wang, C. Zhi and H. Li, *Adv. Energy Mater.*, 2020, **10**, 2000892.
76. S. Li, Y. Zhang, N. Liu, C. Yu, S.-J. Lee, S. Zhou, R. Fu, J. Yang, W. Guo, H. Huang, J.-S. Lee, C. Wang, T. R. Kim, D. Nordlund, P. Pianetta, X. Du, J. Zhao, Y. Liu and J. Qiu, *Joule*, 2020, **4**, 673-687.
77. Q. Zhang, Z. Liu, B. Zhao, Y. Cheng, L. Zhang, H.-H. Wu, M.-S. Wang, S. Dai, K. Zhang, D. Ding, Y. Wu and M. Liu, *Energy Storage Mater.*, 2019, **16**, 632-645.
78. X. Zhao, Z. Zhao-Karger, M. Fichtner and X. Shen, *Angew. Chem., Int. Ed.*, 2020, **59**, 5902-5949.
79. D. T. Thieu, M. H. Fawey, H. Bhatia, T. Diemant, V. S. K. Chakravadhanula, R. J. Behm, C. Kübel and M. Fichtner, *Adv. Funct. Mater.*, 2017, **27**, 1701051.
80. T. Yu, Q. Li, X. Zhao, H. Xia, L. Ma, J. Wang, Y. S. Meng and X. Shen, *ACS Energy Lett.*, 2017, **2**, 2341-2348.
81. P. Gao, M. A. Reddy, X. Mu, T. Diemant, L. Zhang, Z. Zhao-Karger, V. S. K. Chakravadhanula, O. Clemens, R. J. Behm and M. Fichtner, *Angew. Chem., Int. Ed.*, 2016, **55**, 4285-4290.
82. L. Zhu, Y. Liu, C. Su, W. Zhou, M. Liu and Z. Shao, *Angew. Chem., Int. Ed.*, 2016, **55**, 9576-9579.
83. C. T. Alexander, J. T. Mefford, J. Saunders, R. P. Forslund, K. P. Johnston and K. J. Stevenson, *ACS Appl. Mater. Interfaces*, 2019, **11**, 5084-5094.
84. D.-H. Nam and K.-S. Choi, *J. Am. Chem. Soc.*, 2017, **139**, 11055-11063.
85. Y. Zeng, Z. Lin, Z. Wang, M. Wu, Y. Tong and X. Lu, *Adv. Mater.*, 2018, **30**, 1707290.
86. G. Zan, T. Wu, P. Hu, Y. Zhou, S. Zhao, S. Xu, J. Chen, Y. Cui and Q. Wu, *Energy Storage Mater.*, 2020, **28**, 82-90.
87. G. J. May, A. Davidson and B. Monahov, *J. Energy Storage*, 2018, **15**, 145-157.
88. A. Banerjee, M. K. Ravikumar, A. Jalajakshi, P. S. Kumar, S. A. Gaffoor and A. K. Shukla, *J. Chem. Sci.*, 2012, **124**, 747-762.
89. R. Shapira, G. D. Nessim, T. Zimrin and D. Aurbach, *Energy Environ. Sci.*, 2013, **6**, 587-594.
90. I. A. Rodríguez-Pérez, Z. Jian, P. K. Waldenmaier, J. W. Palmisano, R. S. Chandrabose, X. Wang, M. M. Lerner, R. G. Carter and X. Ji, *ACS Energy Lett.*, 2016, **1**, 719-723.
91. T. Sun, J. Xie, W. Guo, D.-S. Li and Q. Zhang, *Adv. Energy Mater.*, 2020, **10**, 1904199.
92. D. Sheberla, J. C. Bachman, J. S. Elias, C.-J. Sun, Y. Shao-Horn and M. Dincă, *Nat. Mater.*, 2017, **16**, 220-224.
93. D. Feng, T. Lei, M. R. Lukatskaya, J. Park, Z. Huang, M. Lee, L. Shaw, S. Chen, A. A. Yakovenko, A. Kulkarni, J. Xiao, K. Fredrickson, J. B. Tok, X. Zou, Y. Cui and Z. Bao, *Nat. Energy*, 2018, **3**, 30-36.
94. M. L. Aubrey and J. R. Long, *J. Am. Chem. Soc.*, 2015, **137**, 13594-13602.
95. K. Sakaushi, E. Hosono, G. Nickerl, T. Gemming, H. Zhou, S. Kaskel and J. Eckert, *Nat. Commun.*, 2013, **4**, 1485.
96. Z. Zhang, X. Hu, Y. Zhou, S. Wang, L. Yao, H. Pan, C.-Y. Su, F. Chen and X. Hou, *J. Mater. Chem. A*, 2018, **6**, 8244-8250.
97. H. Jiang, Z. Wei, L. Ma, Y. Yuan, J. J. Hong, X. Wu, D. P. Leonard, J. Holoubek, J. J. Razink, W. F. Stickle, F. Du, T. Wu, J. Lu and X. Ji, *Angew. Chem., Int. Ed.*, 2019, **58**, 5286-5291.
98. Y. Zhang, Y. An, B. Yin, J. Jiang, S. Dong, H. Dou and X. Zhang, *J. Mater. Chem. A*, 2019, **7**, 11314-11320.
99. K. Lee, I. E. Serdiuk, G. Kwon, D. J. Min, K. Kang, S. Y. Park and J. E. Kwon, *Energy Environ. Sci.*, 2020, **13**, 4142-4156.
100. J. Kim, M. S. Choi, K. H. Shin, M. Kota, Y. Kang, S. Lee, J. Y. Lee and H. S. Park, *Adv. Mater.*, 2019, **31**, 1803444.

101. P. Srimuk, X. Su, J. Yoon, D. Aurbach and V. Presser, *Nat. Rev. Mater.*, 2020, **5**, 517-538.
102. J. Kim, J. Kim, J. H. Kim and H. S. Park, *Chem. Eng. J.*, 2020, **382**, 122996.
103. W. Liu, P. Liu and D. Mitlin, *Chem. Soc. Rev.*, 2020, **49**, 7284-7300.
104. M.-C. Lin, M. Gong, B. Lu, Y. Wu, D.-Y. Wang, M. Guan, M. Angell, C. Chen, J. Yang, B.-J. Hwang and H. Dai, *Nature*, 2015, **520**, 324-328.
105. C. Jiang, Y. Fang, J. Lang and Y. Tang, *Adv. Energy Mater.*, 2017, **7**, 1700913.
106. M. Ue, M. Takeda, M. Takehara and S. Mori, *J. Electrochem. Soc.*, 1997, **144**, 2684-2688.
107. M. Ue, A. Murakami and S. Nakamura, *J. Electrochem. Soc.*, 2002, **149**, A1572.
108. D. Guyomard and J. M. Tarascon, *J. Power Sources*, 1995, **54**, 92-98.
109. X. Zhang, R. Kostecki, T. J. Richardson, J. K. Pugh and P. N. Ross, *J. Electrochem. Soc.*, 2001, **148**, A1341.
110. M. Egashira, H. Takahashi, S. Okada and J.-i. Yamaki, *J. Power Sources*, 2001, **92**, 267-271.
111. B. Garcia, S. Lavallée, G. Perron, C. Michot and M. Armand, *Electrochim. Acta*, 2004, **49**, 4583-4588.
112. L. Xiang, X. Ou, X. Wang, Z. Zhou, X. Li and Y. Tang, *Angew. Chem., Int. Ed.*, 2020, **59**, 17924-17930.
113. M. Zhou, P. Bai, X. Ji, J. Yang, C. Wang and Y. Xu, *Adv. Mater.*, 2021, DOI: 10.1002/adma.202003741.
114. X. Wu, Y. Xu, C. Zhang, D. P. Leonard, A. Markir, J. Lu and X. Ji, *J. Am. Chem. Soc.*, 2019, **141**, 6338-6344.
115. I. A. Rodríguez-Pérez, L. Zhang, D. P. Leonard and X. Ji, *Electrochem. Commun.*, 2019, **109**, 106599.
116. S. Lee, K. Lee, K. Ku, J. Hong, S. Y. Park, J. E. Kwon and K. Kang, *Adv. Energy Mater.*, 2020, **10**, 2001635.
117. B. You and Y. Sun, *Acc. Chem. Res.*, 2018, **51**, 1571-1580.
118. M. Yu, Y. Lu, H. Zheng and X. Lu, *Chem. - Eur. J.*, 2018, **24**, 3639-3649.
119. Z. Liu, Y. Huang, Y. Huang, Q. Yang, X. Li, Z. Huang and C. Zhi, *Chem. Soc. Rev.*, 2020, **49**, 180-232.
120. D. Chao, W. Zhou, F. Xie, C. Ye, H. Li, M. Jaroniec and S.-Z. Qiao, *Sci. Adv.*, 2020, **6**, eaba4098.
121. L. Suo, O. Borodin, T. Gao, M. Olguin, J. Ho, X. Fan, C. Luo, C. Wang and K. Xu, *Science*, 2015, **350**, 938-943.
122. Y. Yamada, K. Usui, K. Sodeyama, S. Ko, Y. Tateyama and A. Yamada, *Nat. Energy*, 2016, **1**, 16129.
123. M. P. Bichat, E. Raymundo-Piñero and F. Béguin, *Carbon*, 2010, **48**, 4351-4361.
124. J. Pokrzywinski, J. K. Keum, R. E. Ruther, E. C. Self, M. Chi, H. Meyer Iii, K. C. Littrell, D. Aulakh, S. Marble, J. Ding, M. Wriedt, J. Nanda and D. Mitlin, *J. Mater. Chem. A*, 2017, **5**, 13511-13525.
125. L. Fan, H. Lu and J. Leng, *Electrochim. Acta*, 2015, **165**, 22-28.
126. Q. Gao, L. Demarconnay, E. Raymundo-Piñero and F. Béguin, *Energy Environ. Sci.*, 2012, **5**, 9611-9617.
127. C. Zhong, Y. Deng, W. Hu, J. Qiao, L. Zhang and J. Zhang, *Chem. Soc. Rev.*, 2015, **44**, 7484-7539.
128. R.-S. Kühnel, D. Reber and C. Battaglia, *ACS Energy Lett.*, 2017, **2**, 2005-2006.
129. L. Suo, O. Borodin, Y. Wang, X. Rong, W. Sun, X. Fan, S. Xu, M. A. Schroeder, A. V. Cresce, F. Wang, C. Yang, Y.-S. Hu, K. Xu and C. Wang, *Adv. Energy Mater.*, 2017, **7**, 1701189.
130. Q. Guo, K.-i. Kim, H. Jiang, L. Zhang, C. Zhang, D. Yu, Q. Ni, X. Chang, T. Chen, H. Xia and X. Ji, *Adv. Funct. Mater.*, 2020, **30**, 2002825.
131. Q. Dou, S. Lei, D.-W. Wang, Q. Zhang, D. Xiao, H. Guo, A. Wang, H. Yang, Y. Li, S. Shi and X. Yan, *Energy Environ. Sci.*, 2018, **11**, 3212-3219.
132. Q. Dou, Y. Lu, L. Su, X. Zhang, S. Lei, X. Bu, L. Liu, D. Xiao, J. Chen, S. Shi and X. Yan, *Energy Storage Mater.*, 2019, **23**, 603-609.
133. F. Wang, O. Borodin, M. S. Ding, M. Gobet, J. Vatamanu, X. Fan, T. Gao, N. Eidson, Y. Liang, W. Sun, S. Greenbaum, K. Xu and C. Wang, *Joule*, 2018, **2**, 927-937.
134. X. Dong, H. Yu, Y. Ma, J. L. Bao, D. G. Truhlar, Y. Wang and Y. Xia, *Chem. - Eur. J.*, 2017, **23**, 2560-2565.
135. Y. Kondo, Y. Miyahara, T. Fukutsuka, K. Miyazaki and T. Abe, *Electrochem. Commun.*, 2019, **100**, 26-29.
136. H. Zhang, X. Liu, B. Qin and S. Passerini, *J. Power Sources*, 2020, **449**, 227594.
137. K. Xu, *Chem. Rev.*, 2014, **114**, 11503-11618.
138. K. Xu, *Chem. Rev.*, 2004, **104**, 4303-4418.
139. P. Ruschhaupt, S. Pohlmann, A. Varzi and S. Passerini, *Batteries Supercaps*, 2020, **3**, 698-707.
140. P. Peljo and H. H. Girault, *Energy Environ. Sci.*, 2018, **11**, 2306-2309.
141. Y. Yamada, K. Furukawa, K. Sodeyama, K. Kikuchi, M. Yaegashi, Y. Tateyama and A. Yamada, *J. Am. Chem. Soc.*, 2014, **136**, 5039-5046.
142. N. D. Trinh, D. Lepage, D. Aymé-Perrot, A. Badia, M. Dollé and D. Rochefort, *Angew. Chem., Int. Ed.*, 2018, **57**, 5072-5075.
143. A. Heckmann, J. Thienenkamp, K. Beltrop, M. Winter, G. Brunklaus and T. Placke, *Electrochim. Acta*, 2018, **260**, 514-525.
144. T. Liu, X. Han, Z. Zhang, Z. Chen, P. Wang, P. Han, N. Ding and G. Cui, *J. Power Sources*, 2019, **437**, 226942.
145. H. Wang and M. Yoshio, *Chem. Commun.*, 2010, **46**, 1544-1546.
146. J. Gao, S. Tian, L. Qi, M. Yoshio and H. Wang, *J. Power Sources*, 2015, **297**, 121-126.
147. X. Zhang, Y. Tang, F. Zhang and C.-S. Lee, *Adv. Energy Mater.*, 2016, **6**, 1502588.
148. S. Zhang, M. Wang, Z. Zhou and Y. Tang, *Adv. Funct. Mater.*, 2017, **27**, 1703035.
149. W.-H. Li, Q.-L. Ning, X.-T. Xi, B.-H. Hou, J.-Z. Guo, Y. Yang, B. Chen and X.-L. Wu, *Adv. Mater.*, 2019, **31**, 1804766.
150. X. Han, G. Xu, Z. Zhang, X. Du, P. Han, X. Zhou, G. Cui and L. Chen, *Adv. Energy Mater.*, 2019, **9**, 1804022.
151. M. Li, C. Wang, Z. Chen, K. Xu and J. Lu, *Chem. Rev.*, 2020, **120**, 6783-6819.
152. K. V. Kravchyk, P. Bhauriyal, L. Piveteau, C. P. Guntlin, B. Pathak and M. V. Kovalenko, *Nat. Commun.*, 2018, **9**, 4469.
153. X. Li, X. Ou and Y. Tang, *Adv. Energy Mater.*, 2020, **10**, 2002567.
154. M. Lee, J. Hong, B. Lee, K. Ku, S. Lee, C. B. Park and K. Kang, *Green Chem.*, 2017, **19**, 2980-2985.
155. M. Watanabe, M. L. Thomas, S. Zhang, K. Ueno, T. Yasuda and K. Dokko, *Chem. Rev.*, 2017, **117**, 7190-7239.
156. H. Yang, X. Shi, T. Deng, T. Qin, L. Sui, M. Feng, H. Chen, W. Zhang and W. Zheng, *ChemElectroChem*, 2018, **5**, 3612-3618.
157. F. Zhang, B. Ji, X. Tong, M. Sheng, X. Zhang, C.-S. Lee and Y. Tang, *Adv. Mater. Interfaces*, 2016, **3**, 1600605.

158. K. Beltrop, J. C. Madrid Madrid, P. Meister, A. Heckmann, M. Winter, T. Akbay, T. Ishihara and T. Placke, *J. Power Sources*, 2020, **469**, 228397.
159. K. Beltrop, S. Beuker, A. Heckmann, M. Winter and T. Placke, *Energy Environ. Sci.*, 2017, **10**, 2090-2094.
160. C.-J. Pan, C. Yuan, G. Zhu, Q. Zhang, C.-J. Huang, M.-C. Lin, M. Angell, B.-J. Hwang, P. Kaghazchi and H. Dai, *Proc. Natl. Acad. Sci. U. S. A.*, 2018, **115**, 5670-5675.
161. M. Angell, C.-J. Pan, Y. Rong, C. Yuan, M.-C. Lin, B.-J. Hwang and H. Dai, *Proc. Natl. Acad. Sci. U. S. A.*, 2017, **114**, 834-839.
162. E. R. Nightingale, *J. Phys. Chem.*, 1959, **63**, 1381-1387.
163. A. Boisset, L. Athouël, J. Jacquemin, P. Porion, T. Brousse and M. Anouti, *J. Phys. Chem. C*, 2013, **117**, 7408-7422.
164. J. Speight, *Lange's Handbook of Chemistry*, McGraw-Hill, New York, 16th edn., 2005.
165. M. Ue, A. Murakami and S. Nakamura, *J. Electrochem. Soc.*, 2002, **149**, A1385.
166. H. Tokuda, K. Hayamizu, K. Ishii, M. A. B. H. Susan and M. Watanabe, *J. Phys. Chem. B*, 2004, **108**, 16593-16600.
167. M. Galiński, A. Lewandowski and I. Stępniak, *Electrochim. Acta*, 2006, **51**, 5567-5580.
168. A. Balducci, *J. Power Sources*, 2016, **326**, 534-540.
169. A. Brandt and A. Balducci, *J. Power Sources*, 2014, **250**, 343-351.
170. P. W. Ruch, D. Cericola, A. Foelske, R. Kötz and A. Wokaun, *Electrochim. Acta*, 2010, **55**, 2352-2357.
171. M. Shi, S. Kou and X. Yan, *ChemSusChem*, 2014, **7**, 3053-3062.
172. M. E. Speer, M. Kolek, J. J. Jassoy, J. Heine, M. Winter, P. M. Bieker and B. Esser, *Chem. Commun.*, 2015, **51**, 15261-15264.
173. M. Kolek, F. Otteny, P. Schmidt, C. Mück-Lichtenfeld, C. Einholz, J. Becking, E. Schleicher, M. Winter, P. Bieker and B. Esser, *Energy Environ. Sci.*, 2017, **10**, 2334-2341.
174. K. Sakaushi, G. Nickerl, F. M. Wisser, D. Nishio-Hamane, E. Hosono, H. Zhou, S. Kaskel and J. Eckert, *Angew. Chem., Int. Ed.*, 2012, **51**, 7850-7854.
175. L. Fan, Q. Liu, Z. Xu and B. Lu, *ACS Energy Lett.*, 2017, **2**, 1614-1620.
176. D. Lu, H. Liu, T. Huang, Z. Xu, L. Ma, P. Yang, P. Qiang, F. Zhang and D. Wu, *J. Mater. Chem. A*, 2018, **6**, 17297-17302.
177. H. Yuan, F. Ma, X. Wei, J.-L. Lan, Y. Liu, Y. Yu, X. Yang and H. S. Park, *Adv. Energy Mater.*, 2020, **10**, 2001418.
178. J. Huang, X. Guo, X. Du, X. Lin, J.-Q. Huang, H. Tan, Y. Zhu and B. Zhang, *Energy Environ. Sci.*, 2019, **12**, 1550-1557.
179. J. S. Yeon, S. Yun, J. M. Park and H. S. Park, *ACS Nano*, 2019, **13**, 5163-5171.
180. Q. Zhang, M. D. Levi, Q. Dou, Y. Lu, Y. Chai, S. Lei, H. Ji, B. Liu, X. Bu, P. Ma and X. Yan, *Adv. Energy Mater.*, 2019, **9**, 1802707.
181. Z. Xiao, Y. Mei, S. Yuan, H. Mei, B. Xu, Y. Bao, L. Fan, W. Kang, F. Dai, R. Wang, L. Wang, S. Hu, D. Sun and H.-C. Zhou, *ACS Nano*, 2019, **13**, 7024-7030.
182. T. Deng, Y. Lu, W. Zhang, M. Sui, X. Shi, D. Wang and W. Zheng, *Adv. Energy Mater.*, 2018, **8**, 1702294.
183. D. E. Turney, J. W. Gallaway, G. G. Yadav, R. Ramirez, M. Nyce, S. Banerjee, Y.-c. K. Chen-Wiegart, J. Wang, M. J. D'Ambrose, S. Kolhekar, J. Huang and X. Wei, *Chem. Mater.*, 2017, **29**, 4819-4832.
184. W. Shang, W. Yu, Y. Liu, R. Li, Y. Dai, C. Cheng, P. Tan and M. Ni, *Energy Storage Mater.*, 2020, **31**, 44-57.
185. J. F. Parker, C. N. Chervin, E. S. Nelson, D. R. Rolison and J. W. Long, *Energy Environ. Sci.*, 2014, **7**, 1117-1124.
186. J. F. Parker, C. N. Chervin, I. R. Pala, M. Machler, M. F. Burz, J. W. Long and D. R. Rolison, *Science*, 2017, **356**, 415-418.
187. D. Chen, X. Xiong, B. Zhao, M. A. Mahmoud, M. A. El-Sayed and M. Liu, *Adv. Sci.*, 2016, **3**, 1500433.
188. S. Ouendi, K. Robert, D. Stievenard, T. Brousse, P. Roussel and C. Lethien, *Energy Storage Mater.*, 2019, **20**, 243-252.
189. J.-C. Grenier, M. Pouchard and A. Wattiaux, *Curr. Opin. Solid State Mater. Sci.*, 1996, **1**, 233-240.
190. S. Kumar, P. Bhauriyal and B. Pathak, *J. Phys. Chem. C*, 2019, **123**, 23863-23871.
191. T. de Boer, J. G. Lapping, J. A. Read, T. T. Fister, M. Balasubramanian, J. Cabana and A. Moewes, *Chem. Mater.*, 2020, **32**, 2036-2043.
192. M. Rajesh, F. Dolhem, C. Davoisne and M. Becuwe, *ChemSusChem*, 2020, **13**, 2364-2370.
193. M. Walter, K. V. Kravchyk, C. Böfer, R. Widmer and M. V. Kovalenko, *Adv. Mater.*, 2018, **30**, 1705644.
194. C. Zhang, W. Ma, C. Han, L.-W. Luo, A. Daniyar, S. Xiang, X. Wu, X. Ji and J.-X. Jiang, *Energy Environ. Sci.*, 2021, **14**, 462-472.
195. H. Lu, F. Ning, R. Jin, C. Teng, Y. Wang, K. Xi, D. Zhou and G. Xue, *ChemSusChem*, 2020, **13**, 3447-3454.
196. C. Fang, Y. Huang, L. Yuan, Y. Liu, W. Chen, Y. Huang, K. Chen, J. Han, Q. Liu and Y. Huang, *Angew. Chem., Int. Ed.*, 2017, **56**, 6793-6797.
197. X. Zhao, Z. Zhao-Karger, D. Wang and M. Fichtner, *Angew. Chem., Int. Ed.*, 2013, **52**, 13621-13624.
198. F. Chen, Z. Y. Leong and H. Y. Yang, *Energy Storage Mater.*, 2017, **7**, 189-194.
199. Z. Lin, E. Goikolea, A. Balducci, K. Naoi, P. L. Taberna, M. Salanne, G. Yushin and P. Simon, *Mater. Today*, 2018, **21**, 419-436.
200. Q. Dou and H. S. Park, *Energy Environ. Mater.*, 2020, **3**, 286-305.
201. H. Tao, C. Lian and H. Liu, *Green Energy Environ.*, 2020, **5**, 303-321.
202. A. C. Forse, C. Merlet, J. M. Griffin and C. P. Grey, *J. Am. Chem. Soc.*, 2016, **138**, 5731-5744.
203. S. Boukhalfa, D. Gordon, L. He, Y. B. Melnichenko, N. Nitta, A. Magasinski and G. Yushin, *ACS Nano*, 2014, **8**, 2495-2503.
204. J. M. Griffin, A. C. Forse, W.-Y. Tsai, P.-L. Taberna, P. Simon and C. P. Grey, *Nat. Mater.*, 2015, **14**, 812-819.
205. C. Merlet, B. Rotenberg, P. A. Madden, P.-L. Taberna, P. Simon, Y. Gogotsi and M. Salanne, *Nat. Mater.*, 2012, **11**, 306-310.
206. S. Kondrat, P. Wu, R. Qiao and A. A. Kornyshev, *Nat. Mater.*, 2014, **13**, 387-393.
207. M. D. Levi, G. Salitra, N. Levy, D. Aurbach and J. Maier, *Nat. Mater.*, 2009, **8**, 872-875.
208. M. D. Levi, S. Sigalov, D. Aurbach and L. Daikhin, *J. Phys. Chem. C*, 2013, **117**, 14876-14889.
209. W.-Y. Tsai, P.-L. Taberna and P. Simon, *J. Am. Chem. Soc.*, 2014, **136**, 8722-8728.
210. M. D. Levi, N. Levy, S. Sigalov, G. Salitra, D. Aurbach and J. Maier, *J. Am. Chem. Soc.*, 2010, **132**, 13220-13222.
211. M. Deschamps, E. Gilbert, P. Azais, E. Raymundo-Piñero, M. R. Ammar, P. Simon, D. Massiot and F. Béguin, *Nat. Mater.*, 2013, **12**, 351-358.

212. H. Wang, A. C. Forse, J. M. Griffin, N. M. Trease, L. Trognko, P.-L. Taberna, P. Simon and C. P. Grey, *J. Am. Chem. Soc.*, 2013, **135**, 18968-18980.
213. C. Prehal, C. Koczwara, N. Jäckel, A. Schreiber, M. Burian, H. Amenitsch, M. A. Hartmann, V. Presser and O. Paris, *Nat. Energy*, 2017, **2**, 16215.
214. C. Prehal, D. Weingarth, E. Perre, R. T. Lechner, H. Amenitsch, O. Paris and V. Presser, *Energy Environ. Sci.*, 2015, **8**, 1725-1735.
215. S. Boukhalfa, L. He, Y. B. Melnichenko and G. Yushin, *Angew. Chem., Int. Ed.*, 2013, **52**, 4618-4622.
216. R. Futamura, T. Iiyama, Y. Takasaki, Y. Gogotsi, M. J. Biggs, M. Salanne, J. Ségalini, P. Simon and K. Kaneko, *Nat. Mater.*, 2017, **16**, 1225-1232.
217. F. W. Richey, B. Dyatkin, Y. Gogotsi and Y. A. Elabd, *J. Am. Chem. Soc.*, 2013, **135**, 12818-12826.
218. Q. Dou, L. Liu, B. Yang, J. Lang and X. Yan, *Nat. Commun.*, 2017, **8**, 2188.
219. H. Ji, X. Zhao, Z. Qiao, J. Jung, Y. Zhu, Y. Lu, L. L. Zhang, A. H. MacDonald and R. S. Ruoff, *Nat. Commun.*, 2014, **5**, 3317.
220. J. Chmiola, G. Yushin, Y. Gogotsi, C. Portet, P. Simon and P. L. Taberna, *Science*, 2006, **313**, 1760-1763.
221. C. Largeot, C. Portet, J. Chmiola, P.-L. Taberna, Y. Gogotsi and P. Simon, *J. Am. Chem. Soc.*, 2008, **130**, 2730-2731.
222. C. Lian, H. Su, C. Li, H. Liu and J. Wu, *ACS Nano*, 2019, **13**, 8185-8192.
223. L. Zhang, X. Yang, F. Zhang, G. Long, T. Zhang, K. Leng, Y. Zhang, Y. Huang, Y. Ma, M. Zhang and Y. Chen, *J. Am. Chem. Soc.*, 2013, **135**, 5921-5929.
224. P. Simon and Y. Gogotsi, *Acc. Chem. Res.*, 2013, **46**, 1094-1103.
225. Q. Wang, J. Yan and Z. Fan, *Energy Environ. Sci.*, 2016, **9**, 729-762.
226. H. Li, C. Qi, Y. Tao, H. Liu, D.-W. Wang, F. Li, Q.-H. Yang and H.-M. Cheng, *Adv. Energy Mater.*, 2019, **9**, 1900079.
227. S. Ghosh, S. Barg, S. M. Jeong and K. Ostrikov, *Adv. Energy Mater.*, 2020, **10**, 2001239.
228. B. Yao, S. Chandrasekaran, H. Zhang, A. Ma, J. Kang, L. Zhang, X. Lu, F. Qian, C. Zhu, E. B. Duoss, C. M. Spadaccini, M. A. Worsley and Y. Li, *Adv. Mater.*, 2020, **32**, 1906652.
229. M. Kota, M. Jana and H. S. Park, *J. Power Sources*, 2018, **399**, 83-88.
230. J. Chen, Y. Han, X. Kong, X. Deng, H. J. Park, Y. Guo, S. Jin, Z. Qi, Z. Lee, Z. Qiao, R. S. Ruoff and H. Ji, *Angew. Chem., Int. Ed.*, 2016, **55**, 13822-13827.
231. K. Gopalsamy, J. Balamurugan, T. D. Thanh, N. H. Kim and J. H. Lee, *Chem. Eng. J.*, 2017, **312**, 180-190.
232. Y. J. Oh, J. J. Yoo, Y. I. Kim, J. K. Yoon, H. N. Yoon, J.-H. Kim and S. B. Park, *Electrochim. Acta*, 2014, **116**, 118-128.
233. C.-M. Chen, Q. Zhang, M.-G. Yang, C.-H. Huang, Y.-G. Yang and M.-Z. Wang, *Carbon*, 2012, **50**, 3572-3584.
234. Y. He, Y. Zhang, X. Li, Z. Lv, X. Wang, Z. Liu and X. Huang, *Electrochim. Acta*, 2018, **282**, 618-625.
235. T. Lin, I.-W. Chen, F. Liu, C. Yang, H. Bi, F. Xu and F. Huang, *Science*, 2015, **350**, 1508-1513.
236. L.-F. Chen, Y. Lu, L. Yu and X. W. Lou, *Energy Environ. Sci.*, 2017, **10**, 1777-1783.
237. O. Ornelas, J. M. Sieben, R. Ruiz-Rosas, E. Morallón, D. Cazorla-Amorós, J. Geng, N. Soin, E. Siores and B. F. G. Johnson, *Chem. Commun.*, 2014, **50**, 11343-11346.
238. C.-M. Chen, Q. Zhang, X.-C. Zhao, B. Zhang, Q.-Q. Kong, M.-G. Yang, Q.-H. Yang, M.-Z. Wang, Y.-G. Yang, R. Schlögl and D. S. Su, *J. Mater. Chem.*, 2012, **22**, 14076-14084.
239. M. Kota, X. Yu, S.-H. Yeon, H.-W. Cheong and H. S. Park, *J. Power Sources*, 2016, **303**, 372-378.
240. D.-W. Wang, F. Li, Z.-G. Chen, G. Q. Lu and H.-M. Cheng, *Chem. Mater.*, 2008, **20**, 7195-7200.
241. X. Zhao, Q. Zhang, C.-M. Chen, B. Zhang, S. Reiche, A. Wang, T. Zhang, R. Schlögl and D. Sheng Su, *Nano Energy*, 2012, **1**, 624-630.
242. E. Hao, W. Liu, S. Liu, Y. Zhang, H. Wang, S. Chen, F. Cheng, S. Zhao and H. Yang, *J. Mater. Chem. A*, 2017, **5**, 2204-2214.
243. Z.-S. Wu, Y.-Z. Tan, S. Zheng, S. Wang, K. Parvez, J. Qin, X. Shi, C. Sun, X. Bao, X. Feng and K. Müllen, *J. Am. Chem. Soc.*, 2017, **139**, 4506-4512.
244. X. Yu, H. J. Kim, J.-Y. Hong, Y. M. Jung, K. D. Kwon, J. Kong and H. S. Park, *Nano Energy*, 2015, **15**, 576-586.
245. X. Yu, L. Feng and H. S. Park, *J. Power Sources*, 2018, **390**, 93-99.
246. H. Peng, B. Yao, X. Wei, T. Liu, T. Kou, P. Xiao, Y. Zhang and Y. Li, *Adv. Energy Mater.*, 2019, **9**, 1803665.
247. Z. Ling, Z. Wang, M. Zhang, C. Yu, G. Wang, Y. Dong, S. Liu, Y. Wang and J. Qiu, *Adv. Funct. Mater.*, 2016, **26**, 111-119.
248. J. Yu, Q. Wang, D. O'Hare and L. Sun, *Chem. Soc. Rev.*, 2017, **46**, 5950-5974.
249. C. Jing, B. Dong and Y. Zhang, *Energy Environ. Mater.*, 2020, **3**, 346-379.
250. C. Chen, L. Tao, S. Du, W. Chen, Y. Wang, Y. Zou and S. Wang, *Adv. Funct. Mater.*, 2020, **30**, 1909832.
251. F. Gu, X. Cheng, S. Wang, X. Wang and P. S. Lee, *Small*, 2015, **11**, 2044-2050.
252. W. He, G. Zhao, P. Sun, P. Hou, L. Zhu, T. Wang, L. Li, X. Xu and T. Zhai, *Nano Energy*, 2019, **56**, 207-215.
253. T. Deng, W. Zhang, O. Arcelus, J.-G. Kim, J. Carrasco, S. J. Yoo, W. Zheng, J. Wang, H. Tian, H. Zhang, X. Cui and T. Rojo, *Nat. Commun.*, 2017, **8**, 15194.
254. G. S. Gund, C. D. Lokhande and H. S. Park, *J. Alloys Compd.*, 2018, **741**, 549-556.
255. P. Sivakumar, M. Jana, M. Kota, M. G. Jung, A. Gedanken and H. S. Park, *J. Power Sources*, 2018, **402**, 147-156.
256. Y. Li, X. Han, T. Yi, Y. He and X. Li, *J. Energy Chem.*, 2019, **31**, 54-78.
257. C. Yuan, J. Li, L. Hou, X. Zhang, L. Shen and X. W. Lou, *Adv. Funct. Mater.*, 2012, **22**, 4592-4597.
258. C. An, Y. Wang, Y. Huang, Y. Xu, L. Jiao and H. Yuan, *Nano Energy*, 2014, **10**, 125-134.
259. P. Sivakumar, M. Jana, M. Kota, H. S. Lee and H. S. Park, *J. Alloys Compd.*, 2019, **781**, 515-523.
260. B. Zhao, L. Zhang, Q. Zhang, D. Chen, Y. Cheng, X. Deng, Y. Chen, R. Murphy, X. Xiong, B. Song, C.-P. Wong, M.-S. Wang and M. Liu, *Adv. Energy Mater.*, 2018, **8**, 1702247.
261. X. Gao, X. Liu, D. Wu, B. Qian, Z. Kou, Z. Pan, Y. Pang, L. Miao and J. Wang, *Adv. Funct. Mater.*, 2019, **29**, 1903879.
262. T. Pettong, P. Iamprasertkun, A. Krittayavathananon, P. Sukha, P. Sirisinudomkit, A. Seubsai, M. Chareonpanich, P. Kongkachuichay, J. Limtrakul and M. Sawangphruk, *ACS Appl. Mater. Interfaces*, 2016, **8**, 34045-34053.
263. M. Gong, Y. Li, H. Zhang, B. Zhang, W. Zhou, J. Feng, H. Wang, Y. Liang, Z. Fan, J. Liu and H. Dai, *Energy Environ. Sci.*, 2014, **7**, 2025-2032.
264. T. Kavinkumar, K. Vinodgopal and B. Neppolian, *Appl. Surf. Sci.*, 2020, **513**, 145781.

265. P. Sivakumar, M. Jana, M. G. Jung, A. Gedanken and H. S. Park, *J. Mater. Chem. A*, 2019, **7**, 11362-11369.
266. Y. Tang, H. Shen, J. Cheng, Z. Liang, C. Qu, H. Tabassum and R. Zou, *Adv. Funct. Mater.*, 2020, **30**, 1908223.
267. S. Pappu, K. Nanaji, S. Mandati, T. N. Rao, S. K. Martha and S. V. Bulusu, *Batteries Supercaps*, 2020, **3**, 1209-1219.
268. L. Xu, Q. Jiang, Z. Xiao, X. Li, J. Huo, S. Wang and L. Dai, *Angew. Chem., Int. Ed.*, 2016, **55**, 5277-5281.
269. S. Yang, Y. Liu, Y. Hao, X. Yang, W. A. Goddard III, X. L. Zhang and B. Cao, *Adv. Sci.*, 2018, **5**, 1700659.
270. X. Wang, R. Zhou, C. Zhang, S. Xi, M. W. M. Jones, T. Tesfamichael, A. Du, K. Gui, K. Ostrikov and H. Wang, *J. Mater. Chem. A*, 2020, **8**, 9278-9291.
271. S. Li, N. Sharma, C. Yu, Y. Zhang, G. Wan, R. Fu, H. Huang, X. Sun, S.-J. Lee, J.-S. Lee, D. Nordlund, P. Pianetta, K. Zhao, Y. Liu and J. Qiu, *Adv. Mater.*, 2021, **33**, 2006147.
272. S. Sun, D. Rao, T. Zhai, Q. Liu, H. Huang, B. Liu, H. Zhang, L. Xue and H. Xia, *Adv. Mater.*, 2020, **32**, 2005344.
273. J. Zhao, C. Ge, Z. Zhao, Q. Wu, M. Liu, M. Yan, L. Yang, X. Wang and Z. Hu, *Nano Energy*, 2020, **76**, 105026.
274. M. Jana, P. Sivakumar, M. Kota, M. G. Jung and H. S. Park, *J. Power Sources*, 2019, **422**, 9-17.
275. Y. Xiao, D. Su, X. Wang, S. Wu, L. Zhou, S. Fang and F. Li, *Sci. China Mater.*, 2018, **61**, 263-272.
276. Y. Lin, X. Xie, X. Wang, B. Zhang, C. Li, H. Wang and L. Wang, *Electrochim. Acta*, 2017, **246**, 406-414.
277. S. Li, C. Yu, J. Yang, C. Zhao, M. Zhang, H. Huang, Z. Liu, W. Guo and J. Qiu, *Energy Environ. Sci.*, 2017, **10**, 1958-1965.
278. T. Yang, Q. Ye, Y. Liang, L. Wu, X. Long, X. Xu and F. Wang, *J. Power Sources*, 2020, **449**, 227590.
279. J. Yang, C. Yu, C. Hu, M. Wang, S. Li, H. Huang, K. Bustillo, X. Han, C. Zhao, W. Guo, Z. Zeng, H. Zheng and J. Qiu, *Adv. Funct. Mater.*, 2018, **28**, 1803272.
280. Z.-H. Huang, F.-F. Sun, M. Batmunkh, W.-H. Li, H. Li, Y. Sun, Q. Zhao, X. Liu and T.-Y. Ma, *J. Mater. Chem. A*, 2019, **7**, 11826-11835.
281. Q. Li, C. Lu, C. Chen, L. Xie, Y. Liu, Y. Li, Q. Kong and H. Wang, *Energy Storage Mater.*, 2017, **8**, 59-67.
282. X. Ge, C. Gu, Z. Yin, X. Wang, J. Tu and J. Li, *Nano Energy*, 2016, **20**, 185-193.
283. X. Wang, H. Li, H. Li, S. Lin, J. Bai, J. Dai, C. Liang, X. Zhu, Y. Sun and S. Dou, *J. Mater. Chem. A*, 2019, **7**, 2291-2300.
284. T.-F. Yi, J.-J. Pan, T.-T. Wei, Y. Li and G. Cao, *Nano Today*, 2020, **33**, 100894.
285. H. S. Lee, G. S. Gund and H. S. Park, *J. Power Sources*, 2020, **451**, 227763.
286. Z. Liu, C. Pan, W. Li, S. Wei, M. Zhang and S. Chen, *Electrochim. Acta*, 2020, **338**, 135897.
287. C. Li, J. Balamurugan, N. H. Kim and J. H. Lee, *Adv. Energy Mater.*, 2018, **8**, 1702014.
288. W. Li, B. Zhang, R. Lin, S. Ho-Kimura, G. He, X. Zhou, J. Hu and I. P. Parkin, *Adv. Funct. Mater.*, 2018, **28**, 1705937.
289. Y. Liu, Q. Xu, R. Wang, Y. Zheng, L. Zhu, Z. Wang and W. Zheng, *J. Mater. Chem. A*, 2020, **8**, 797-809.
290. X. Song, C. Huang, Y. Qin, H. Li and H. C. Chen, *J. Mater. Chem. A*, 2018, **6**, 16205-16212.
291. H. Liu, H. Guo, N. Wu, W. Yao, R. Xue, M. Wang and W. Yang, *J. Alloys Compd.*, 2021, **856**, 156535.
292. Y.-L. Liu, C. Yan, G.-G. Wang, F. Li, Q. Kang, H.-Y. Zhang and J.-C. Han, *Nanoscale*, 2020, **12**, 4040-4050.
293. B. Ye, X. Cao, Q. Zhao, A. Zhou and J. Wang, *Nanotechnology*, 2020, **31**, 335706.
294. F. Liu, L. Zeng, Y. Chen, R. Zhang, R. Yang, J. Pang, L. Ding, H. Liu and W. Zhou, *Nano Energy*, 2019, **61**, 18-26.
295. J. Balamurugan, T. T. Nguyen, V. Aravindan, N. H. Kim and J. H. Lee, *Adv. Funct. Mater.*, 2018, **28**, 1804663.
296. M. Ishaq, M. Jabeen, W. Song, L. Xu, W. Li and Q. Deng, *Electrochim. Acta*, 2018, **282**, 913-922.
297. J. Jiang, Z. Li, X. He, Y. Hu, F. Li, P. Huang and C. Wang, *Small*, 2020, **16**, 2000180.
298. S. He, Z. Li, H. Mi, C. Ji, F. Guo, X. Zhang, Z. Li, Q. Du and J. Qiu, *J. Power Sources*, 2020, **467**, 228324.
299. H. Liang, C. Xia, Q. Jiang, A. N. Gandi, U. Schwingenschlögl and H. N. Alshareef, *Nano Energy*, 2017, **35**, 331-340.
300. W. Song, J. Wu, G. Wang, S. Tang, G. Chen, M. Cui and X. Meng, *Adv. Funct. Mater.*, 2018, **28**, 1804620.
301. S. Jin, *ACS Energy Lett.*, 2017, **2**, 1937-1938.
302. H. Nan, M. Liu, Q. Zhang, M. Wang, S. Liu, L. Qiao, X. Hu and H. Tian, *J. Power Sources*, 2020, **451**, 227822.
303. L. Wang, Z. Feng, H. Zhang, D. Li and P. Xing, *Nanotechnology*, 2020, **31**, 125403.
304. N. Mahmood, M. Tahir, A. Mahmood, J. Zhu, C. Cao and Y. Hou, *Nano Energy*, 2015, **11**, 267-276.
305. S. Dai, Z. Zhang, J. Xu, W. Shen, Q. Zhang, X. Yang, T. Xu, D. Dang, H. Hu, B. Zhao, Y. Wang, C. Qu, J. Fu, X. Li, C. Hu and M. Liu, *Nano Energy*, 2019, **64**, 103919.
306. D. Choi and P. N. Kumta, *J. Electrochem. Soc.*, 2006, **153**, A2298.
307. A. Djire, P. Pande, A. Deb, J. B. Siegel, O. T. Ajenifujah, L. He, A. E. Sleightholme, P. G. Rasmussen and L. T. Thompson, *Nano Energy*, 2019, **60**, 72-81.
308. X. Lu, T. Liu, T. Zhai, G. Wang, M. Yu, S. Xie, Y. Ling, C. Liang, Y. Tong and Y. Li, *Adv. Energy Mater.*, 2014, **4**, 1300994.
309. J. Balamurugan, G. Karthikeyan, T. D. Thanh, N. H. Kim and J. H. Lee, *J. Power Sources*, 2016, **308**, 149-157.
310. P. J. Hanumantha, M. K. Datta, K. Kadakia, C. Okoli, P. Patel and P. N. Kumta, *Electrochim. Acta*, 2016, **207**, 37-47.
311. A. Achour, R. Lucio-Porto, M. Chaker, A. Arman, A. Ahmadpourian, M. A. Soussou, M. Boujtita, L. Le Brizoual, M. A. Djouadi and T. Brousse, *Electrochem. Commun.*, 2017, **77**, 40-43.
312. Y. Yi, L. Yu, Z. Tian, Y. Song, Y. Shao, L. Gao, J. Sun and Z. Liu, *Adv. Funct. Mater.*, 2018, **28**, 1805510.
313. G.-H. An, D.-Y. Lee and H.-J. Ahn, *J. Mater. Chem. A*, 2017, **5**, 19714-19720.
314. X. Jiang, W. Lu, Y. Li, Y. Yu, X. Zhou, X. Liu and Y. Xing, *ChemElectroChem*, 2019, **6**, 3445-3453.
315. Y. Wu, Y. Yang, X. Zhao, Y. Tan, Y. Liu, Z. Wang and F. Ran, *Nano-Micro Lett.*, 2018, **10**, 63.
316. Y. Tan, Y. Liu, Z. Tang, Z. Wang, L. Kong, L. Kang, Z. Liu and F. Ran, *Sci. Rep.*, 2018, **8**, 2915.
317. Y. Liu, L. Liu, Y. Tan, L. Niu, L. Kong, L. Kang and F. Ran, *Electrochim. Acta*, 2018, **262**, 66-73.
318. Y. Wang, M. Jiang, Y. Yang and F. Ran, *Electrochim. Acta*, 2016, **222**, 1914-1921.
319. Q. Yang, Q. Wang, Y. Long, F. Wang, L. Wu, J. Pan, J. Han, Y. Lei, W. Shi and S. Song, *Adv. Energy Mater.*, 2020, **10**, 1903193.
320. Q. Wang, Y. Luo, R. Hou, S. Zaman, K. Qi, H. Liu, H. S. Park and B. Y. Xia, *Adv. Mater.*, 2019, **31**, 1905744.
321. D. Kong, Y. Wang, S. Huang, J. Hu, Y. V. Lim, B. Liu, S. Fan, Y. Shi and H. Y. Yang, *Energy Storage Mater.*, 2019, **23**, 653-663.

322. F. Cao, M. Zhao, Y. Yu, B. Chen, Y. Huang, J. Yang, X. Cao, Q. Lu, X. Zhang, Z. Zhang, C. Tan and H. Zhang, *J. Am. Chem. Soc.*, 2016, **138**, 6924-6927.
323. C. Ren, X. Jia, W. Zhang, D. Hou, Z. Xia, D. Huang, J. Hu, S. Chen and S. Gao, *Adv. Funct. Mater.*, 2020, **30**, 2004519.
324. C. Qu, B. Zhao, Y. Jiao, D. Chen, S. Dai, B. M. deglee, Y. Chen, K. S. Walton, R. Zou and M. Liu, *ACS Energy Lett.*, 2017, **2**, 1263-1269.
325. Y. Li, Y. Xu, Y. Liu and H. Pang, *Small*, 2019, **15**, 1902463.
326. C. Qu, Z. Liang, Y. Jiao, B. Zhao, B. Zhu, D. Dang, S. Dai, Y. Chen, R. Zou and M. Liu, *Small*, 2018, **14**, 1800285.
327. Y. Yan, P. Gu, S. Zheng, M. Zheng, H. Pang and H. Xue, *J. Mater. Chem. A*, 2016, **4**, 19078-19085.
328. W. Xia, A. Mahmood, R. Zou and Q. Xu, *Energy Environ. Sci.*, 2015, **8**, 1837-1866.
329. S. Bi, H. Banda, M. Chen, L. Niu, M. Chen, T. Wu, J. Wang, R. Wang, J. Feng, T. Chen, M. Dincă, A. A. Kornyshev and G. Feng, *Nat. Mater.*, 2020, **19**, 552-558.
330. W. Che, M. Wei, Z. Sang, Y. Ou, Y. Liu and J. Liu, *J. Alloys Compd.*, 2018, **731**, 381-388.
331. Z. Li, W. Zhang, H. Wang and B. Yang, *Electrochim. Acta*, 2017, **258**, 561-570.
332. G. Guo, K. Ouyang, J. Yu, Y. Liu, S. Feng and M. Wei, *ACS Appl. Energy Mater.*, 2020, **3**, 300-308.
333. R. P. Forslund, J. Pender, C. T. Alexander, K. P. Johnston and K. J. Stevenson, *J. Mater. Chem. A*, 2019, **7**, 21222-21231.
334. Y.-L. Song, Z.-C. Wang, Y.-D. Yan, M.-L. Zhang, G.-L. Wang, T.-Q. Yin, Y. Xue, F. Gao and M. Qiu, *J. Energy Chem.*, 2020, **43**, 173-181.
335. Z. A. Elsiddig, H. Xu, D. Wang, W. Zhang, X. Guo, Y. Zhang, Z. Sun and J. Chen, *Electrochim. Acta*, 2017, **253**, 422-429.
336. Y. Cao, B. Lin, Y. Sun, H. Yang and X. Zhang, *J. Alloys Compd.*, 2015, **624**, 31-39.
337. X. W. Wang, Q. Q. Zhu, X. E. Wang, H. C. Zhang, J. J. Zhang and L. F. Wang, *J. Alloys Compd.*, 2016, **675**, 195-200.
338. Y. Liu, Z. Wang, J.-P. M. Veder, Z. Xu, Y. Zhong, W. Zhou, M. O. Tade, S. Wang and Z. Shao, *Adv. Energy Mater.*, 2018, **8**, 1702604.
339. Z. Wang, Y. Liu, Y. Chen, L. Yang, Y. Wang and M. Wei, *J. Alloys Compd.*, 2019, **810**, 151830.
340. Y. Liu, Z. Wang, Y. Zhong, X. Xu, J.-P. M. Veder, M. R. Rowles, M. Saunders, R. Ran and Z. Shao, *Chem. Eng. J.*, 2020, **390**, 124645.
341. A. K. Tomar, A. Joshi, S. Atri, G. Singh and R. K. Sharma, *ACS Appl. Mater. Interfaces*, 2020, **12**, 15128-15137.
342. C. T. Alexander, R. P. Forslund, K. P. Johnston and K. J. Stevenson, *ACS Appl. Energy Mater.*, 2019, **2**, 6558-6568.
343. A. Rezanezhad, E. Rezaie, L. S. Ghadimi, A. Hajalilou, E. Abouzari-Lotf and N. Arsalani, *Electrochim. Acta*, 2020, **335**, 135699.
344. W. Shi, R. Ding, X. Li, Q. Xu, D. Ying, Y. Huang and E. Liu, *Chem. - Eur. J.*, 2017, **23**, 15305-15311.
345. R. Ding, X. Li, W. Shi, Q. Xu, X. Han, Y. Zhou, W. Hong and E. Liu, *J. Mater. Chem. A*, 2017, **5**, 17822-17827.
346. N. Hussain, F. Wu, W. Younas and L. Xu, *New J. Chem.*, 2019, **43**, 11959-11967.
347. H. Fan, X. Zhang, Y. Wang, R. Gao and J. Lang, *J. Colloid Interface Sci.*, 2019, **557**, 546-555.
348. H. Fan, X. Zhang, Y. Wang, J. Lang and R. Gao, *J. Power Sources*, 2020, **474**, 228603.
349. K.-P. Cheng, R.-J. Gu and L.-X. Wen, *RSC Adv.*, 2020, **10**, 11681-11693.
350. J. Ma, X. Guo, Y. Yan, H. Xue and H. Pang, *Adv. Sci.*, 2018, **5**, 1700986.
351. H. Liu, X. Liu, S. Wang, H.-K. Liu and L. Li, *Energy Storage Mater.*, 2020, **28**, 122-145.
352. R. Li, Y. Wang, C. Zhou, C. Wang, X. Ba, Y. Li, X. Huang and J. Liu, *Adv. Funct. Mater.*, 2015, **25**, 5384-5394.
353. Y. Tao, C. Ding, D. Tan, F. Yu and F. Wang, *ChemSusChem*, 2018, **11**, 4269-4274.
354. C. Liu, Q. Li, J. Cao, Q. Zhang, P. Man, Z. Zhou, C. Li and Y. Yao, *Sci. Bull.*, 2020, **65**, 812-819.
355. Q. Li, Q. Zhang, C. Liu, W. Gong, Z. Zhou, P. Man, J. Guo, B. He, K. Zhang, W. Lu and Y. Yao, *Energy Storage Mater.*, 2020, **27**, 316-326.
356. J. Guan, Y. Chen, L. Cao, Y. Liu, P. Lian, Y. Gao and X. Shi, *J. Power Sources*, 2020, **469**, 228307.
357. C. Wang, L. Zhang, M. Li, J. Zhang, Y. Chen, M. Sun, L. Dong and H. Lu, *Chem. - Eur. J.*, 2019, **25**, 5005-5013.
358. Z. Sun, H. Lin, F. Zhang, X. Yang, H. Jiang, Q. Wang and F. Qu, *J. Mater. Chem. A*, 2018, **6**, 14956-14966.
359. A. Mohammadi Zardkhoshoui, S. S. Hosseiny Davarani, M. Maleka Ashtiani and M. Sarparast, *J. Mater. Chem. A*, 2019, **7**, 10282-10292.
360. A. Śliwak, A. Moyseowicz and G. Gryglewicz, *J. Mater. Chem. A*, 2017, **5**, 5680-5684.
361. K. A. Owusu, L. Qu, J. Li, Z. Wang, K. Zhao, C. Yang, K. M. Hercule, C. Lin, C. Shi, Q. Wei, L. Zhou and L. Mai, *Nat. Commun.*, 2017, **8**, 14264.
362. D. Wang, Y. Zhao, G. Liang, F. Mo, H. Li, Z. Huang, X. Li, T. Tang, B. Dong and C. Zhi, *Nano Energy*, 2020, **71**, 104583.
363. W. Zuo, W. Zhu, D. Zhao, Y. Sun, Y. Li, J. Liu and X. W. Lou, *Energy Environ. Sci.*, 2016, **9**, 2881-2891.
364. Y. Zeng, M. Wang, W. He, P. Fang, M. Wu, Y. Tong, M. Chen and X. Lu, *Chem. Sci.*, 2019, **10**, 3602-3607.
365. Q. Zhu, M. Cheng, X. Yang, B. Zhang, Z. Wan, Q. Xiao and Y. Yu, *J. Mater. Chem. A*, 2019, **7**, 6784-6792.
366. L. Ma, M. A. Schroeder, O. Borodin, T. P. Pollard, M. S. Ding, C. Wang and K. Xu, *Nat. Energy*, 2020, **5**, 743-749.
367. C. Zhong, B. Liu, J. Ding, X. Liu, Y. Zhong, Y. Li, C. Sun, X. Han, Y. Deng, N. Zhao and W. Hu, *Nat. Energy*, 2020, **5**, 440-449.
368. C. Wang, G. Zhu, P. Liu and Q. Chen, *ACS Nano*, 2020, **14**, 2404-2411.
369. B. J. Hopkins, M. B. Sassin, C. N. Chervin, P. A. DeSario, J. F. Parker, J. W. Long and D. R. Rolison, *Energy Storage Mater.*, 2020, **27**, 370-376.
370. Y. Wu, Y. Zhang, Y. Ma, J. D. Howe, H. Yang, P. Chen, S. Aluri and N. Liu, *Adv. Energy Mater.*, 2018, **8**, 1802470.
371. Y. Zhang, Y. Wu, W. You, M. Tian, P.-W. Huang, Y. Zhang, Z. Sun, Y. Ma, T. Hao and N. Liu, *Nano Lett.*, 2020, **20**, 4700-4707.
372. M. B. Lim, T. N. Lambert and E. I. Ruiz, *J. Electrochem. Soc.*, 2020, **167**, 060508.
373. J. F. Parker, I. R. Pala, C. N. Chervin, J. W. Long and D. R. Rolison, *J. Electrochem. Soc.*, 2015, **163**, A351-A355.
374. Y. Yang, L. Zhao, K. Shen, Y. Liu, X. Zhao, Y. Wu, Y. Wang and F. Ran, *J. Power Sources*, 2016, **333**, 61-71.
375. A. K. Tomar, G. Singh and R. K. Sharma, *ChemSusChem*, 2018, **11**, 4123-4130.
376. M. Wei, W. Che, H. Li, Z. Wang, F. Yan, Y. Liu and J. Liu, *Appl. Surf. Sci.*, 2019, **484**, 551-559.
377. W. Zong, F. Lai, G. He, J. Feng, W. Wang, R. Lian, Y.-E. Miao, G.-C. Wang, I. P. Parkin and T. Liu, *Small*, 2018, **14**, 1801562.

378. L. B. Ebert, *Annu. Rev. Mater. Sci.*, 1976, **6**, 181-211.
379. Y. Li, Y. Lu, P. Adelhelm, M.-M. Titirici and Y.-S. Hu, *Chem. Soc. Rev.*, 2019, **48**, 4655-4687.
380. P. Jeżowski, O. Crosnier, E. Deunf, P. Poizot, F. Béguin and T. Brousse, *Nat. Mater.*, 2018, **17**, 167-173.
381. S. Miyoshi, T. Akbay, T. Kurihara, T. Fukuda, A. T. Staykov, S. Ida and T. Ishihara, *J. Phys. Chem. C*, 2016, **120**, 22887-22894.
382. S. Pisana, M. Lazzeri, C. Casiraghi, K. S. Novoselov, A. K. Geim, A. C. Ferrari and F. Mauri, *Nat. Mater.*, 2007, **6**, 198-201.
383. G. Schmuelling, T. Placke, R. Kloepsch, O. Fromm, H.-W. Meyer, S. Passerini and M. Winter, *J. Power Sources*, 2013, **239**, 563-571.
384. T. Placke, G. Schmuelling, R. Kloepsch, P. Meister, O. Fromm, P. Hilbig, H.-W. Meyer and M. Winter, *Z. Anorg. Allg. Chem.*, 2014, **640**, 1996-2006.
385. D. Novko, Q. Zhang and P. Kaghazchi, *Phys. Rev. Appl.*, 2019, **12**, 024016.
386. J. Li, Q. Liu, R. A. Flores, J. Lemmon and T. Bligaard, *Phys. Chem. Chem. Phys.*, 2020, **22**, 5969-5975.
387. S. Y. Leung, C. Underhill, G. Dresselhaus, T. Krapchev, R. Ogilvie and M. S. Dresselhaus, *Phys. Lett. A*, 1980, **76**, 89-91.
388. S. Schweidler, L. de Biasi, A. Schiele, P. Hartmann, T. Brezesinski and J. Janek, *J. Phys. Chem. C*, 2018, **122**, 8829-8835.
389. Z. Jian, W. Luo and X. Ji, *J. Am. Chem. Soc.*, 2015, **137**, 11566-11569.
390. Y. Gao, C. Zhu, Z. Chen and G. Lu, *J. Phys. Chem. C*, 2017, **121**, 7131-7138.
391. S. C. Jung, Y.-J. Kang, D.-J. Yoo, J. W. Choi and Y.-K. Han, *J. Phys. Chem. C*, 2016, **120**, 13384-13389.
392. M. S. Wu, B. Xu, L. Q. Chen and C. Y. Ouyang, *Electrochim. Acta*, 2016, **195**, 158-165.
393. M. L. Agiorgousis, Y.-Y. Sun and S. Zhang, *ACS Energy Lett.*, 2017, **2**, 689-693.
394. S. Thinius, M. M. Islam, P. Heitjans and T. Bredow, *J. Phys. Chem. C*, 2014, **118**, 2273-2280.
395. Z. Chen, T. Liu, Z. Zhao, Z. Zhang, X. Han, P. Han, J. Li, J. Wang, J. Li, S. Huang, X. Zhou, J. Zhao and G. Cui, *J. Power Sources*, 2020, **457**, 227994.
396. T. Ishihara, M. Koga, H. Matsumoto and M. Yoshio, *Electrochem. Solid-State Lett.*, 2007, **10**, A74.
397. A. Heckmann, O. Fromm, U. Rodehorst, P. Münster, M. Winter and T. Placke, *Carbon*, 2018, **131**, 201-212.
398. C. Nowak, L. Froboese, M. Winter, T. Placke, W. Haselrieder and A. Kwade, *Energy Technol.*, 2019, **7**, 1900528.
399. D.-Y. Wang, C.-Y. Wei, M.-C. Lin, C.-J. Pan, H.-L. Chou, H.-A. Chen, M. Gong, Y. Wu, C. Yuan, M. Angell, Y.-J. Hsieh, Y.-H. Chen, C.-Y. Wen, C.-W. Chen, B.-J. Hwang, C.-C. Chen and H. Dai, *Nat. Commun.*, 2017, **8**, 14283.
400. J. H. Xu, D. E. Turney, A. L. Jadhav and R. J. Messinger, *ACS Appl. Energy Mater.*, 2019, **2**, 7799-7810.
401. L. Zhang, L. Chen, H. Luo, X. Zhou and Z. Liu, *Adv. Energy Mater.*, 2017, **7**, 1700034.
402. H. Chen, F. Guo, Y. Liu, T. Huang, B. Zheng, N. Ananth, Z. Xu, W. Gao and C. Gao, *Adv. Mater.*, 2017, **29**, 1605958.
403. A. Ejigu, L. W. Le Fevre, K. Fujisawa, M. Terrones, A. J. Forsyth and R. A. W. Dryfe, *ACS Appl. Mater. Interfaces*, 2019, **11**, 23261-23270.
404. H. Huang, F. Zhou, P. Lu, X. Li, P. Das, X. Feng, K. Müllen and Z.-S. Wu, *Energy Storage Mater.*, 2020, **27**, 396-404.
405. Y. Wu, M. Gong, M.-C. Lin, C. Yuan, M. Angell, L. Huang, D.-Y. Wang, X. Zhang, J. Yang, B.-J. Hwang and H. Dai, *Adv. Mater.*, 2016, **28**, 9218-9222.
406. T.-S. Lee, S. B. Patil, Y.-T. Kao, J.-Y. An, Y.-C. Lee, Y.-H. Lai, C.-K. Chang, Y.-S. Cheng, Y.-C. Chuang, H.-S. Sheu, C.-H. Wu, C.-C. Yang, R.-H. Cheng, C.-Y. Lee, P.-Y. Peng, L.-H. Lai, H.-H. Lee and D.-Y. Wang, *ACS Appl. Mater. Interfaces*, 2020, **12**, 2572-2580.
407. C. Zhan, X. Zeng, X. Ren, Y. Shen, R. Lv, F. Kang and Z.-H. Huang, *J. Energy Chem.*, 2020, **42**, 180-184.
408. C. Zhang, R. He, J. Zhang, Y. Hu, Z. Wang and X. Jin, *ACS Appl. Mater. Interfaces*, 2018, **10**, 26510-26516.
409. G. Zhang, X. Ou, C. Cui, J. Ma, J. Yang and Y. Tang, *Adv. Funct. Mater.*, 2019, **29**, 1806722.
410. K. Yang, L. Jia, X. Liu, Z. Wang, Y. Wang, Y. Li, H. Chen, B. Wu, L. Yang and F. Pan, *Nano Res.*, 2020, **13**, 412-418.
411. J. Kim, J. H. Kim and K. Ariga, *Joule*, 2017, **1**, 739-768.
412. Y. Lu, Q. Zhang, L. Li, Z. Niu and J. Chen, *Chem*, 2018, **4**, 2786-2813.
413. S. Muench, A. Wild, C. Friebe, B. Häupler, T. Janoschka and U. S. Schubert, *Chem. Rev.*, 2016, **116**, 9438-9484.
414. P. Poizot, J. Gaubicher, S. Renault, L. Dubois, Y. Liang and Y. Yao, *Chem. Rev.*, 2020, **120**, 6490-6557.
415. Z. Song and H. Zhou, *Energy Environ. Sci.*, 2013, **6**, 2280-2301.
416. J. Xie, P. Gu and Q. Zhang, *ACS Energy Lett.*, 2017, **2**, 1985-1996.
417. T. B. Schon, B. T. McAllister, P.-F. Li and D. S. Seferos, *Chem. Soc. Rev.*, 2016, **45**, 6345-6404.
418. I. A. Rodríguez-Pérez and X. Ji, *ACS Energy Lett.*, 2017, **2**, 1762-1770.
419. S. Dong, Z. Li, I. A. Rodríguez-Pérez, H. Jiang, J. Lu, X. Zhang and X. Ji, *Nano Energy*, 2017, **40**, 233-239.
420. É. Deunf, P. Jiménez, D. Guyomard, F. Dolhem and P. Poizot, *Electrochem. Commun.*, 2016, **72**, 64-68.
421. E. Deunf, F. Dolhem, D. Guyomard, J. Simonet and P. Poizot, *Electrochim. Acta*, 2018, **262**, 276-281.
422. M. Kato, T. Masese, M. Yao, N. Takeichi and T. Kiyobayashi, *New J. Chem.*, 2019, **43**, 1626-1631.
423. G. Dai, Y. He, Z. Niu, P. He, C. Zhang, Y. Zhao, X. Zhang and H. Zhou, *Angew. Chem., Int. Ed.*, 2019, **58**, 9902-9906.
424. H. Gao, L. Xue, S. Xin and J. B. Goodenough, *Angew. Chem., Int. Ed.*, 2018, **57**, 5449-5453.
425. F. Wan, L. Zhang, X. Wang, S. Bi, Z. Niu and J. Chen, *Adv. Funct. Mater.*, 2018, **28**, 1804975.
426. F.-Z. Cui, Z. Liu, D.-L. Ma, L. Liu, T. Huang, P. Zhang, D. Tan, F. Wang, G.-F. Jiang and Y. Wu, *Chem. Eng. J.*, 2021, **405**, 127038.
427. Y. Sun, L. Jiao, D. Han, F. Wang, P. Zhang, H. Li and L. Niu, *Mater. Des.*, 2020, **188**, 108440.
428. A. Di Fabio, A. Giorgi, M. Mastragostino and F. Soavi, *J. Electrochem. Soc.*, 2001, **148**, A845.
429. A. Laforgue, P. Simon, J. F. Fauvarque, M. Mastragostino, F. Soavi, J. F. Sarrau, P. Lailler, M. Conte, E. Rossi and S. Saguatti, *J. Electrochem. Soc.*, 2003, **150**, A645.
430. P. Sivaraman, A. R. Bhattacharrya, S. P. Mishra, A. P. Thakur, K. Shashidhara and A. B. Samui, *Electrochim. Acta*, 2013, **94**, 182-191.
431. P. Sivaraman, A. P. Thakur and K. Shashidhara, *Synth. Met.*, 2020, **259**, 116255.

432. A. Balducci, W. A. Henderson, M. Mastragostino, S. Passerini, P. Simon and F. Soavi, *Electrochim. Acta*, 2005, **50**, 2233-2237.
433. K. Nakahara, S. Iwasa, M. Satoh, Y. Morioka, J. Iriyama, M. Suguro and E. Hasegawa, *Chem. Phys. Lett.*, 2002, **359**, 351-354.
434. K. Koshika, N. Sano, K. Oyaizu and H. Nishide, *Chem. Commun.*, 2009, DOI: 10.1039/B818087C, 836-838.
435. T. Suga, H. Konishi and H. Nishide, *Chem. Commun.*, 2007, DOI: 10.1039/B618710B, 1730-1732.
436. K. Oyaizu, T. Suga, K. Yoshimura and H. Nishide, *Macromolecules*, 2008, **41**, 6646-6652.
437. K. Oyaizu and H. Nishide, *Adv. Mater.*, 2009, **21**, 2339-2344.
438. K. Oyaizu, Y. Ando, H. Konishi and H. Nishide, *J. Am. Chem. Soc.*, 2008, **130**, 14459-14461.
439. A. Wild, M. Strumpf, B. Häupler, M. D. Hager and U. S. Schubert, *Adv. Energy Mater.*, 2017, **7**, 1601415.
440. M. Kolek, F. Otteny, J. Becking, M. Winter, B. Esser and P. Bieker, *Chem. Mater.*, 2018, **30**, 6307-6317.
441. F. Otteny, M. Kolek, J. Becking, M. Winter, P. Bieker and B. Esser, *Adv. Energy Mater.*, 2018, **8**, 1802151.
442. F. Otteny, V. Perner, D. Wassy, M. Kolek, P. Bieker, M. Winter and B. Esser, *ACS Sustainable Chem. Eng.*, 2020, **8**, 238-247.
443. S. C. Han, E. G. Bae, H. Lim and M. Pyo, *J. Power Sources*, 2014, **254**, 73-79.
444. M. Tang, C. Jiang, S. Liu, X. Li, Y. Chen, Y. Wu, J. Ma and C. Wang, *Energy Storage Mater.*, 2020, **27**, 35-42.
445. T. M. Figueira-Duarte, S. C. Simon, M. Wagner, S. I. Druzhinin, K. A. Zachariasse and K. Müllen, *Angew. Chem., Int. Ed.*, 2008, **47**, 10175-10178.
446. X. Dong, Z. Guo, Z. Guo, Y. Wang and Y. Xia, *Joule*, 2018, **2**, 902-913.
447. P. Kuhn, M. Antonietti and A. Thomas, *Angew. Chem., Int. Ed.*, 2008, **47**, 3450-3453.
448. Y. Su, Y. Liu, P. Liu, D. Wu, X. Zhuang, F. Zhang and X. Feng, *Angew. Chem., Int. Ed.*, 2015, **54**, 1812-1816.
449. Z. Zhang, H. Yoshikawa and K. Awaga, *Chem. Mater.*, 2016, **28**, 1298-1303.
450. C. H. Hendon, D. Tiana and A. Walsh, *Phys. Chem. Chem. Phys.*, 2012, **14**, 13120-13132.
451. K. Wada, K. Sakaushi, S. Sasaki and H. Nishihara, *Angew. Chem., Int. Ed.*, 2018, **57**, 8886-8890.
452. M. Amores, K. Wada, K. Sakaushi and H. Nishihara, *J. Phys. Chem. C*, 2020, **124**, 9215-9224.
453. S. Dühnen, R. Nölle, J. Wrogemann, M. Winter and T. Placke, *J. Electrochem. Soc.*, 2019, **166**, A5474-A5482.
454. L. Mu, S. Xu, Y. Li, Y.-S. Hu, H. Li, L. Chen and X. Huang, *Adv. Mater.*, 2015, **27**, 6928-6933.
455. X. Lou, F. Geng, B. Hu, C. Li, M. Shen and B. Hu, *ACS Appl. Energy Mater.*, 2019, **2**, 413-419.
456. H.-g. Wang, H. Wang, Z. Si, Q. Li, Q. Wu, Q. Shao, L. Wu, Y. Liu, Y. Wang, S. Song and H. Zhang, *Angew. Chem., Int. Ed.*, 2019, **58**, 10204-10208.
457. N. Sugumaran, P. Everill, S. W. Swogger and D. P. Dubey, *J. Power Sources*, 2015, **279**, 281-293.
458. D. Pavlov and P. Nikolov, *J. Electrochem. Soc.*, 2012, **159**, A1215-A1225.
459. M. Saravanan, M. Ganesan and S. Ambalavanan, *J. Power Sources*, 2014, **251**, 20-29.
460. J. Wang, H. Hou, J. Hu, X. Wu, Y. Hu, M. Li, W. Yu, P. Zhang, S. Liang, K. Xiao, R. V. Kumar and J. Yang, *Electrochim. Acta*, 2019, **299**, 682-691.
461. J. Lannelongue, M. Cugnet, N. Guillet and A. Kirchev, *J. Power Sources*, 2017, **352**, 194-207.
462. B. Li, Y. Wang, N. Jiang, L. An, J. Song, Y. Zuo, F. Ning, H. Shang and D. Xia, *Nano Energy*, 2020, **72**, 104727.
463. Q. Li, Y. Qiao, S. Guo, K. Jiang, Q. Li, J. Wu and H. Zhou, *Joule*, 2018, **2**, 1134-1145.
464. M. Anji Reddy and M. Fichtner, *J. Mater. Chem.*, 2011, **21**, 17059-17062.
465. F. Gschwind, H. Euchner and G. Rodriguez-Garcia, *Eur. J. Inorg. Chem.*, 2017, **2017**, 2784-2799.
466. F. Gschwind, G. Rodriguez-Garcia, D. J. S. Sandbeck, A. Gross, M. Weil, M. Fichtner and N. Hörmann, *J. Fluorine Chem.*, 2016, **182**, 76-90.
467. X. Zhao, Q. Li, T. Yu, M. Yang, K. Fink and X. Shen, *Sci. Rep.*, 2016, **6**, 19448.
468. X. Hu, F. Chen, S. Wang, Q. Ru, B. Chu, C. Wei, Y. Shi, Z. Ye, Y. Chu, X. Hou and L. Sun, *ACS Appl. Mater. Interfaces*, 2019, **11**, 9144-9148.
469. H. Jiang and X. Ji, *Carbon Energy*, 2020, **2**, 437-442.
470. G. Chen, F. Zhang, Z. Zhou, J. Li and Y. Tang, *Adv. Energy Mater.*, 2018, **8**, 1801219.
471. K. Shin, F. Zhang, X. Ou, N. Wu, C.-S. Lee and Y. Tang, *J. Mater. Chem. A*, 2019, **7**, 10930-10935.
472. J. Holoubek, Y. Yin, M. Li, M. Yu, Y. S. Meng, P. Liu and Z. Chen, *Angew. Chem., Int. Ed.*, 2019, **58**, 18892-18897.
473. L. Zhang and H. Wang, *ChemElectroChem*, 2019, **6**, 4637-4644.
474. X. Xu, K. Lin, D. Zhou, Q. Liu, X. Qin, S. Wang, S. He, F. Kang, B. Li and G. Wang, *Chem*, 2020, **6**, 902-918.
475. D. Xie, M. Zhang, Y. Wu, L. Xiang and Y. Tang, *Adv. Funct. Mater.*, 2020, **30**, 1906770.
476. G. Wang, B. Kohn, U. Scheler, F. Wang, S. Oswald, M. Löffler, D. Tan, P. Zhang, J. Zhang and X. Feng, *Adv. Mater.*, 2020, **32**, 1905681.
477. Y. Luo, F. Zheng, L. Liu, K. Lei, X. Hou, G. Xu, H. Meng, J. Shi and F. Li, *ChemSusChem*, 2020, **13**, 2239-2244.
478. P. Liu, J. Liu, S. Cheng, W. Cai, F. Yu, Y. Zhang, P. Wu and M. Liu, *Chem. Eng. J.*, 2017, **328**, 1-10.
479. Y. Zhang, H. Hu, Z. Wang, B. Luo, W. Xing, L. Li, Z. Yan and L. Wang, *Nano Energy*, 2020, **68**, 104226.
480. J. Bao, N. Lin, H. Lin, J. Guo, H. Gao and W. Gao, *J. Energy Chem.*, 2021, **55**, 509-516.
481. D. Pei, J. Bao, C. Liang, Y. Chen, M. Zhao and H. Lu, *Mater. Lett.*, 2020, **280**, 128553.
482. S. Muduli, N. K. Rotte, V. Naresh and S. K. Martha, *J. Energy Storage*, 2020, **29**, 101330.
483. S. Muduli, V. Naresh and S. K. Martha, *J. Electrochem. Soc.*, 2020, **167**, 090512.
484. F. Yu, Z. Liu, R. Zhou, D. Tan, H. Wang and F. Wang, *Mater. Horiz.*, 2018, **5**, 529-535.
485. X. Ding, F. Zhang, B. Ji, Y. Liu, J. Li, C.-S. Lee and Y. Tang, *ACS Appl. Mater. Interfaces*, 2018, **10**, 42294-42300.
486. H. Wang, M. Yoshio, A. K. Thapa and H. Nakamura, *J. Power Sources*, 2007, **169**, 375-380.
487. Y. Wang, C. Zheng, L. Qi, M. Yoshio, K. Yoshizuka and H. Wang, *J. Power Sources*, 2011, **196**, 10507-10510.
488. C. Arbizzani, S. Beninati, M. Lazzari, F. Soavi and M. Mastragostino, *J. Power Sources*, 2007, **174**, 648-652.

489. D. D. Potphode, S. P. Mishra, P. Sivaraman and M. Patri, *Electrochim. Acta*, 2017, **230**, 29-38.
490. K. Machida, S. Suematsu, S. Ishimoto and K. Tamamitsu, *J. Electrochem. Soc.*, 2008, **155**, A970.
491. H.-q. Li, Y. Zou and Y.-y. Xia, *Electrochim. Acta*, 2007, **52**, 2153-2157.
492. J. Zhu, Y. Xu, Y. Fu, D. Xiao, Y. Li, L. Liu, Y. Wang, Q. Zhang, J. Li and X. Yan, *Small*, 2020, **16**, 1905838.
493. P. Yu, Y. Zeng, Y. Zeng, H. Dong, H. Hu, Y. Liu, M. Zheng, Y. Xiao, X. Lu and Y. Liang, *Electrochim. Acta*, 2019, **327**, 134999.
494. Z. Zhou, X. Zhou, M. Zhang, S. Mu, Q. Liu and Y. Tang, *Small*, 2020, **16**, 2003174.
495. Y. Zhu, X. Ye, H. Jiang, J. Xia, Z. Yue, L. Wang, Z. Wan, C. Jia and X. Yao, *J. Power Sources*, 2020, **453**, 227851.
496. P. Liu, W. Liu, Y. Huang, P. Li, J. Yan and K. Liu, *Energy Storage Mater.*, 2020, **25**, 858-865.
497. P. Liu, Y. Gao, Y. Tan, W. Liu, Y. Huang, J. Yan and K. Liu, *Nano Res.*, 2019, **12**, 2835-2841.
498. Y. Lu, Z. Li, Z. Bai, H. Mi, C. Ji, H. Pang, C. Yu and J. Qiu, *Nano Energy*, 2019, **66**, 104132.
499. J. Han, K. Wang, W. Liu, C. Li, X. Sun, X. Zhang, Y. An, S. Yi and Y. Ma, *Nanoscale*, 2018, **10**, 13083-13091.
500. N. Chang, T. Li, R. Li, S. Wang, Y. Yin, H. Zhang and X. Li, *Energy Environ. Sci.*, 2020, **13**, 3527-3535.
501. Z. Huang, A. Chen, F. Mo, G. Liang, X. Li, Q. Yang, Y. Guo, Z. Chen, Q. Li, B. Dong and C. Zhi, *Adv. Energy Mater.*, 2020, **10**, 2001024.
502. N. Wu, W. Yao, X. Song, G. Zhang, B. Chen, J. Yang and Y. Tang, *Adv. Energy Mater.*, 2019, **9**, 1803865.
503. M. E. Arroyo-de Dompablo, A. Ponrouch, P. Johansson and M. R. Palacín, *Chem. Rev.*, 2020, **120**, 6331-6357.
504. M. Wang, C. Jiang, S. Zhang, X. Song, Y. Tang and H.-M. Cheng, *Nat. Chem.*, 2018, **10**, 667-672.
505. H. D. Yoo, I. Shterenberg, Y. Gofer, R. E. Doe, C. C. Fischer, G. Ceder and D. Aurbach, *J. Electrochem. Soc.*, 2014, **161**, A410-A415.
506. H. D. Yoo, S.-D. Han, R. D. Bayliss, A. A. Gewirth, B. Genorio, N. N. Rajput, K. A. Persson, A. K. Burrell and J. Cabana, *ACS Appl. Mater. Interfaces*, 2016, **8**, 30853-30862.
507. H. Jiao, J. Wang, J. Tu, H. Lei and S. Jiao, *Energy Technol.*, 2016, **4**, 1112-1118.
508. H. Lei, J. Tu, D. Tian and S. Jiao, *New J. Chem.*, 2018, **42**, 15684-15691.
509. L. O. Valøen and J. N. Reimers, *J. Electrochem. Soc.*, 2005, **152**, A882.
510. X. Jiang, L. Luo, F. Zhong, X. Feng, W. Chen, X. Ai, H. Yang and Y. Cao, *ChemElectroChem*, 2019, **6**, 2615-2629.
511. D. Bernardi, E. Pawlikowski and J. Newman, *J. Electrochem. Soc.*, 1985, **132**, 5-12.
512. M. F. Lagadec, R. Zahn and V. Wood, *Nat. Energy*, 2019, **4**, 16-25.
513. B. W. Ricketts and C. Ton-That, *J. Power Sources*, 2000, **89**, 64-69.
514. J. H. Jang, S. Yoon, B. H. Ka, Y.-H. Jung and S. M. Oh, *J. Electrochem. Soc.*, 2005, **152**, A1418.
515. L. Xing, O. Borodin, G. D. Smith and W. Li, *J. Phys. Chem. A*, 2011, **115**, 13896-13905.
516. O. Borodin, W. Behl and T. R. Jow, *J. Phys. Chem. C*, 2013, **117**, 8661-8682.
517. A. von Wald Cresce, M. Gobet, O. Borodin, J. Peng, S. M. Russell, E. Wikner, A. Fu, L. Hu, H.-S. Lee, Z. Zhang, X.-Q. Yang, S. Greenbaum, K. Amine and K. Xu, *J. Phys. Chem. C*, 2015, **119**, 27255-27264.
518. Z. Chen, Y. Tang, X. Du, B. Chen, G. Lu, X. Han, Y. Zhang, W. Yang, P. Han, J. Zhao and G. Cui, *Angew. Chem., Int. Ed.*, 2020, **59**, 21769-21777.
519. Y. Wang, Y. Zhang, Q. Duan, P.-K. Lee, S. Wang and D. Y. W. Yu, *J. Power Sources*, 2020, **471**, 228466.
520. W. Hong, L. Wang, K. Liu, X. Han, Y. Zhou, P. Gao, R. Ding and E. Liu, *J. Alloys Compd.*, 2018, **746**, 292-300.
521. N. M. Shinde, Q. X. Xia, J. M. Yun, P. V. Shinde, S. M. Shaikh, R. K. Sahoo, S. Mathur, R. S. Mane and K. H. Kim, *Electrochim. Acta*, 2019, **296**, 308-316.
522. D. Qu, L. Wang, D. Zheng, L. Xiao, B. Deng and D. Qu, *J. Power Sources*, 2014, **269**, 129-135.
523. X. Lang, H. Mo, X. Hu and H. Tian, *Dalton Trans.*, 2017, **46**, 13720-13730.
524. H. Mo, H. Nan, X. Lang, S. Liu, L. Qiao, X. Hu and H. Tian, *Ceram. Int.*, 2018, **44**, 9733-9741.
525. S. S. Patil, D. P. Dubal, V. G. Deonikar, M. S. Tamboli, J. D. Ambekar, P. Gomez-Romero, S. S. Kolekar, B. B. Kale and D. R. Patil, *ACS Appl. Mater. Interfaces*, 2016, **8**, 31602-31610.
526. C. M. Ghimbeu, E. Raymundo-Piñero, P. Fioux, F. Béguin and C. Vix-Guterl, *J. Mater. Chem.*, 2011, **21**, 13268-13275.
527. C. Wang, P. Zhou, Z. Wang, Y. Liu, P. Wang, X. Qin, X. Zhang, Y. Dai, M.-H. Whangbo and B. Huang, *RSC Adv.*, 2018, **8**, 12841-12847.
528. D. P. Dubal, N. R. Chodankar, D.-H. Kim and P. Gomez-Romero, *Chem. Soc. Rev.*, 2018, **47**, 2065-2129.
529. B. C. Kim, J.-Y. Hong, G. G. Wallace and H. S. Park, *Adv. Energy Mater.*, 2015, **5**, 1500959.
530. C. Lethien, J. Le Bideau and T. Brousse, *Energy Environ. Sci.*, 2019, **12**, 96-115.
531. P. Zhang, Y. Li, G. Wang, F. Wang, S. Yang, F. Zhu, X. Zhuang, O. G. Schmidt and X. Feng, *Adv. Mater.*, 2019, **31**, 1806005.
532. K. Robert, C. Douard, A. Demortière, F. Blanchard, P. Roussel, T. Brousse and C. Lethien, *Adv. Mater. Technol.*, 2018, **3**, 1800036.
533. W. Wang, Y. Lu, M. Zhao, R. Luo, Y. Yang, T. Peng, H. Yan, X. Liu and Y. Luo, *ACS Nano*, 2019, **13**, 12206-12218.
534. X. He, R. Li, J. Liu, Q. Liu, R. chen, D. Song and J. Wang, *Chem. Eng. J.*, 2018, **334**, 1573-1583.
535. X. Cao, Y. Liu, Y. Zhong, L. Cui, A. Zhang, J. M. Razal, W. Yang and J. Liu, *J. Mater. Chem. A*, 2020, **8**, 1837-1848.
536. J. Xie, Y. Yang, G. Li, H. Xia, P. Wang, P. Sun, X. Li, H. Cai and J. Xiong, *RSC Adv.*, 2019, **9**, 3041-3049.
537. N. Zhang, Y. Li, J. Xu, J. Li, B. Wei, Y. Ding, I. Amorim, R. Thomas, S. M. Thalluri, Y. Liu, G. Yu and L. Liu, *ACS Nano*, 2019, **13**, 10612-10621.
538. K. Silambarasan and J. Joseph, *ChemSusChem*, 2018, **11**, 3081-3086.
539. K. Silambarasan and J. Joseph, *ChemElectroChem*, 2018, **5**, 2808-2815.
540. Z. Li, D. Chen, Y. An, C. Chen, L. Wu, Z. Chen, Y. Sun and X. Zhang, *Energy Storage Mater.*, 2020, **28**, 307-314.
541. L. Han, H. Huang, J. Li, X. Zhang, Z. Yang, M. Xu and L. Pan, *J. Mater. Chem. A*, 2020, **8**, 15042-15050.
542. G.-H. An, J. Hong, S. Pak, Y. Cho, S. Lee, B. Hou and S. Cha, *Adv. Energy Mater.*, 2020, **10**, 1902981.
543. S. Chen, L. Ma, K. Zhang, M. Kamruzzaman, C. Zhi and J. A. Zapien, *J. Mater. Chem. A*, 2019, **7**, 7784-7790.
544. K. Li, Y. Shao, S. Liu, Q. Zhang, H. Wang, Y. Li and R. B. Kaner, *Small*, 2017, **13**, 1700380.

545. M. E. Suss and V. Presser, *Joule*, 2018, **2**, 10-15.
546. M. E. Suss, S. Porada, X. Sun, P. M. Biesheuvel, J. Yoon and V. Presser, *Energy Environ. Sci.*, 2015, **8**, 2296-2319.
547. Q. Li, Y. Zheng, D. Xiao, T. Or, R. Gao, Z. Li, M. Feng, L. Shui, G. Zhou, X. Wang and Z. Chen, *Adv. Sci.*, 2020, **7**, 2002213.
548. M. Pasta, C. D. Wessells, Y. Cui and F. La Mantia, *Nano Lett.*, 2012, **12**, 839-843.
549. J. Chang, F. Duan, C. Su, Y. Li and H. Cao, *Environ. Sci.: Water Res. Technol.*, 2020, **6**, 373-382.
550. F. Chen, Y. Huang, L. Guo, M. Ding and H. Y. Yang, *Nanoscale*, 2017, **9**, 10101-10108.
551. H. Kong, M. Yang, Y. Miao and X. Zhao, *Energy Technol.*, 2019, **7**, 1900835.
552. D. Li, S. Wang, G. Wang, C. Li, X. Che, S. Wang, Y. Zhang and J. Qiu, *ACS Appl. Mater. Interfaces*, 2019, **11**, 31200-31209.
553. W. Xi and H. Li, *Environ. Sci.: Nano*, 2020, **7**, 764-772.
554. W. Xi and H. Li, *Environ. Sci.: Water Res. Technol.*, 2020, **6**, 296-302.
555. Q. Ren, G. Wang, T. Wu, X. He, J. Wang, J. Yang, C. Yu and J. Qiu, *Ind. Eng. Chem. Res.*, 2018, **57**, 6417-6425.
556. K. Silambarasan and J. Joseph, *Energy Technol.*, 2019, **7**, 1800601.
557. S. Tian, X. Zhang and Z. Zhang, *Desalination*, 2020, **479**, 114348.
558. P. Srimuk, J. Halim, J. Lee, Q. Tao, J. Rosen and V. Presser, *ACS Sustainable Chem. Eng.*, 2018, **6**, 3739-3747.
559. P. Srimuk, F. Kaasik, B. Krüner, A. Tolosa, S. Fleischmann, N. Jäckel, M. C. Tekeli, M. Aslan, M. E. Suss and V. Presser, *J. Mater. Chem. A*, 2016, **4**, 18265-18271.
560. W. Shi, X. Liu, T. Deng, S. Huang, M. Ding, X. Miao, C. Zhu, Y. Zhu, W. Liu, F. Wu, C. Gao, S.-W. Yang, H. Y. Yang, J. Shen and X. Cao, *Adv. Mater.*, 2020, **32**, 1907404.
561. Y. Li, Z. Ding, J. Li, J. Li, T. Lu and L. Pan, *Desalination*, 2019, **469**, 114098.
562. Y. Li, Z. Ding, X. Zhang, J. Li, X. Liu, T. Lu, Y. Yao and L. Pan, *J. Mater. Chem. A*, 2019, **7**, 25305-25313.
563. M. Torkamanzadeh, L. Wang, Y. Zhang, Ö. Budak, P. Srimuk and V. Presser, *ACS Appl. Mater. Interfaces*, 2020, **12**, 26013-26025.
564. J. Cao, Y. Wang, L. Wang, F. Yu and J. Ma, *Nano Lett.*, 2019, **19**, 823-828.
565. D. Sriramulu and H. Y. Yang, *Nanoscale*, 2019, **11**, 5896-5908.
566. F. Xing, T. Li, J. Li, H. Zhu, N. Wang and X. Cao, *Nano Energy*, 2017, **31**, 590-595.
567. L. Gao, Q. Dong, S. Bai, S. Liang, C. Hu and J. Qiu, *ACS Sustainable Chem. Eng.*, 2020, **8**, 9690-9697.
568. J. Lee, S. Kim, C. Kim and J. Yoon, *Energy Environ. Sci.*, 2014, **7**, 3683-3689.
569. N. Y. Yip, D. Brogioli, H. V. M. Hamelers and K. Nijmeijer, *Environ. Sci. Technol.*, 2016, **50**, 12072-12094.
570. D. Brogioli, *Phys. Rev. Lett.*, 2009, **103**, 058501.
571. F. La Mantia, M. Pasta, H. D. Deshazer, B. E. Logan and Y. Cui, *Nano Lett.*, 2011, **11**, 1810-1813.
572. F. Zhan, G. Wang, T. Wu, Q. Dong, Y. Meng, J. Wang, J. Yang, S. Li and J. Qiu, *J. Mater. Chem. A*, 2017, **5**, 20374-20380.
573. F. Zhan, G. Wang, T. Wu, Q. Dong, Y. Meng, J. Wang and J. Qiu, *Energy Technol.*, 2018, **6**, 238-241.
574. M. Ye, M. Pasta, X. Xie, Y. Cui and C. S. Criddle, *Energy Environ. Sci.*, 2014, **7**, 2295-2300.
575. M. Ye, M. Pasta, X. Xie, K. L. Dubrawski, J. Xu, C. Liu, Y. Cui and C. S. Criddle, *ACS Omega*, 2019, **4**, 11785-11790.
576. G. Tan and X. Zhu, *Energy Technol.*, 2020, **8**, 1900863.